

**Development of Novel Micaceous Glass Ceramics for Dental
Applications using CAD/CAM Systems**

Sebastian Broady

Submitted in accordance with the requirements for the degree of
PhD

The University of Leeds
Leeds Dental Institute

December, 2009

The candidate confirms that the work submitted is his/her own and that appropriate credit has been given where reference has been made to the work of others.

This copy has been supplied on the understanding that it is copyright material and that no quotation from the thesis may be published without proper acknowledgement.

Acknowledgements

I would like to thank, my supervisors, Prof. David Wood and Dr. Nigel Bubb for their kind advice and patience throughout the course of my research.

I, additionally, would like to express my sincerest gratitude to the following; many of whom have proven invaluable.

Prof. Sue Kilcoyne of the University of Salford for her advice and help throughout the project.

Colin Kilner, University of Leeds, Chemistry; Geoff Parr, University of Salford, School of Computing, Science & Engineering and David Wright, University of Leeds, Institute of Materials Research for their help with XRD. Dr. Eric Condliffe, Leeds University Institute for Materials Research, for help with EMPA.

Phil Bentley, Clemens Ritter, Thomas Hansen, Institut Laue-Langevin, Maisoon Al-Jawad, Barts and The London School of Medicine and Dentistry for their help and advice with regard to the neutron experiments both on sample environment and data collection and manipulation.

Prof. James Nobbs, University of Leeds, Colour Chemistry, for the colour-space measurements.

David Rowe of H.C.Stark for his helpful advice on the design and fabrication of the niobium furnace insert.

Jackie Hudson (Oral Biology, Leeds Dental Institute) and Geoff Parr for their help with the electron microscopy.

David Foakes, Leeds Dental Institute, Workshop, for his invaluable help in manufacturing various bespoke items.

All staff and co-students in Leeds Dental Institute, Oral Biology, for their help and moral support.

Lastly, I would like to thank the Engineering and Physical Sciences Research Council (EPSRC) for funding this research and my studentship.

Abstract

The original aim of this project was to develop and characterise machinable glass-ceramic materials for dental applications with the final outcome of producing a range of materials matching tooth enamel for aesthetics and mechanical properties.

The candidate glass is a micaceous glass-ceramic which is compositionally based on a ternary phase system of 90 molar % Ba-phlogopite ($\text{Ba}_{0.5}\text{Mg}_3(\text{Si}_3\text{AlO}_{10})\text{F}_2$), 6 molar % calcium phosphate ($\text{Ca}_3(\text{PO}_4)_2$) and 4 molar % cordierite ($\text{Mg}_2\text{Al}_4\text{Si}_5\text{O}_{18}$). Initial assumptions about the structure and phase composition of this material have been proven wrong. Since effective material development can only occur where one is knowledgeable of its prior state; a significant amount of work was focused on phase characterisation using a number of novel techniques such as single crystal diffraction, acid dissolution and spray drying in conjunction with neutron diffraction at ILL and conventional powder XRD. Results have been analysed with an array of software including *GSAS* and *Shelx '97* for refinement of powder and single crystal data, respectively. Successful data refinement has significantly advanced understanding of phase formation and development in this material.

A thorough analysis of mechanical properties is also presented and includes BFS (biaxial flexure) and Vickers microhardness tests with comparisons between samples after different heat treatments. DTA analysis including activation energy and nucleation temperature determination has been performed on two variants of the same composition in order to determine the sensitivity of this composition to the effects of differing grades of feedstocks on the resulting material; and is the basis of an assessment of commercial viability. Optical/SEM micrographs and EDS/EMPA data sets are also presented. Progress in the colouring of these glass-ceramics with the aim of matching natural dental shades is encouraging and work includes colour-space data for the first time. Ultimately, the final goal is the production of a machinable glass-ceramic, suitable for dental restoration, which possesses a high degree of machinability and is also reproducible under industrial high-volume conditions.

Contents

Acknowledgements	ii
Abstract	iii
Contents	iv
Figures	viii
Tables	xiii
1 Introduction	1
1.1 Aims of Project	1
1.2 Objectives.....	2
1.3 Prior Investigations of Fluormica Glass-Ceramics.....	2
1.4 Effect of Fluorine and Alumina Additions.....	4
1.5 Commercial Fluormica Glass-Ceramics	6
1.6 Translucent Mica Glass-Ceramics	9
1.7 Ca-Phlogopite Machinable Glass-Ceramics	9
1.8 Outline of Thesis	10
2 Literature Review	12
2.1 Mica Structure.....	12
2.1.1 Ideal Mica Structure.....	12
2.1.2 Distortions of the Ideal Structure.....	14
2.1.3 Polytypism.....	16
2.1.4 ‘Brittle’ Micas	17
2.1.5 Kinoshitalite	18
2.2 Theory of Glasses.....	18
2.2.1 Amorphous state.....	18
2.2.2 Eutectic Glasses	20
2.2.3 Glass Formation	21
2.2.3.1 Goldschmidt Theory.....	21
2.2.3.2 Zachariasen Theory	21
2.2.3.3 Goodman Model.....	22
2.2.3.4 Inorganic Polymer Model	23
2.2.3.5 Dietzel’s structural model	24
2.3 Glass-Ceramics	24
2.3.1 Crystallisation of Glasses.....	25

2.3.2 Homogeneous Nucleation	25
2.3.3 Heterogeneous Nucleation	27
2.3.4 Glass Phase Separation	28
2.3.5 Crystal Growth	29
2.3.6 Ostwald Ripening.....	29
2.4 X-Ray and Neutron Diffraction	30
2.4.1 Bragg's Law	30
2.4.2 'Real' Crystal Structure.....	31
2.4.3 Reciprocal Lattice	33
2.4.4 Ewald's Sphere.....	34
2.4.5 Powder/Amorphous Case.....	35
2.4.6 Powder Diffraction.....	35
2.4.7 The Structure Factor.....	36
2.4.8 Types of scattering.....	37
2.4.9 Compton scattering	38
2.4.10 Multiple Scattering.....	38
2.4.11 Sample Attenuation.....	39
2.4.12 X-ray Fluorescence	39
2.4.13 Coherent/Incoherent Scattering.....	39
2.5 Rietveld Refinement (Theory)	40
2.5.1 Le Bail and Pawley Methods	45
2.6 Single Crystal Diffraction	45
3 Materials and Methods	47
3.1 Frit Preparation.....	47
3.1.1 Original Feedstock.	48
3.1.2 Commercial Feedstock.....	48
3.2 Making Glass Rods	48
3.3 Investment of Glass Rods.....	50
3.4 Heat Treatment of Glass Rods	51
3.5 Sectioning of Glass-Ceramic Rods.	52
3.6 Polishing of Samples.....	52
3.7 Bi-axial Flexure.....	53
3.8 Vickers Hardness	54
3.9 SEM/EDS	55
3.10 Electron Microprobe Analysis (EMPA).....	56

3.11 Glass Grinding and Sieving	56
3.12 Differential Thermal Analysis.....	56
3.12.1 Optimum Nucleation Temperature	57
3.12.2 Activation Energy Determination	57
3.13 Coloured LDIG 24 Commercial Samples	58
3.13.1 Coloured Frits.....	59
3.14 Coloured Glass-Ceramics.....	60
3.14.1 Colour Spaces.....	60
3.15 Single Crystal Growth.....	61
3.16 X-ray Diffraction.....	64
3.16.1 Powder XRD	64
3.16.2 Single Crystal XRD.....	65
3.17 Software	65
3.17.1 <i>Dirdif 2008</i>	65
3.17.2 <i>Shelx '97</i>	66
3.17.3 <i>GSAS</i>	67
3.17.4 Le Bail fit in <i>GSAS</i>	67
3.17.5 Rietveld fit in <i>GSAS</i>	68
3.17.6 <i>Platon</i>	69
3.17.7 <i>Searchmatch</i> (version 3, 1, 0, 0)	69
3.17.8 <i>Vesta</i> (version 2.1.1)	70
3.17.9 <i>Turbo Pascal</i> (version 7).....	70
3.18 Spray Drying (XRD).....	70
3.19 Acid Treatment (XRD)	72
3.20 Neutron Diffraction.....	73
3.20.1 Mirror Furnace	74
4 Results and Discussion.....	76
4.1 Material Properties of LDIG 24	76
4.1.1 Preliminary Analysis	76
4.1.2 Optimum Nucleation.....	77
4.1.3 Activation Energy	79
4.1.4 Energy Dispersive X-ray Spectroscopy	80
4.1.5 Acid Solubility	81
4.1.6 Mechanical Testing.....	83
4.1.7 SEM/Optical Microscopy.....	86

4.1.8 Gloss Measurements	89
4.1.9 Colour Measurement.....	90
4.2 X-ray Analysis	94
4.2.1 Single Crystal Growth Experiment	94
4.2.2 Powder X-ray Diffraction	101
4.2.2.1 Preferred Orientation in Sample Rods	101
4.2.2.2 Surface Nucleation.....	104
4.2.2.2.1 Phase identification and discussion.....	108
4.2.2.3 XRD Analysis of Bulk Sample Cerammed by Standard Heat Treatment.....	111
4.2.2.3.1 Phase identification and discussion.....	115
4.2.2.4 Rietveld/Le Bail fit of Powdered Single Crystal Bulk Sample (Untreated)	117
4.2.2.5 Full Rietveld Refinement of Powdered Single Crystal Bulk Sample	121
4.2.2.5.1 Phase Identification and Discussion.....	128
4.2.2.6 Spray Dried Sample of Bulk Cerammed by Standard Heat Treatment.....	133
4.2.2.7 Summary	137
4.2.2.8 Relationships with Material Properties of LDIG 24 Commercial	140
4.3 Neutron Diffraction.....	142
4.3.1 Experimental Problems	142
4.3.2 Vacuum Neutron Diffraction on LDIG 24 Glass-Ceramics (28/6/2002).....	146
4.3.3 Neutron diffraction in Air Experiment with Mirror Furnace (2/5/2007).....	156
5 Conclusions	159
5.1 Future Work	163
References	164

Figures

Figure 1.01. Ternary phase diagram with the LDIG 24 glass composition highlighted.	1
Figure 1.02. Micrograph of Macor® glass ceramic showing poor interlocking microstructure of mica crystallites. (Beall, 1972)	8
Figure 1.03. Micrograph of Macor® glass ceramic showing ‘house of cards’ microstructure. (Beall, 1972)	8
Figure 1.04. A crown fabricated by dental CAD/CAM system with glass ceramic KZr-1050 (above glass ceramic article heat treated at 1050 °C) (Li <i>et al.</i> , 2006).....	10
Figure 2.01. Specimen of rare zinnwaldite mica (KLiFeAl(AlSi ₃)O ₁₀ (OH,F) ₂) (own work).....	12
Figure 2.02. The structure of the three layer TOT unit.	14
Figure 2.03. Undistorted hexagonal net of apical oxygens in a trioctahedral mica (Fleet, 2003).....	16
Figure 2.04. Distorted hexagonal net of apical oxygens in a dioctahedral mica (Fleet, 2003).	16
Figure 2.05. A plot of specific volume versus temperature.	20
Figure 2.06. Plot of rate versus temperature for nucleation (1) and crystal growth (2) curves.....	25
Figure 2.07. A plot of change in free energy ΔG versus embryo radius for each energy term.	27
Figure 2.08. An example of heterogeneous nucleation.....	28
Figure 2.09. Unit cell with the symmetry elements of space group Pmna.	33
Figure 2.10. Reciprocal lattice.....	34
Figure 2.11. Ewald construction for a set of planes at the correct Bragg angle. (Hammond, 2001).....	35
Figure 2.12. Diffraction from a powder	36
Figure 3.01. Schematic of the single 18 mm rod mould, left, and the larger multiple 14 mm rod mould, right.....	50
Figure 3.02. 18 mm glass rod, left, and the standard treatment regime, right.	51
Figure 3.03. Pictures of the biaxial flexure mounting with glass-ceramic disc under test.....	54
Figure 3.04. Cerammed LDIG 24 commercial + 2% Ni(II)O ₂ (by mol), left, and LDIG 24 commercial + 3 % Ni(II)O ₂ + 1 % Fe(II)SO ₄ .7H ₂ O (by mol), right.....	60
Figure 3.05. Apparatus used to manufacture single crystal.....	62

Figure 3.06. Temperature-time profile.....	63
Figure 3.07. Crystal in situ after experiment.....	63
Figure 3.08. Single crystals extracted after experiment; the scale on the left is in millimetres (mm).....	64
Figure 3.09. Pictures of the spray dryer from the side and from above.	72
Figure 3.10. Clockwise from the top; the sample stick holder, the mirror furnace (shown with aluminium shielding), an 8 mm sample rod undergoing heat-treatment.and a schematic of D20 at ILL (http://www.ill.eu/).	75
Figure 4.01. DTA trace of a selection of particle sizes for commercial LDIG 24.....	77
Figure 4.02. DTA trace of selection of particle sizes for original LDIG 24.	77
Figure 4.03. DTA with 1 hour nucleation hold for the original feedstock.	78
Figure 4.04. DTA with 1 hour nucleation hold for the commercial feedstock.....	78
Figure 4.05. Graph of $(T_{p1} - T_{p1}^0)$ for original (red) and commercial (black) formulations.....	79
Figure 4.06. Modified Kissinger plot for activation energy of commercial LDIG 24.....	80
Figure 4.07. Modified Kissinger plot for activation energy of original LDIG 24.....	80
Figure 4.08. Dual plot of BFS (MPa) (red line) and Vickers hardness (VHN) (blue line) versus hold temperature.	85
Figure 4.09. Optical micrograph of polished surface of LDIG 24 commercial (heat-treated @ 1100°C for 3 hours) showing a cell-like or grain structure; this may represent the separation of phases.	87
Figure 4.10. Optical micrograph of polished LDIG 24 commercial glass-ceramic (heat-treated @1100 °C for 3 hours).....	88
Figure 4.11. SEM (Secondary Electron Microscopy) micrograph of LDIG 24 commercial glass-ceramic, heat treated @ 1050 °C for 3 hours, showing voids in the polished sample surface.	88
Figure 4.12. Back-scattered electron micrograph of LDIG 24 commercial glass-ceramic heat treated @ 1050 °C for 3 hours; shows some acicular interlocking, although, there is no well formed ‘house of cards’ microstructure.	89
Figure 4.13. Coloured frits with corresponding cerammed article underneath after standard heat treatment.	91
Figure 4.14. Polyhedral structure of the single crystal specimen with octahedral layer (orange), tetrahedral layer (blue) and interlayer sites (green).	96
Figure 4.15. View along the b axis.	96
Figure 4.16. View along the c axis.....	97

Figure 4.17. The upper apical oxygen hexagonal layer corresponds to the highlighted octahedral surface.....	97
Figure 4.18. Pseudo X-ray powder diffraction pattern generated from the single crystal <i>.hkl</i> data file, in black, with an overlapping pattern of the refined model, from the <i>Shelxl.cif</i> , in red. The simulated X-ray source is Mo K α ($\lambda = 0.711 \text{ \AA}$).	101
Figure 4.19. Schematic showing the different sections cut from the same 18 mm sample rod.	102
Figure 4.20. Diffraction pattern of the sample taken from a lengthwise section of the rod.	102
Figure 4.21. Diffraction pattern of the sample taken from a cross-wise section of the rod.	103
Figure 4.22. Top section from a 14 mm glass-ceramic stud.	104
Figure 4.23. Le Bail fit of the full X-ray powder pattern of surface nucleated LDIG 24 commercial glass-ceramic heat treated @ 1150 °C for 3 hours.	105
Figure 4.24. Le Bail fit of the same pattern showing a reduced 2 theta range.	105
Figure 4.25. Le Bail fit of data with celsian phase marked in pink.	106
Figure 4.26. Le Bail fit of data with hexa-celsian phase marked in blue.	106
Figure 4.27. Le Bail fit of data with proto-enstatite phase marked in brown.....	107
Figure 4.28. Le Bail fit of data with clino-enstatite phase marked in yellow.....	107
Figure 4.29. Le Bail fit of powder pattern of a sample of powdered LDIG 24 commercial glass-ceramic after standard heat treatment (@1150 °C for 3 hours).	112
Figure 4.30. Le Bail fit with reduced 2 theta scale range.	112
Figure 4.31. Le Bail fit with F-kinoshitalite phase marked in red.....	113
Figure 4.32. Le Bail fit with clinoenstatite phase marked in turquoise.	113
Figure 4.33. Le Bail fit with proto-enstatite phase marked in blue.....	114
Figure 4.34. Le Bail fit with fluorapatite phase marked in brown.	114
Figure 4.35. Le Bail fit with dummy phase (isostructural with cristobalite) in yellow.....	115
Figure 4.36. Combined Rietveld/Le Bail fit of the powdered bulk single crystal sample.	119
Figure 4.37. Fit with the barium fluorophosphates phase (BFP) marked in brown.....	120
Figure 4.38. Close up of fit with BFP phase marked in brown.....	120
Figure 4.39. Visualisation of the BFP <i>.cif</i> (Crystallographic Information File) created to fit the pattern.	121

Figure 4.40. DTA trace of LDIG 24 commercial frit showing melting endotherm (red line).	122
Figure 4.41. Overlapping EDS spectra of two single crystals (platelets) of mica taken from the bulk specimen of section 4.2.2.4 (the black line is from the other crystal)	124
Figure 4.42. Full pattern Rietveld refinement of LDIG 24 commercial glass-ceramic taken from the single crystal growth experiment.	125
Figure 4.43. Rietveld refinement of the same pattern showing reduced 2 theta range.	125
Figure 4.44. Rietveld refinement with refined depleted F-kinoshitalite phase marked in pink.	126
Figure 4.45. Rietveld refinement with clinoenstatite phase marked in blue....	126
Figure 4.46. Rietveld refinement with cristobalite phase marked in yellow....	127
Figure 4.47. Rietveld refinement with sellaite phase marked in brown.....	127
Figure 4.48. Spray dried sample heat treated @ 1150 °C for 3 hours.	134
Figure 4.49. Sample heat treated @ 925 °C for 3 hours (not spray dried).	135
Figure 4.50. Neutron pattern of the sample holder in <i>GSAS</i>	144
Figure 4.51. Attempted match in <i>Searchmatch</i> with niobium (vacuum experiment).	144
Figure 4.52. Background image after initial vacuum furnace replacement; note the missing peak at ~ 60°.	145
Figure 4.53. Pattern of background plus amorphous signal with corundum and platinum patterns shown in black and red respectively.....	145
Figure 4.54. Thermogram of full pattern over heat treatment cycle.....	146
Figure 4.55. Thermogram of the same ramp viewing, front, the onset of crystallisation and growth.	147
Figure 4.56. Peak at 62.20° marked out previously, at a temperature of 805 °C just before the onset of crystallisation.....	147
Figure 4.57. Onset of crystallisation at 845 °C.....	148
Figure 4.58. @ 945 °C.	148
Figure 4.59. @ 906 °C.	149
Figure 4.60. @ 1002 °C.	149
Figure 4.61. @ 1066 °C.	150
Figure 4.62. Overlain patterns from above one can clearly see a fall in the 62 ° peak as the others rise.	150
Figure 4.63. Fluorapatite peaks.	151
Figure 4.64. Le Bail fit of pattern after subtraction of background by computer program, the temperature of the sample is 1201 °C.....	153

Figure 4.65. Le Bail fit of 1201 °C pattern with F-kinoshitalite phase marked in red.	154
Figure 4.66. Le Bail fit of 1201 °C with clinoenstatite phase marked in blue.	154
Figure 4.67. Le Bail fit of pattern at 1225 °C.	155
Figure 4.68. Le-Bail fit of 1225 °C pattern showing match with F-kinoshitalite.....	155
Figure 4.69. Le-Bail fit of 1225 °C pattern showing match with clinoenstatite.	156
Figure 4.70. Thermogram of entire run.	157
Figure 4.71. Same thermogram with a different view.	157
Figure 4.72. Possible sellaite and main phase interactions.....	158

Tables

Table 3.01. Showing the feedstock composition of LDIG 24 commercial glass and the origins of each feedstock component.	47
Table 3.02. Colour observations.	59
Table 3.03. Heat treatment regimes for each sample cerammed on the beam-line at ILL (RT (room temperature) is 24 °C).	74
Table 4.01. T_{p1} and T_g for different particle size fractions of both commercial (Com) and original (Orig) LDIG 24.	76
Table 4.02. Compositional analysis of commercial LDIG 24.	81
Table 4.03. Compositional analysis of original LDIG 24.	81
Table 4.04. Biaxial flexure with standard deviation and Vickers hardness with associated t-statistic for two sets of 25 readings and average standard deviation for a range of samples produced from different heat treatments.	83
Table 4.05. LDIG 24 glass-ceramics cerammed by different heat treatments with associated gloss measurement for three different surface finishes.	90
Table 4.06. Colour space parameters for a number of coloured commercial LDIG 24 glass-ceramics doped by mol %; the undoped material is listed as 'none'.	92
Table 4.07. Results of EMPA on the single crystal (post-experiment).	95
Table 4.08. Lattice parameters of mica specimen with absolute errors below.	98
Table 4.09. Refined structural parameters of the triclinic cell as found in a .cif file; the absolute error is listed below each value in bold and is only included where parameters have been directly refined.	98
Table 4.10. Lattice parameters of monoclinic unit cell.	99
Table 4.11. Comparison of tetrahedral rotation and octahedral flattening for natural kinoshitalite mica ($Ba(Mg_{2.64}Mn_{0.31})(Si_2Al_2)O_{10}(OH_{1.61}F_{0.37})$) and the crystal sample (Fleet, 2003).	100
Table 4.12. Phases and associated lattice parameters used to fit the data, ortho-celsian is included for completeness. Absolute errors are listed where appropriate.	108
Table 4.13. Phases and their respective lattice parameters used to fit the pattern; errors are shown where applicable.	115
Table 4.14. Lattice parameters used in the refinement with absolute errors listed underneath.	128

Table 4.15. Showing the calculated weight fraction and volume fraction for each phase in the sample, after acid treatment, with the associated scale fractions produced by <i>GSAS</i>.....	128
Table 4.16. Showing the calculated weight fraction, volume fraction and scale fraction for each phase in the pattern of figure 4.48.	137

1 Introduction

1.1 Aims of Project

This thesis concerns a single glass-ceramic material known as LDIG 24; the candidate glass composition is produced from a ternary system based on 90 molar % barium fluormica ($\text{Ba}_{0.5}\text{Mg}_3(\text{Si}_3\text{AlO}_{10})\text{F}_2$), 6 molar % calcium phosphate ($\text{Ca}_3(\text{PO}_4)_2$) and 4 molar % cordierite ($\text{Mg}_2\text{Al}_4\text{Si}_5\text{O}_{18}$). The first machinable micaceous glass-ceramics based on the general stoichiometry of fluormica were developed in the 1970s as either tri-silicic Macor® or tetra-silicic Dicor® (Grossman, 1974). Studies on barium-mica glass-ceramics have been relatively recent and coincide with interest in applications with CAD/CAM technology and restorative dentistry.

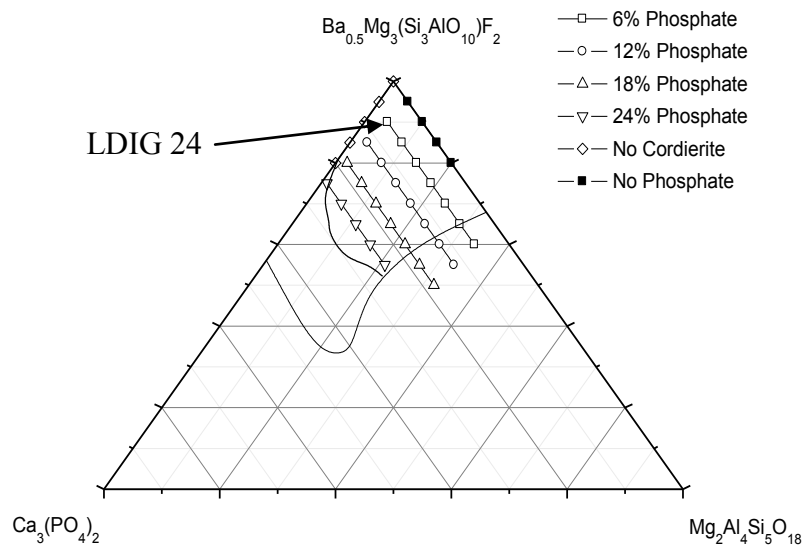


Figure 1.01. Ternary phase diagram with the LDIG 24 glass composition highlighted.

The overall aims of the project were to produce a mica glass-ceramic from ‘commercial’ feedstock and to compare the crystallisation and subsequent structure and properties of the resultant materials with those of glass-ceramics produced using

analar grade reagents, with a view to taking the 'commercial' material towards a viable commercial route for manufacture. The original composition of this material, studied prior to 2006, had the same nominal composition, however, different impurities in the original analar grade feedstocks lead to noticeable differences in both appearance and melting viscosity of the original formulation glass. These impurities are below the detection limit of EDS (Energy Dispersive Spectroscopy) and have not been successfully determined despite a number of attempts.

1.2 Objectives

The main objectives of this project were as follows.

The comparison of commercial and pure reagents derived LDIG 24 in terms of crystallisation temperatures, activation energies, compositions, and physical properties.

The production of coloured glass-ceramics through the addition of suitable dopants to LDIG 24 base glass.

To devise methods that elucidate the composition of the crystal phases formed during crystallisation.

The use of kinetic neutron diffraction to better understand the mechanism of crystallisation in these materials, performed for the first time in air rather than a vacuum in order to simulate likely commercial conditions of manufacture.

1.3 Prior Investigations of Fluormica Glass-Ceramics.

The LDIG 24 ternary glass system, and similar variants thereof, has been studied prior to this work for the purposes of structure characterisation and microstructural enhancement with varying degrees of success. The compositional system on which current work is based was first patented in 2004 (Wood *et al.*, 2004).

Hoda and Beall (1982) undertook the first studies of alkali earth fluor mica glass-ceramics with Ba, Ca and Sr (strontium) substitutions. Difficulties were found in casting, although, several compositions were investigated. The first detailed studies of glass-ceramics produced from the same tertiary phase diagram as that for the

current work were by Uno *et al* (1991). Glasses in the system $70(\text{Ba}_{0.5}\text{Mg}_3(\text{Si}_3\text{AlO}_{10})\text{F}_2) - (30 - x)(\text{Mg}_2\text{Al}_4\text{Si}_5\text{O}_{18}) - x(\text{Ca}_3(\text{PO}_4)_2)$, where $x = 0$ to 10 wt%, were investigated to determine the effect of calcium phosphate on crystallisation. Excess MgF_2 (3 wt %) was added as a precaution against fluorine volatilisation from the melt. Batches were melted in platinum crucibles at 1500 °C, cast in graphite moulds, and annealed at 600 °C prior to crystallisation at reheated temperatures of 850 °C to 1150 °C. EDS work carried out on the mica phase found a barium - calcium solid solution of compositions and small quantities of enstatite and tri-calcium phosphate. A relationship between $\text{Ca}_3(\text{PO}_4)_2$ content (wt %) and bending strength of glass ceramics heat-treated at 1050 °C was found. The bending strength of glass-ceramic samples containing 2 wt % $\text{Ca}_3(\text{PO}_4)_2$ was 220 MPa, whereas for glass-ceramics containing 8 wt %, bending strength was 350 MPa. It was theorised that calcium phosphate formation improved crystal growth and glass stability, enabling a dense ‘house of cards’ crystalline microstructure. A substantial proportion of the mica volume fraction was reported to be approaching the nanocrystalline limit with particle sizes $< 1\mu\text{m}$ when glasses were reheated at 1000 °C.

A second paper of the same authors (Uno *et al.*, 1993) investigated the properties of glass-ceramics produced from a composition of $91.75[\text{Ca}_{0.46}\text{K}_{0.14}\text{Mg}_3(\text{Si}_3\text{Al})\text{O}_{10}\text{F}_2] - 8.25 [\text{ZrO}_2]$ (wt%). Attempts were made to improve the fracture toughness of these materials by incorporation of zirconia nanocrystals into the glass-ceramic matrix. They concluded that two zirconia polytypes were precipitated and a unique nanocomposite material was formed with calcium mica platelets up to 2 μm long and ZrO_2 nano-particles 20 - 50 nm in size. Bending strength and fracture toughness values of 500 MPa and $3.2 \text{ MPa m}^{0.5}$ were reported respectively for samples reheated at 950 °C. Transmission electron microscopy (TEM) observations showed that the sizes of mica platelets increased with increasing crystallization hold temperatures.

Hill *et al* (2009) have characterised fluormica glass-ceramics by ^{19}F magic spinning nuclear magnetic resonance spectroscopy; including the same LDIG 24 formulation that concerns the present study. MAS-NMR measures isotropic chemical shift which is dependent on the chemical environment of the isotope in the sample. The chemical shift anisotropy is measured in ppm and measurements were taken with spinning rates exceeding 20 kHz. This glass-ceramic was determined to contain a

large volume fraction of fluorphlogopite (F-Mg₃) corresponding to a sharp peak at 178 ppm and very small quantities of another highly ordered phase corresponding to either Al-F-Ca(n) or Al-F-Mg(n) compositions. Measurements also revealed that very little fluorine remained in the residual glass (< 10 %).

Kinetic neutron diffraction, at ILL, has also been used to characterise bioactive glass-ceramics, intended for bone replacement, based upon a glass composition of 12 mol % fluorapatite, 3 mol % cordierite and 85 mol % barium mica (Bentley *et al.*, 2007). Cylindrical glass rods, 14 mm in diameter, were placed into niobium (Nb) cans in an Nb furnace and subjected to five-stage heat treatments including isothermal holds at 622 °C and 1040 °C. Kinetic patterns were recorded at 3 minute intervals and data were analysed in Fullprof and Lamp. It was found that the main fluormica phase forms as a 2Or polytype at 827 °C and that the volume fraction reached 80 % of maximum only nine minutes after the onset of crystallisation. At 883 °C, additional peaks occur which have been interpreted as a phase transition of the fluormica phase from 2Or to 1M polytypes. A second phase of fluorapatite precipitates at the start of the high temperature crystallisation hold (1040 °C), however, there is no other phase formation during the remainder of the heat treatment and cooling cycles. The volume fraction of calcium phosphate was reported to be less than expected and less than that of the residual glass. Lattice parameters for both phases were determined by the 'pattern matching mode' in Fullprof. Small angle neutron scattering (SANS) was also performed in order to examine microstructural evolution through nucleation and growth

1.4 Effect of Fluorine and Alumina Additions

Hill *et al.* (1996) have shown that increased fluorine content in fluorine containing glasses reduce the glass transition temperature (T_g). Increased fluorine content disrupts the glass network and reduces the activation energy for nucleation and growth. The same authors have also shown that for mullite-fluorapatite glass compositions :- $1.5 \text{ SiO}_2 \cdot \text{Al}_2\text{O}_3 \cdot 0.5\text{P}_2\text{O}_5 \cdot \text{CaO} \cdot x\text{CaF}_2$, where x was varied between 0 and 1, that parent glass with high fluoride content was readily castable and underwent bulk nucleation and crystallization to fluorapatite (FAP) and mullite. Compositions with low values of x ($x < 0.5$) surface nucleated and crystallised to anorthite ($\text{CaAl}_2\text{Si}_2\text{O}_6$), a calcium analogue of celsian.

Clifford *et al.* (2000) have described the effects of fluorine content on the crystallisation behaviour of glasses based on the composition $4.5\text{Si}_3\text{Al}_2\text{O}_3 \cdot 1.5\text{P}_2\text{O}_5 \cdot (5-z)\text{CaO} \cdot \text{CaF}_2$, where z was varied from 0 to 3. All glasses apart from that with $z = 0.5$, had Ca: P ratios of 1.67 which corresponds to apatite stoichiometry, the exception had a Ca: P: F ratio of 5:3:1 corresponding to FAP. DTA analysis was used to determine optimum nucleation temperatures, glass transition temperatures T_g and crystallisation temperatures, T_{p1} and T_{p2} , where T_{p1} is the first order and T_{p2} is the second. Glasses with $x < 0.5$ exhibited surface nucleation in agreement with previous studies, whereas those with $x > 0.67$ exhibited bulk nucleation irrespective of particle size; two crystallisation peaks were in evidence for all fluorinated compositions. It was concluded that fluorine content affects nucleation and crystallisation in ionomer glasses and is critical to phase formation and the precipitation of apatite. In addition, fluorine reduces T_g by disruption of the glass network and replacement of bridging oxygens with non-bridging fluorine.

Tian *et al.* (2002) have studied the effect of fluorine content on the crystallisation of fluorsilicic mica glass ceramics and identified $\text{KMg}_{3.25}\text{Si}_{3.625}\text{O}_{10}\text{F}_2$ as the main mica phase. It was theorized that increasing fluorine reduces the activation energy for crystal growth and increases the frequency factor (relating temperature with reaction rate), by increasing disorder at the crystal-glass interface and reducing the melt viscosity respectively. The influence of fluorine content on the crystallisation and microstructure of barium fluorphlogopite glass-ceramics, based on the system $\text{BaO} \cdot 4\text{MgO} \cdot \text{Al}_2\text{O}_3 \cdot 6\text{SiO}_2 \cdot 2\text{MgF}_2$, has been investigated by Maiti *et al.* (2009). Data from DTA, XRD and SEM were collected and analysed. Conclusions were that the glass transition and crystallisation temperatures (T_g and T_{p1}) reduced as fluorine content increased (with excess added from 0 – 10 %). The first crystallisation peak (T_{p1}) was found to correspond to BFP ($\text{BaMg}_3(\text{Al}_2\text{Si}_2)\text{O}_{10}\text{F}_2$) and minor secondary phases of enstatite (MgSiO_3) and BAS ($\text{BaAl}_2\text{Si}_2\text{O}_8$) were also identified. Calculation of the Avrami exponent (from JMA theory) revealed that the crystallisation was homogeneous and assumed a 3-dimensional crystal growth pattern. These findings indicated that fluorine acts to promote crystalline growth in these materials.

The effects of varying the alumina (Al_2O_3) content on the nucleation kinetics of barium phlogopite glass-ceramics based on $8\text{SiO}_2 \cdot y\text{Al}_2\text{O}_3 \cdot 4\text{Mg}_2\text{O}_2\text{MgF}_2\text{BaO}$ were

investigated by Henry *et al.* (2004). It was discovered that reducing alumina had the same effect on the glass-transition (T_g) and first peak crystallisation temperatures (T_{p1}), therefore, appearing to act as a bulk nucleating agent; optimum nucleation temperatures coincided with T_g indicating a possible amorphous phase separation mechanism. The first crystallisation peak (T_{p1}) corresponded to BFP formation and T_{p2} represented secondary phase formation, including aluminium rich cordierite and BAS, T_{p2} was also found to reduce with alumina content. A relationship, however, between activation energy for crystallisation and alumina content could not be found.

1.5 Commercial Fluormica Glass-Ceramics

Macor® and Dicor® are two of the most widely used glass-ceramics and were developed at Corning Glass Works by G.H.Beall (1972) and D.G.Grossman (1974), respectively. These ceramic materials were designed to be machinable by conventional metal tooling but also lend well to CAD/CAM. Macor® is used widely in engineering applications and Dicor® is a machinable dental glass-ceramic. Dicor® is a group of tetrasilicic fluorine mica glass compositions consisting of 45-70 wt % SiO_2 , 8 – 20 wt % MgO , 8 – 15 wt % MgF_2 and 5 – 35 wt % [$\text{R}_2\text{O} + \text{RO}$], wherein RO is mono-valent oxide SrO , BaO or CdO and R_2O is a suitable divalent group 1 metal oxide such as Cs_2O . Additions of up to 10 wt % of other oxides and 5 wt % of colourants are possible. The main precipitated phase in Dicor® is boron fluoro-phlogopite with various substitutions of the large cationic end-member including K^+ and Ba^{2+} . These glass-ceramics are heat-treated via a two step process with a nucleation hold at between 750 °C and 850 °C for 1 – 6 hours and a crystallisation hold between 1,000 – 1,150 °C for approx. 1 – 8 hours; numerous modifications to the heating regime, including annealing at between 550 – 650 °C, are permitted. Grossman theorised that the first phase to crystallise upon heating was sellaite (MgF_2) and that subsequent heating to higher temperatures caused mica crystallisation at sites occupied by sellaite nuclei; although this is difficult to prove as sellaite is invariably supplanted by the fluormica phase in this case. Secondary phases of enstatite and cristobalite have been also found in very small quantities when heating at higher temperatures. Grossman discovered various impurity additions for imparting both translucence and colour, both As_2O_5 and Sb_2O_5

produced translucence in the cerammed article with As_2O_5 preferred due to concurrent improvements to machinability; glass ceramic colourants were found to consist of transition metal oxides of V, Cr, Mn, Ni and rare earths such as Nd_2O_3 . The maximum weight fraction of additions is limited to less than 8 % as no beneficial effect was found above this.

G.H.Beall (1972) performed an extensive study of the Macor® glass system prior to his patent application of 1970. The main crystalline phase is a fluorphlogopite solid solution consisting of three components: - normal K-phlogopite ($\text{KMg}_3\text{AlSi}_3\text{O}_{10}\text{F}_2$), boron fluorphlogopite ($\text{KMg}_3\text{BSi}_3\text{O}_{10}\text{F}_2$) and a K depleted aluminous phlogopite of composition $\text{K}_{0.5}\text{Mg}_2\text{Al}_{0.33}\text{BSi}_3\text{O}_{10}\text{F}_2$. The final cerammed articles were found to be between 50 - 90 %, by volume, crystalline. Minor additions can be tolerated up to 10 %, by volume, for this invention and may include ZrO_2 , TiO_2 , BaO and K_2O ; potassium oxide (K_2O) was found to be preferred, however, due to its limited effect on dielectric properties. Beall also devised a composition for optimised mechanical strength, dielectric properties, thermal shock resistance and machinability consisting of 35 - 48 wt % SiO_2 , 5 - 15 wt % B_2O_3 , 14 - 22 wt % Al_2O_3 , 15 - 25 wt % MgO , 3 - 8 wt % K_2O and 5 - 10 wt % F. The preferred heating regime for these materials consists of two stages, the first is a nucleation hold at between 750 - 850 °C and the second is a crystallisation hold between 850 - 1100 °C; hold time is a function of the desired crystallinity of the end product. Beall suggested that a lower heating rate was preferable (< 5 °C per minute) to reduce slumping of the residual glass. It was found that the microstructures, determined by SEM, of those cerammed articles with compositions containing less than 5 % B_2O_3 exhibit high crystallinity but low aspect ratios for crystallites of the mica phase; leading to poor mechanical, dielectric and thermal shock properties due to the lack of a 'house of cards' microstructure and attendant reduction in the critical flaw size, as shown in figures 1.02 and 1.03. By comparison, compositions with $\text{B}_2\text{O}_3 > 5$ % precipitate large interlocking platelets of mica with high aspect ratios and possess excellent machinability. Low B_2O_3 compositions first precipitate sellaite as a nucleating phase, whereas, those with high B_2O_3 precipitate fluorborate. In the compositions nucleated by sellaite (MgF_2) this phase remained even after full crystallisation of the mica phase and was particularly evident for compositions high in MgO and fluorine. Ideally, for optimum machinability, Beall found that the cerammed Macor® should have a high

crystalline volume fraction ($> 50\%$) and a large mica platelet aspect ratio of at least 5:1 to ensure the house of cards microstructure. The extraneous formation of secondary phases was noted but was typically found to occupy less than 15% of the total crystalline volume.

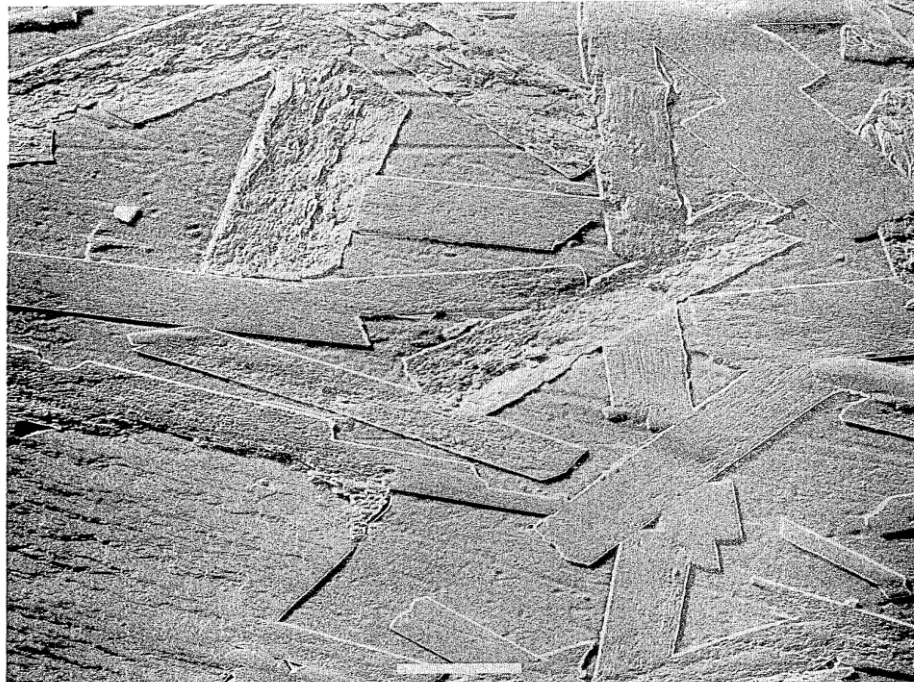


Figure 1.02. Micrograph of Macor® glass ceramic showing poor interlocking microstructure of mica crystallites. (Beall, 1972)

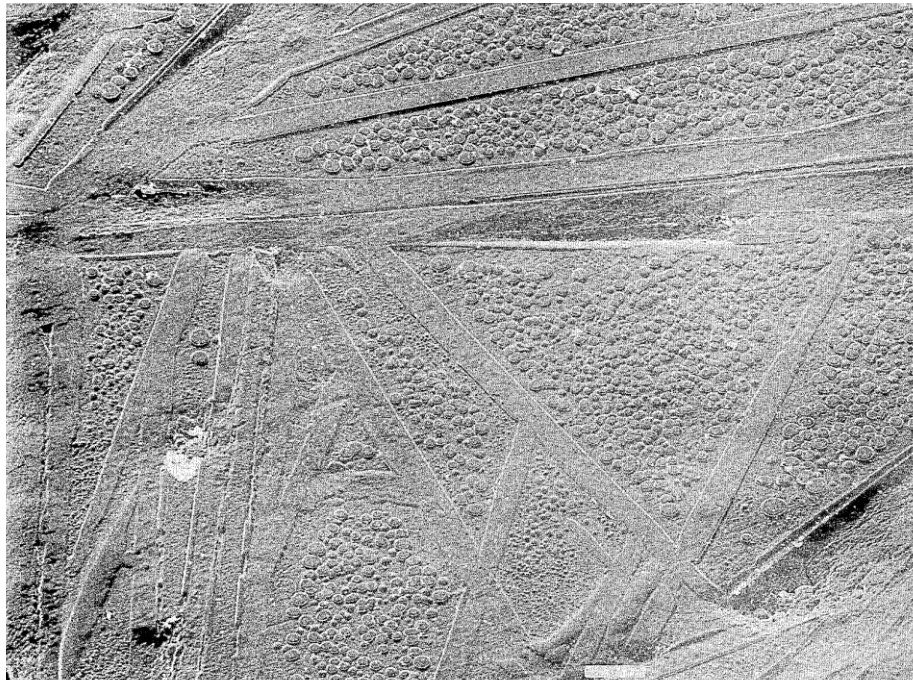


Figure 1.03. Micrograph of Macor® glass ceramic showing 'house of cards' microstructure. (Beall, 1972)

1.6 Translucent Mica Glass-Ceramics

Transparency or translucency in glass ceramics is a product of either matching of the refractive indices of low birefringence crystalline phases with the residual glass or precipitation of a crystalline nanostructure with crystallite dimensions less than the wavelength of visible light (< 200 nm). Reise *et al.*(2000) have invented a translucent mica glass-ceramic with ZrO_2 as a secondary phase (US Patent n^o :- 6,080,692); containing 0 – 9 wt % K_2O , 0 – 9 wt % Na_2O , 35 – 60 wt % SiO_2 , 10 – 25 wt % MgO , 7 – 30 wt % Al_2O_3 , 4 – 12 wt % ZrO_2 , 2 – 10 wt % F^- , where percentages are by weight. A high degree of translucence, in this case, is achieved by the formation of a very fine mica grain size between $0.5 \mu m$ and $3 \mu m$ with the formation of a house of cards microstructure ensuring processibility. The main mica phase precipitated in this case is potassium phlogopite, although a broad range of compositions is possible. Heat treatments employ nucleation and growth stages with nucleation temperatures about 20 – 200 K above the transformation temperature and nucleation times between 0.5 to 3 hours; crystallisation temperatures are between 200 to 450 K above T_g and are held for approximately 0.5 to 5 hours. Processing by CAD/CAM techniques is possible for this material although subsequent heat treatments may be required if higher machinability is required. The presence of tetragonal ZrO_2 improves strength by conversion strengthening, whereby stress induces martensitic transformation to monoclinic ZrO_2 leading to suppression of micro-crack growth. A number of additions for improving machinability and colour have been found for example:- CeO_2 , La_2O_3 , MnO_2 , Fe_2O_3 , TiO_2 , Y_2O_3 and B_2O_3 with no more than a total of 10 wt % added to feedstocks; additions of lithium (Li_2O) at > 0.1 wt % are known to reduce glass resistance to hydrolysis and must be minimised. This material is claimed to be an improvement on previous glass-ceramics which have exhibited comparatively low strength and are therefore limited in dental applications.

1.7 Ca-Phlogopite Machinable Glass-Ceramics

A new type of glass-ceramic by Li *et al.* (2006) has been developed for dental applications. The main precipitated phase is a Ca-phlogopite, however, studies have shown that there is significant K^+ (potassium) substitution such that the general

formula becomes $K_{1-x}Ca_xMg_3AlSi_3O_{10}F_2$. The parent glass composition consists of :- 40 wt % SiO_2 , 12 wt % Al_2O_3 , 10 wt % MgO , 24 wt % MgF_2 , 5 wt % CaO and 1 wt % K_2O . Cast glass was nucleated at 660 °C for 1 hour then heated at a rate of 3 to 5 °C/min and held at either 800 °C., 900 °C or 1050 °C for 4 hours to fully crystallise the sample. The visible microstructure was typical of mica glass ceramics, however, higher bending strengths (228.11 ± 7.55 MPa) were found and high machinability was exhibited. The increases in strength are thought to be a direct result of the higher bonding strengths of divalent (e.g. Ba^{+2} , Ca^{+2}) interlayer cations. The aspect ratios of mica lath crystals were also high and typically 1-3 μm thick and 10 μm long. In cerammed condition, these materials appear opaque but exhibit potential as CAD/CAM restorations.



Figure 1.04. A crown fabricated by dental CAD/CAM system with glass ceramic KZr-1050 (above glass ceramic article heat treated at 1050 °C) (Li *et al.*, 2006).

1.8 Outline of Thesis

Firstly, chapter 2 presents a literature review of the necessary background; chapter 3 is a discussion of experimental rationale and description of all the experimental techniques applied during this work. Chapter 4 is the results and discussion and is split into three main parts, 4.1, 4.2 and 4.3. Section 4.1 presents all data from physical property testing, including DTA (Differential Thermal Analysis), hardness

and colour-space measurements, this section includes many comparisons between the commercial and original LDIG 24 glass-ceramics, although, colouring work and measurements relating to new heat treatments only concern the commercial variant as this is intended for future development. Section 4.2 presents all of the XRD data and related analyses carried out on LDIG 24 commercial glass-ceramics and determines the mica phase structure and composition; many, previously unknown, phases have also been identified in this material (appendix 1.17) by application of a number of novel techniques and several different heat treatments. Section 4.3 presents data from two separate kinetic neutron experiments (ILL, France); the first is a vacuum furnace experiment on the original LDIG 24 glass, the second is my own data and concerns a mirror furnace experiment in air on the commercial variant, both data sets are compared and results are related back to section 4.2. Finally conclusions and suggestions for future work are presented in chapter 5 with references and appendices at the back.

2 Literature Review

2.1 Mica Structure

Mica structure and characteristics, notably excellent machinability, are relevant to the main precipitated phase of the glass ceramics produced at Leeds Dental Institute and influence the mechanical properties of materials developed in this thesis.

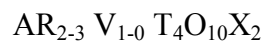


Figure .2.01. Specimen of rare zinnwaldite mica ($\text{KLiFeAl}(\text{AlSi}_3)\text{O}_{10}(\text{OH},\text{F})_2$) (own work).

From Brazil, note the pseudo-hexagonal habit of the crystal.

2.1.1 Ideal Mica Structure

Micas are layer silicates (phyllosilicates), whose structure is based either on trioctahedral or dioctahedral nature, with a general formula:



Where:

A	=	interlayer cation (Ba, K)
R	=	octahedral layer cation (Al, Mg)
V	=	octahedral vacancy
T	=	tetrahedral layer cation (Si, Al)
O, X	=	oxygen and anion (OH ⁻ , F ⁻) respectively

The subscript represent numbers of atoms in the formula unit, the most significant substitutions are in the octahedral and interlayer sites.

Naturally occurring micas are found in hexagonal tabular (book-like) form (see figure 2.01 above) and exhibit a distinct cleavage perpendicular to the [001] direction. Mica is often referred to as a sandwich structure or a 2:1/TOT layer unit which is stacked in the direction normal to (001). This structure consists of layers of cations in tetrahedral coordination with oxygen (tetrahedral layer), octahedral coordination with oxygen and other anions such as fluorine (octahedral layer) and 12 fold co-ordination with basal oxygen at the interlayer sites.

Ideally 'trioctahedral' refers to 3 octahedra per unit cell that are fully occupied with suitable cations - usually magnesium e.g. $Mg_3O_4(OH)_2$; 'dioctahedral' refers to 2 of these 3 octahedra being occupied with cations such as tri-valent aluminium [e.g. $Al_2O_4(OH)_2$]. This 'module' is sandwiched between a pair of oppositely orientated tetrahedral sheets, these sheets consist of $Si_x(Al_{(4-x)})$ tetrahedral cations per formula unit which share three of four basal oxygens to form a 2D hexagonal net, when viewed from below in this case, with apical (unshared) oxygens and tetrahedral cations above each vertex and basal oxygens equidistant along each side. The octahedral anion, either F^- or OH^- , is located at the centre of each hexagonal ring (unbonded to T), of diameter equal to lattice parameter a , located at the same height as the apical oxygens. Both tetrahedral layers are displaced by $a/3$ with respect to each-other to ensure optimum AB close-packing of the apical oxygens over the octahedral institices

The mica module plus an interlayer cation (usually potassium) forms the basic building block of the mica monoclinic crystal structure; figure 2.02 illustrates this structural unit for the case of mica mineral phlogopite. Interlayer cation valency has consequences for the mechanical properties with barium (2+) micas typically referred to as 'brittle' whilst those with cations of valency (+1) such as potassium

micas are known as ‘true’; this is because the bonds between the interlayer cation and bridging oxygens are strongest in the divalent case (i.e. Ba. or Ca), compromising flexibility. Interlayer cations have a significant bearing on the mechanical properties of micas, for example, it has been reported that barium micas exhibit high strength (Hirano *et al*, 1989). Real micas differ substantially from the ideal case and include various cationic substitutions, such as Fe^{3+} and Mn^{2+} , and structural distortions - particularly in the tetragonal layer (Fleet, 2003).

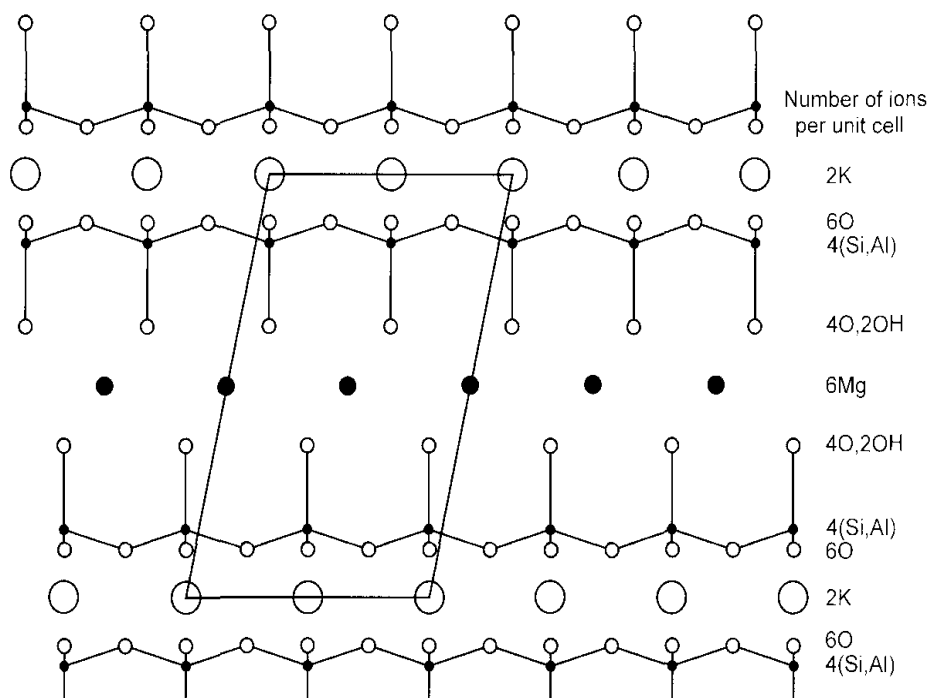


Figure 2.02. The structure of the three layer TOT unit.

Illustrated for K- phlogopite, viewed along the y-axis. The monoclinic unit cell is also shown (Fleet, 2003).

2.1.2 Distortions of the Ideal Structure

The ideal mica structure is distorted in real micas by tetrahedral-octahedral layer misfit. Figure 2.04 shows an octahedral sheet sandwiched between two tetrahedral sheets; this example illustrates the structure of dioctahedral mica with the octahedral sheet partially depleted due to the presence of aluminium. The high +3 charge on the aluminium cations leads to strong repulsion such that anions on shared edges between occupied octahedra contract whereas the lateral edges of the unoccupied octahedra remain unchanged. Anions in this case move in directions diagonal to the sheet surface such that the sheet expands as the thickness reduces. Apparently, two of the six lateral edges connecting apices of the hexagonal rings are expanded and

the remaining four twisted. The twisting causes rotation of the upper and lower anion triad around each octahedral cation this action shortens the shared edges even further. Trioctahedral mica anions are repulsed equally in all directions, so electrostatic energy is minimized by movement inwards to reduce the sheet thickness, meaning that trioctahedral mica layers can be thin as dioctahedral layers but without the accompanying distortion, shown in figure 2.03. Ideal lateral dimensions assume a free state in which each layer is the same size with no mismatch and no strain between layers; this does not occur in nature and there is often some structural reorientation required for planes to fit over each other.

In the great majority of micas lateral dimensions of the tetrahedral sheet are larger than those of the octahedral sheet as a result of tetrahedral substitution of Al or Fe⁺³ for Si⁺⁴. It can be shown mathematically that by rotating adjacent tetrahedra in opposite directions in the (001) plane, these dimensions are reduced. The amount of rotation necessary to relieve misfit can be expressed by the formula:-

$$\text{Cos}(\alpha) := b(\text{obs})/b(\text{ideal})$$

This in any case is only an approximation due to difficulty in estimation of b(ideal), however, this relationship successfully explains observed behaviour. In the case of synthetic micas with more controlled compositions tetrahedral rotation is reduced. Another significant distortion is tetrahedral 'tilt' exclusively found in dioctahedral micas; the separation of apical oxygens by enlarged unoccupied M1 octahedra prevents free counter rotation of the tetragonal layers. This results in tetrahedra, along the extended sides of the hexagonal apical oxygen layer, that are inclined away from one another. The effect of canting is to elevate basal oxygens such that corrugations are formed in the basal tetragonal layer; parallel to the long sides of the apical oxygen layer.

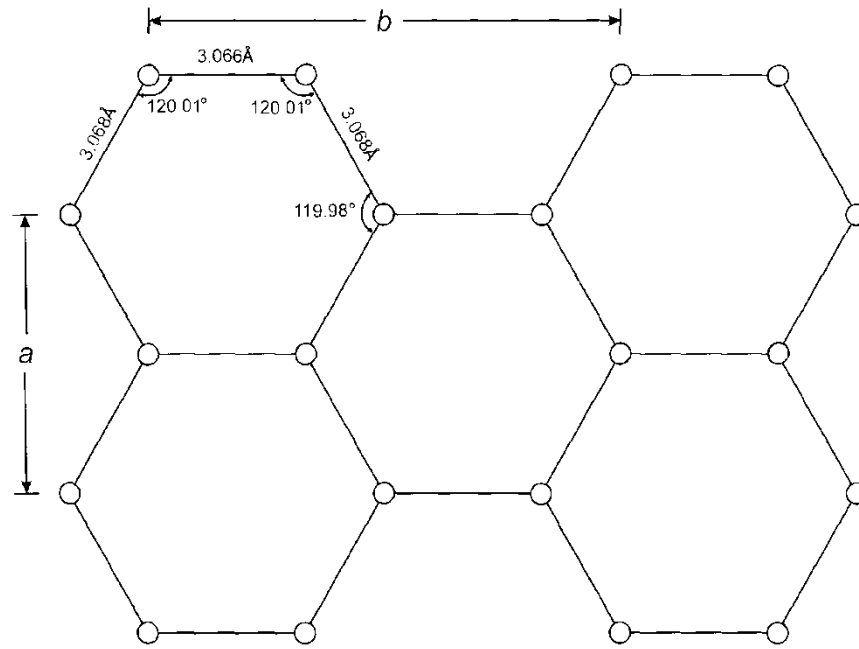


Figure 2.03. Undistorted hexagonal net of apical oxygens in a trioctahedral mica (Fleet, 2003).

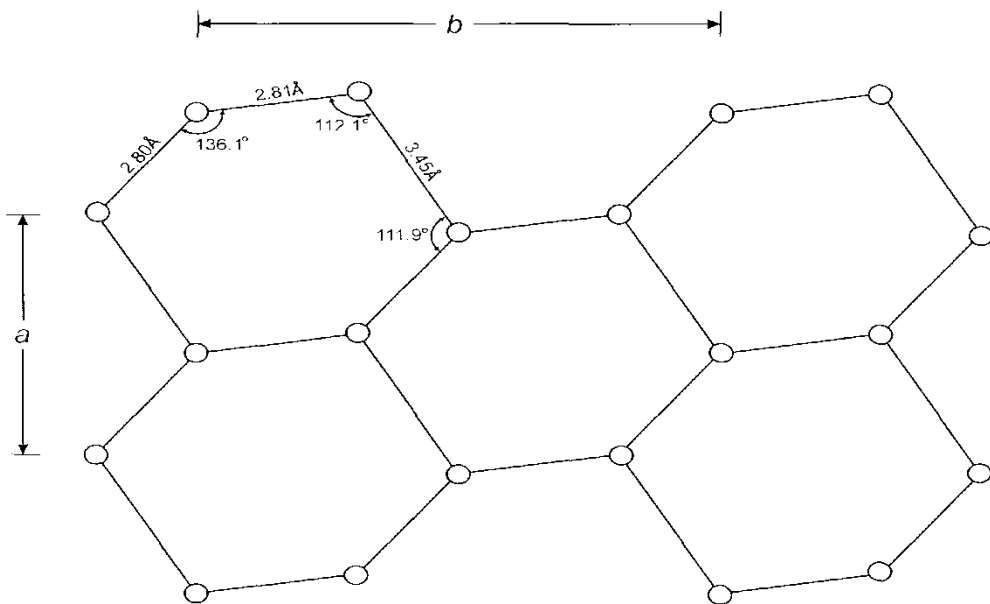


Figure 2.04. Distorted hexagonal net of apical oxygens in a dioctahedral mica (Fleet, 2003).

2.1.3 Polytypism

A polytype is a structural modification due to different forms of stacking in a layered structure such as mica. Mica polytypes are a result of either rotations or translations of successive layers. Considering epitaxial growth of the mica crystal, each layer is added on top of an existing layer where the hexagonal tetragonal basal structures are directly superimposed over the interlayer site. The upper and lower

layers have hexagonal symmetry, therefore, all rotations of multiples of $\pm 60^\circ$ are equivalent; this means that the $a/3$ translation between layers, in the ideal case, may subtend any angle between 0° and 360° of factor 60. Symmetry considerations for the mica case define only four ways of stacking layers due to equivalency of certain rotations such as 60° and 300° .

There are six standard ordered polytypes of mica, identified by Smith & Yoder (1956), due to the four ways of rotating individual mica layers; these are denoted by a space group symbol alongside shorthand notation (in brackets) of Ramsdell (1947) as follows - $C2/m$ (1M), $Ccmm$ (2Or), $C2/c$ ($2M_1$), $P3_112$ (3T), $C2/c$ ($2M_2$) and $P6_122$ (6H). The first symbol gives the number of layers in the repeating unit, the second letter gives the lattice type (M for monoclinic) and the subscript is for distinguishing different polytypes with the same lattice and repeat length. Only polytypes 1M and 2O are based on successive layer rotations of 0° and 180° respectively and 1M is the most abundant of trioctahedral micas. The hexagonal geometry assumed in the derivation of the standard polytypes is idealized and does not apply as strictly for the dioctahedral case which is more distorted. Disordered stacking sequences, such as $1M_d$ with d subscripted, have also been identified (Fleet, 2003).

2.1.4 'Brittle' Micas

Brittle mica is defined as one in which no less than 50 % of the total interlayer cations are divalent (Fleet, 2003). End member brittle micas have a 2:1 layer charge of (-2) per formula unit compared to (-1) for ideal true micas giving rise to brittle cleavage. The TOT layer charge of (-2) comes from Al for Si tetrahedral cation substitution such that the occupancy of this site is shared (1:1) in the ideal case. Divalent end-member species are limited to calcium and barium (alkaline earth metals) in nature due to their relative abundancy, however, other large cations are possible. The mica phase precipitated in glass-ceramics prepared for this study is a trioctahedral Ba fluormica which has an analogue brittle mica structure closely resembling kinoshitalite. Fluormicas exhibit higher melting points (up to 1400°C) and superior chemical resistance when compared with their hydrated equivalents.

2.1.5 Kinoshitalite

Kinoshitalite, a Ba-Mg trioctahedral mica, was first described by Yoshii *et al* (1973) and named after Kameki Kinoshita. Hydrated Kinoshitalite is di-silicic, translucent and has the chemical formula: $\text{BaMg}_3[\text{Al}_2\text{Si}_2\text{O}_{10}](\text{OH}, \text{F})_2$. Polytypes 1M and 2M₁ occur in nature with 1M common. Kinoshitalite 1M has lattice parameters: $a = 5.345 \text{ \AA}$, $b = 9.250 \text{ \AA}$, $c = 10.256 \text{ \AA}$, $\beta = 99.99^\circ$ and a space group of C2/m, although, many solid solutions with different end-members are possible including (Ba-K), (Ba-Ca) and (Ba-Na) and all permutations thereof. In the case of extensive substitution of Ba with K or Na, charge balance is achieved through the coupled substitution $[(\text{K}, \text{Na}) + \text{Si} = \text{Ba} + \text{Al}]$ representing a solid solution between kinoshitalite and phlogopite $((\text{K}, \text{Na})\text{Mg}_3[\text{AlSi}_3\text{O}_{10}](\text{OH}, \text{F})_2)$. The trioctahedral structure is relatively close to ideal, in this case, although studies by Gnos & Armbruster (2000) have theorised that Si and Al, while ordered within a single tetrahedral layer, show disorder along [001] due to stacking faults (Fleet (2003)). Minerals such as celsian ($\text{BaAl}_2\text{Si}_2\text{O}_8$), quartz (SiO_2), enstatite ($\text{Mg}_2\text{Si}_2\text{O}_6$), spessartine ($\text{Mn}_3\text{Al}_2(\text{SiO}_4)_3$) and rhodonite (MnSi_3) can also be found in kinoshitalite bearing rock but cannot form intimate mixtures with Ba-micas due to the lack of a shared poly-phase stability field (King *et al.*, 2000).

2.2 Theory of Glasses

2.2.1 Amorphous state

Glasses are a special subset of 'amorphous' materials which include all organic polymers.

There are several definitions of glasses found in academic texts. One popular definition is by the American Society for Testing and Materials (ASTM) which states that – '*glass is an inorganic product of fusion which has been cooled to a rigid condition without crystallising*'. This definition, however, is restrictive as it excludes glasses formed with organic products and specifies the formation of glass from a super-cooled melt. A more inclusive and accurate definition has been proposed by Zarzycki – '*A glass is a non-crystalline solid exhibiting the phenomenon of glass transition*' (Zarzycki, 1991).

Vitrifiable substances have the potential to form either crystalline or glass phases based on the conditions of their formation. Glasses invariably form viscous liquids with viscosities of 10^5 to 10^7 poise above the melting temperature (T_m), whereas solids typically exceed 10^{15} poise; the cooling regime is the main factor in determining whether a glass solidifies as an amorphous or crystalline phase. The nature of the transformation from liquid to solid can be shown by plotting a thermodynamic variable such as specific volume against temperature, as shown in figure 2.05. The volume of a glass melt decreases in a linear fashion with temperature above T_m . If the melt is held for a short time at a temperature just below the freezing point and then cooled, it will tend to crystallise. This occurs because the crystalline phase is more thermodynamically stable than the super-cooled melt. In this case there is a discontinuous step reduction at T_m as a result of a sudden change in the free energy of the system. Alternatively, if the same melt is similarly cooled from a temperature just above the freezing point after a short hold, there is no crystallisation and the viscosity of the melt steadily increases until it solidifies as an amorphous solid known as a glass.

Whether or not any crystallisation occurs in the second case depends on the rate of cooling of the liquid phase and the presence of impurities. The coefficient of contraction of the melt $> T_m$ is identical to that $< T_m$ as there are no discontinuities at this point, hence, the continuation of the original line shown in figure 2.05. The region over which the change of gradient occurs is known as the glass transition temperature (T_g), the transition to the glassy state is continuous so this temperature is ill-defined. At T_g the glass is defined as solid such that the coefficient of contraction reduces to match that of the crystalline form at the same temperature, in the figure both lines appear parallel at $T < T_g$. T_g is, therefore, indicative of glass formation (Elliott, 1983).

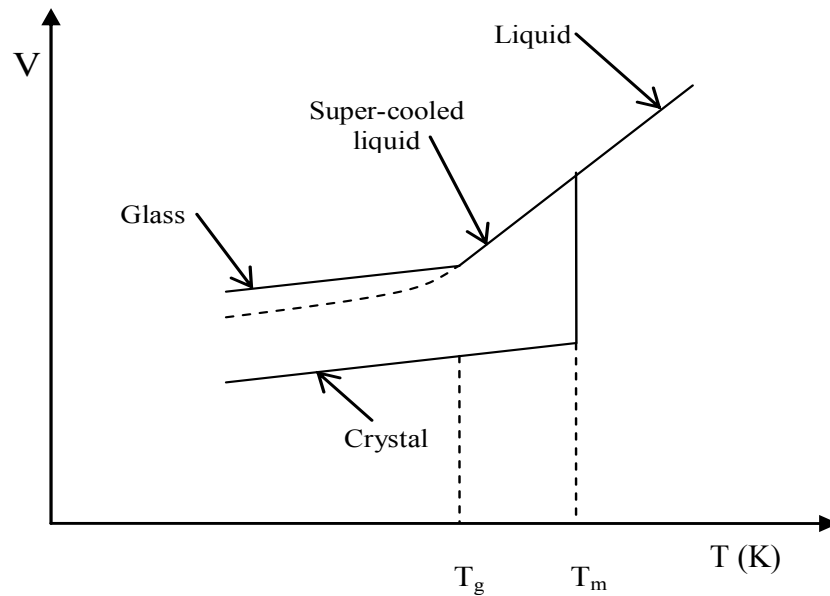


Figure 2.05. A plot of specific volume versus temperature.

A consequence of thermal expansion match-up between the crystalline and glassy phases below T_g is ‘free volume’ theory. This relates thermal expansion of the solid and liquid phases through free volume, unoccupied space, which is temperature dependant in the liquid but fixed in the solid. T_g is not strictly the freezing point but refers to the temperature at which the free-volume in the glass reaches a critical constant value. Free-volume theory allows the development of empirical relationships between T_g , melt viscosity and melt cooling rate; proving that T_g is a product of experimental conditions and not just the glass composition and molecular chemistry (Elliott, 1983).

2.2.2 Eutectic Glasses

Consider a binary glass of two compounds A and B such as $V_2O_5 - PbO$ and its phase diagram. Both are miscible in liquid form but remain immiscible as solids along much of the liquidus; within a narrow range of compositions, however, there is a deep ‘eutectic’ or minima in the melting point of the glass which reduces the supercooling required to reach T_g , thereby, reducing the risk of crystallisation and ensuring a continuous random glass network. Deep eutectic points are a feature of the phase diagrams of all glass forming compositions and ensure that glasses remain workable at lower temperatures (Elliot, 1983).

2.2.3 Glass Formation

There have been many theories and models proposed for the structure of inorganic glasses over the last century. Below is a brief summary of the main structural models.

2.2.3.1 Goldschmidt Theory

Goldschmidt (Goldschmidt, 1926) was the first to prepare a theory based on empirical observations of glass formation. Goldschmidt observed that for oxides (SiO_2 , GeO_2 etc) the ratios of the radius of the anion to the radius of the cation were between 0.2 and 0.4 for glass forming materials. The structure of the glass former in this case consists of four anions around each cation with the anions positioned at the corners of a tetrahedron. Zachariasen's theory is widely regarded as the most successful and generally disagrees with the conclusions of Goldschmidt. He reasoned that BeO will allow oxygen tetrahedra around the Be cations and yet BeO is not vitrifiable. This clearly represented a failure in the Goldschmidt theory.

2.2.3.2 Zachariasen Theory

Zachariasen theorised that the structure of oxide glasses consisted of oxygen polyhedra around single cation atoms. He concluded that atomic forces of an oxide glass and its corresponding crystalline phase were almost identical. The structure of glass is random and non-symmetrical as shown by X-ray diffraction experiments which produce a diffuse halo without the characteristic Bragg peaks of crystalline materials. Zachariasen stated that the energy difference between the glass and crystalline form could not be large, otherwise the material would devitrify to a crystalline phase. It followed that the glass must contain polyhedra of the same type as the crystal but without the long range order and with different orientations for neighbouring polyhedra. Zachariasen set out a number of criteria which he believed were necessary for an oxide to be a glass former:

- An oxygen atom must not be linked to more than two cations.
- The cation coordination number must be small, 3 or 4.
- The oxygen polyhedra must share corners with each other not edges or faces
- For a three dimensional network at least three corners of each polyhedra must be shared.

There were also additional rules formulated for complex glasses.

- A sample must contain a large proportion of cations which are surrounded either by oxygen triangles or tetrahedra.
- The oxygen tetrahedra share only corners with each other.
- Some oxygen atoms are linked to only two cations and do not form bonds with any other.

Zachariasen also identified two other oxides present in complex glasses called network modifying oxides and intermediate oxides; both can have the effect of weakening the glass network and reducing viscosity in the melt. These rules imply that oxide glasses must contain substantial proportions of glass-forming cations which can be substituted 'isomorphously' without disrupting the random network. Network modifiers break up the continuous silica network with non-bridging oxygens which are shielded by the equal and opposite charge of the cation. Intermediate oxides such as TeO_2 , MoO_3 , only form glasses in the presence of other modifiers, however, Al_2O_3 is also classed as an intermediate oxide but can part-take as both a network former and network modifier and is present in either tetrahedral (AlO_4) or octahedral (AlO_6) forms (Zachariasen, 1932). The LDIG 24 glass composition of this study consists of a high proportion of network modifiers, such as barium and magnesium, resulting in a lower melting point, lower glass transition temperature and lower melt viscosity than possible without.

2.2.3.3 Goodman Model

Goodman (Goodman, 1985) based his model on those of Zachariasen and others. He realised that most glass forming systems have a major and minor component existing in two or more polymorphic forms with slightly different free energy. If the liquid is super-cooled then a number of different transient types of cluster will form in the melt called a mixed cluster liquid above T_g . below T_g clusters become bonded across their interface; the solid network that results is called a mixed cluster network.

At lower temperatures residual liquid surrounds the interfaces and strains in compression and tension will be generated in the networks due to thermal expansion mismatch causing an increase in the enthalpy of the system. The theory suggests that

the addition of a modifier ion reduces the stress build up by introducing disorder in the inter-cluster interfaces. The residual liquid phase completely solidifies upon further cooling to produce small voids and a glass network with a completely random strain field by cancellation of positive and negative terms. This model can be used to interpret glass formers and non-bridging oxygen on a basis which is consistent with observed stability.

2.2.3.4 Inorganic Polymer Model

This model suggests that glasses behave as macro-molecular systems similar in behaviour to organic polymers with high melt viscosities and long chains of covalently bonded glass former atoms (Si-O) linked by oxygen anions (Ray, 1978). Oxide glasses are described as network polymers consisting of oxygen atoms bridged by multivalent atoms such as silicon and aluminium. Many properties of oxide glasses can be related in this way to two simple parameters known as 'cross-link' density and 'packing' density. Characteristic properties of this model include high elastic modulus, low ductility and heat resistance consistent with a high level of cross-link density as is the case with some thermo-plastics. Clearly, an increase in the number of cross-linkages will lead to an increase in T_g and improvement to mechanical strength and hardness. The equation below gives the relationship between T_g and cross-link density (CLD).

$$\frac{T_x}{T_o} = 1/(1 - KX)$$

Where:

- T_x = glass transition temperature of cross-linked polymer
- T_o = glass transition temperature of linear polymer
- K = independent constant of material
- X = CLD of polymer

The cross-link density (CLD) includes terms such as the number of bridging oxygens (BO) and number of non-bridging oxygens (NBO) in the equation below, $CLD = 1$ for a fully cross-linked polymer.

$$\text{Crosslink density (CLD)} = \frac{(BO - NBO)}{\text{Total number of bridges}}$$

2.2.3.5 Dietzel's structural model

Dietzel studied the ionic forces exerted between cations and anions during solidification from the glass melt. Interaction forces were modelled as electro-static Coulomb forces with an inverse square law R^{-2} . Cations are classified according to their field strengths for simple binary glasses. During super-cooling of the melt cations attract oxygen anions and minimize their potential by forming a close-packed structure; those cations with higher charge attract more anions and have more influence over the atomic structure. For binary alloys a minimum field strength difference of $0.3 (Z/a^2) (\text{\AA}^2)$ is required for glass formation (Vogel, 1971).

2.3 Glass-Ceramics

A glass ceramic is formed from a glass by controlled heat treatment. Glass-ceramics, unlike ceramics, have a residual glass component in addition to crystal phases; the composition and volume fraction of this amorphous phase partly determines the strength of a glass ceramic article. Heat treatments promote growth and nucleation of crystallites in the glassy matrix. The heat treatment regime of a glass specifies the heating rates, the number of holds and the hold times, and in the standard regime for a glass-ceramic there are two holds one for nucleation and the other for crystal growth. Tammann determined the crystallisation or glass formation from super-cooled liquids. Region 2, in figure 2.06, is called the metastable zone of undercooling; region 1 is called the metastable zone of high viscosity. Region 2 is located below the melting temperature, in this zone nuclei are unable to form, as ΔG tends to zero and stable nuclei become too large, but crystallites can grow if the nuclei are provided as impurities added to the melt (Shelby, 2005). Region 1 is at a much lower temperature resulting in the glass melt being highly viscous, both nucleation and crystal growth are inhibited. The critical region for crystallisation is between region 1 and 2. The probability of crystallisation depends upon the overlap of the nucleation (1) and crystal growth rate curves (2) and the height of the overlap region. If the rate of nucleation is lower than the crystal growth rate then the material will consist of large crystals grown from a small number of centres. If the rate of growth is low and that of nucleation high then the material will be partially crystalline with a fine grain structure (Tammann, 1923).

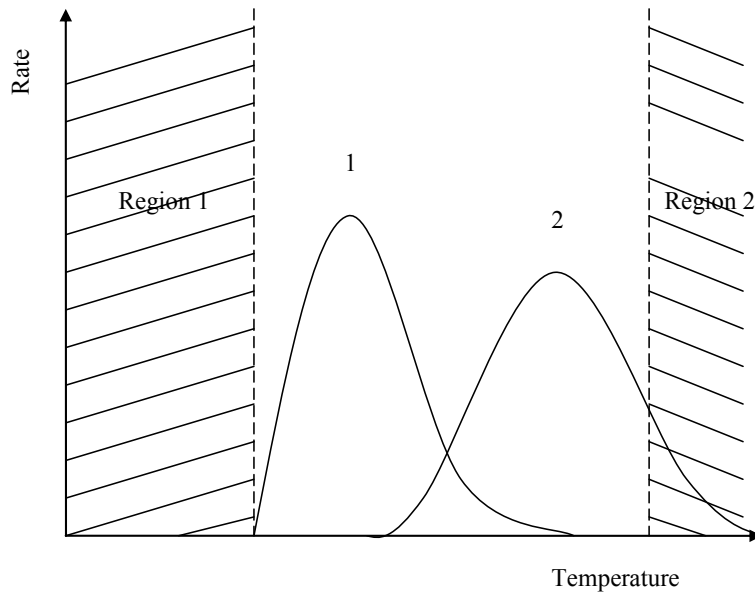


Figure 2.06. Plot of rate versus temperature for nucleation (1) and crystal growth (2) curves.

Regions 1 and 2 are the metastable zone of high viscosity and the metastable zone of undercooling respectively.

2.3.1 Crystallisation of Glasses

Phase transformations in glass generally start with a nucleation stage initiated by phase separation followed by a bulk or/and surface crystal growth process. There are a number of different transformation steps in the conversion of glass to glass-ceramic. Additions to the melt such as nucleating agents will change the nature of the phase transitions and lead to materials with very different optical and mechanical properties. This work is concerned with fluormica-based glass ceramics which are nucleated prior to crystal growth, although the presence of a very fine microstructure indicates that other growth mechanisms may also be involved.

2.3.2 Homogeneous Nucleation

Embryo crystals are first formed spontaneously in the melt when super-cooled; nucleation can then proceed according to free energy considerations. The homogeneous nucleation process can be modelled by simple energy relations. The total free energy of nucleation consists of a volume component $(\Delta G)_v$ and a surface component $(\Delta G)_s$ as shown in figure 2.07. The volume component accounts for the difference in free energy between the highly ordered embryo and the surrounding

phase, leading to a reduction in free energy as the nucleation progresses. The surface component relates to the formation of a liquid crystal interface which results in a gain in the free energy. If large nuclei are produced, the surface term is small and there is a negative free-energy. A maximum r-value corresponds to a critical radius r_c . The associated free energy represents the limit for stable nucleus formation. Free energy considerations also allow calculation of nucleation rates at different temperatures.

The total free energy in this case is represented by:

$$\Delta G = \left(\left(-\frac{4}{3} \right) \pi r^3 \cdot \Delta G_v \right) + 4\pi r^2 \gamma$$

Where:

$$\begin{aligned} \Delta G &= \text{Total free energy change} \\ r &= \text{Radius of embryo} \\ \gamma &= \text{Surface tension of the solid liquid interface} \end{aligned}$$

Differentiating the above by r and setting $d(\Delta G)/d(r) = 0$, to find the free energy minimum, yields the critical radius (r_c) upon re-arranging:

$$r_c = 2\gamma/\Delta G_v$$

Volmer and Weber (Volmer *et al.*, 1925) described the rate of homogeneous nucleation as:

$$I = A \exp\left(-\frac{\Delta G}{kT}\right)$$

$$\begin{aligned} A &= \text{Constant} \\ \Delta G &= \text{Max free energy change} \\ k &= \text{Boltzmann constant} \\ T &= \text{Absolute temperature} \end{aligned}$$

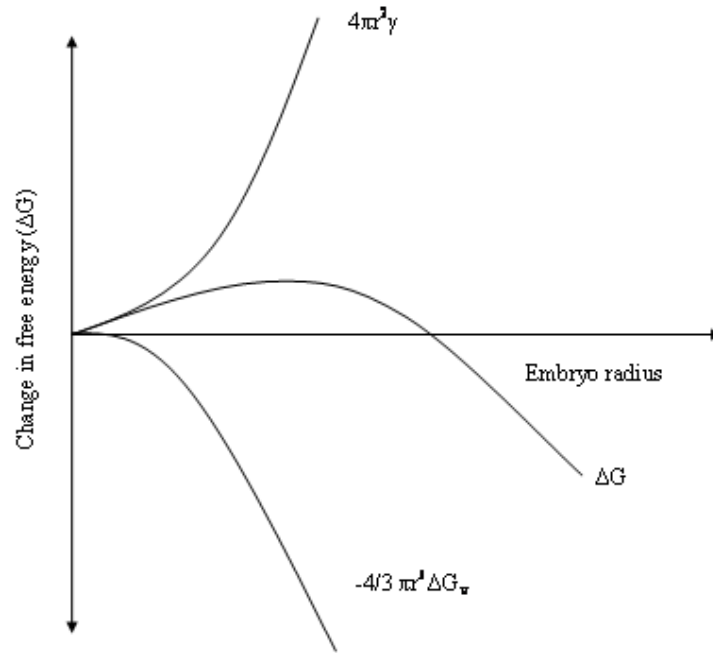


Figure 2.07. A plot of change in free energy ΔG versus embryo radius for each energy term.

2.3.3 Heterogeneous Nucleation

Heterogeneous nucleation also known as catalysed nucleation occurs at container walls and impurity surfaces of the sample. These surfaces have the effect of reducing the energy barrier for nucleation by reducing the size of the crystal liquid interface. Sometimes catalyst impurities are added to increase the amount of heterogeneous nucleation in a sample. The likelihood of heterogeneous nucleation can be determined by the wetting angle of the nucleus on the impurity surface. For any contact angle less than 180° the free energy barrier favours heterogeneous nucleation (McMillian, 1979). A semi-spherical drop in contact with a surface generates two interfacial surface energy terms, drop-liquid and liquid-substrate as shown in figure 2.08. The algebraic sum of these terms gives the total surface energy for a heterogeneous nucleus.

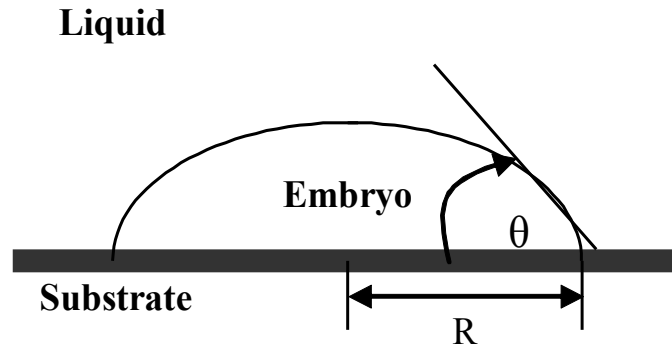


Figure 2.08. An example of heterogeneous nucleation.

$$\Delta G_s = \Delta G_s^b \cos\theta + \Delta G_s^c$$

Where:

- θ = contact angle
- ΔG_s = embryo-liquid interfacial energy
- ΔG_s^b = substrate-embryo interfacial energy
- ΔG_s^c = liquid substrate interfacial energy

The surface tension term decreases as the contact angle (θ) reduces to zero such that the nucleation barrier also descends. Generally, heterogeneous nucleation will dominate if the heterogeneous free energy term is less than that of the homogeneous term; this can lead to the formation of different phases on the surface of a glass-ceramic sample when compared with the bulk.

2.3.4 Glass Phase Separation

There are two types of phase separation in glasses at high temperatures, stable phase separation (SPS) and unstable phase separation (UPS). SPS occurs in the liquidus region of the glass melt upon cooling the phases remain partially crystalline and give rise to a milky discolouration in the glass. UPS occurs beneath the liquidus region of the glass melt; super-cooling prevents crystallisation at high temperatures and allows a homogeneous glass phase to be retained. Heat treatments give rise to two different mechanisms based on nucleation and growth and spinodal decomposition respectively. These processes differ fundamentally in that nucleation and growth requires a large compositional fluctuation called 'nucleation', whereas, spinoidal phase separation does not.

Spinodal decomposition is a mechanism by which a solution of two or more components can separate into distinct regions (or phases) with distinctly different chemical compositions and physical properties. Compositional fluctuations reduce the free energy towards the extremes of the miscibility gap of the phase diagram leading to spontaneous phase separation. This mechanism differs from classical nucleation in that phase separation due to spinodal decomposition is much more subtle, and occurs uniformly throughout the material - not just at discrete nucleation sites. There is no thermodynamic barrier to the reaction inside the spinodal region of the phase diagram, the decomposition is determined solely by diffusion, thus, it can be treated purely as a diffusion problem, and many of the characteristics of the decomposition can be described by an approximate analytical solution; in contrast, theories of nucleation and growth are more complicated. Spinodal decomposition provides a means of producing a very finely dispersed microstructure that can significantly enhance the physical properties of the material (Carter, 2002).

2.3.5 Crystal Growth

Once a stable nucleus has formed it will continue to grow at a rate determined by both the speed with which the required atoms are able to diffuse through the crystal/liquid interface, the concentration gradient and the rate of heat flow away from the crystal. The temperature dependence of crystal growth is similar to that for the nucleation process; the main difference is in the lack of a metastable zone for the former. Growth can occur at any temperature below T_m and above T_g on any available nucleus, which need not have the same composition as the growing crystal. Low melt viscosity leads to high growth rates such that decreasing temperatures act to slow and eventually halt crystal growth. Heat treatments attempt to optimise the optical and physical properties of glass-ceramic materials by directly interfering with the growth process. Glass-ceramic materials made for this study all exhibit a form of crystal growth called Ostwald ripening (Wang *et al.*, 2005).

2.3.6 Ostwald Ripening

Upon nucleation, the solution is far from thermodynamic equilibrium and a decrease in the free-energy is achieved by coarsening the precipitate through crystal growth. This process depends on the Kelvin effect which theorises that smaller particles have a higher solubility. The equations below express particle solubility in terms of

surface tension (σ), particle radius (r), absolute temperature (T) and molar volume (V_m).

$$C(r) = C(\infty)\exp(\alpha/r)$$

$$\alpha = \frac{2k_a\sigma V_m}{3k_vRT}$$

Where:

- $C(r)$ = solubility of phase particle with radius (r)
- $C(\infty)$ = solubility of particle with infinite radius
- R = Boltzmann constant
- σ = surface tension term
- k_v, k_a = volume and area shape factors

The critical radius R_c defines the barrier for crystal growth, all nuclei with radii below this value will dissolve. The critical radius is characteristic of the particle size distribution which is generally skewed towards larger particle sizes. In cases where crystal growth occurs by molecular diffusion, R_c is the mean particle size irrespective of the type of distribution (Finsy, 2004). Assuming the mass of dispersed material is conserved, the critical radius can be determined from particle size distributions at any point in the Ostwald ripening process (Qin-bo *et al.*, 2005).

2.4 X-Ray and Neutron Diffraction

2.4.1 Bragg's Law

Laue is generally credited with the discovery of diffraction, although W.H.Bragg devised an equation which predicted when diffraction would actually take place. This equation became known as Bragg's Law and is arguably the single most important equation in diffraction theory:

$$n \lambda = 2 d \sin \theta$$

Where λ is the wavelength of the incident radiation, d is the inter-planar spacing and θ is the angle between the incident (or diffracted) ray and the relevant crystal planes; n is an integer, referred to as the order of diffraction (Hammond, 2001).

The basic idea behind Bragg's Law is that, when satisfied, X-ray beams scattered from the successive planes of a single crystal have path-lengths differing by exactly one wavelength (for the case of $n = 1$); this can be proven by simple geometrical analysis. In the direction denoted by the Bragg angle θ , X-rays scattered from successive planes interact constructively such that the X-ray detector registers the passage of an intense beam called the diffracted beam. This geometrical approach to X-ray diffraction is, naturally, an over-simplification of a complex quantum mechanical description of X-ray/matter interactions. However, Bragg's law demonstrates the relationship between crystal planes of atoms and the diffraction of incident monochromatic radiation (λ) – this greatly simplifies the subject and is the reason that planar reflection is used to describe atomic scattering in single planes.

One of the concluding ideas from Bragg's Law is that diffraction is, in effect, an "arranged event"; three parameters need to be harmonised: the wavelength of the X-rays, λ , the crystal orientation as defined by the angle θ and the spacing d of the crystal planes under consideration. For a given wavelength and set of planes one can conspire to arrange for diffraction to occur by, for example, continuously changing the orientation, i.e. changing theta or 2θ , until a point arrives when the Bragg condition is satisfied (Kittel, 1996).

2.4.2 'Real' Crystal Structure

Crystallographic theory is essential for the interpretation of diffraction patterns. The real-space lattice is a regular periodic array of points in space which correspond to elements of the real crystal structure such that:-

$$\text{Lattice} + \text{Basis} = \text{Crystal structure.}$$

The 'basis' is either a single atom or a cluster of atoms that is attached identically to each lattice point with the atom coordinates centred at each point. The Miller indices (h,k,l) denote reflection planes in the crystal lattice such that the cube faces of a cubic crystal are (1,0,0),(0,1,0),(0,0,1),(1,0,0),(0,1,0),(0,0,1) where 1 is negative with respect to the origin. The indices h,k,l are defined as the smallest ratio of the reciprocals of the intercepts of the plane on the axes (x, y, z) in terms of lattice constants (a, b, c). The same notation can also be used for crystallographic directions

but with square brackets [h,k,l]. Millar indices, therefore, denote all equivalent planes and directions in the lattice.

There are 14 bravais 3-D lattice types and 7 unique types of lattice cell each with different geometry. The seven systems are triclinic, monoclinic, orthorhombic, tetragonal, cubic, trigonal and hexagonal where the triclinic case is referred to as a 'general' case and the others as 'special' cases. The unit cell is a whole multiple of the primitive cell which is the only unique part of the lattice required to construct the complete space lattice by translation symmetry. The primitive cell is a minimum volume parallelepiped also called the Wigner-Seitz cell (Kittel, 1996). Space groups allow whole real unit cells to be constructed from a few atoms positions by using the cells' natural symmetry; there are 230 unique 3-D space groups in total which are divided into 7 groups for the 7 unit cell types. Common space group symmetry elements are rotation axes, screw axes, mirror planes and glide planes.

An example of the space group Pnma for the orthorhombic system can be used to illustrate the notation and basic concepts of space group theory. The first symbol P informs us that the bravais lattice is primitive orthorhombic, the next three symbols (mna) represent mirror/glide planes parallel and perpendicular to the axes (x, y, z) respectively. Symbol 'm' represents a true mirror/reflection plane; 'n' represents the n-glide plane which reflects accompanied by a translation of $a/2$ and $c/2$ and 'a' represents the a-glide plane which reflects as well as translating by $a/2$. The symmetry elements implied by this space group are illustrated in figure 2.09. The open circles are points of inversion, the closed circles are two-fold screw axes along the z direction, the arrows are two-fold axes along the x-axis at a height of $\frac{1}{4}c$ above the x-y plane, the arrow in the top right-hand corner is the 'a' glide plane in the x-y plane and the dashed-dotted line represents the n-glide plane perpendicular to the x-y plane.

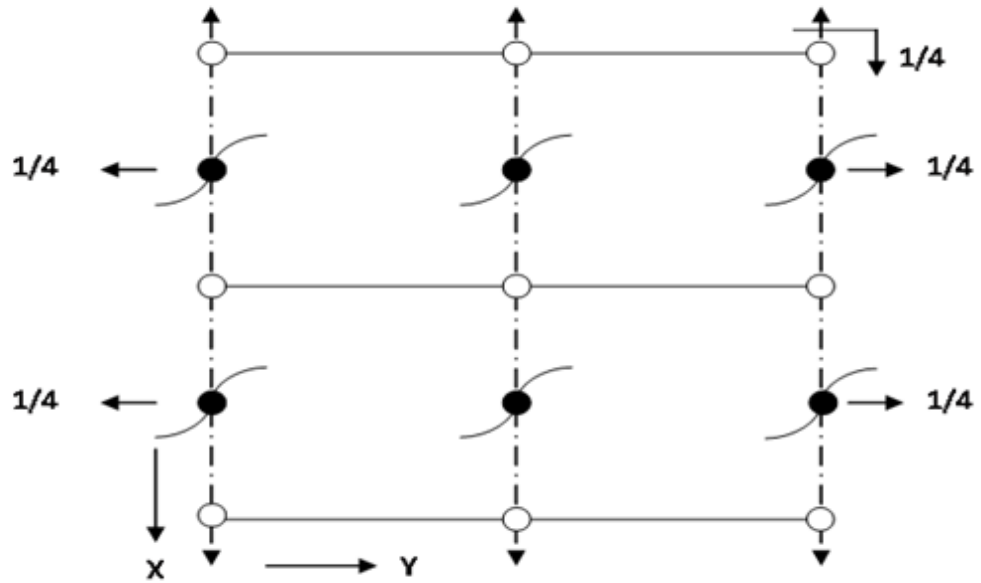


Figure 2.09. Unit cell with the symmetry elements of space group Pmna.

For applications such as Rietveld refinement knowledge of the correct space group is very important as this affects the crystal structure generated (Brown *et al.*, 1973).

2.4.3 Reciprocal Lattice

The reciprocal lattice is the inverse of the real lattice such that the reciprocal unit cell vectors are: $a^* = 1/d_{100}$, $b^* = 1/d_{010}$ and $c^* = 1/d_{001}$. These parameters are normal to the diffraction planes of (100), (010) and (001), respectively, with a magnitude of one over the d-spacing. In vector notation, each reciprocal lattice point (hkl) can be expressed in terms of the reciprocal unit cell vectors, a^* , b^* and c^* , as follows.

$$\mathbf{d}_{hkl}^* = h\mathbf{a}^* + k\mathbf{b}^* + l\mathbf{c}^*.$$

It is possible to build up as many sections of the reciprocal lattice as required with each point representing an individual crystal plane of Millar index (h,k,l) from which diffraction may occur were the Bragg condition satisfied. A schematic reciprocal lattice is illustrated in figure 2.10 and shows just a two-dimensional slice (for simplicity) with the c^* vector perpendicular to the page such that the 221 reciprocal lattice point is one step above 220 and so on, meaning that hkl is above $hk0$ and $hk0$ above $hk-l$. Negative indices, in figure 2.10, are written with a bar accent above (Hammond, 2001).

beam before diffraction can occur. A perfect crystal is composed of many sets of planes that extend along axes defined by Millar indices. If one were to rotate the crystallite, shown in figure 2.12, the planes would rotate with the crystal and there would come a point, diagram 2, when these planes were correctly oriented with respect to the X-ray beam - with atoms scattering in phase to produce an intense diffracted ray.

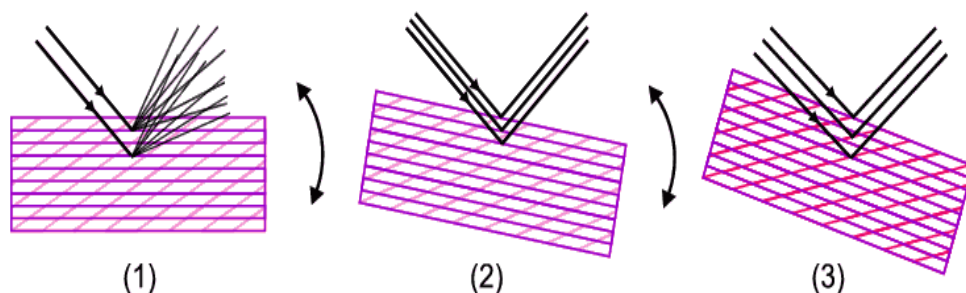


Figure 2.12. Diffraction from a powder

(Chemistry Department UCL, 2005).

In rotating, there would come another point, diagram 3, when an alternative set of planes (in red) orientates to produce diffraction. Clearly, one would eventually reorient the crystallite through all the possible orientations that allow each plane to diffract (when the Bragg condition is satisfied). A proper powder consists of many millions of crystallites, each at different orientations and so in presenting a powder to an incident beam, every possible orientation of a given set of planes is exposed; some, therefore, are certain to be at the correct orientation for diffraction to occur. For this reason, sample re-orientation is never necessary when recording a powder diffraction pattern (Giacovazzo *et al.*, 2002)

2.4.7 The Structure Factor

The concepts of Ewald sphere and reciprocal lattice or Bragg's law predict when diffraction will occur but give no indication of the intensity of a given diffraction event. The structure factor (F_{hkl}) is defined as the ratio of the amplitude scattered by the atoms in a unit cell to that scattered by a single electron; and is determined by the following equation :-:

$$F_{hkl} = \sum_{n=0}^{n=N} f_n e^{2\pi i(r_n)}$$

Where:-

$$f_n = \frac{\text{Amplitude Scattered by Atom}}{\text{Amplitude Scattered by Single Crystal}}$$

The position, \mathbf{r} , of the atoms is described by the use of fractional coordinates (x, y, z) and Millar indices h, k and l .

$$r_n = hx_n + ky_n + lz_n$$

The term $2\pi(hx_n + ky_n + lz_n)$ is the phase angle of the n^{th} atom in the motif (unit cell) and the summation gives the vector sum of all the atomic scattering factors (f_n).

Substitution of the above gives:-

$$F_{hkl} = \sum_{n=0}^{n=N} f_n e^{2\pi i(hx_n + ky_n + lz_n)}$$

This summation can also be written in the form:-

$$F_{hkl} = \sum_x \sum_y \sum_z f_n e^{2\pi i(hx_n + ky_n + lz_n)}$$

Recognising that to sum over all space (x, y, z) within a unit cell is equivalent in diffraction terms to summing over all atoms (n) within the unit cell. A plot of this function shows that as n tends to infinity the form of a Bragg pattern appears with sharp peaks, corresponding to constructive interference, and low background (Hammond, 2001).

For neutrons the above equation also holds, however, f_n is replaced by the atomic scattering length b_n (Squires, 1996).

2.4.8 Types of scattering

Raw diffraction data ($I(Q)$) may first be corrected for anomalous scattering before any form of structural analysis is performed, although this is not always possible.

The total corrected scattering intensity is referred to as $S(Q)$. Anomalous scattering consists of a number of matter and X-ray/neutron interactions described below.

2.4.9 Compton scattering

The scattering of photons from charged particles is called Compton scattering after Arthur Compton who was the first to measure photon-electron scattering in 1922. Compton observed the scattering of X-rays from electrons in a carbon target and found scattered X-rays with a longer wavelength than that incident upon the target. The shift of the wavelength increased with scattering angle according to the Compton formula:

$$\lambda_f - \lambda_i = \Delta\lambda = \frac{h}{m_e c} (1 - \cos \theta)$$

Compton explained and modelled the data by assuming a particle (photon) nature for light and applying conservation of energy and conservation of momentum to the collision between the photon and the electron. The scattered photon has lower energy and therefore a longer wavelength according to the Planck relationship. Compton scattering is incoherent and does not involve a phase relation between incident/scattered radiation, therefore, there is no way to determine its effect. In any case, its contribution to the intensity is a sum of amplitudes squared instead of the vector sum of amplitudes squared as for the coherent case explained below.

2.4.10 Multiple Scattering

An atom absorbs an x-ray of energy E , destroying a core electron with energy E_0 and emitting a photoelectron with kinetic energy $(E - E_0)$. The core state is eventually filled, ejecting a fluorescent x-ray or Auger electron. Once the x-ray energy is large enough to promote a core electron to the continuum, there is a sharp increase in absorption. The ejected photo-electrons can scatter from neighbouring atoms; atomic radius has some relationship to λ and there is a phase shift associated with the scattering event. Thus the outgoing and scattered waves interfere and the scattering of the photo-electron wave function interferes with itself.

2.4.11 Sample Attenuation

This is calculated from the mass attenuation coefficient (μ/ρ) which may be determined by transmission experiments.

Emergent intensity (I) is given by the exponential attenuation law

$$I/I_0 = \exp[-(\mu/\rho)x]$$

This equation can be rewritten as

$$\mu/\rho = x^{-1} \ln I_0/I$$

Where:

$$\begin{aligned} I_0 &= \text{Incident Intensity} \\ \mu/\rho &= \text{Mass attenuation coefficient} \\ t &= \text{Sample thickness} \\ \rho &= \text{Sample density} \\ x &= \rho \times t \end{aligned}$$

Sample attenuation (μt) can be obtained from measured values of I_0 , I , ρ and t ; alternatively, an estimate can be calculated by weighted algebraic sum of the atomic constituents.

2.4.12 X-ray Fluorescence

The phenomenon of X-ray fluorescence is due to absorption of an X-ray photon with simultaneous ejection of an electron whose energy level is similar to that of the incident energy of the photon. This is immediately followed by an outer electron filling the hole with the emission of an incoherent X-ray photon, the latter appearing as background noise in the diffraction data. An example is the fluorescence of iron atoms when irradiated with X-rays produced from a copper $K\alpha$ anode.

2.4.13 Coherent/Incoherent Scattering

This is a phenomenon which concerns neutrons only and complicates the correction of raw neutron data. The scattering lengths of isotopes of the same element are often

quite different such that an elemental crystalline solid produces two types of scattering; only one of these, Bragg scattering, is useful for structural determination.

By definition incoherent scattering is due to correlations between positions of the same nucleus at different times; whereas, coherent scattering accounts for both correlations between the same nucleus and different nuclei in time leading to interference effects and Bragg diffraction (Squires, 1996).

2.5 Rietveld Refinement (Theory)

Structural refinement is an important part of practical crystallography and will play an important role in this study, as a tool for analysing diffraction data.

Refinement means taking an approximate model of the structure and refining it so that the diffraction data calculated from the model more closely resemble those which are observed. This process does not solve structures but provides a best fit scenario. There are several software packages available for this type of refinement, GSAS (Larson *et al.*, 2004) and Fullprof are among the most common. Most software refines structures semi-automatically requiring only minimal input from the user in the form of the order in which the refinement of parameters takes place.

Structural parameters are refined by 'least squares minimisation' of the function:-

$$\sum_i \{Y_i(\text{obs}) - Y_i(\text{calc})\}^2$$

$Y_i(\text{obs})$ in this case refers to the set of observable values provided by the diffraction data; in powder experiments this value can either be the intensity (counts) of individual data points on the time (msec) or 2 theta axis or the total intensity of groups of reflections $\Sigma I(\text{hkl})$. $Y_i(\text{calc})$ is the calculated intensity of each profile point (i) derived from the structural model. Structural refinement techniques before Rietveld were unreliable and attempted to extract overlapping hkl reflection intensities in powder diffraction as a means of structural solution; this led to fewer refinable parameters and a less accurate result.

Rietveld (Rietveld, 1969) considered the case of the angle-dispersive diffractometer, but his theory is applicable to all types of diffractometer including time-of-flight. In

this case, the profile of a single neutron diffraction peak depends on neutron spectral width, sample shape, crystallinity, transmission functions of the collimator and other parameters relating to the instrument and detector. Convolution of these components produces a Gaussian-type peak shape, in some cases asymmetry can occur and additional parameters exist to correct for this. Rietveld realised that the whole profile could be fitted on a point by point basis using the Gaussian peak-shape function without needing to extract the intensities of composite reflections (hkl).

The intensity y_i of the i^{th} profile point may be written as the sum of the contributions of the profiles of all the reflections to that point.

$$y_i = \sum_{hkl} G(x_i, I_{hkl}, H)$$

$$y_i = \sum_{hkl} \sqrt{(4 \log_e 2 / \pi) c j_{hkl} L(2\theta) F^2(hkl) \exp\{-4 \log_e 2 (x_i - 2\theta_{hkl})^2 / H^2\}} / H$$

Where:

c	=	Scale factor
j_{hkl}	=	Multiplicity of hkl reflection
$L(2\theta)$	=	Lorentz correction for the reflection at scattering angle 2θ
$F^2(hkl)$	=	Square of the structure factor of the hkl reflection
I_{hkl}	=	Total intensity of the hkl reflection
$2\theta_{hkl}$	=	Centre of the peak as determined by the d-spacing
H	=	Full width at half maximum height (FWHM)
x_i	=	2θ value of the i^{th} profile point

This can be simply written for a two reflection case as:-

$$Y_i(3) = Y_i(1) + Y_i(2)$$

The quantity to be minimised in this instance is:-

$$\Delta = \sum_i w_i \{y_i(\text{obs}) - y_i(\text{calc})\}^2$$

Where w_i is the statistical weight associated with each data point (i).

The weighting scheme for profile points, indicated above, was introduced after Rietveld's original theory. This is a statistical quantity based on the error on each profile point (i) ($Y_i(err)$).

From theory:-

$$W_i = 1/Y_i(err)^2$$

In most cases a powder diffraction profile has a background count due to the sample environment, incoherent scattering, detector noise and other effects.

This is normally subtracted from the profile as no useful structural information is present. The above expression seems complex, but in practice is simplified to reduce the computing time per refinement.

Although the summation is over all reflections hkl, it is not necessary to sum over all available reflections for each point (i). The shape of the Gaussian profile, which falls rapidly to zero beyond the FWHM, allows any point with a separation of more than 1.5 times the peak width from the i^{th} data point position to be ignored, as expressed by the relation :- $(2\theta_{hkl} - 1.5H < X_i < 2\theta_{hkl} + 1.5H)$. Advance generation of the d-spacing and (hkl) reflection positions along with corresponding structure factors ensure that the codes are as efficient as possible.

There are several ways of treating the background count, one is by graphical method and linear interpolation, this assumes that background exists in the absence of diffraction peaks, however, this is likely to be inaccurate for cases with multiple peak overlap and high (hkl) reflection density.

A more successful technique is to use a polynomial function or other type of power series with refinable parameters; these functions work better for amorphous glassy phases and uneven backgrounds. GSAS, Fullprof (Larson *et al.*, 2004) and others offer a large array of functions for the purposes of background fitting. Generally refinable parameters are split into two groups, the first relates to instrument parameters such as the zero point and those belonging to profile function such as the Lorentz correction, whereas the second concerns structural parameters such as overall scale factor, lattice parameters, atomic coordinates, site occupation number

and isotropic/anisotropic temperature factors. Normally, the user will refine the structural parameters first as these have the most dramatic effect on the quality of the fit, refinement of instrument and profile parameters is largely unnecessary as these are likely to have been pre-set. A common order for parameter refinement is as follows – lattice parameters, atomic coordinates, appropriate profile coefficients such as the Lorentzian coefficients, used for this example, for particle size and micro-strain and others such as the asym parameter. The success of the refinement ultimately depends on the quality of the data set and the accuracy of the initial structural model used.

The mathematics of the refinement is outlined below:-

Rietveld uses non-linear least-squares fitting to minimize the delta function Δ , stated above. Non-linear techniques require iterative numerical methods for solution.

As is the case for all least squares methods this function is a minimum when the partial derivative with respect to each parameter is zero. Differentiating the above equation with respect to each parameter (P_j) by straight forward application of the 'chain rule' yields the following:-

$$\left(\frac{\partial \Delta}{\partial p_j}\right)_k = \sum_{i=1}^N \left\{ 2w_i(y_i(obs) - y_i(calc)) \left(\frac{\partial y_i}{\partial p_j}\right)_k \right\} = 0$$

If M denotes the number of parameters (P_j) where M is denoted by variable k then there is M of the above equations.

Assuming that the parameters of P_j differ from the true minimum by a small quantity δP_j allows application of Taylor's Theorem such that the differential equation above can be written in the form below:-

$$f(x + \Delta x) = f(x) + \Delta x \frac{df(x)}{dx} + \frac{(\Delta x)^2}{2!} \frac{d^2 f(x)}{dx^2} + \frac{(\Delta x)^3}{3!} \frac{D^3 f(x)}{dx^3} + \dots$$

In the case that Δx tends to zero the above expression is simplified to:-

$$f(x + \Delta x) = f(x) + \Delta x \left(\frac{df(x)}{dx}\right)$$

Substitution of this result into y (calc) gives:-

$$y_i(\text{calc}) = y_i(p_1 \dots p_M) + \sum_{k=1}^M \partial p_k \left(\frac{\partial y_i}{\partial p_k} \right)_j$$

Substitution of this alternative form of y (calc) into Δ gives:-

$$\sum_{i=1}^N \sum_{k=1}^M w_i \partial p_k \left(\frac{\partial y_i}{\partial p_k} \right)_j \left(\frac{\partial y_i}{\partial p_j} \right)_k = \sum_{i=1}^N \left\{ w_i (y_i(\text{obs}) - y_i(p_1 \dots p_M)) \left(\frac{\partial y_i}{\partial p_j} \right)_k \right\}$$

This can now be reformulated into matrix notation:-

$$[A][B] = [C]$$

Where A is a square matrix and B and C are column matrices.

Matrix B contains the δP_j shifts to be added to the parameters and matrix C contains the experimental data. Solution of this kind of equation can be achieved through matrix inversion; in order to solve for B one inverts matrix A to form the relation:-

$$B = A^{-1} \times C$$

For the equation above:-

Elements of matrix A are:-

$$A(j, k) = \sum_{i=1}^N w_i \left(\frac{\partial y_i}{\partial p_k} \right)_j \left(\frac{\partial y_i}{\partial p_j} \right)_k$$

Elements of matrix C are:-

$$V(j) = \sum_{i=1}^N \left\{ w_i (y_i(\text{obs}) - y_i(p_1 \dots p_M)) \left(\frac{\partial y_i}{\partial p_j} \right)_k \right\}$$

Modern computing power allows quick solution of this equation (Department of Chemistry, UCL, 2005) (Larson *et al.*, 2004).

2.5.1 Le Bail and Pawley Methods

There are two techniques separate to Rietveld available for extraction or removal of complex backgrounds due to sample environments. Since, most diffraction experiments will have some sort of sample environment signal which needs removing knowledge of these is invaluable. Le Bail and Pawley fit the diffraction pattern without prior knowledge of the sample structure and extract the 'observed structure' factors (F_{hkl}) for each reflection (h,k,l). Both methods are described as decomposition techniques as they attempt to extract individual reflection peaks from single peaks in the diffraction profile. Pawley suggested that powder diffraction profiles could be fitted by least squares method by refining only a few parameters; these were the intensity of each reflection (h,k,l), the lattice parameters of the unit cell and various profile function parameters. Le Bail, on the other hand, only required a fit with the lattice and profile function parameters. Each method has its advantages and Le Bail was a more computer efficient way of fitting a diffraction trace, however, modern computing power allows both techniques to be used indiscriminately. However, where substantial peak overlap occurs both methods will fail as the program will be unable to extract unique reflection intensities for each (h,k,l), in this case a model weighted technique is preferred (Larson *et al*, 2004).

2.6 Single Crystal Diffraction

Rietveld refinement is a technique used for powder data as there is simply not sufficient resolution to separate individual peaks at low Q. Single crystal diffraction uses a single crystal to scatter the beam and records each diffraction peak separately. For single crystals of sufficient purity and regularity, X-ray data can determine the mean chemical bond lengths and angles to within a few thousandths of an angstrom and a few tenths of a degree respectively. Unit cell parameters can also be resolved with much greater accuracy than possible with powder methods. High quality data allows accurate determination of the anisotropic temperature factors for each atom in the asymmetric unit, such that comprehensive crystallographic information files (.cif) and other formats are created and published using this technique. Obtaining a diffraction quality crystal, however, is the chief barrier to solving an atomic resolution structure. Crystals typically need to be > 0.1 mm in all dimensions,

regular in structure and relatively perfect without cracks or twinning; examination under an optical microscope will usually help identify suitable single crystals.

In order to solve a structure one needs all the diffracted intensities that can be measured within the diffraction limit, that is, the reciprocal lattice nodes found within the limiting sphere of radius $2/\lambda$. In most experiments the ideal diffracting sphere cannot be explored due to instrument constraints; since the high angle data for a given wavelength defines the maximum resolving power between two points in reciprocal space, diffraction data are collected to a maximum resolution R_{\max} in Angstroms. The experimentally measurable diffraction intensities are therefore, enclosed in a sphere of radius $D^* = 1/R_{\max}$. When extracting diffraction intensities from single crystals an instrument known as a single crystal diffractometer is used. This technique rotates the single crystal on three or more goniometers so that all of the reciprocal lattice nodes cross the Ewald sphere allowing each to be measured separately in turn. The data produced are highly accurate and should allow full structure solution provided that the single crystal is of sufficient quality. Single crystal diffraction is the only suitable way of resolving macromolecules such as viruses and DNA with thousands of atoms per unit cell and is an important technique in the field of molecular biology and chemistry (Giacovazzo *et al.*, 2002).

3 Materials and Methods

3.1 Frit Preparation

Glasses of a single composition with various added dopants were prepared from both laboratory and commercial feed-stocks. The suffixes original and commercial are added to the glass designator LDIG 24 to identify both the feedstock type and key differences in the processing route of the glass frits. The candidate glass composition is produced from a ternary system based on 90 mol % barium fluormica ($\text{Ba}_{0.5}\text{Mg}_3(\text{Si}_3\text{AlO}_{10})\text{F}_2$), 6 mol % calcium phosphate ($\text{Ca}_3(\text{PO}_4)_2$) and 4 mol % cordierite ($\text{Mg}_2\text{Al}_4\text{Si}_5\text{O}_{18}$).

	Weight %	Mole %	Supplier	Product Code
SiO ₂	39.0	42.25	Hoben Industrial Minerals	125586
Al ₂ O ₃	8.0	6.85	Calmot AD	233294
BaCO ₃	19.9	6.56	Johnson Matthey	230029
MgF ₂	12.6	13.11	Glassworks Services	125585
MgO	17.0	27.39	Peter Whiting	125590
CaCO ₃	4.0	2.62	Johnson Matthey	232844
Al ₃ PO ₄	4.7	1.21	Brenntag (UK)	125578

Table 3.01. Showing the feedstock composition of LDIG 24 commercial glass and the origins of each feedstock component.

Feed stock was weighed out on a 2 decimal place electronic balance; the weights required were calculated in a computational spreadsheet for the desired mass of every batch. Each component was placed in a plastic screw top bottle and weighed out individually using the ‘tare’ function of the balance. The usual safety precautions applied when handling feed stock powders namely gloves, lab-coats, aprons and dust masks. Once the full batch had been weighed a stainless steel rod (L: - 100 mm, Ø: - 10 mm) was added and the container lid replaced and screwed tightly. The container was then tumbled in a rotary mill (US stoneware) for 60 minutes to mix and homogenise the contents; the purpose of the metal rod was to break up agglomerates which are common with finely ground materials. After this stage commercial and original forms of feed stock are treated differently.

3.1.1 Original Feedstock.

Homogenised batches were then transferred to large mullite crucibles (SGP, Dyson Precision Ceramics) complete with a lid to reduce weight loss of volatilized components such as SiF_4 during heating. Crucibles were first pre-heated for 30 minutes inside a heat-treatment furnace (Lenton, UK) at around the glass transition temperature (T_g), to reduce stresses from thermal cycling, and then placed in a higher temperature furnace (Pyrotherm, UK) at 1440 °C to allow the molten glass to form. After 1 hour the molten glass was poured into a quenching tank filled with cold deionised water. The resultant glass frit was collected using an in-house sieve and aqua-pump assembly and then dried in a drying cabinet (RC 2000 drying cabinet, Marrutt Ltd). Once dry frit was labelled and stored in resealable plastic bags for later use.

3.1.2 Commercial Feedstock

Homogenised batches were then transferred to slip cast alumina crucibles (Elite Thermal Systems), as these are found to have a much greater chemical resistance to molten glass. These were smaller than the mullite crucibles used previously and typically had a capacity of about 400 grams. The alumina crucible was then placed inside the larger crucible and bedded on sintered powdered alumina for support; the lid of the mullite crucible was then replaced as before and pre-heating took place prior to transfer to the main furnace. All subsequent steps match those of the original process.

3.2 Making Glass Rods

The standard rod diameter for most purposes was 18mm; approximately 80g of coarse ground glass frit was poured into a slip-cast alumina crucible. The alumina crucible was placed in a larger SPG mullite crucible (Dyson Thermal Technologies, U.K.), and bedded with Al_2O_3 (alumina) powder, the lid was then replaced on top. After 30 minutes the crucible was removed and transferred to the glass melting furnace which had been pre-heated to 1440 °C. The temperature of the heat treatment furnace was set to a value of T_g-70 ; approximately equal to 571 °C for LDIG 24. After forty-five minutes a graphite mould with an 18mm internal diameter was placed in the heat treatment furnace. Fifteen minutes later the crucible was

removed from the main furnace and placed on a sand tray; the graphite mould was then taken from the annealing furnace at Tg-70 with tongs and held in place adjacent to the crucible in the sand tray at an angle of 45°. A second operator then quickly removed the crucible lid, lifted out the alumina crucible with the molten glass and poured the glass smoothly into the mould, trying their best to avoid trapping air, until it was completely filled; after which the mould was replaced in the annealing furnace. The annealing regime consisted of a 1 hour hold at Tg-70 and subsequent natural cooling to room temperature which was programmed into the furnace controller by the user. The glass rods were removed from the moulds when they were cool enough to handle, typically after 12 hours.

In many cases, however, with different heat treatments there were problems with machining these 18 mm samples to produce sample rod diameters suitable for bi-axial flexure and hardness measurements. Attempts to use similar single rod moulds for smaller diameters failed due to the high viscosity of LDIG 24 melt glass; large air bubbles would freeze into the glass making the sample unsuitable for mechanical testing. A solution was to cast a large number (≈ 10) of glass 'studs' (L: - 20 mm, \varnothing : - 14 mm) in specially designed moulds, figure 3.01. These studs were still appropriate for sectioning with a diamond saw and short enough that glass viscosity had negligible effect on the quality of the cast product. The quantity of glass cast per mould was double that originally possible, greatly improving the efficiency of the casting process.

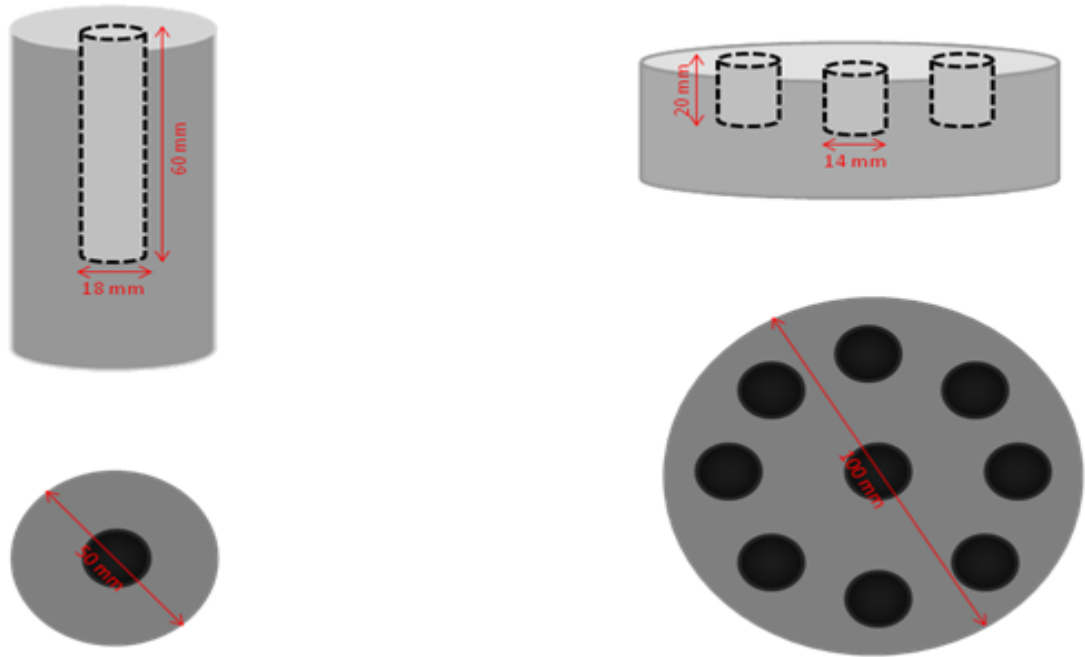


Figure 3.01. Schematic of the single 18 mm rod mould, left, and the larger multiple 14 mm rod mould, right.

3.3 Investment of Glass Rods

In order to prevent the larger (18 mm) glass rods from deforming or slumping during the heat treatment, the glass rod was invested using a phosphate bonded investment material (Hi-temp, WM Mix Corporation, USA). The rod was first pressed end-on into a base of soft dental wax and surrounded with an equal height plastic tube (\O : 28 mm) fashioned from acetate; the tube was pressed firmly into the surrounding base to form a temporary seal. The investment material was then prepared according to the manufacturer's instructions and manually mixed until a suitable consistency had been achieved, at which point the mixture was poured into the investment mould until the top of the rod became submerged. The mould mixture was then left to stand for 30 minutes until set and the plastic tube removed prior to heat-treatment.

In the case of smaller (14 mm) glass studs investment was not essential, particularly if samples were heat-treated in a lengthwise position instead of upright. The investment used here is a porous medium and is not suitable for very high temperatures approaching the melting point of the glass ($> 1200\text{ }^{\circ}\text{C}$ for commercial LDIG 24). All laboratory heating regimes had crystallisation hold temperatures below this.

3.4 Heat Treatment of Glass Rods

Investment supported rods were placed inside a heat treatment furnace and subjected to several different heat treatment regimes. The standard regime for the original glass (LDIG 24 original) was a 10 °C/ min ramp to the nucleation hold at 644 °C, a subsequent isothermal for 2 hours, a 10 °C/ min ramp to 1225 °C, an isothermal hold for 3 hours and then natural cooling to room temperature. This regime remained unchanged throughout the course of this work as it was found that it was no longer possible to make this glass in-house due to unknown changes in the frit impurity levels. New heat-treatments, as shown in figure 3.02, were designed for LDIG 24 commercial frits with lower crystallisation hold temperatures due to an unexplained overall lower melting point when compared to the original formulation. Crystallisation rates in LDIG 24 are rapid even when un-doped; therefore, heating rates are unlikely to have an effect. Changes to the original heat treatment focused on the crystallisation hold temperature which directly affects the crystalline volume fraction in the cerammed product, the nucleation hold temperature (644 °C) and duration (2 hours) were left unaltered. Five crystallisation hold temperatures were investigated between 950 °C and 1150 °C in successive intervals of 50 °C for the purposes of comparing mechanical and optical properties. Heating rates and hold times remained unchanged in each case.

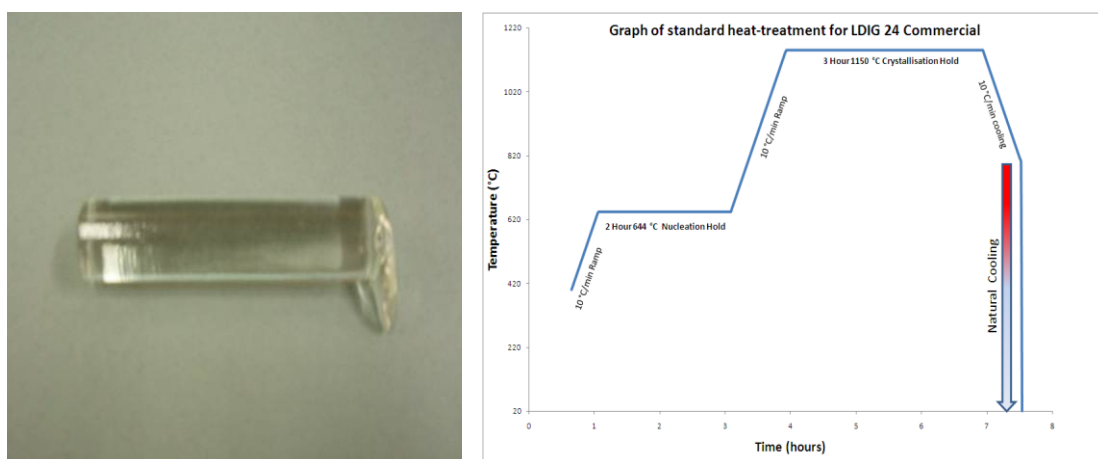


Figure 3.02. 18 mm glass rod, left, and the standard treatment regime, right.

3.5 Sectioning of Glass-Ceramic Rods.

The diameter of samples is limited by the ISO: 6972:2007 standard for bi-axial flexure testing in dental ceramics which specifies a diameter in the range of 12 mm to 16 mm for machinable ceramics. For all work involving mechanical testing samples were either machined (with a lathe) or cast to the modal value of 14 mm. Disc thicknesses for BFS are required to be within 1.2 mm (± 0.2 mm) requiring precision cutting with a 1 mm diamond saw. A digital micrometer (Mitutoya, Japan) with 0.001 mm resolution was used to ensure that each disc was cut to no less than 1.4 mm to allow sufficient margin for grinding and polishing. A minimum of 10 discs were prepared for each material under test, with one discarded exception, and 20 discs were prepared where possible. The samples were recycled after BFS for the purposes of Vickers hardness and scanning electron microscopy (SEM) to reduce sample preparation time.

3.6 Polishing of Samples

An automatic grinding and polishing machine fitted with a Power Head PH123 (Impec 302 DVT Grinder Polisher, Bennetec, UK) was used for disc grinding and polishing. This was performed for specimens required for bi-axial flexure, SEM and gloss-meter measurements. Although automatic grinding and polishing is possible, a manual technique was preferred due to difficulties in using the alternative and the potential for sample losses. Grinding and polishing took place in several stages. At the start of the grinding process silicon carbide paper of 280 grit was used to reduce the sample thickness to approximately 1.30 mm then a finer grit of 480 was applied to remove scratches and surface imperfections, finally 6 micron diamond suspension impregnated cloth was used to polish both sides of each disc intended for BFS. This is sufficient for the ISO which stipulates an upper limit of 16 microns. In the case of gloss measurements several finer surface finishes were achieved to determine the effect of surface roughness on gloss, these were 1 micron (Bennetec diamond suspension) and 0.3 micron (Bennetec α -alumina suspension). During grinding and polishing the discs were thoroughly rinsed in water and dried after each stage to allow for surface examination.

3.7 Bi-axial Flexure

A piston-on-three-ball biaxial flexure test fitting was mounted on a LR10K Universal Testing Machine (UTM) (Lloyd Instruments Ltd, Hampshire, UK) with a 5 kN ($\pm 0.5\%$) load cell, the bearings sat on a circle of 10 mm diameter and the diameter of the piston loading pin was 1.43 mm.

The diameters and thicknesses of pre-prepared specimens were determined using a digital micrometer screw gauge (Mitutoyo, Japan) with 0.001mm resolution. Four measurements were made in each case and then an average was taken. Each disc was sandwiched between two polyethylene pieces and placed centrally over the three supporting bearings, figure 3.03. The UTM was operated in manual mode with a cross-head speed of 1 mm min^{-1} and the peak load set to record at failure; in accordance with ISO 6872:2007 Dental Ceramics. The procedure was repeated for all suitable specimens.

Data were collected and entered into an excel spreadsheet based on the following equations:-

$$\sigma = \frac{-0.2387 \cdot P(X - Y)}{d}$$

$$X = (1 + \nu) \ln \left(\frac{r_2}{r_3} \right)^2 + \left[\frac{1 - \nu}{2} \right] \cdot \left(\frac{r_2}{r_3} \right)^2$$

$$Y = (1 + \nu) \left[1 + \ln \left(\frac{r_1}{r_3} \right)^2 \right] + (1 - \nu) \cdot \left(\frac{r_2}{r_3} \right)^2$$

Where:

- P = load at failure (N)
- d = mean thickness (mm)
- ν = Poisson's ratio
- r_1 = radius of circle ball bearings (mm)
- r_2 = radius of piston pin (mm)
- r_3 = radius of specimen disc (mm)
- σ = tensile stress (MPa)



Figure 3.03. Pictures of the biaxial flexure mounting with glass-ceramic disc under test.

3.8 Vickers Hardness

Hardness is a measure of a solid materials' ability to resist permanent deformation. The aim of a hardness indentation test is to obtain a hardness value from measuring the depth or area of indentation left by an indenter of a specific shape with a set load and with a certain indentation time.

The Vickers hardness tester is versatile and relatively straight-forward to use. For each material under test two fragments from two discs from different rods each from the same batch were tested independently. This allowed use of the two sample t-test to evaluate the equivalency of both means.

A computer controlled micro indenter (Struers) with an optical microscope and attached CCD camera with computer imaging software was used in the test. The Vickers indenter applied a load of 1 kg for 15 seconds to produce a measureable indentation in the surface of the sample; these conditions were applied to every sample except one. In the case of LDIG 24 original a load of 0.1 kg and a 5 second application time gave the best results. Once the test was complete an image of the indent appeared on a screen with movable cross-hairs, once these had been correctly positioned an optical measurement of the two diagonals of the indentation was made. The Vickers hardness was automatically calculated using the following equation.

$$VHN = 1854.4 \times \frac{F}{d^2}$$

Where:

VHN = Vickers hardness number
F = load (gf)
d = mean diagonal of indentation (μm)

3.9 SEM/EDS

SEM (Scanning Electron Microscopy) is analogous to optical microscopy in that electrons rather than light are used to form an image; the beam that originates from the top of the microscope is a result of thermionic emission from a filament. The beam is accelerated and passes through a series of magnetic lenses which focus the beam onto the sample. Low energy electrons are, subsequently, ejected from the sample either as scattered or secondary electrons which are recorded by detectors; information is then displayed in the form of optical images. These instruments have a large depth of field and can produce high resolution images down to a few microns (100,000 x).

Images were collected from sample surfaces in both secondary electron imaging (SEI) and back-scattered electron imaging (BSI) modes using a Phillips XL 30 SFEG SEM @ 15 kV. Sample discs, 14 mm in diameter and 1 mm thick, were polished down to 0.3 μm in preparation for viewing surface morphology under SEI and fractured or rough cut fragments were prepared for viewing phase composition under BSI. Each sample was mounted on a SEM stub with a carbon adhesive tab and platinum-palladium sputter coated, using a Cressington® 208 sputter coater, to improve surface conductivity and prevent static charging. Sputter coating with elemental metals is preferable, in this case, as carbon is prone to scaling and can mask topological features. SEM was used to display the microstructure and surface morphology of several LDIG 24 commercial samples after different heat-treatments. In addition to topographical information, elemental compositional information at the sample's surface was obtained by EDS (Energy Dispersive X-ray Spectroscopy) using an EDAX Phoenix Analysis System.

3.10 Electron Microprobe Analysis (EMPA)

This technique is similar to EDS, although usually more accurate due to the use of standards, an electron beam is directed at a sample to determine its chemical composition from measured spectra. The single crystal sample was mounted on a glass slide, after the single crystal diffraction experiment of section 3.16.2, and carbon sputter coated. EMPA was used to accurately determine the chemical composition of the single crystal (Chapter 4) and allow refinement of a reasonably accurate starting model for the mica structure. A Camera Sx-50 micro-probe analyser, with a 15 kV electron beam, was used to take five different readings of the crystal surface; some oil contamination was present on the sample after the single crystal diffraction experiment, however, good consistency in the results was noted.

3.11 Glass Grinding and Sieving

Glass frit in batches up to 100 grams were ground on a vibratory mill (Glen Creston Gyro Mill) in a steel puck-ring and dish apparatus for 2 minutes. Ground glass was sieved through a number of stainless steel mesh brass sieves stacked in order of increasing particle size from 45 μm up to 1 mm. The stack was placed on a vibrating sieve shaker for 90 minutes until each particle size fraction had been separated. This procedure produced a number of different particle sizes for DTA. In XRD sample preparation the gyro mill was not appropriate, due to contamination issues, and a porcelain pestle and mortar was used instead.

3.12 Differential Thermal Analysis

A DTA trace is a graph of the differential temperature between the sample and a reference material, in this case alumina. Alumina remains inert with respect to phase changes even at very high temperatures. DTA is a sensitive method for evaluating the thermal properties of samples covering both exothermic and endothermic energies. The sample and the reference are placed in matching platinum crucibles and temperature changes are measured by two thermocouples in direct contact with the crucible bases. Data were collected using a Stanton Redcroft Differential thermal analysis unit interfaced with a P.C.

The reference sample weighs 0.15 g; therefore, all samples used in the DTA must weigh the same. It is common for the selected sample to have a narrow range of particle sizes recovered by sieving, most particle sizes used in DTA fall into the categories: > 2mm, > 90 μ m and < 90 μ m to > 45 μ m. The operation of the DTA is controlled by a computer program; the heating regime including holds, heating rates and temperature ranges over which DTA data are collected is programmed by the user. Once the data have been downloaded from the DTA it is processed in Excel.

Differential thermal analysis has been used for determination of the activation energy, optimum nucleation temperature and thermal properties such as melting point for both the commercial and original forms of LDIG 24.

3.12.1 Optimum Nucleation Temperature

This technique analyses the effect of different isothermal hold temperatures on the peak crystallisation temperature T_p ($^{\circ}$ C) when compared to the original value T_o . Successive DTA runs with nucleation holds between 600 $^{\circ}$ C and 680 $^{\circ}$ C, in ten degree intervals, were performed for both commercial and original LDIG 24 samples in coarse frit form. Plots of ($T_p - T_o$) versus nucleation temperature ($^{\circ}$ C) were produced and the optimum nucleation temperatures, corresponding to the maxima of the resulting curves, recorded in each case.

3.12.2 Activation Energy Determination

This work is based on the technique devised by Kissinger (Wang *et al.*, 1990). This procedure measures the variation in the peak crystallisation temperature with different heating rates ranging from 2 to 10 $^{\circ}$ C/min in one degree intervals for this case. The activation energy of crystallisation (E_a) was calculated by the Marotta *et al.* (1981) and Matusita *et al.* (1982) methods. Matusita's technique was used to take account of the crystallisation kinetics involved and expresses a more meaningful activation energy value. The activation energy for a glass-ceramic calculated by either method should be approximately the same. This is ensured by the use of Avrami exponents (**m** and **n**) which refer to the crystallisation behaviour. For instance, when **n** = **m** either bulk nucleation with a constant number of nuclei or surface nucleation is indicated, with **n** = **m** = 3 corresponding to 3D crystal growth.

The Ea Morotta method is expressed as:

$$\ln\left(\frac{1}{\beta}\right) = \frac{E_a}{RT_p} + C$$

Where:

- β = heating rate
- E_a = activation energy
- T_p = peak crystallisation temperature
- R = gas constant

A plot of $\ln(1/\beta)$ against $(1/T_p)$ yields a linear plot with a gradient that represents the activation energy of crystallisation E_a .

The Matusita method is expressed as:

$$\ln\left(\frac{\beta^n}{T_p^2}\right) = \frac{-mE_a}{RT_p} + C$$

Where:

- β = heating rate
- E_a = activation energy
- T_p = peak crystallisation temperature
- n/m = Avrami coefficients

A plot of $\ln(\beta^n/T_p^2)$ against $(-m/T_p)$ yields a linear plot as before, however, with a gradient that represents the activation energy for a certain crystallisation mechanism (n and m values).

3.13 Coloured LDIG 24 Commercial Samples

This work attempted to develop a doping regime for producing coloured glasses which when heat-treated (cerammed), for conversion to glass-ceramics, would be suitably aesthetic for use in chair side CAD/CAM applications

3.13.1 Coloured Frits

Dopants were added to the experimental parent glass frit by mol %. The mixture was tumbled for one hour and transferred to an alumina crucible, subsequent processing was identical to that described for undoped glass frit production. The colours of doped frits were photographed and crudely noted as shown in table 3.02 and figure 3.04.

These frits were cerammed using the standard heat treatment optimised for the parent glass (LDIG 24 commercial). The bulk and surface colours of the respective glass-ceramics were also noted and photographed.

mol %	Dopant	GF Colour	S-GC Colour	B-GC Colour
2	Ce(IV)O ₂	Yellow	Cream	Cream
4	Ce(IV)O ₂	Yellow	Cream	Cream
2	Cr(III) ₂ O ₃	Green	Grey	Dark Grey
2	Ti(IV)O ₂	Clear	White	White
2	Ni(II)O ₂	Brown	Pale Yellow	Pale Yellow
2	Fe(III) ₂ O ₃	Yellow/Green	Orange	Cream
2	Fe(II)SO ₄ ·7H ₂ O	Yellow/Green	Dark Cream	Dark Cream
1+1	Ni(II)O ₂ +Fe(II)Cl ₃	Brown	Orange	Yellow
1+1	Ni(II)O ₂ +Fe(II)SO ₄ ·7H ₂ O	Brown	Orange	Yellow
3+1	Ni(II)O ₂ +Fe(II)SO ₄ ·7H ₂ O	Yellow/Green	Orange	Strong Yellow
1	Fe(II)Cl ₃	Yellow/Green	Dark Cream	Dark Cream

Table 3.02. Colour observations.

Colours of glass frit (GF), surface glass-ceramic (S-GC) and bulk glass-ceramic (B-GC) for parent glass LDIG 24 commercial with added dopants by mole %.



Figure 3.04. Cerammed LDIG 24 commercial + 2% Ni(II)O₂ (by mol), left, and LDIG 24 commercial + 3 % Ni(II)O₂ + 1 % Fe(II)SO₄.7H₂O (by mol), right.

3.14 Coloured Glass-Ceramics

Coloured frits for sample rods were prepared in the same way; frit was melted and then cast in multiple 14 mm rod graphite moulds and heat treated in the standard regime (@1150 °C for 3 hours), as described in section 3.2. A range of six different coloured glass-ceramic discs were prepared, one from a rod of each composition, and measured in colour space using an X-Rite 939 ® spectrophotometer. Colour data were subsequently exported into an Excel spreadsheet using X-Rite Color Master software.

3.14.1 Colour Spaces

Colour space is a mathematical description of perceived colour. The usual reference standard is CIELAB or CIEXYZ colour spaces which were designed to measure all colours visible to the human eye. A colour space attempts to assign ‘tristimulus’ values with each colour, usually denoted by X, Y and Z. Tristimulus parameters represent red green and blue primary colours and approximately correspond to the wavelength peak sensitivities of the colour photoreceptors (cones) in the eye. Tristimulus values, therefore, represent real colour perception, any two colours with the same X, Y, and Z parameters will always appear identical to an observer. Since field of view affects colour perception of the eye, as cones are unevenly distributed, a standard observer is defined for each colour space. The standard observer definition determines the numerical solutions of three colour matching functions used in the evaluation of X, Y and Z (Kuehni, 2003).

3.15 Single Crystal Growth

Many industrial scale techniques exist for growing large synthetic single crystals of almost any material a notable example is the silicon wafer inside the microchip. One such technique is the vertical Bridgeman (VB) method whereby single crystals are grown by directional solidification in vertical bottom seeded crucibles (Ostrogorsky, 1990). This technique employs a tube furnace to heat the melt radially through the walls of the crucible as it is slowly drawn through the furnace; immersion heaters are often used to directly control temperature gradients at the crystal/melt growth interface. The melt temperature is typically just above the melting point of the crystalline growth phase. Large crystals require that radial temperature gradients are minimized to avoid segregation in the growing crystal interface and an effect known as convective mixing. Axial temperature gradients are responsible for controlling the crystal growth and are typically an order of magnitude greater. A quantity known as the axial Rayleigh number (R_{axial}) describes the nature of heat transfer along the axis of the melt; high axial temperature gradients lead to a high value of R_{axial} which stratifies the melt and promotes crystal growth.

For the purposes of this experiment an apparatus was designed and built using non-specialized equipment that attempted to simulate some of the conditions described above; particularly a higher axial than radial temperature gradient. The crystal phase in this case is mica, a layer silicate. A procedure was designed with the aid of a computer program (refer to appendix 3.1) to ensure that large mica crystals would surface nucleate and crystallize from the melt

The apparatus (figure 3.05) consisted of a ground glass bearing cylindrical alumina crucible (D:- 4.2 cm , L:- 10 cm) surrounded by an alumina powder compact of outer radius 5cm inside a large mullite crucible which was thermally insulated with kaolin ring-binder. An alumina sheath containing a Pt-Rd thermocouple was inserted through the outer crucible to allow for accurate and independent determination of the melt temperature. A lid completely covered the assembly which was placed inside a Pyrotherm® furnace at room temperature (300 K) along with a second smaller alumina lid for the inner crucible; care was taken to ensure that the thermocouple lead wires were fed under the furnace door without making contact

with any metal surfaces. The furnace was then programmed through its Eurotherm® controller to ramp at 10°C/min up to 1440 °C and hold. The furnace temperature was held at 1440 °C for approximately 5 hours whilst the inner most glass bearing crucible equilibrated. Once this had occurred, an elaborate cooling regime designed for the crystal growth phase of the experiment was initialised (figure 3.06).

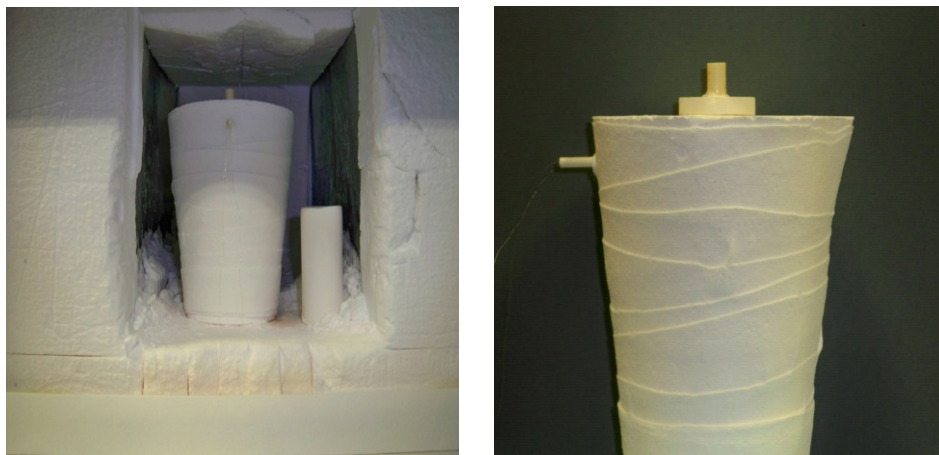


Figure 3.05. Apparatus used to manufacture single crystal.

The furnace was cooled from the hold temperature at a maximum rate of approx. 15 °C/min to a new hold temperature of 1260 °C - the predetermined melting point of the glass phase, the lid on the outer crucible was then removed and replaced with the smaller alumina lid covering just the inner crucible. This was to prevent rapid cooling of the melt surface which must nucleate the single crystals in this case. After several minutes cooling resumed down to a lower hold temperature of 1200 °C. At this point the temperature was cycled between the two hold temperatures at approx. 10 °C/min for 1 hour; the computer model had shown that the effect of cycling was to maintain a high melt temperature and the relative magnitudes of the axial and radial temperature gradients which became significantly reduced with time (in appendix 3.1). In Bridgeman furnaces crystal growth rates are typically 1 - 2 mm per hour, hence, the purpose of temperature cycling to maintain conditions for crystal growth for as long as possible.

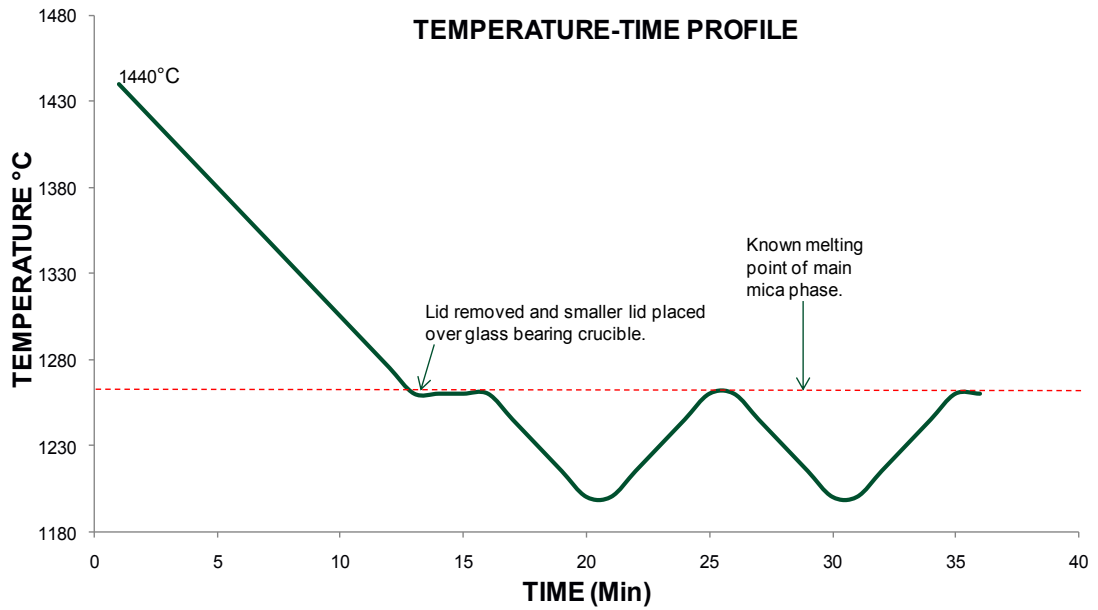


Figure 3.06. Temperature-time profile.

Melt stratification is key to crystal growth and was determined to be significantly reduced after 1 hour; after this time had elapsed the furnace was cooled at 10°C/min down to room temperature - typically taking around 12 hours. Once cooling was complete the glass bearing crucible could be removed and handled; Figure 3.07 clearly shows the presence of mica platelets which have nucleated on the surface of the melt. Single crystals grown with this technique were up to 5000× larger than those found in a sample of standard heat treated glass and are subsequently large enough for single crystal X-ray diffraction.



Figure 3.07. Crystal in situ after experiment.

Careful removal of the platelets from the melt surface was achieved by accurate sectioning with a diamond circular saw and the use of a razor blade to ease the crystals away. Figure 3.08 shows that many of the crystals were less than perfect, with twinning and cracks evident, and as such unsuitable for diffraction; however, the yield was large enough that a number of suitable specimens were found on inspection under an optical microscope.

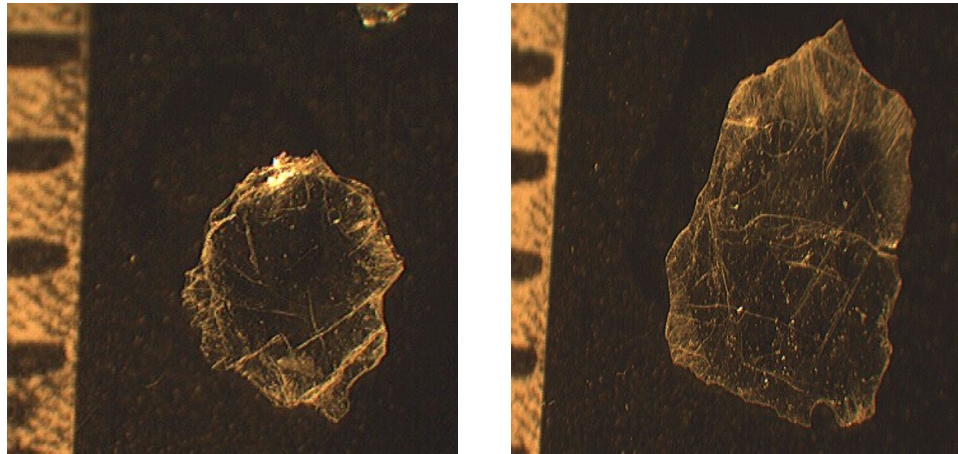


Figure 3.08. Single crystals extracted after experiment; the scale on the left is in millimetres (mm).

3.16 X-ray Diffraction

3.16.1 Powder XRD

XRD is a quantitative and qualitative technique which can be used for characterisation of glass-ceramics and the structures of crystalline phases. This technique has been used in this case to identify secondary phases and perform basic quantitative analysis by intensity integration. Powder X-ray diffraction is complimentary to other diffraction techniques such as those described in this work. The computer software used to identify secondary phases, apart from mica, was *Crystallographica Search-Match* (version 3, 1, 0, 0). XRD was performed on a Siemens 5000 diffractometer with a copper anode (40 kV, 35 mA), typically within a scan range of 5 to 100 degrees two theta. The step size and dwell time were set to 0.02° and 7 seconds, respectively. All of the glass-ceramic samples measured exhibited significant noise in the patterns, hence, a long dwell time was chosen to minimise this (McCusker *et al.*, 1999). The vast majority of samples were powdered with particle

sizes typically less than 45 μm to reduce preferred orientation. Powders were packed into standard holders, 25 mm in diameter and 5 mm deep, to ensure a flat level surface; in the case of smaller samples, powders were dusted over a greased shallow (< 1 mm) sample holder. Samples were also rotated around their vertical axis, during the diffraction experiment, to reduce preferred orientation in the sample plane. Both surface samples and bulk samples of LDIG 24 commercial glass-ceramics were examined with XRD analysis.

3.16.2 Single Crystal XRD

A single crystal diffractometer consists of an X-ray source, an X-ray detector and a goniostat that orients the crystal so that any diffracted beam can be received by the detector. The crystal chosen, after the experiment in section 3.15, was transparent and had dimensions of: - 0.28 x 0.19 x 0.01 mm, after being cut from a larger platelet under an optical microscope. Data were collected by a Bruker-Nonius X8 diffractometer with a molybdenum (Mo) $K\alpha$ source ($\lambda = 0.711 \text{ \AA}$); the sample was pre-cooled with liquid nitrogen to 150 K. Sample cooling, in this case, helped to improve the quality of the data and reduce signal noise. Software packages *Dirdif 2008* and *Shelx '97* were used for the initial solution and refinement of data, respectively. This instrument is based in the Department of Chemistry at the University of Leeds and was operated by Mr. Colin Kilner.

3.17 Software

3.17.1 *Dirdif 2008*

Dirdif is a collection of programs for solving and refining structures from single crystal data; written by Beurskens *et al.* (2008). Programs, from this suite, used in this work for initial structure solution of the single crystal, section 4.2.1, were *Patty* and *Orient*.

Patty is a program designed to calculate and interpret a sharpened Patterson map of the data. A Patterson map represents the distribution of vectors between atoms in the unit cell and allows determination of all the atomic positions. This particular program is only suitable for heavy atom structures, and requires at least one heavy atom in an otherwise light atom structure to be effective; barium mica satisfies this

criterion. The required input files are a crystal data (.dat) file, containing unit cell parameters, space group and an estimate of unit cell contents, and an .hkl file containing h k l values with associated observed intensities and errors; the latter was exported from the single crystal diffractometer. The output is a .res file, which is compatible with *Shelx* software and other refinement programs, containing the unit cell parameters, space group and atoms with associated fractional coordinates and occupancies.

Orient was used to refine the results of *Patty* and is programmed to find the correct orientation of a molecular fragment (model) by means of vector search methods by Norman (1966). The mica structure derived from the first *Patty* run was inputted into an .atmod file, which is the input file for *Orient*. The program was then executed to produce a refined version of the .res file outputted by *Patty*.

3.17.2 *Shelx* '97

Shelx is a suite of programs for the structure solution and refinement of crystal structures from diffraction data, and is primarily intended for single crystal X-ray data of small (non-macromolecular) structures (Sheldrick, 2008). In this work only the structure refinement program *Shelxl* was used. The output .ins file from *Dirdif 2008* was imported into the *Shelxl* software along with the same .hkl diffraction file used in the *Dirdif* refinements. The .ins file needs to be modified with *Shelx* instructions before a refinement can be initiated. Variables such as atom occupancies, fractional co-ordinates and iso-thermal agitation factors (UIISO) were refined either individually or collectively, subject to appropriate constraints, against a 'Goodness of Fit' (Goof) parameter defined as:-

$$Goof = \left\{ \frac{[w(f_o^2 - f_c^2)]}{(n - p)} \right\}^{\frac{1}{2}}$$

Where:

w	=	weighting factor (normally 0.1)
n	=	number of reflections
p	=	number of parameters refined
f_o^2	=	experimental intensity data
f_c^2	=	simulated data based on model

The single crystal structure, in this case, was refined using the difference Fourier calculation (FMAP 2) or the difference between the electron densities derived from the model and the real data. Once the refinement was complete, with a Goof parameter less than unity, it was possible to export the model as a *.cif* (Crystallographic Information File) or a number of other different formats for use with non-*Shelx* compatible software.

3.17.3 GSAS

GSAS (General Structure Analysis System) software by Larson *et al.* (2004) is a suite of many programs for analysing both X-ray and neutron powder data, although, some facility also exists for analysing single crystal data. This study includes Le Bail and Rietveld fits of both neutron and X-ray data that help develop understanding of phase formation in LDIG 24 commercial glass-ceramics. The vast majority of this work has been completed by use of the *GSAS* GUI (Graphical User Interface). In order to work in *GSAS* one needs, at a minimum, the correct lattice parameters and space group of the phase/phases concerned, the experimental raw data file in *GSAS* format and an instrument parameter file (*.prm*) that gives the characteristics of the diffractometer such as radiation wavelength (λ) and line profile coefficients. CW (Constant Wavelength) profile functions 2 and 3, in *GSAS*, have been used for neutron and X-ray data respectively. Both of these pseudo-Voigt type functions are identical apart from additional terms in function 3 that account for axial divergence in the beam – a phenomenon that causes asymmetric tails to form on peaks at low 2θ , apparent in many of the XRD patterns from this work. Profile coefficients U, V, W and P were defined using sample standards throughout and determine how the Gaussian variance of the Bragg peak varies with 2θ .

3.17.4 Le Bail fit in GSAS

The Le-Bail fit begins with a set of identical structure factors to obtain an initial set of F_o (observed structure factors) and only requires accurate phase lattice parameters

and profile coefficients to work. Over a pre-defined number of least squares cycles, each set of F_o extracted from the previous cycle is used in the next such that the χ^2 factor is minimised. It was also possible to refine parameters such as lattice parameters and sample dependant profile coefficients using this technique.

3.17.5 Rietveld fit in *GSAS*

The Rietveld fit uses the technique first devised by Rietveld (1969). This method applies the same least squares approach of the Le-Bail fit to refine the theoretical line profile until it matches that measured by the raw data. A full structural model of each phase in the sample is required before the Rietveld technique can work, which is often difficult to achieve; *.cif* files of all the relevant phases were imported through the GUI interface. Least-square refinements, as before, seek to minimise the χ^2 (chi squared) parameter which is defined as:-

$$\chi^2 = \frac{M}{(N_{obs} - N_{var})}$$

Where:

- M = minimisation function
- N_{obs} = number of experimental data points
- N_{var} = number of refined parameters

With:

$$M = \sum_i w_i \left\{ y_i^{obs} - \frac{1}{c} y_i^{calc} \right\}^2$$

Where:

- w_i = weighting factor
- y^{calc} = calculated data
- y^{obs} = observed data
- i = data point i
- c = scaling factor

The optimum value of χ^2 is unity although this is rarely achievable for powder data. Preferred orientation of powdered samples, found throughout this work, necessitated

the use of correction factors determined by the March-Dollase and Spherical Harmonics functions. The March-Dollase function assumes that the sample has cylindrical symmetry and that there is a preferred orientation axis which lies either normal to the diffraction plane or coincident with the diffraction vector. The refinable coefficient, R_o , gives the effective sample compression or extension along the cylinder axis due to preferred orientation. If there is no preferred orientation then $R_o = 1.0$, whereas, in cases where platy crystals pack normal to the diffraction plane $R_o < 1.0$. The spherical harmonics function (also known as the general axis equation) does not assume a single preferred orientation axis through the sample and is as a result more effective. *GSAS* allows refinement of significant numbers of spherical harmonic coefficients; care was taken, however, to restrict the number of coefficients refined to produce a fit. This work only applies the general axis equation once and in that case the sample symmetry was assumed to be cylindrical – which seemed reasonable as the sample was flat and rotated in its own plane throughout the diffraction experiment. All of the results of the Rietveld refinement such as lattice parameters and phase weight fractions can be found in the relevant *.list* output file in the *GSAS* directory (Larson *et al.*, 2004).

3.17.6 *Platon*

Platon by Speck (2001) is a general crystallographic tool for treating diffraction data. This software performs geometrical calculations, visualizes structures and converts data into various formats. The HKL2Powder feature was used in this work to convert the single crystal *.hkl* file into a pseudo-powder diffraction file for comparison with a similar pattern created from the *.cif* file of the refined model exported from *Shelxl*. The pseudo-powder pattern of the experimental data draws on the measured intensities and lattice parameters and is an accurate means of comparing a bulk powder with a single crystal of the same material.

3.17.7 *Searchmatch* (version 3, 1, 0, 0)

Searchmatch is a search-match program designed for use with the Powder Diffraction File (PDF), produced by the International Centre for Diffraction Data (ICDD). This software was essential for much of the phase identification in the following chapter; diffraction patterns were inputted as *.xy* files and matched to the PDF database using the *Searchmatch* facility.

3.17.8 *Vesta* (version 2.1.1)

Vesta (Visualisation for Electronic and Structural Analysis) is visualization software created by Momma *et al.* (2008). The input file format can be either a *.cif* or any *Shelx*-compatible structure file. This program was used both during the refinement of the single crystal, as a means of checking refinement quality, and to generate several images that appear in this thesis. Images of refined structures were exported as bitmap files.

3.17.9 *Turbo Pascal* (version 7)

Turbo Pascal by Borland (1992) is a *Pascal* program builder, *Pascal* is an object orientated programming language similar to *Fortran*, which allows the user to write and execute *Pascal* programs of any size or type in DOS. This software was used to write a thermal simulation of the single crystal growth apparatus of section 3.15 (appendix 3.1) and several programs for data analysis.

3.18 Spray Drying (XRD)

Preferred orientation has been observed in both solid and powdered cerammed LDIG 24 samples. Attempts to apply the March-Dolase equation in GSAS to correct the problem have failed due the difficulty of Rietveld refinement of these materials (McCusker *et al.*, 1999). Fine grained particles of fibrous and platy minerals (like mica) form orientated aggregates when subjected to mild pressure by aligning along their major (long) axes. Spray drying is a relatively simple experimental solution; this is a process by which a water or solvent based fluid feed material is transformed into a dry powder by spraying the feed into a hot medium, usually air. Several experimental procedures exist for producing randomly orientated samples but spray drying is the most reliable

The spray dryer consists of two parts, the spraying system and the drying chamber; the dimensions of the chamber are based on those of (Hillier, 1999). The chamber is a galvanised steel straight sided bin 45 cm in diameter and 60 cm in height; placed upside down on an A1 sized section of laminated chip board. Holes were drilled around the base to allow air flow and a 2 cm hole was punched at the top, along the axis of the chamber, to allow sample spraying into the chamber from above. A type

IGS high temperature 1600 W heating tape (length:- 4 m, width:- 25 mm, by ESH Trace Heating LTD) was wrapped around the base of the cylinder and held in place with adhesive glass fibre tape, the chamber was earthed with RCD (Residual Current Device) protection provided as recommended by the manufacturer. An expanded neoprene seal was attached to the base rim to eliminate direct contact with the wooden board underneath. The top half of the chamber was insulated with a combination of aluminium foil, glass-fibre fabric and polyethylene bubble wrap, figure 3.09.

The spray was produced by a BD-128 airbrush with a suction feed and 0.35 mm needle from a 22 ml sample bottle. The air compressor was a model AS18-2 complete with an air regulator and manometer; the working air pressure was set to 30 psi (2×10^5 Pa) for the duration of this work. Powdered samples were mixed into a 10 ml solution of acetone with 0.6 % (mass/vol) of PVA (Poly Vinyl Acetate) and 0.4 % PEG (Poly Ethylene Glycol), which acts as a binder giving strength to the dried product (Klaus *et al.*, 1992). A piece of A2 paper was placed underneath the drying chamber to collect the spray dried sample and the chamber was heated to a maximum temperature of 120 °C which took approximately 45 mins, the temperature was monitored throughout with a 150 mm thermometer probe inserted through the top of the dryer.

The sample suspension was then transferred to the spray bottle and manually sprayed into the chamber through the 2 cm bore at the top. The sample was continuously agitated throughout to reduce sedimentation which increases viscosity. Once the available sample had been sprayed, the heater was de-energised and, after a brief period of cooling, the chamber was removed allowing sample collection from the A2 paper beneath. Poor sample recovery was noted at typically less than 25%, possibly due to losses in the air stream. Powder XRD was performed on two spray dried samples to compare with existing data.

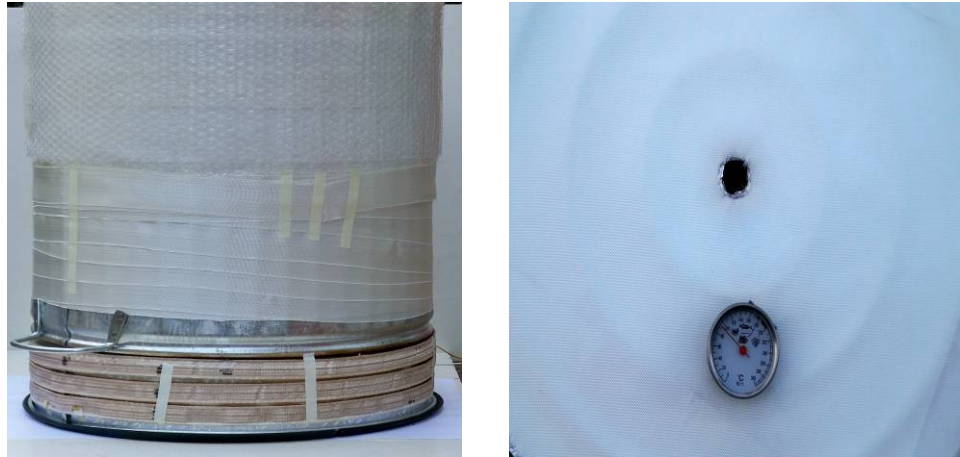


Figure 3.09. Pictures of the spray dryer from the side and from above.

3.19 Acid Treatment (XRD)

Previous work failed to identify the phase composition of LDIG 24 (Bentley *et al.*, 2007), an important part of the current experimental work attempted to identify and quantify the correct phase composition. The amorphous component of glass-ceramics presents many problems and prevents complete Rietveld refinement, particularly in multi-phase systems. LDIG 24 possesses a large amorphous halo due to a substantial amorphous volume fraction in the final product, this is especially noticeable with XRD powder data and results in a poor signal to noise ratio in both neutron and XRD cases. Chemically dissolving the background would solve these problems if the phases were preserved; however, this is highly unlikely. Acid dissolution has been used to help prove the identity of a third unknown phase, this technique also dissolved the amorphous component of the material but fortuitously left the two previously determined phases unaltered. Dissolution of the third phase is expected (Wolf *et al.*, 1973) and was observed. Powdered samples with a mass of approximately 4 grams were placed in a Pyrex beaker with around 200 ml of 4 M hydrochloric acid (HCl), made from 34 % conc. HCl and distilled water in the ratio of 1:3; a magnetic stirring bar was added to the solution and the beaker was sealed with paraffin film. The beaker was then placed on a hot plate in a fume cupboard and heated and stirred continuously for 4 hours; the temperature of the solution was monitored with a thermometer and held below 50 °C. After 4 hours, insoluble material was removed by filtering with filter paper and rinsed with distilled water; the filtrate was subsequently dried in a furnace

(Lenton, UK) at 130°C for 1 hour. A significant mass loss of approximately 1.6 grams was measured for each sample; the procedure was then repeated in each case to ensure that all soluble material was dissolved. XRD was performed on two samples treated in this way.

An attempt was made initially to exclusively dissolve the amorphous component; however, this failed and has not consequently been reported in the results. Powdered samples were treated with acetic acid for 24 hours at approximately 80 °C and then with sodium hydroxide (NaOH) at room temperature (300 K) for 5 hours using the same procedure as above.

3.20 Neutron Diffraction

Diffraction experiments were performed on D20, at ILL (Institut Laue- Langevin), France, with $\lambda = 2.4189 \text{ \AA}$ with samples in air. This required a mirror furnace which was adapted for 8 mm cylindrical glass samples. The standard heat treatment regime was repeated on a single sample from each feedstock group and variations of the first heating regime were applied to a further two bulk-commercial samples. D20 is a very high intensity 2 axis neutron diffractometer equipped with a large 160° arc PSD (Position Sensitive Detector). It allows real-time neutron experiments on very small samples for structural characterisation purposes. The option of various high temperature and cryogenic sample stages is also available. A complete diffraction pattern consists of 1516 points covering a scattering range of 153.16°; a single scan can be obtained in a few seconds allowing for monitoring of real time changes in material structure such as crystallite growth and phase changes. Comparisons have been made between these data and data taken from the same instrument with LDIG 24 original heat treated in a vacuum instead of air.

Commercial	10 °C/min to 644 °C	2 h hold 644 °C	10 °C.min to 1225 °C	3 h hold 1225 °C	Cool to RT @ maximum rate
Commercial	10 °C/min to 1225 °C	2 h hold 1225 °C	Cool to RT @ maximum rate		
Commercial	10 °C/min to 644 °C	2 h hold 644 °C	10 °C.min to 1225 °C	3 h hold 1225 °C	10 °C/min to RT °C
Original	10 °C/min to 644 °C	2 h hold 644 °C	10 °C.min to 1225 °C	3 h hold 1225 °C	Cool to RT @ maximum rate

Table 3.03. Heat treatment regimes for each sample cerammed on the beam-line at ILL (RT (room temperature) is 24 °C).

3.20.1 Mirror Furnace

Mirror furnaces employ at least 2 parabolic mirrors to focus heat from a heating lamp onto the sample. In this case, the sample was supported on the alumina sheath of the temperature control thermocouple, positioned at the mirror focal point, and held in place with alumina cement, shown in figure 3.10. Samples were replaced after each heat treatment run. A total of 4 samples were run over the course of the experiment, three bulk commercial samples and one of the original feedstock. The heat treatments employed are shown in table 3.03. Originally, an insert, to be inserted in an ILL pool furnace, was designed; however, this could not be manufactured in time. The insert was an open-ended niobium cylinder (IØ: - 19 mm, L: - 406 mm) with a flange for an air seal, small niobium sample cans were also designed to allow sample removal after each run. These niobium components were to be coated with Muride®, the commercial name for a diffusion coated di-silicide layer (NbSi₂), to protect against oxidation but technical difficulties prevented completion of the project.

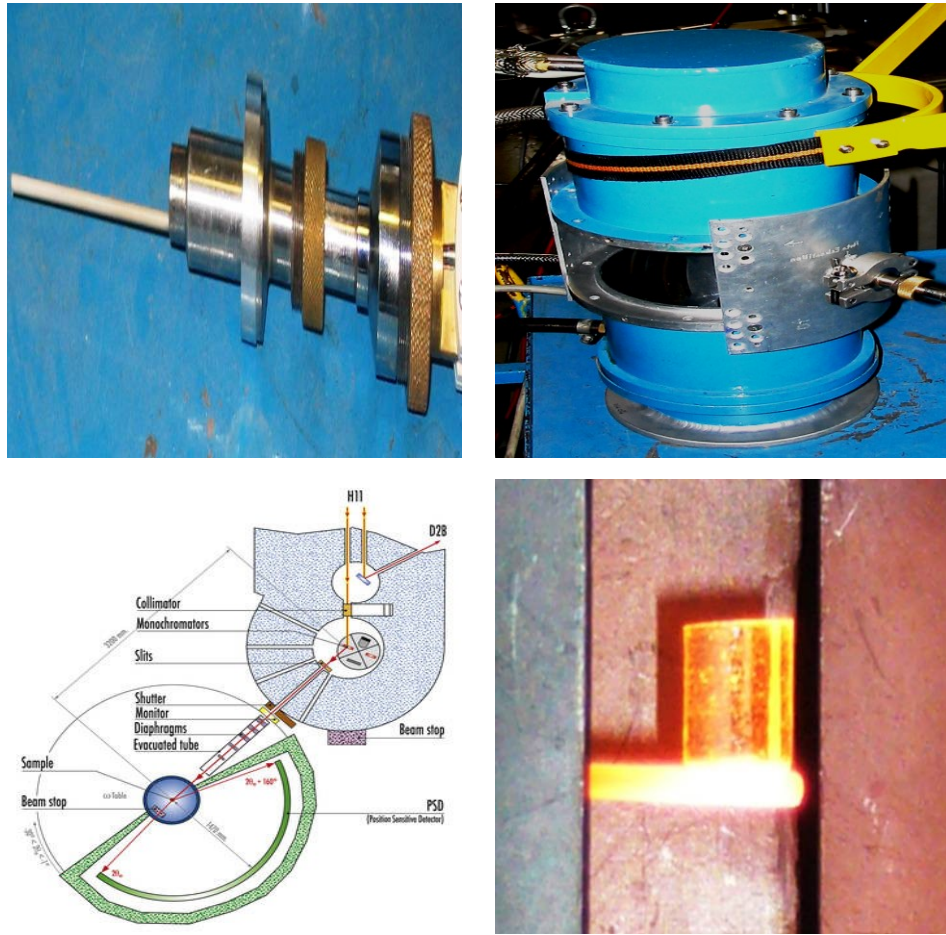


Figure 3.10. Clockwise from the top; the sample stick holder, the mirror furnace (shown with aluminium shielding), an 8 mm sample rod undergoing heat-treatment and a schematic of D20 at ILL (<http://www.ill.eu/>).

4 Results and Discussion

4.1 Material Properties of LDIG 24

This chapter presents results of DTA, Bi-axial flexure, hardness tests, microscopy, gloss and colour space measurements for LDIG 24 glass-ceramics generally but with emphasis on the commercial variety.

4.1.1 Preliminary Analysis

The glass frits used for DTA were clear and free from inclusions; figures 4.01 and 4.02 below show results for both the commercial and original formulations of the glass for different particle sizes. Both formulations exhibit an endotherm at approximately 1260 °C which is associated with melting or phase dissolution in the glass. Results from DTA in both cases indicate that nucleation is of a surface and/or bulk variety with some dependence on particle size; if bulk nucleation were dominant then the exothermal peak positions would remain constant with reducing particle sizes as the activation energy for nucleation remains unchanged. However, surface nucleation effects, which significantly reduce the free energy of nucleation, would produce the opposite effect with significant peak shifts related to particle size reduction. It is not clear whether both surface and bulk nucleation occur in frit samples, however, strong surface nucleation is not seen. A table of the transition temperatures (T_g) and the peak crystallisation temperatures (T_{p1}) for a range of particle sizes for each composition is shown in table 4.01.

	T_g (Com)	T_g (Orig)	T_{p1} (Com)	T_{p1}(Orig)
2000 – 1000 μm	653 °C	655 °C	767 °C	774 °C
90 – 45 μm	647 °C	654 °C	765 °C	776 °C
<45 μm	649 °C	652 °C	772 °C	768 °C

Table 4.01. T_{p1} and T_g for different particle size fractions of both commercial (Com) and original (Orig) LDIG 24.

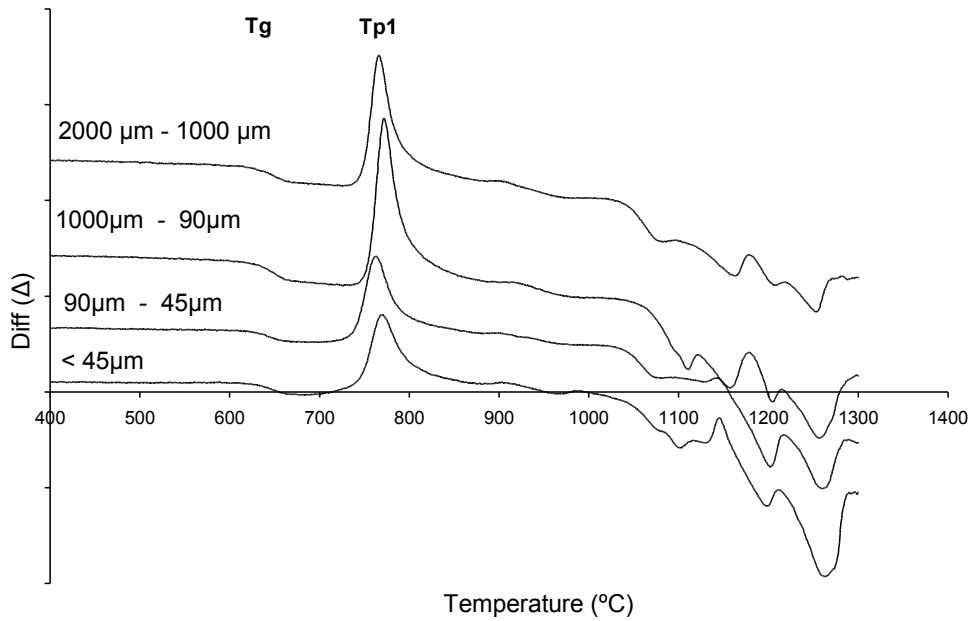


Figure 4.01. DTA trace of a selection of particle sizes for commercial LDIG 24.

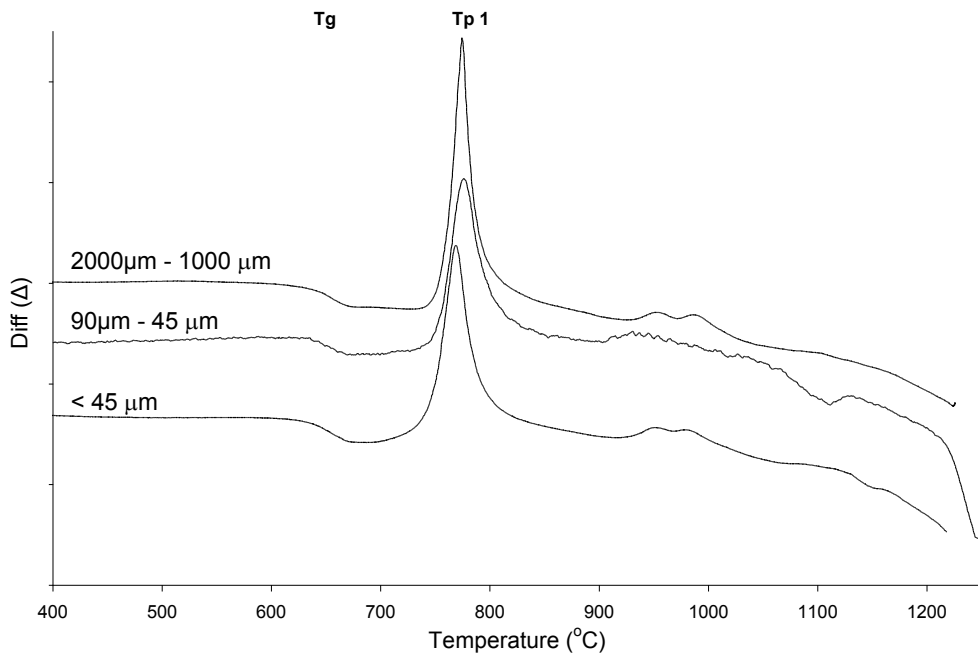


Figure 4.02. DTA trace of selection of particle sizes for original LDIG 24.

4.1.2 Optimum Nucleation

Optimum nucleation studies have revealed that nucleation temperatures of 640 °C and 653 °C correspond to the highest nucleation rates possible for original and commercial compositions respectively (figures 4.03, 4.04 and 4.05). The curves shown, in figure 4.05, are relatively flat, with the apex position poorly defined; this indicates that some surface nucleation, in addition to bulk, may be involved in cases

of small particle sizes approaching that used for the DTA analysis (< 2 mm). The differences between the two variants of LDIG 24 is not particularly apparent in measurements by DTA, partly, as a consequence of perhaps poor accuracy, compared to DSC, and the almost identical compositions of each as determined by EDS shown in tables 4.02 and 4.03.

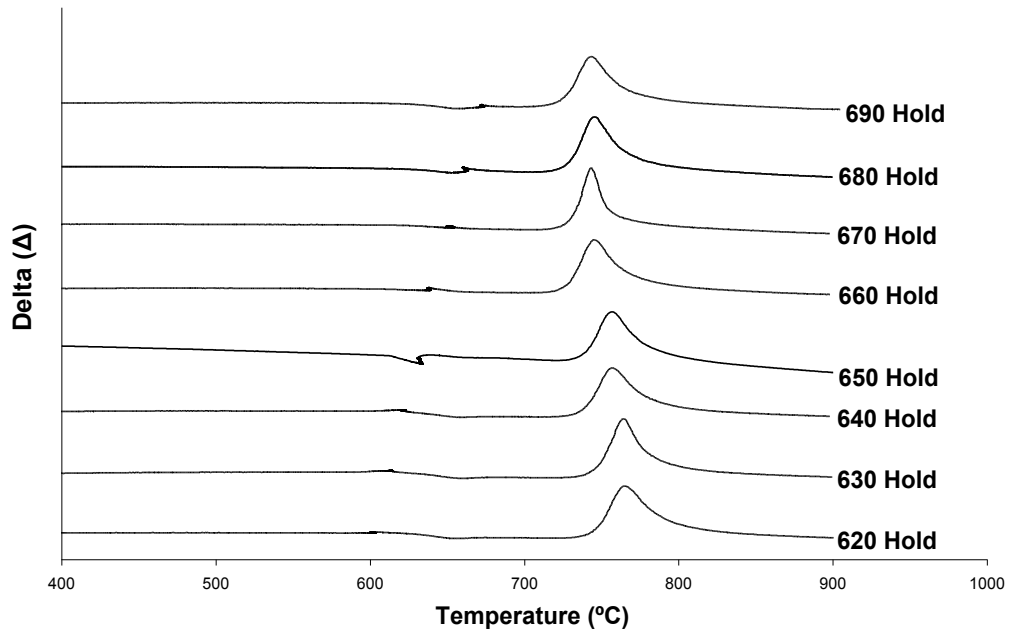


Figure 4.03. DTA with 1 hour nucleation hold for the original feedstock.

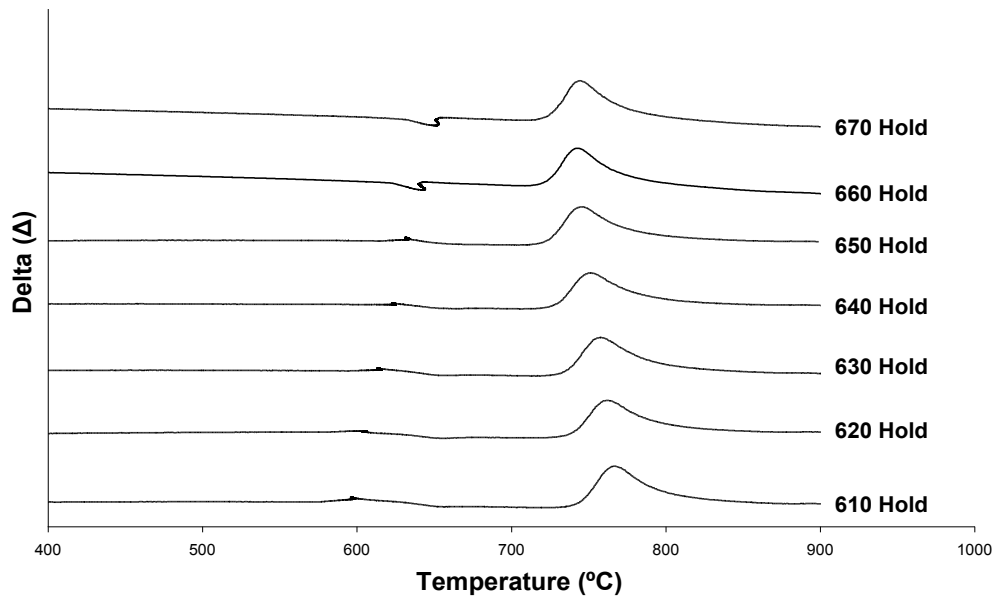


Figure 4.04. DTA with 1 hour nucleation hold for the commercial feedstock.

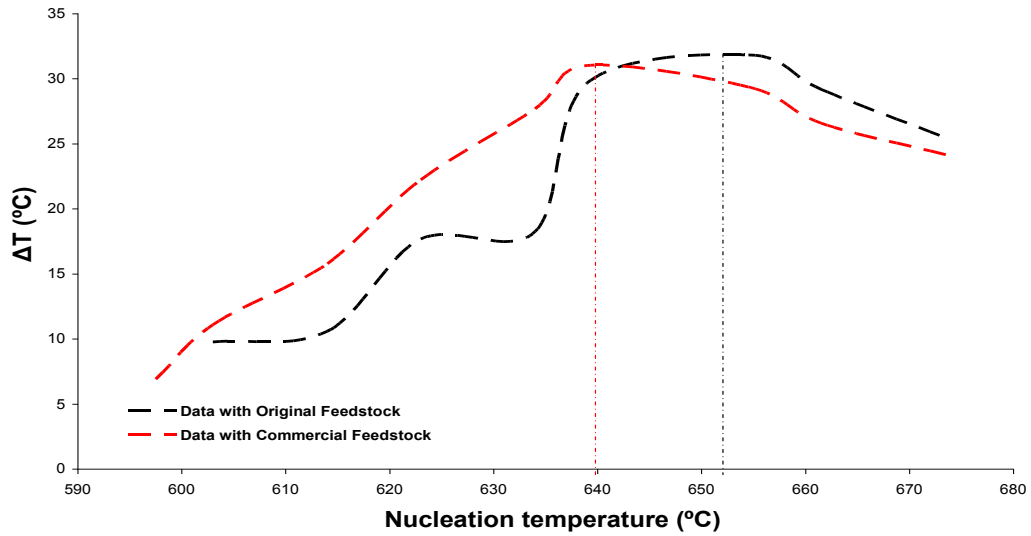


Figure 4.05. Graph of $(T_{p1} - T_{p1}^0)$ for original (red) and commercial (black) formulations.

4.1.3 Activation Energy

Activation energy represents the kinetic barrier for crystal growth and is determined by measuring the shift in the T_{p1} peak relative to T_{p1}^0 , the original peak crystallisation temperature, resulting from changes to the applied heating rates during a DTA run. It cannot be interpreted as an indicator of nucleation mechanism (Marotta *et al.*, 1981), however, the crystallisation mechanism can be determined using the modified Kissinger method developed by Matusita and Saka (1980). First, activation energies (E_a) of 193.8 kJ/mol and 178.29 kJ/mol were determined for the commercial and original compositions, respectively, by application of the conventional Kissinger method (Marotta *et al.*, 1981); these values were then used to determine the Avrami coefficients (n and m) of the modified Kissinger equation. Plots of this function appear in figures 4.06 and 4.07 with $n = m = 3$, as these values were found to give the closest match to the original activation energies. Avrami numbers of $n = m = 3$ suggest bulk nucleation from a constant number of nuclei and 3D growth in both compositions.

Activation energies of 189.7 kJ/mol and 173.9 kJ/mol were determined from the gradients of figures 4.06 and 4.07 respectively; these energies are comparable with that known for Dicor® of 203 kJ/mol, Bapna *et al.* (1996). The linear fit quality in figures 4.06 and 4.07 is expressed by R^2 parameters of between 0.98 and 0.99. These results are consistent with previous published work and similar values of activation energy are found for many of the mica glass-ceramics produced at LDI

(Jambi, 2007). It is theorised, therefore, that bulk nucleation and 3D crystal growth is the dominant mechanism in LDIG 24 glass-ceramics. Maiti *et al.* (2009) also identified the same 3D crystal growth in another barium–fluorophlogopite glass-ceramic (chapter 1).

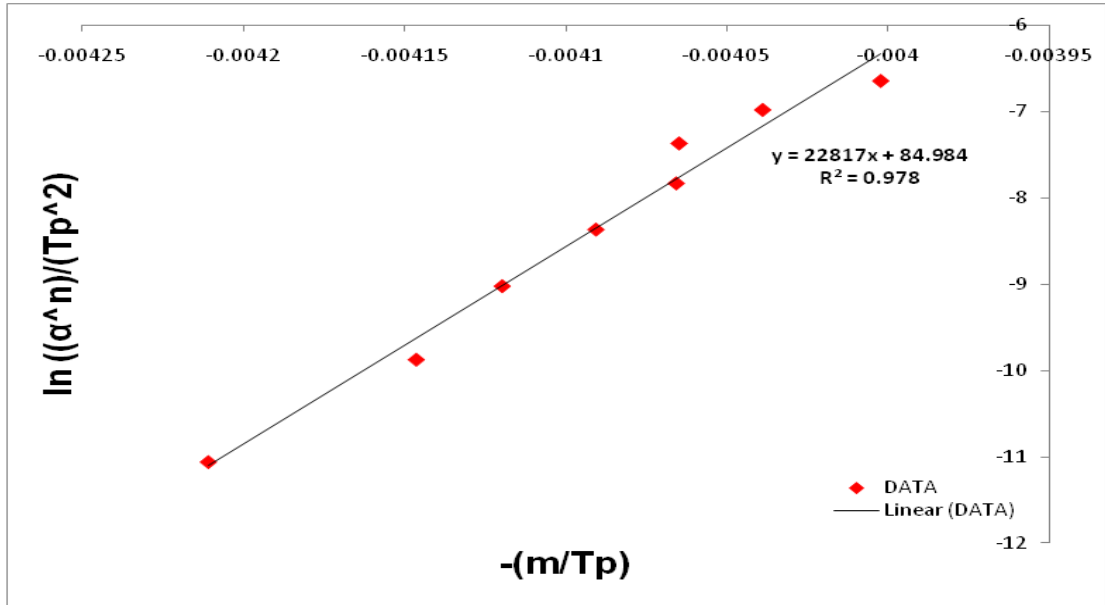


Figure 4.06. Modified Kissinger plot for activation energy of commercial LDIG 24.

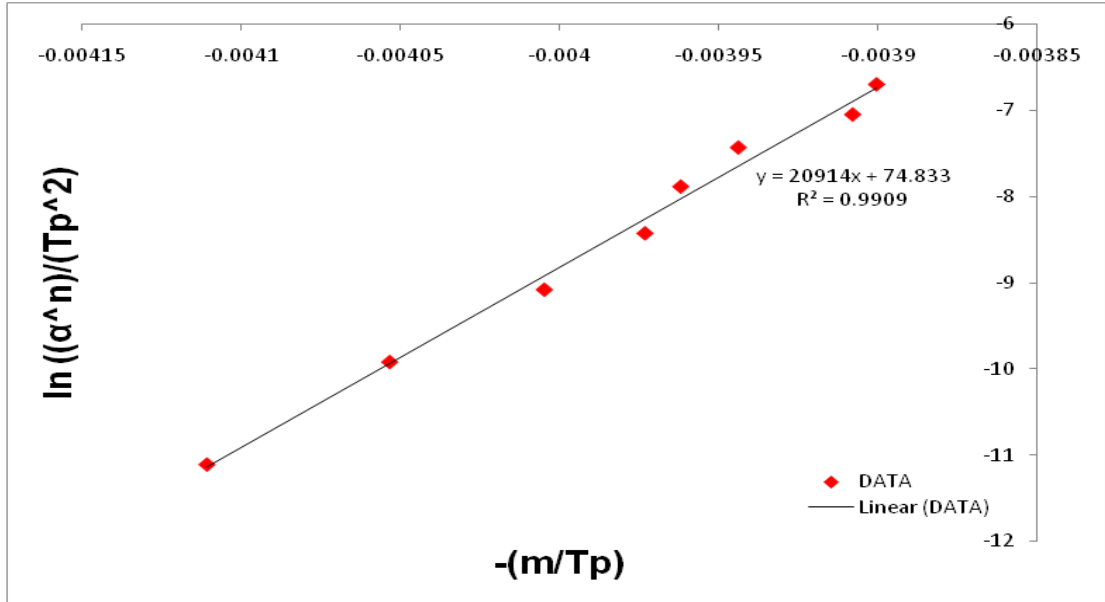


Figure 4.07. Modified Kissinger plot for activation energy of original LDIG 24.

4.1.4 Energy Dispersive X-ray Spectroscopy

Energy Dispersive X-ray Spectroscopy (EDS) was applied to samples cerammed by the standard heat treatment, heat treated at 1150 °C for 3 hours, and tables 4.02 and 4.03 of elemental constituents show relatively minor differences with only slightly

less barium and a larger weight fraction of fluorine apparent for the original LDIG 24. In all, DTA related analyses show little difference between LDIG 24 produced by the original feed stocks and that produced by ‘commercial grade’ feed stocks with the aim of assessing commercial viability of the material. It should be noted, however, that EDS has a detection limit of ~ 1-2 % and is not, therefore, suitable for detecting small amounts of impurities which may still have a significant effect on the physical properties of a glass-ceramic.

Element	Atoms (%)	Weight (%)
Mg	12.0	13.2
Al	3.9	4.7
Si	14.7	18.7
P	0.5	0.7
Ca	0.8	1.4
Ba	2.0	12.2
F	7.7	6.7
O	58.5	42.5

Table 4.02. Compositional analysis of commercial LDIG 24.

Element	Atoms (%)	Weight (%)
Mg	10.9	12.4
Al	5.8	7.4
Si	12.3	16.2
P	0.4	0.6
Ca	0.9	1.6
Ba	1.3	8.4
F	10.3	9.2
O	58.2	43.8

Table 4.03. Compositional analysis of original LDIG 24.

4.1.5 Acid Solubility

These measurements are based on an obsolete ISO standard (ISO 6872:1998) but are still worth noting. Sample discs of 14 mm diameter and 1.6 mm thickness (approx.) were prepared from both original and commercial varieties of LDIG 24; results were averaged over 5 specimens in each case to produce a value of mass (g) lost per cm². A significant difference appears between the chemical solubilities of original and commercial samples. The value calculated for the original material was 1.52 mg/cm², normally for exposed use in the mouth the above standard requires a maximum solubility of no greater than 100 µg/cm², thus, LDIG 24, in its original form, appears unsuitable for use in oral cavities, although application as a core

material would still be allowed. The solubility of the commercial variant was 8.48 mg/cm^2 which is, again, well in excess of the maximum solubility listed but also significantly greater than that evidenced by the former. A likely reason for this is a change to the procedure used for making batch glass due to problems with the original mullite crucibles which had a tendency to dissolve into the glass melt possibly altering the alumina content, indeed, some discrepancy appears in EDS analysis of the original LDIG 24 with a value of 5.8 wt % alumina versus 3.85 wt % for the commercial sample. Alumina addition is known to increase cross-link density in glass and reduce disorder; it is conceivable that this acts to improve the acid resistance of the general glass-ceramic in this case. The absence of alumina additions in the commercial samples, due to the selection of appropriate crucibles for glass production, may be the reason for the observed discrepancy in chemical solubility between two otherwise compositionally identical materials. These results may not be truly representative of the corrosive effects of long-term exposure to saliva, however, some improvement is required possibly by the selective addition of impurities; an increase in the silica content of the residual glass would also be effective. This author is confident that adequate changes can and will be made to allow material development with the intended application.

Generally DTA analysis is a good first step for characterisation purposes; although, extractable information is somewhat limited. In this instance there is clearly a second T_{p2} crystallisation peak at approximately $900 \text{ }^\circ\text{C}$ which appears as barely detectable on a DTA trace, a more sensitive technique such as DSC (Differential Scanning Calorimetry) would allow precise determination of phase transitions and even heat capacity measurements that would allow the development of a more thorough understanding of the sequence and type of phase development in these materials by complimenting neutron and X-ray data sets.

4.1.6 Mechanical Testing

	BFS (MPa)	Std (Ω_{n-1})	Hardness (VHN)	Welch's T	Std (Ω_{n-1})
LDIG 24 Original (1225 °C)	-109.6	4.4	68.9	4.7	12.7
LDIG 24 Commercial (1150 °C)	-100.7	7.3	275.5	1.6	22.3
LDIG 24 Commercial (1100 °C)	-132.9	13.6	329.8	10.2	52.6
LDIG 24 Commercial (1050 °C)	-149.6	15.4	389.6	2.7	57.4
LDIG 24 Commercial (950 °C)	-125.4	11.1	435.7	1.1	40.8

Table 4.04. Biaxial flexure with standard deviation and Vickers hardness with associated t-statistic for two sets of 25 readings and average standard deviation for a range of samples produced from different heat treatments.

Mechanical tests employed, listed in table 4.04, however, demonstrate significant differences in Vickers hardness and biaxial flexural strength (BFS) values, indicating that changes to the heat treatment regime are more significant than compositional changes, in this case. One can observe from the table a trend in both hardness and BFS for an inverse relationship with the temperature of the isothermal hold applied, the lower hold temperatures give higher levels of mechanical strength. Certainly beyond 900 °C; it is clear, therefore, that there is a trade off between strength and hardness in that low hardness, higher temperature samples are more likely to suffer mechanical failure in an oral environment. This is a useful observation as often there is a divergence between conditions for producing both high strength and good aesthetic/optical properties for applications in which appearance is probably more important than optimum mechanical properties. This author has also found that by lowering the isothermal hold temperature applied to LDIG 24 commercial glass-ceramics it is possible to develop levels of translucency approaching that of natural teeth.

Unfortunately, material hardness becomes inhibitive at < 1050 °C and is likely to cause an article to shatter or chip in grinding and sectioning; although aesthetic properties will improve somewhat when lowering the hold temperatures, it is inadvisable to use this as the sole mechanism for developing the appearance of a material with potential application with CAD/CAM technology. As discussed

previously, a combination of both optimum heat treatments and various impurity additions to the nominal composition is likely to yield the best results in this case.

Unusually for glass-ceramics, low accuracy has been demonstrated in micro-hardness measurements for all samples; micro-hardness accuracy is dependent on measurement repeatability and sample homogeneity, which appears poor in every case. Welsh's t test is based on two means, from two sets of 25 measurements in this case, and applied when two samples have unequal variances as a means of determining a statistical relationship; if the value of the t-statistic (table 4.04) exceeds 3 then samples are effectively independent; this means that several of the measurements shown are not representative of the bulk. A possible solution would be to use a macro-hardness indenter with higher loads as a means of measuring the bulk property which is more useful in engineering applications. If one can assume that the t-statistic in this case is a measure of sample inhomogeneity, in terms of mechanical properties, then clearly this is an effect associated with the temperature of the applied crystallisation hold although no discernible linear relationship exists.

Comparison between the results, in table 4.04, and commercial ceramics such as Macor® or Vita Mark II is revealing. In BFS measurements, standard original LDIG 24 (109.6 MPa) has a higher value than Macor® (94 MPa) (Chaysuwan, 2001) and Vita Mark II® (84 MPa) (Al-Shammary, 2004) but is comparable in flexure strength to variants Dicor MGC-Light® (113 MPa) and Dicor MGC-Dark® (110 MPa) (Thompson *et al.*, 1996). LDIG 24 commercial heat treated at 1050 °C (150 MPa), however, is comparable to ZrO₂ reinforced phlogopite glass-ceramics (140 - 160 MPa) and appears significantly stronger than ordinary mica glass-ceramics, a lower temperature heat treatment also has the advantage of imparting translucency to the cerammed article. The exact sequence of phase development in LDIG 24 glass-ceramics is unknown; however, the relationship between strength and isothermal hold temperature is non-linear indicating perhaps a strengthening mechanism in the 950 – 1050 °C temperature range.

Vickers hardness measurements also indicate that commercial LDIG 24, heat treated at lower temperatures, is significantly harder than all equivalent commercial brands (e.g. Macor® with a VHN of 152.22) and exceeds that of natural tooth enamel (~ 270 VHN determined by Ma *et al.*, 1997) for hold temperatures below 1050 °C, as a

result of the hardness of LDIG 24 base glass. It is clear that values exceeding the hardness of tooth enamel are unacceptable; future study, therefore, may focus on LDIG 24 glass-ceramics cerammed in the temperature range of 1050 – 1100 °C. A fitted plot of hardness versus isothermal hold temperature for commercial LDIG 24, figure 4.08, shows a clear relationship despite acknowledged inaccuracy in the data.

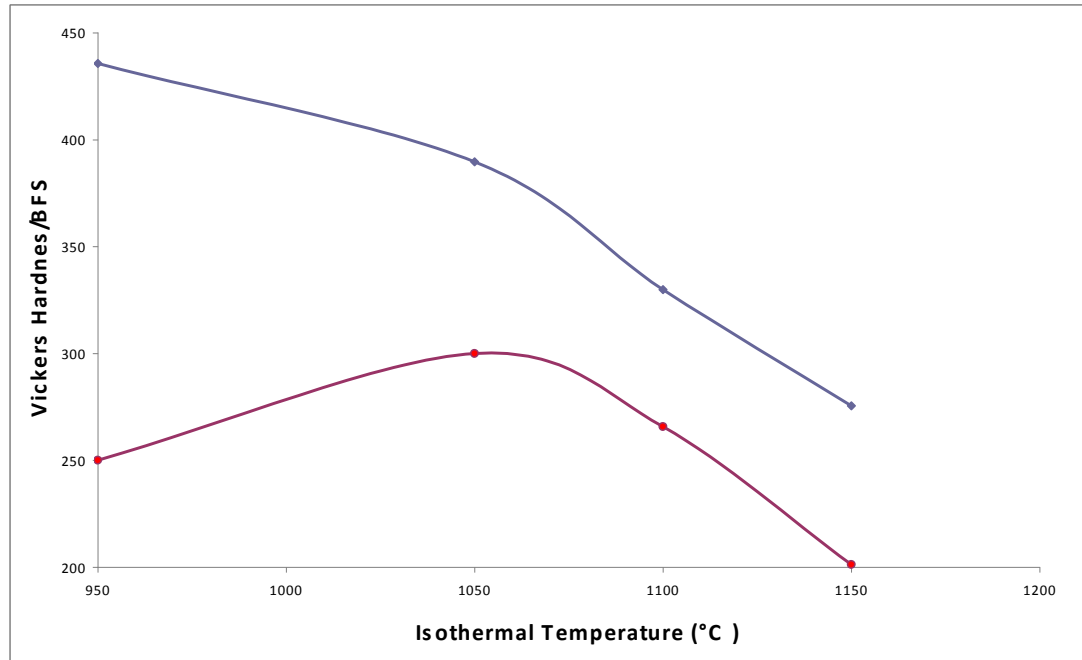


Figure 4.08. Dual plot of BFS (MPa) (red line) and Vickers hardness (VHN) (blue line) versus hold temperature.

The lines are added to aid visualisation of possible trend.

The graph above clearly shows a transition point in the relationship between BFS and hardness; at temperatures < 1050 °C both hardness and BFS are diverging whereas at temperatures > 1050 °C a parallel-line direct proportionality is observed. Presently, one would need to compromise both the strength and optical properties of LDIG 24 commercial glass ceramics in order to match the hardness of CAD/CAM restorations currently in use.

Studies of lithium di-silicate glass-ceramics, by Hing *et al.* 1973, relate the mechanical strength of a glass-ceramic to the mean free path of micro-cracks in the glass matrix as follows:-

$$\lambda = L \left(\frac{1 - v_c}{v_c} \right)$$

Where:

- λ = mean free path (m)
- v_c = volume fraction of crystalline phases
- L = average crystallite size

With:

$$\sigma = K_2 \lambda^{-1/2}$$

Where:

- λ = mean free path (m)
- K_2 = constant
- σ = mechanical strength (MNm⁻²)

This equation also predicts the behaviour observed in figure 4.08, if one assumes that increasing crystallisation hold temperatures up to 1050 °C improves strength by coarsening of the microstructure combined with an increasing crystalline volume fraction and that the apparent reduction in strength at higher temperatures corresponds to the growth of crystallites with constant volume fraction – known as Ostwald ripening. The peak in the BFS curve, in figure 4.08, probably represents the formation of an optimum interlocking microstructure with the highest density of smaller crystallites, creating a high strength material in agreement with the Hall-Petch relationship (Zhang *et al.*, 1994). Internal phase transformations and possibly related porosity, identified in section 4.1.7, may also have an effect.

4.1.7 SEM/Optical Microscopy

Polished 18 mm discs, sectioned from heat treated commercial LDIG 24 rods, display bulk phase morphology and have been examined by SEM and high resolution optical microscopy; several images are shown, in figures 4.09 to 4.12. Samples examined by optical microscopy were highly polished, however, upon magnification, in figure 4.10, they appear to have noticeable surface defects resulting from voids in the residual glass, these defects appear to reduce the quality of the surface finish achievable; the secondary electron micrograph, in figure 4.11, also shows the presence of μm sized voids after a lower heat treatment at 1050 °C – also in appendix 2.7. In figure 4.09 is the appearance of a grain structure with darker spheroidal areas surrounded by lighter interstitial regions; the formation of a relict

microstructure, in this case, indicates phase separation. Application of back-scattered electrons (BS) produces contrast in images with lighter areas representative of higher concentrations of heavier elements such as barium. The lighter areas, in figure 4.12, appear to correspond to Ba-mica precipitation and this has been subsequently confirmed by EDS as the large dark regions are exclusively composed of magnesium silicates; supporting the conclusion of relict microstructure for figure 4.09. It is clear that a well developed 'house of cards' (interlocking platelet) microstructure texture, shown in figures 1.02 and 1.03, does not form.



Figure 4.09. Optical micrograph of polished surface of LDIG 24 commercial (heat-treated @ 1100°C for 3 hours) showing a cell-like or grain structure; this may represent the separation of phases.

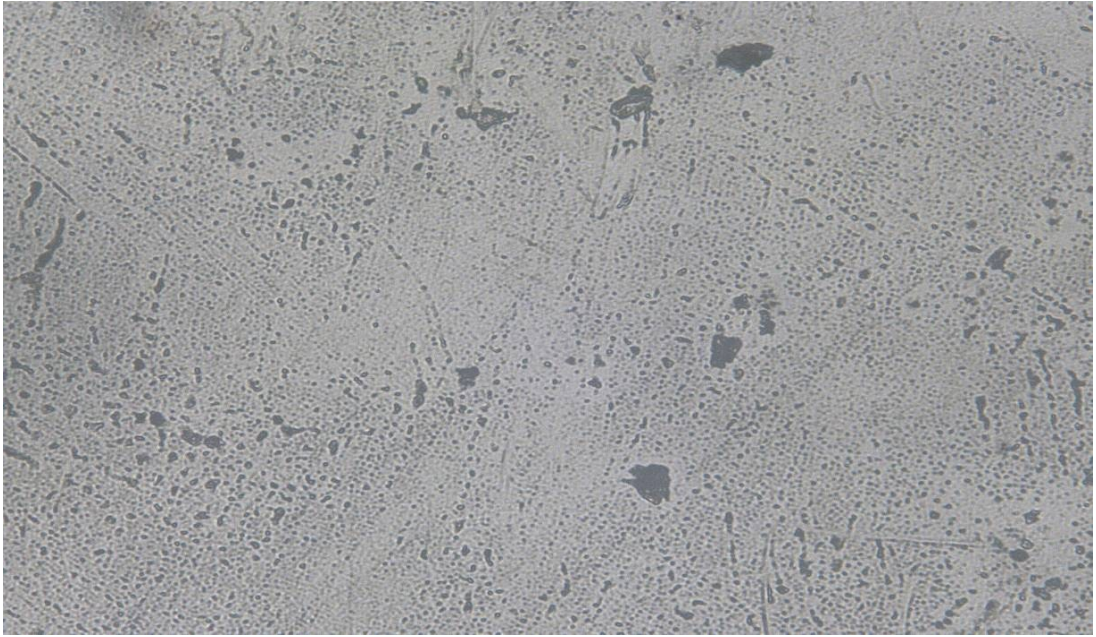


Figure 4.10. Optical micrograph of polished LDIG 24 commercial glass-ceramic (heat-treated @1100 °C for 3 hours).

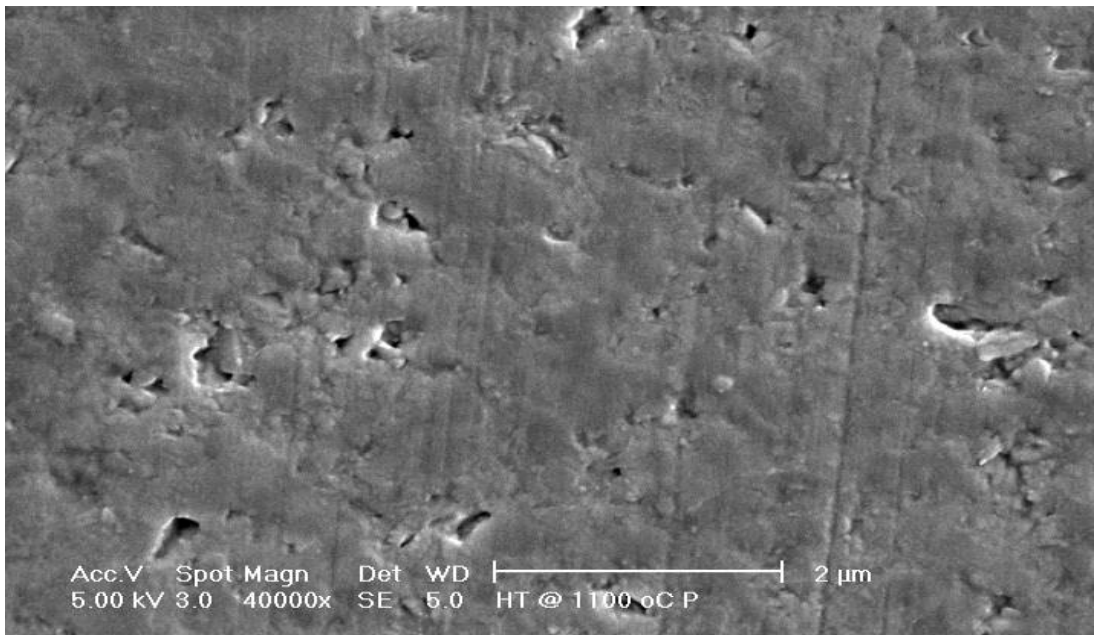


Figure 4.11. SEM (Secondary Electron Microscopy) micrograph of LDIG 24 commercial glass-ceramic, heat treated @ 1050 °C for 3 hours, showing voids in the polished sample surface.

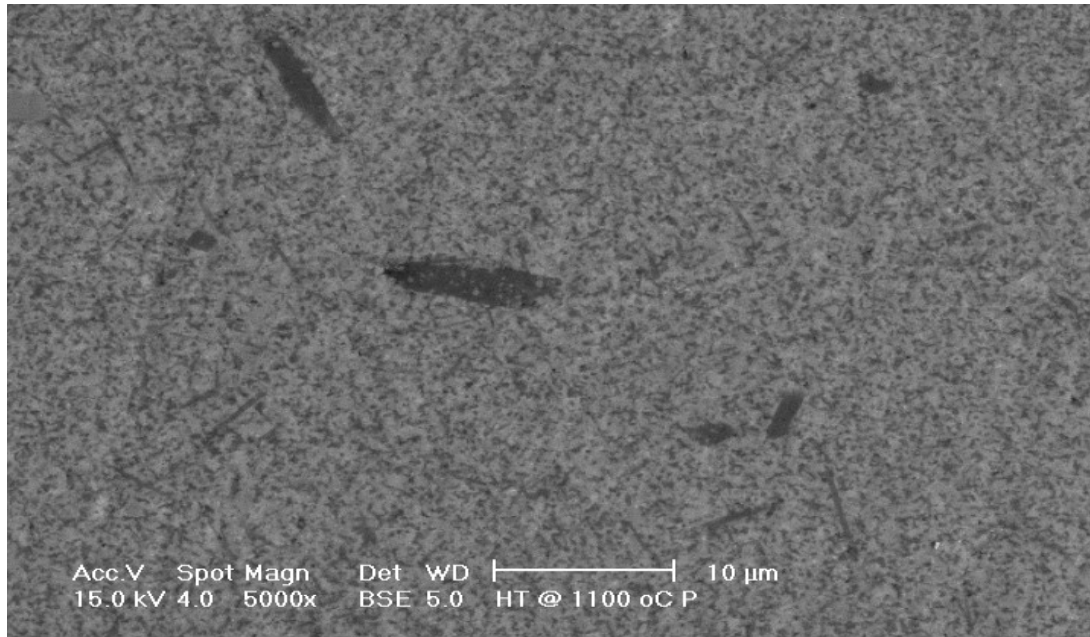


Figure 4.12. Back-scattered electron micrograph of LDIG 24 commercial glass-ceramic heat treated @ 1050 °C for 3 hours; shows some acicular interlocking, although, there is no well formed ‘house of cards’ microstructure.

4.1.8 Gloss Measurements

Table 4.05 contains results from gloss measurements; values approaching 100 indicate that the surface has the reflectivity or gloss value of the polished glass standard used to calibrate the instrument. Comparison is made between four commercial type samples held at different crystallization temperatures and the original formulation after the standard heat treatment, each sample was prepared with a number of different surface finishes which improved the gloss value in every case, although, higher temperature heat treatments produced duller surfaces. Reference to a commercial CAD/CAM material, Cerec® Vitabloc Mark II (Vita Zahnfabrik), shows that samples crystallized at 950°C most closely approximate the expected standard.

	6 μm finish	1 μm finish	0.3 μm finish
LDIG 24 original	43.6	77.2	85.4
LDIG 24 commercial (950°C)	98.2	98.4	98.2
LDIG 24 commercial (1050 °C)	77.5	92.3	96.9
LDIG 24 commercial (1100 °C)	62.8.	84.3	88.6
LDIG 24 commercial (1150 °C)	39.7	66.8	78.9
CAD/CAM commercial	93.5	93.7	86.8

Table 4.05. LDIG 24 glass-ceramics cerammed by different heat treatments with associated gloss measurement for three different surface finishes.

4.1.9 Colour Measurement

LDIG 24 after a standard heat treatment is white in colour and opaque, which is not appropriate for dental restorations. This study attempted to develop a doping regime for producing coloured glasses which when heat-treated, would be suitably aesthetic for use in chair side CAD/CAM applications. Both glass frit and the cerammed material were coloured by dopants which are similar to those applied by Wang *et al.* (2002) in the colouring of potassium (K) mica glass-ceramics. Some of the colours produced are very close to those of teeth, although precise matching of dental shade guides was not attempted. It was observed that all of the doped glass-ceramic samples were more opaque than any un-doped parent material in the same condition; it is assumed that this is caused by the added impurities acting as nucleating agents thus increasing the crystalline volume fraction. A possible solution to this problem is to reduce the crystallisation hold temperature; however, the optimum value for both desirable aesthetic and mechanical properties still needs to be determined, as discussed previously. Dopants were added to the experimental parent glass frit by mol %. The mixture was tumbled for one hour then transferred to an alumina crucible; each composition was melted in a furnace @ 1440 °C for 1 hour then quenched in water. These frits were cerammed using the standard heat treatment applied to the parent glass: - 10 °C/min to 644 °C held for 2 hours then 10 °C/min to 1150 °C held for 3 hours and cooled at 10 °C/min. The colours of doped frits and corresponding glass-ceramics have been noted and photographed; several appear in figure 4.13.



Figure 4.13. Coloured frits with corresponding cerammed article underneath after standard heat treatment.

Frits left to right are doped with: 1 mol % Cr_2O_3 , 1 mol % $\text{Fe}_2\text{SO}_4 \cdot 7\text{H}_2\text{O}$ and (3 + 1) mol % $\text{Ni}(\text{II})\text{O}_2$ and $\text{Fe}_2\text{SO}_4 \cdot 7\text{H}_2\text{O}$, respectively. All samples were heat-treated @ 1150 °C for 3 hours.

Surface nucleation creates a problem when attempting to interpret the effect of each impurity on the bulk condition of a frit sample; indeed, samples doped with Ni(II) and Fe(II) oxides appeared brown on the surface but were yellow in the bulk. Sample rods, 14 mm in diameter, were prepared of the most promising compositions in order to obtain information on the effects of additions on the colouring of bulk LDIG 24. Visible colours were recorded in colour space with a spectrophotometer and the results are listed in table 4.06; five parameters are listed: - L^* , a^* , b^* , C^* and h^* - which represent a hybrid of CIELAB colour space and hue (h^*) and chroma (C^*) also found in the Munsell colour system. These results have been produced by two standard illumination sources A and D65 with the instrument in both SPEX and SPIN modes meaning Specular Excluded and Specular Included, respectively, as different levels of gloss will alter perceived colour (Randall, Datacolor International). Hue and chroma are useful for matching shade guides, however, CIELAB gives a more tangible means of comparison, for instance, L^* represents black when equal to zero and diffuse white when equal to 1, a^* indicates green when negative and magenta when positive, whereas, b^* describes blue when negative and yellow when positive (Kuehni, 2003). Applying the information, above one may determine some basic facts about the type of colouration in each sample.

Dopant	Mole (%)	SPEX						SPIN				
		Illumination	L*	a*	b*	C*	h*	L*	a*	b*	C*	h*
Ni(II)O ₂	2	A/10 °	93.96	0.12	11.16	11.16	89.38	93.93	0.12	10.82	10.82	89.37
		D65/10 °	93.44	-1.93	11.13	11.30	99.82	93.43	-1.88	10.79	10.95	99.87
Fe(II)SO ₄ .7H ₂ O	2	A/10 °	90.89	2.1	6.52	6.85	72.11	91.01	2.00	6.30	6.61	72.4
		D65/10 °	90.43	0.24	6.33	6.33	87.85	90.56	0.20	6.11	6.12	88.11
Ni(II)O ₂ + Fe(II)Cl ₂	1 + 1	A/10 °	92.46	0.88	11.7	11.73	85.7	92.34	0.86	11.55	11.58	85.72
		D65/10 °	91.86	-1.37	11.59	11.67	96.74	91.74	-1.34	11.43	11.51	96.67
Ni(II)O ₂ + Fe(II)SO ₄ .7H ₂ O	1 + 1	A/10 °	87.28	2.39	11.87	12.11	78.6	87.00	2.39	11.68	11.92	78.42
		D65/10 °	86.54	-0.22	11.61	11.61	91.08	86.27	-0.17	11.41	11.41	90.46
Ni(II)O ₂ + Fe(II)SO ₄ .7H ₂ O	3 + 1	A/10 °	88.97	1.95	17.56	17.67	83.68	88.89	1.97	17.48	17.59	83.56
		D65/10 °	88.00	-0.91	17.15	17.17	93.02	87.91	-0.83	17.04	17.06	92.79
Fe(II)Cl ₂	1	A/10 °	94.4	0.97	4.08	4.19	76.66	93.92	0.95	3.9	4.01	76.34
		D65/10 °	94.13	-0.10	3.97	3.97	91.48	93.66	-0.08	3.79	3.79	91.24
Ce(IV)O ₂ + Ni(II)O ₂	1 + 1	A/10 °	93.67	0.22	9.43	9.43	88.69	93.65	0.22	9.24	9.25	88.61
		D65/10 °	93.24	-1.80	9.53	9.69	101.7	93.22	-1.75	9.34	9.50	100.6
None	-	A/10 °	95.38	-0.20	0.87	0.89	103.3	95.27	-0.22	0.7	0.73	107.8
		D65/10 °	95.36	-0.46	0.95	1.06	115.6	95.26	-0.43	0.78	0.89	119.0

Table 4.06. Colour space parameters for a number of coloured commercial LDIG 24 glass-ceramics doped by mol %; the undoped material is listed as 'none'.

Referring to table 4.06, one can see that generally values of L^* are unchanged across the compositional range and indicate a white or light background; a^* tends to give either small positive or negative values, whereas, b^* gives the largest positive deflection. Values of a^* appear to be more a function of the type of illumination with negative values typically for D65 and positive for A. However, there appears to be a strong correlation between b^* and the samples; all values are positive indicating a colour shifted towards the yellow spectrum with higher magnitude numbers denoting a greater shift. The largest value of b^* is measured for the sample doped with (1 + 3) mol % Ni(II)O₂ and Fe₂SO₄.7H₂O at ~17 in both SPEX and SPIN modes, whereas, the smallest value (< 1) coincides with the undoped standard. This agrees with observation as the former sample appears yellow; the table indicates that the most effective compositions for producing yellow or potentially natural tooth colour shades are those containing Ni(II)O₂ with the highest values attained by those compositions containing both Ni(II)O₂ and another metal oxide impurity. Based on a relatively small trial, combinations of Ni(II) and Fe(II) appear highly effective in generating darker yellow colours in the bulk glass-ceramic. It is conceivable that by selection of the above impurities full matching of dental shades might be possible; this work represents a promising first step towards the further development of commercial LDIG 24 glass-ceramics.

4.2 X-ray Analysis

This section presents the results of X-ray analyses carried out for this work on both bulk and surface nucleated samples of commercial LDIG 24 and an experimentally grown single crystal of the main mica phase.

Phase identification and quantification in glass ceramics has often proven difficult due to an unknown amorphous background which is impossible to subtract from the Bragg contribution to the diffraction pattern. Several techniques exist including the use of an internal standard (Yasukawa *et al.*, 1998) for determining sample crystallinity; however, full pattern Rietveld refinement is not usually possible. Difficulties in phase identification for this work have also arisen from substantial peak overlap of multiple crystalline phases, which necessitates a novel approach to structure solution in this case.

4.2.1 Single Crystal Growth Experiment

Barium mica is the main phase in these materials; however, its true composition was unknown partly because of an affinity for forming solid solutions (Uno *et al.*, 1991). An experimental technique for growing large single crystals of mica from the melt was devised (chapter 3) with the aim of producing a single crystal suitable for single-crystal X-ray diffraction and structure solution by direct methods. Electron micro-probe analysis (EMPA) on the same crystal following this experiment was essential in ensuring the accuracy of subsequent crystal structure refinements, in *Shelx '97*, and is presented in Table 4.07. Five measurements were taken at different points on the sample surface and averaged to give an approximate chemical formula of: - $\text{Ba}_{0.75}\text{Mg}_3(\text{Al}_{1.5}\text{Si}_{2.5})\text{O}_{10}\text{F}_2$. The model structure solution was then refined to a 'goodness of fit' (GooF) of 0.946 with the observed data, generally, solutions with a GooF of approximately 1 or less are acceptable. Tables 4.08 to 4.11 display all of the pertinent structural data from the refinement, including errors where appropriate. The images in the following figures were generated using *Vesta* (ver. 2.1.1).

Oxide Weight Percent (%)	1	2	3	4	5
SiO ₂	28.4	26.7	26.6	26.8	27.8
Al ₂ O ₃	13.3	12.4	12.9	12.6	13.2
FeO	0.0	0.0	0.0	0.0	0.0
MnO	0.0	0.1	0.1	0.0	0.1
MgO	21.3	21.3	22.0	21.2	21.5
CaO	0.0	0.1	0.1	0.0	0.1
Na ₂ O	0.1	0.1	0.1	0.1	0.1
BaO	21.9	22.3	21.9	22.7	22.9
H ₂ O	0.5	0.1	0.0	0.0	0.5
F	5.9	6.5	7.1	6.6	5.9
Cl	0.0	0.0	0.0	0.0	0.0
Total	91.5	89.5	90.6	90.2	91.8
O=F	2.5	2.7	3.0	2.80	2.50
O=Cl	0.0	0.0	0.0	0.0	0.0
Total	89.0	86.7	87.7	87.4	89.3
Cations to 24 O, OH, F, Cl					
Si	5.17	5.07	4.95	5.06	5.09
Al	2.86	2.77	2.83	2.81	2.85
Fe ₂	0.00	0.00	0.00	0.00	0.00
Mn	0.01	0.01	0.01	0.00	0.01
Mg	5.78	6.02	6.13	5.97	5.87
Ca	0.01	0.01	0.01	0.01	0.01
Na	0.04	0.04	0.04	0.05	0.03
Ba	1.56	1.65	1.60	1.68	1.64
OH	0.61	0.10	0.00	0.05	0.57
F	3.39	3.90	4.19	3.95	3.43
Cl	0.00	0.00	0.00	0.00	0.00
Total	19.42	19.57	19.75	19.56	19.50

Table 4.07. Results of EMPA on the single crystal (post-experiment).

Noticeable inaccuracies appear (chapter 3); however, cationic ratios are sufficient, in this case, to give an approximate chemical formula.

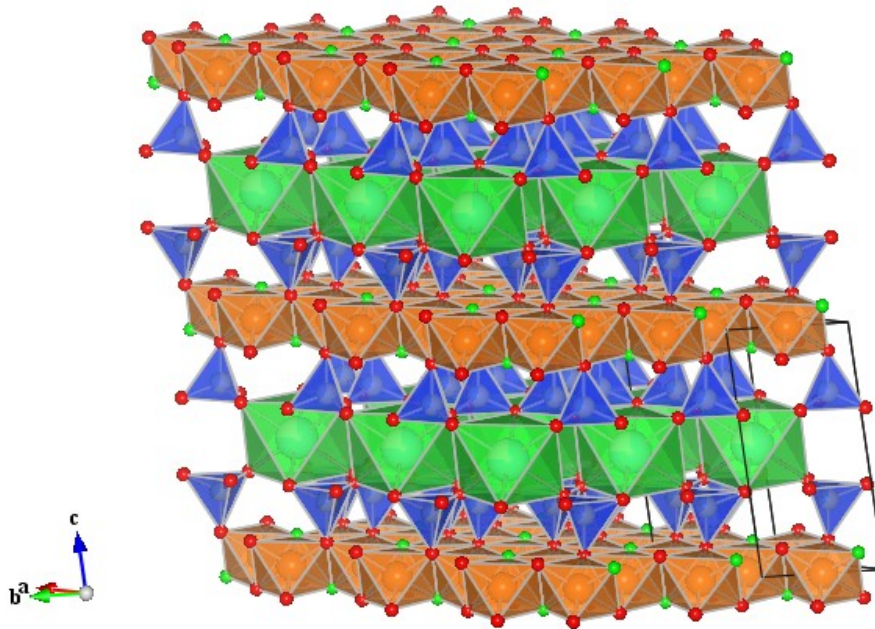


Figure 4.14. Polyhedral structure of the single crystal specimen with octahedral layer (orange), tetrahedral layer (blue) and interlayer sites (green).

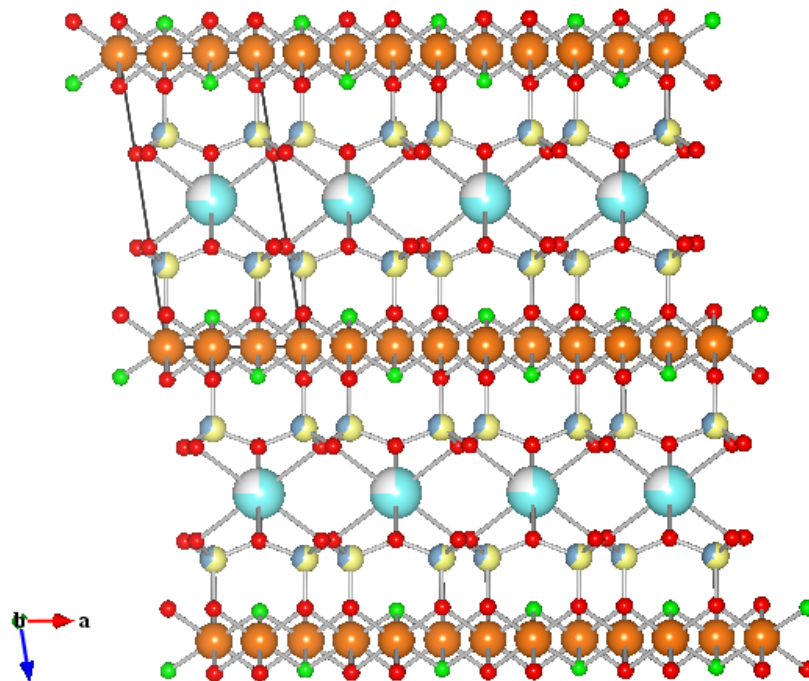


Figure 4.15. View along the **b** axis.

Note the partial vacancy of the interlayer site (shown in white); with oxygen (red), fluorine (green), aluminium (grey), magnesium (orange), silicon (yellow), barium (light blue).

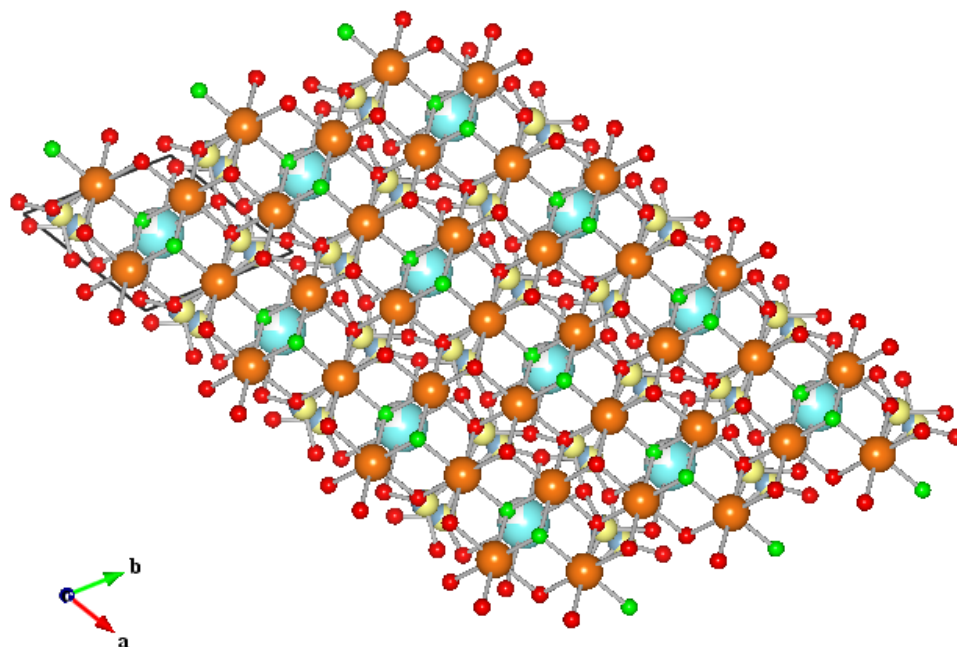


Figure 4.16. View along the c axis.

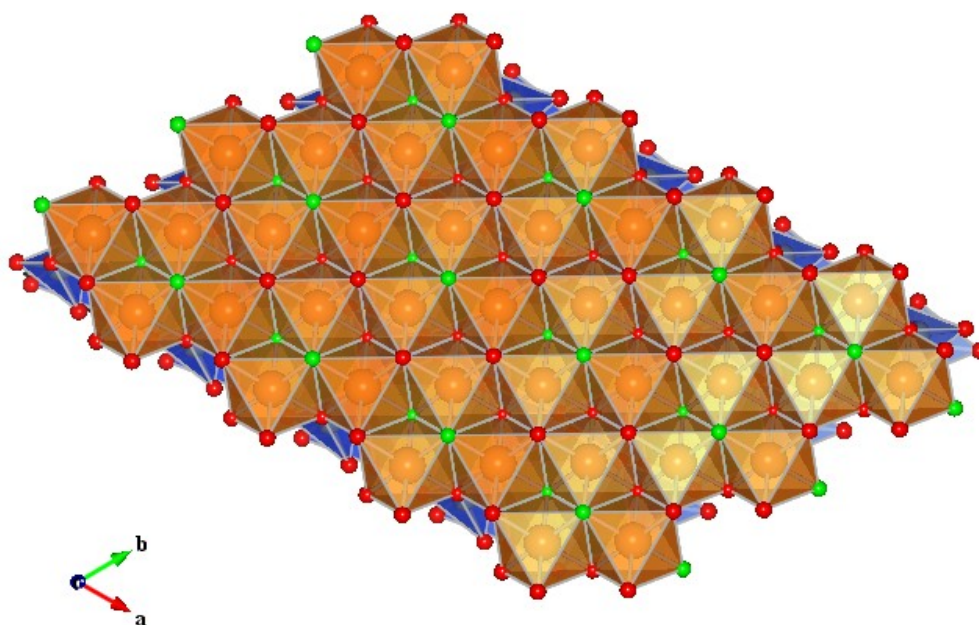


Figure 4.17. The upper apical oxygen hexagonal layer corresponds to the highlighted octahedral surface.

a (Å)	b (Å)	c (Å)	α (°)	β (°)	γ (°)
5.397	5.412	10.227	84.95	79.89	60.00
± 0.0006	± 0.0007	± 0.0014	± 0.009	± 0.007	± 0.006

Table 4.08. Lattice parameters of mica specimen with absolute errors below.

ATOM	x	y	z	Occupancy	UIISO
Ba	0.5	0.5	0.5	0.764	0.018
				± 0.00134	± 0.00021
Si	0.241	0.167	0.278	0.618	0.010
	± 0.00023	± 0.00024	± 0.00011		± 0.00023
Al	0.241	0.167	0.278	0.382	0.010
	± 0.00023	± 0.00024	± 0.00011		± 0.00023
Si	-0.092	0.833	0.278	0.618	0.010
	± 0.00023	± 0.00024	± 0.00011		± 0.00023
Al	-0.092	0.833	0.278	0.382	0.010
	± 0.00023	± 0.00024	± 0.00011		± 0.00023
Mg	0.0000	0.50000	0.00000	1.00000	0.011
					± 0.00031
Mg	0.331	0.839	0.00000	1.00000	0.011
	± 0.00027	± 0.00028			± 0.00031
F	-0.369	0.50000	0.10	1.00000	0.012
	± 0.00042		± 0.00022		± 0.00050
O	0.011	0.50000	0.341	1.00000	0.019
	± 0.00058		± 0.00031		± 0.00065
O	0.553	0.043	0.340	1.00000	0.020
	± 0.00067	± 0.00070	± 0.00032		± 0.00065
O	-0.355	0.833	0.110	1.00000	0.011
	± 0.00058	± 0.00060	± 0.00027		± 0.00058
O	0.097	-0.043	0.340	1.00000	0.020
	± 0.00067	± 0.00069	± 0.00032		± 0.00064
O	0.296	0.168	0.110	1.00000	0.011
	± 0.00058	± 0.00060	± 0.00027		± 0.00058

Table 4.09. Refined structural parameters of the triclinic cell as found in a *.cif* file; the absolute error is listed below each value in bold and is only included where parameters have been directly refined.

UISO is the isometric thermal agitation factor of the atom and should only ever be positive, with a typical value of 0.025, (Larson *et al.*, 2005).

The parameters and coordinates in tables 4.08 and 4.09 refer to the triclinic unit cell, with a space group of P -1. The lowest possible lattice symmetry was assumed by the instrument user to ensure that peaks were not omitted. The mica specimen is actually monoclinic trioctahedral (1M) with a space group of C2/m and lattice parameters as listed in the table below.

a (Å)	b (Å)	c (Å)	α (°)	β (°)	γ (°)
5.397	9.375	10.227	90	100.12	90
± 0.0006	± 0.0013	± 0.0014		± 0.007	

Table 4.10. Lattice parameters of monoclinic unit cell.

Z (the number of formula units per unit cell) is equal to 2 instead of 1 for the triclinic case due to the fact that the volume of the monoclinic unit cell is twice that of the former.

The chemical formula of the sample was determined to be: - $\text{Ba}_{0.76}\text{Mg}_3(\text{Al}_{1.53}\text{Si}_{2.47})\text{O}_{10}\text{F}_2$, from the *.cif* file generated by the *Shelx* refinement software; the same file was also used to generate figures 4.14 to 4.17. This differs from that assumed by the ternary compositional phase diagram for this system (Uno *et al.*, 1991), which is Ba-fluorphlogopite brittle mica, with formula: - $\text{Ba}_{0.5}\text{Mg}_3(\text{AlSi}_3)\text{O}_{10}\text{F}_2$; whereas the sample formula resembles a depleted analogue of kinoshitalite, $\text{BaMg}_3(\text{Al}_2\text{Si}_2)\text{O}_{10}(\text{OH}_2)$. Partial occupancy of the interlayer cation has been forced by the stoichiometry of the feedstock composition and the refined value matches that approximated by EMPA, however, this value is much higher than expected and the tetrahedral composition is between di-silicic and tri-silicic which is unusual. Kinoshitalite, not phlogopite, mica structure seems favoured in this case, hence, the higher barium occupancy. Hatch *et al.* (1957) noted that synthetic F-kinoshitalite could not be formed below 1000 °C at atmospheric pressure and Dasgupta *et al.* (1989) described an apparent continuous series between phlogopite and kinoshitalite where exchange vectors operating are:- $\text{K} + \text{Si} \leftrightarrow \text{Ba} + \text{Al}$. The transition from phlogopite to kinoshitalite structures is known to occur when the Ba:K ratio reaches or exceeds 1:2 (Gnos *et al.*, 2000) indicating that melt composition and importantly barium content is the main determining factor in the type of barium mica precipitated. The barium content of the melt, in this case, is

high (~ 13 % by weight) with no large monovalent cations present, therefore, the chemical formula of the sample is consistent with current theory.

The barium-calcium solid solution, previously reported by Uno *et al.* (1991), is not evident and would not be expected from theory in any case due to the significant size difference between cations - calcium is about 40% smaller than barium. The monoclinic lattice parameters, listed in table 4.10, appear unusual if one expects that they resemble those of Ba-kinoshitalite, indeed, the unit cell appears to have expanded at lower temperatures which seems counter-intuitive. One realises that vacancies in the mica structure must lead to an overall expansion of the unit cell as it is sensible to assume that changes to these parameters are energetically favoured. The octahedral layer, however, appears relatively undistorted with identical polyhedral volumes around the M1 and M2 sites; indeed, work by the author has shown that the fractional coordinates listed above (table 4.09) are almost identical to those of fully occupied kinoshitalite, which indicates that vacancies in the inter-layer region have little effect on the overall structure of micas.

Tetrahedral and octahedral layers exhibit rotation and flattening angles respectively. Octahedral flattening is the angle made by the body-diagonal of an octahedron to the vertical, where 54.73° is ideal. Tetrahedral rotation describes the degree of counter-rotation of tetrahedra, in the tetragonal layer, required to relieve misfit with the smaller octahedral layer. Parameters have been extracted from the refined model via geometrical analysis and averaged; results are compared with a natural kinoshitalite specimen, from literature, in table 4.11 (Fleet, 2003).

	Tetrahedral Rotation	Octahedral Flattening
Single crystal	8.49°	59.13°
Natural kinoshitalite	17.9°	58.36°

Table 4.11. Comparison of tetrahedral rotation and octahedral flattening for natural kinoshitalite mica ($\text{Ba}(\text{Mg}_{2.64}\text{Mn}_{0.31})(\text{Si}_2\text{Al}_2)\text{O}_{10}(\text{OH}_{1.61}\text{F}_{0.37})$) and the crystal sample (Fleet, 2003).

The most notable difference is in the tetrahedral rotation angle which appears significantly lower for the experimental sample. It is generally observed that, in micas, tetrahedral rotation reduces where either the Al:Si ratio of the tetrahedral

cation decreases or there is an increase in Fe^{+2} for Mg substitution in the octahedral layer (Fleet, 2003). In this case, a lower Al:Si ratio than typical for di-silicic kinoshitalite appears largely responsible for this discrepancy; therefore, lower values of tetrahedral rotation are a direct result of the depleted interlayer cationic site; which also supports the chemical formula of the refined model.

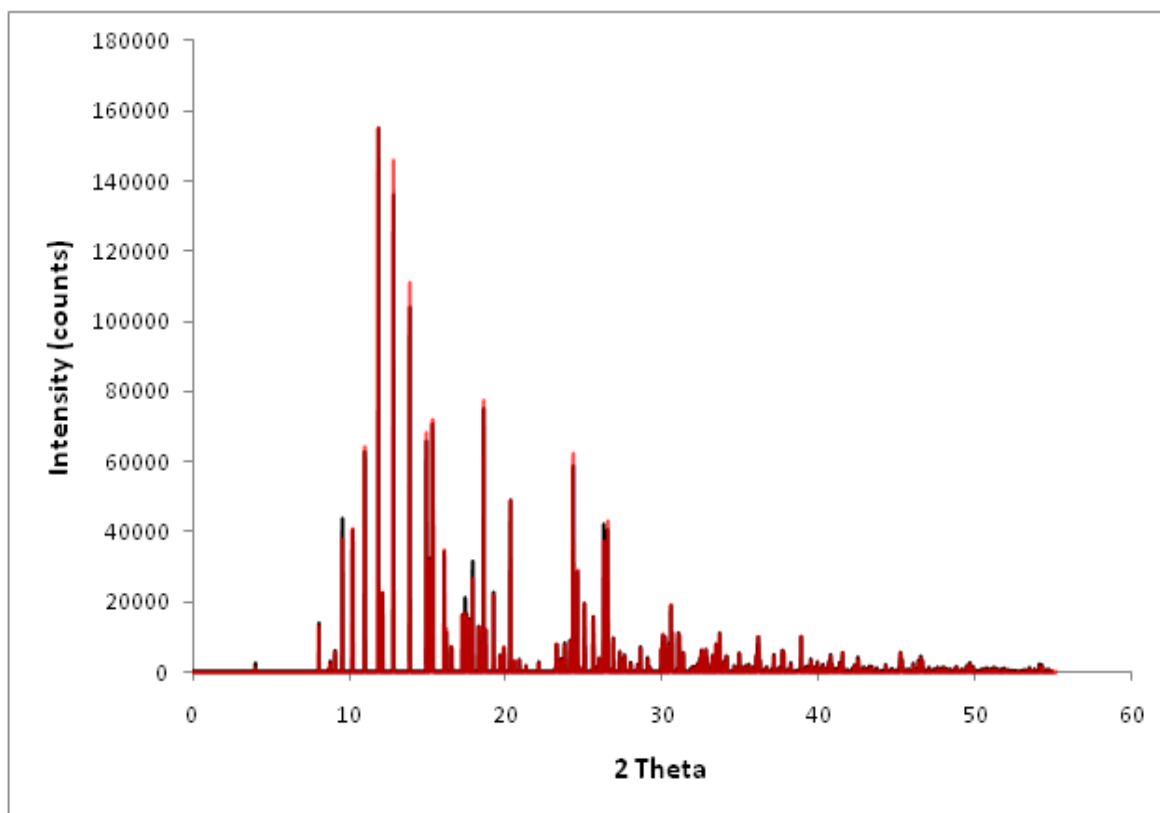


Figure 4.18. Pseudo X-ray powder diffraction pattern generated from the single crystal *.hkl* data file, in black, with an overlapping pattern of the refined model, from the *Shelxl .cif*, in red. The simulated X-ray source is Mo $\text{K}\alpha$ ($\lambda = 0.711 \text{ \AA}$).

A visual representation of the fit quality between the model and original data appears in figure 4.18. An *.FCF* file of the actual data and associated fit, in *.hkl* format, appears in appendix 7.1.

4.2.2 Powder X-ray Diffraction

4.2.2.1 Preferred Orientation in Sample Rods

Initially, unpowdered discs cut from 18 mm rods, heat-treated at $1150 \text{ }^\circ\text{C}$, were used for X-ray powder diffraction measurements as it was assumed that crystallites were randomly orientated within the glass matrix, however, problems with pattern

reproducibility suggested that this was not the case. In order to determine the extent of preferred orientation in the sample rod, two samples were cut - one from across the rod and one along the vertical (long) axis, as shown in figure 4.19. It was theorised that thermal gradients related to sample geometry have a direct influence on the preferred orientation as reported by Ochi *et al.*, 2006. X-ray powder diffraction was performed on each sample and the results compared.

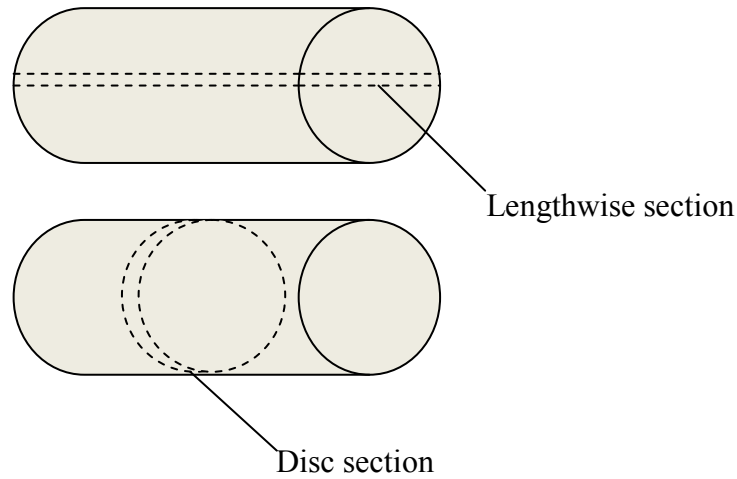


Figure 4.19. Schematic showing the different sections cut from the same 18 mm sample rod.

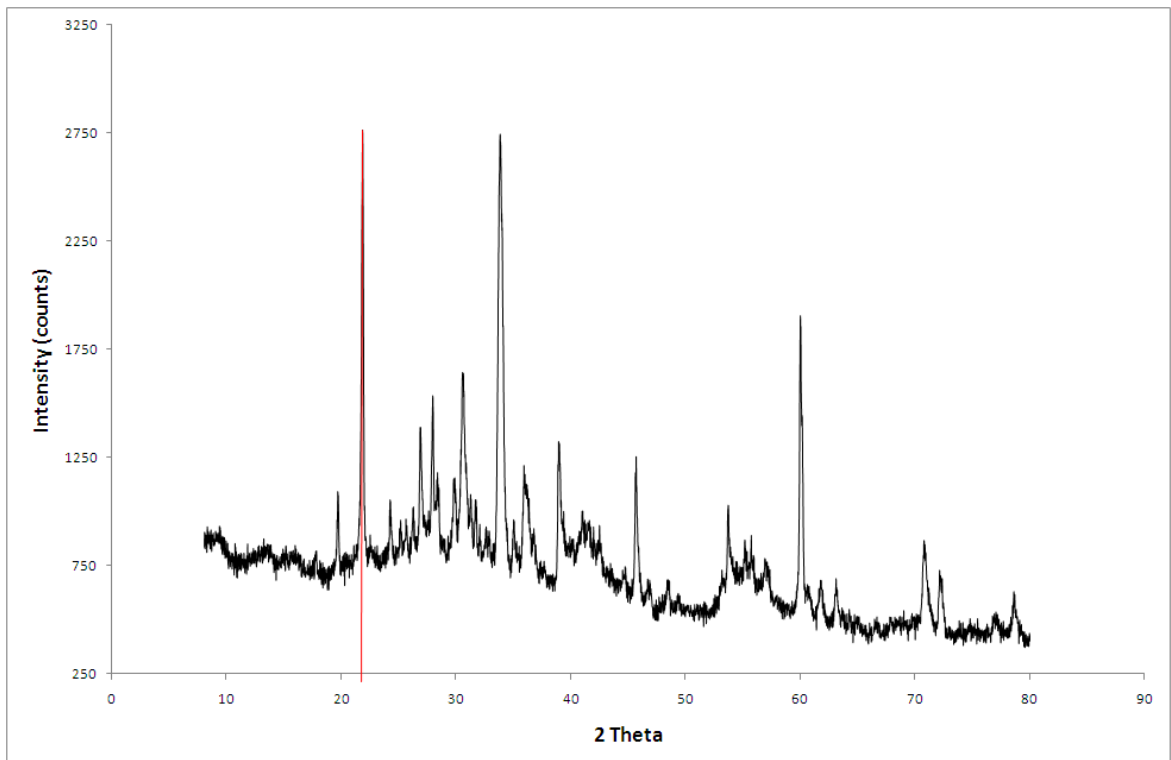


Figure 4.20. Diffraction pattern of the sample taken from a lengthwise section of the rod.

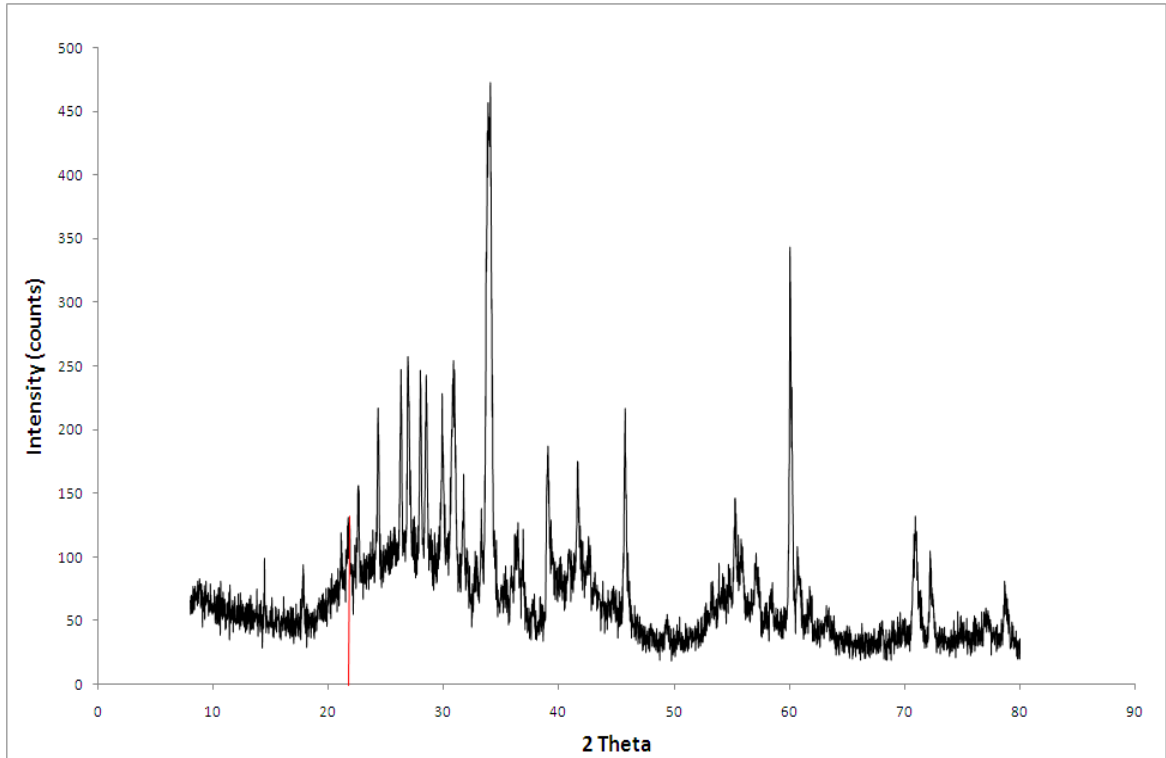


Figure 4.21. Diffraction pattern of the sample taken from a cross-wise section of the rod.

The peaks marked in red, in figures 4.20 and 4.21, were initially assumed to correspond to the 22° (210) reflections of the secondary clinoenstatite phase. However, the relationship between the intensities of the (220) reflections at 30° appears to be the inverse of that observed for the (210) case, in that one increases when the other decreases. This is not possible as both lie parallel to the c axis so preferential orientation would act to increase both intensities. Later work, in section 4.2.2.3, has identified the presence of a cristobalite (SiO_2) secondary phase in this material with a large characteristic (011) peak at 22° . There is a considerable increase in the (011) peak intensity for the sample taken from the length-wise section of the rod which is consistent with an orientation of the [011] vector perpendicular to the diffracting surface in reflection geometry. The cross-wise section effectively rotates the [011] vector through 90° such that the plane is parallel to the surface vector, hence, the reduction in intensity. Ochi *et al.* (2006) have theorised that temperature gradients cause orientated diffusion which can lead to orientated crystal growth in glass-ceramics; this may explain why different planes taken through the sample exhibit different amounts of preferred orientation. Further work may investigate the effects of thermal gradients on the resultant mechanical

properties of mica glass-ceramics, and whether such a mechanism can be used to directly influence the development of crystalline microstructure.

4.2.2.2 Surface Nucleation

Surface nucleation in barium mica glass-ceramics has been reported by Henry (2001), and is known to produce different phases from those found in the bulk. The figure below shows a distinct skin on the cerammed sample surface of coloured LDIG 24 commercial glass-ceramic with a thickness of less than 1 mm.

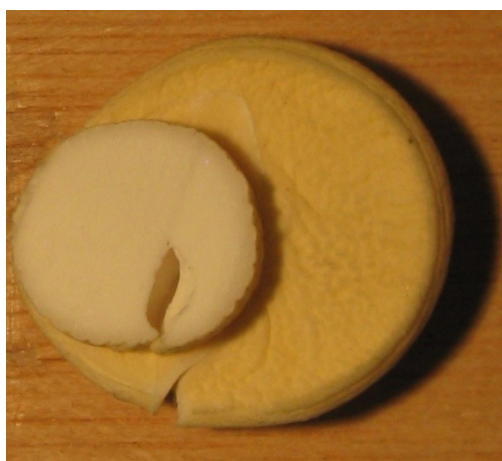


Figure 4.22. Top section from a 14 mm glass-ceramic stud.

LDIG 24 commercial + 1 % by mole of Fe(II)Cl_2 ; the outer skin, visible on the overflow, is yellow, whereas, the internal bulk is cream coloured.

Due in part to the thickness of the surface layer it was not possible to collect this material from a bulk sample. An experiment was devised to produce quantities of surface nucleated glass-ceramic sufficient for powder XRD. Approximately 10 glass discs were cut from a single 18 mm glass rod and ground to thicknesses of less than 1 mm. These discs were subsequently heat treated according to the standard regime and then powdered for XRD analysis in order to reduce the effects of preferred orientation. The powder pattern in figures 4.23 to 4.28 has been fitted by Le Bail's method - with the profile parameters GU, GV, GW and GP of profile function 3, in *GSAS*, derived from a silicon standard to ensure a good fit. A number of significant phases have been identified which do not appear in the bulk sample (section 4.2.2.3). The fit quality, in this case, is defined by a χ^2 parameter of 2.00 which is acceptable.

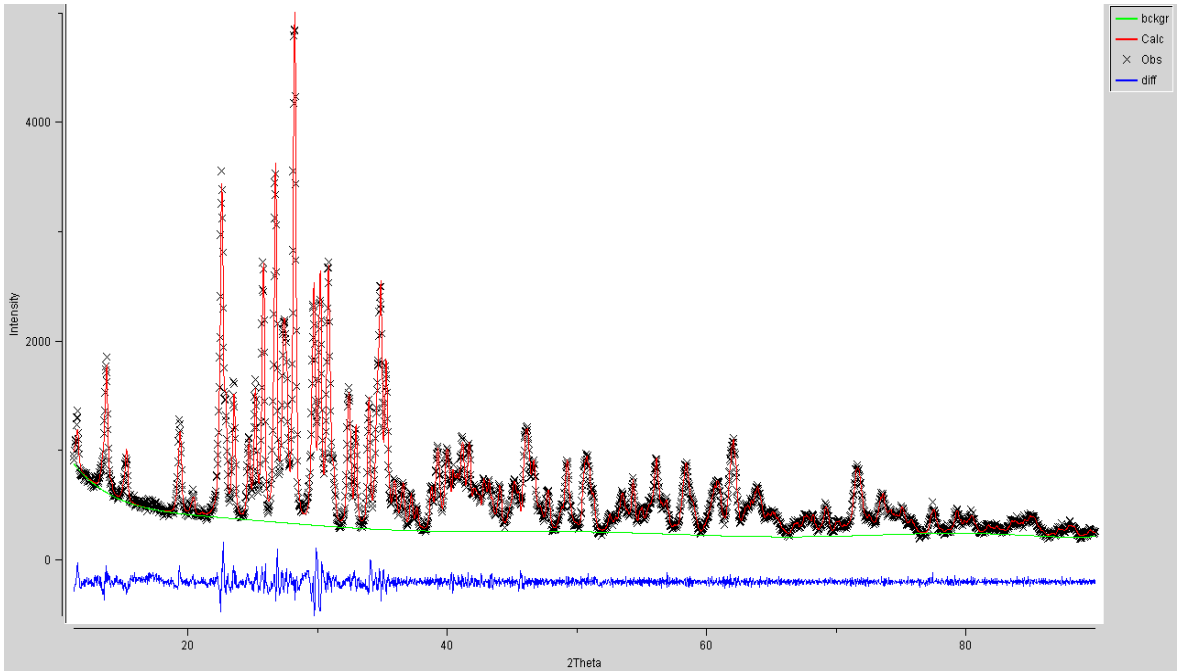


Figure 4.23. Le Bail fit of the full X-ray powder pattern of surface nucleated LDIG 24 commercial glass-ceramic heat treated @ 1150 °C for 3 hours.

The red line represents the calculated fit, the blue line is the difference curve and the green line is the fitted background.

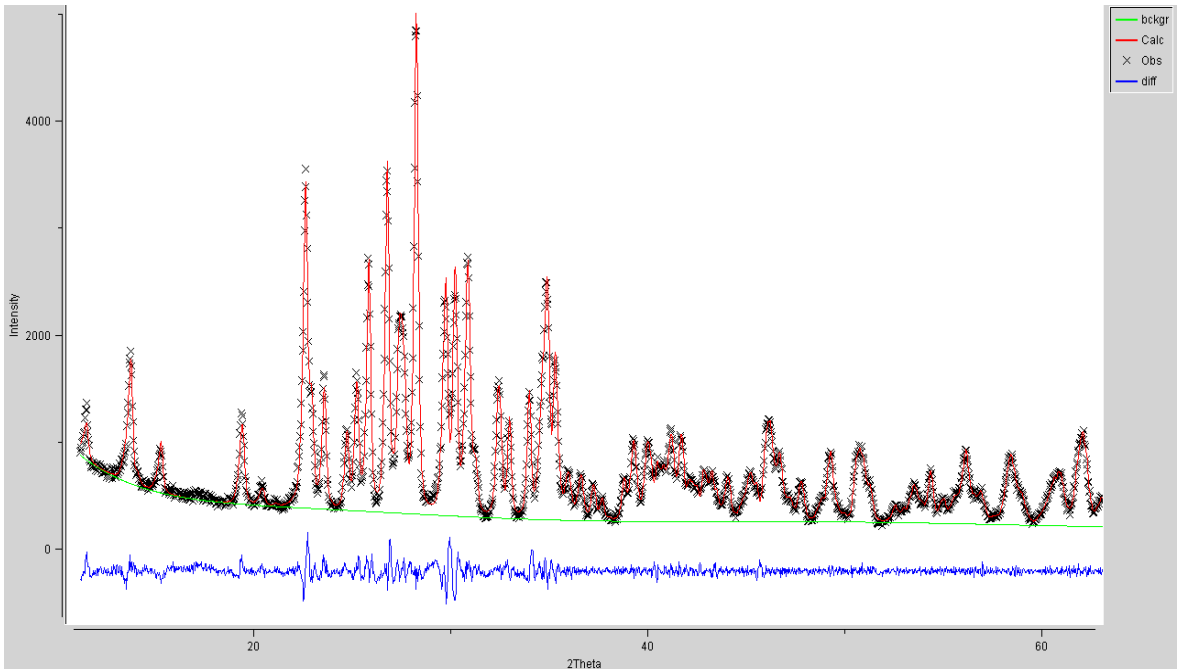


Figure 4.24. Le Bail fit of the same pattern showing a reduced 2 theta range.

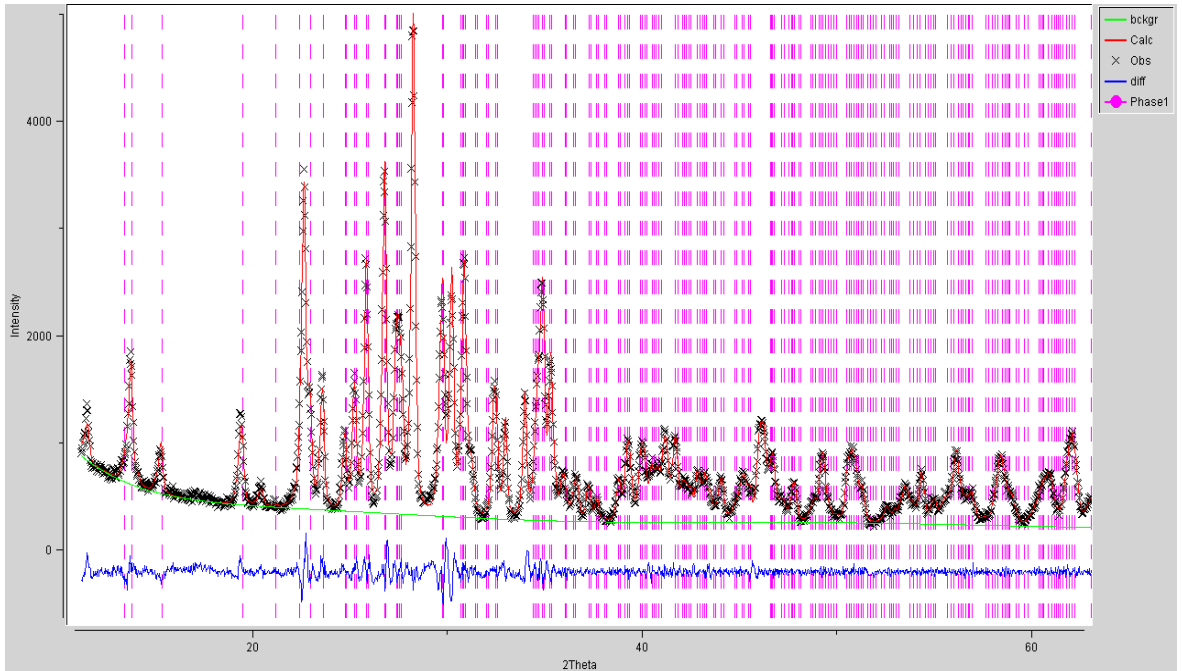


Figure 4.25. Le Bail fit of data with celsian phase marked in pink.

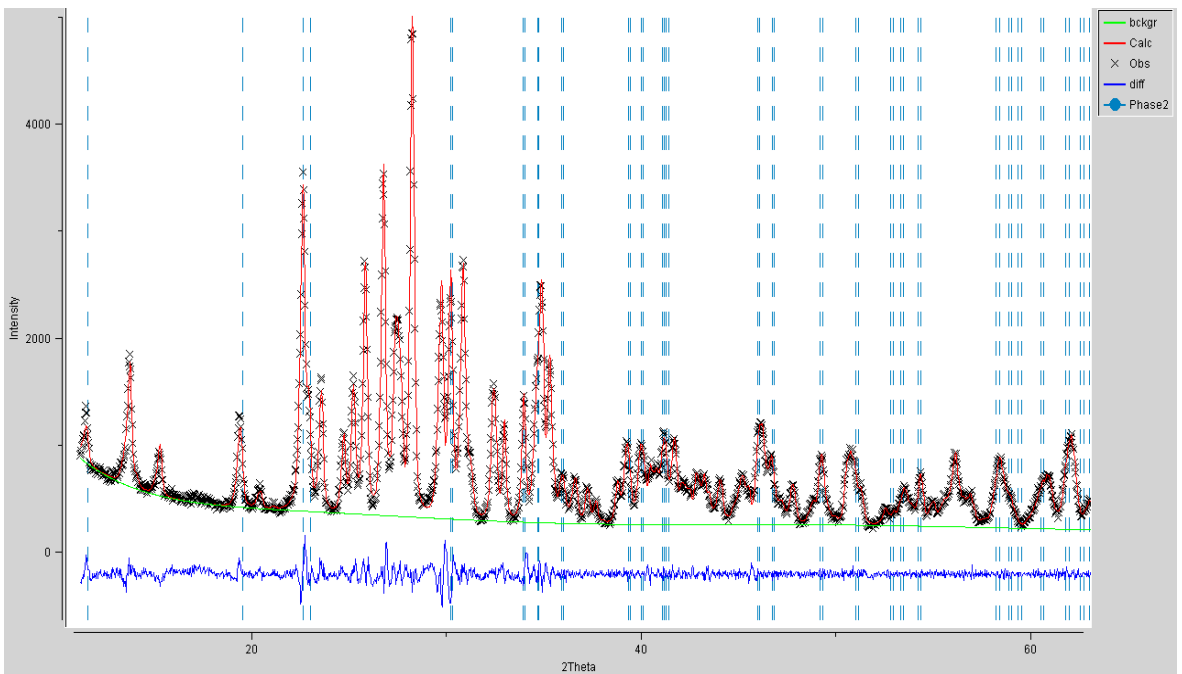


Figure 4.26. Le Bail fit of data with hexa-celsian phase marked in blue.

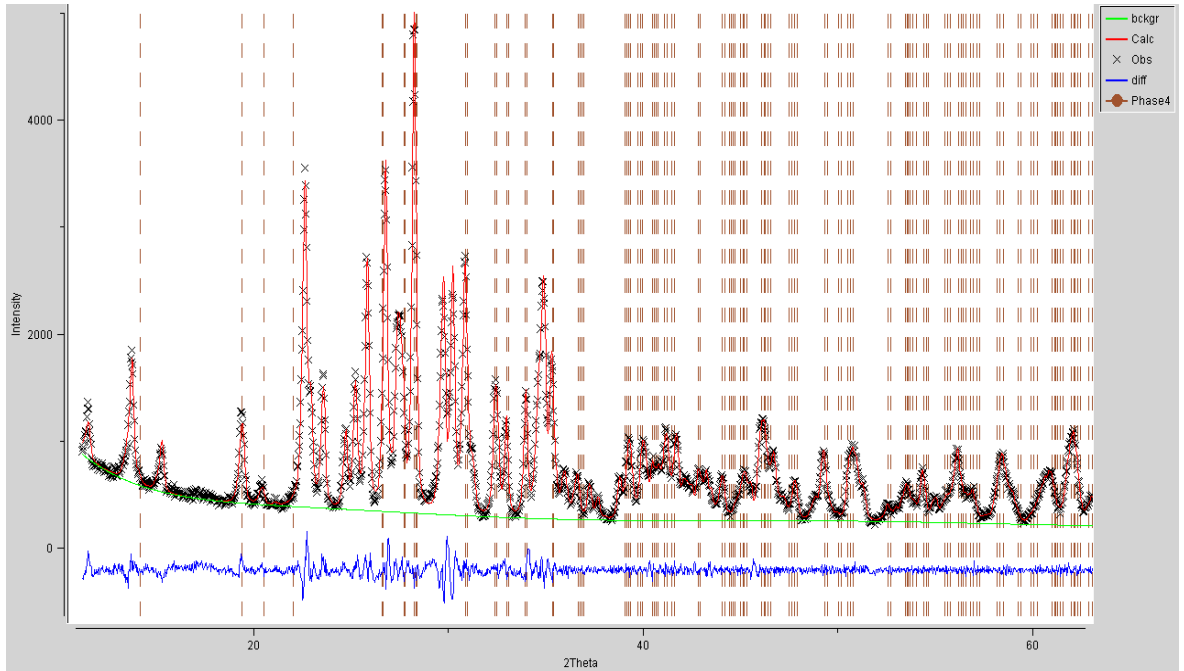


Figure 4.27. Le Bail fit of data with proto-enstatite phase marked in brown.

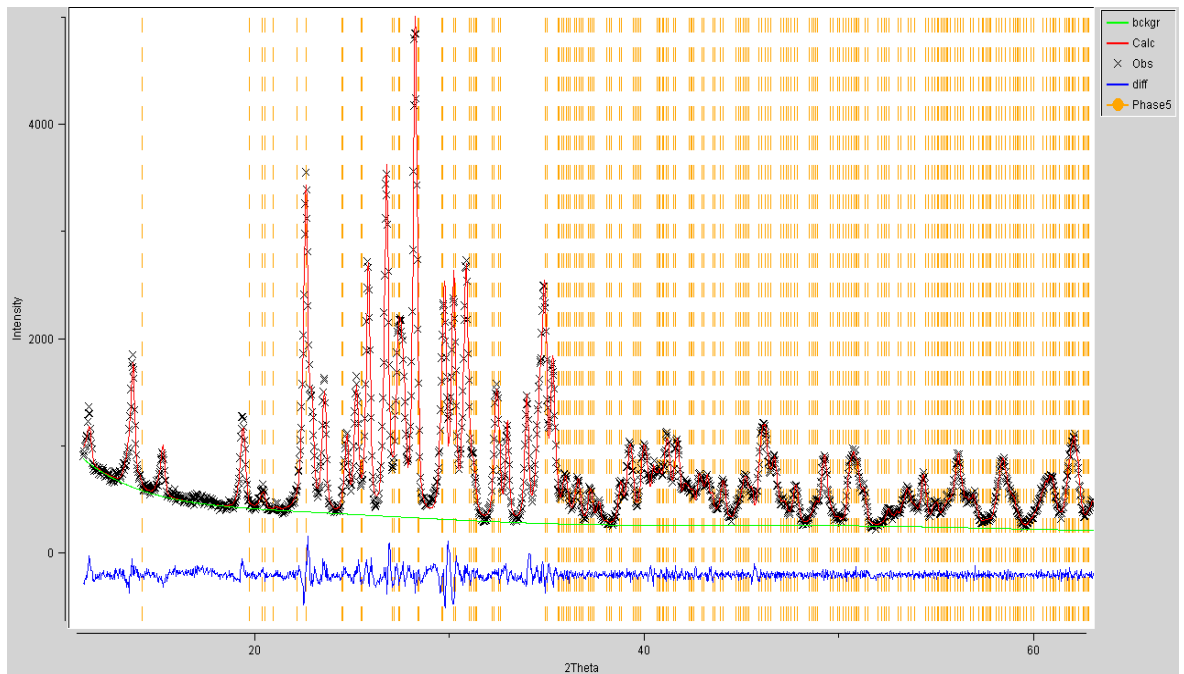


Figure 4.28. Le Bail fit of data with clino-enstatite phase marked in yellow.

	a(Å)	b(Å)	c(Å)	$\alpha(^{\circ})$	$\beta(^{\circ})$	$\gamma(^{\circ})$
Celsian	8.641	13.047	7.203	90	115.08	90
	± 0.00026	± 0.00044	± 0.00025	± 0.0	± 0.0031	± 0.0
Hexacelsian > 300 °C	5.313	5.313	7.805	90	90	120
	± 0.00057	± 0.00049	± 0.00035	± 0.0	± 0.0056	± 0.0
Orthocelsian < 300 °C	5.293	9.168	7.790	90	90	90
Protoenstatite	9.266	8.746	5.315	90	90	90
	± 0.00040	± 0.00040	± 0.00021	± 0.0	± 0.0	± 0.0
Clinoenstatite	9.602	8.817	5.173	90	108.29	90

Table 4.12. Phases and associated lattice parameters used to fit the data, orthocelsian is included for completeness. Absolute errors are listed where appropriate.

The phases listed above are main phases that have been identified with reasonable accuracy; there may be residual phases that cannot be identified due to excessive peak overlap. Hexacelsian, orthocelsian and protoenstatite (in appendix 1.13, 1.7 and 1.8) have hexagonal and orthorhombic unit cells, with space groups of P6/mmm, P6₃/mcm and Pbcn respectively; in contrast celsian and clinoenstatite (in appendix 1.6 and 1.9) are both monoclinic with space groups of C2/m and P 2₁/c respectively. A *Searchmatch* simulation of these phases alongside the raw data, in figures 4.25 - 4.28, appears in appendix 1.1.

4.2.2.2.1 Phase identification and discussion.

If one begins with the tertiary phase diagram in section 1.1, it is possible to eliminate both Ba-mica and cordierite (Mg₂Al₄Si₅O₁₈) as main phases. Cordierite produces significant peaks at 10.46° (110), 18.24° (200), 21.71° (112) and 28.50° (222) all of which are absent from the pattern, whereas, mica has characteristic peaks at ~ 8.85° (001), ~ 17.86° (002) and ~ 28.58° (112) which again fail to appear. Spinel (MgAl₂O₄), reported by Henry (2001) for K-phlogopite glass-ceramic, with a principal peak at ~ 38.50° (311) was also ruled out as a main phase. Since barium is a large component of LDIG 24 glass-ceramics, it is logical to assume that another barium containing phase is present in place of mica. The development of enstatite

(MgSiO₃) – celsian (BaAl₂Si₂O₈) glass-ceramics by El-Meliegy *et al.* (2005) concerns a similar chemical composition but without fluorine and was a suitable starting point for the analysis. A number of possibilities were subsequently investigated by comparison of the raw data with various multi-phase simulations in *Searchmatch*; a final solution was achieved when all of the visible peaks of the original pattern matched those of the simulated phases (appendix 1.1) – good agreement with peak heights was also evident in this case after scaling each component. These identified phases (Table 4.12) were then used to generate the Le Bail fit, shown in the previous figures.

The average value of profile parameter Lx, known as the Lorentzian coefficient for particle size, is 8.25 when averaged over 4 phases. Using basic equations described in the *GSAS* manual (Larson *et al.*, 2004), it is possible to convert this value into the average crystallite diameter, assuming plate-like morphology for the phases identified, as follows.

$$P = 18000K\lambda/\pi x$$

$$x = \Delta d/d^2$$

Parameter P is the crystallite size in Angstroms (Å), λ is the wavelength of X-ray radiation, x is the Lorentzian coefficient for particle size outputted by *GSAS*, d is the d-spacing (equivalent to 2 theta) and K is the Scherrer coefficient - 1.84 for flat hexagonal crystals (Sadale *et al.*, 2005). Substitution into the above yields an averaged crystal size of: - 1968.7 Å (2.d.p) or ~ 0.2 μm. The small size may be a result of grinding and the assumption that crystallites are hexagonal when, in fact, they are likely to be acicular and lath-like, apparent from the SEM micrographs in section 4.1.7. Anisotropic coefficients can often be refined; however, in cases of complex low-symmetry multi-phase systems accuracy is likely to be very poor.

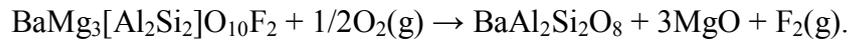
Early studies of protoenstatite by Smith *et al.* (1958) established a relationship between proto and clinoenstatite (MgSiO₃) polymorphs; it is widely accepted that clinoenstatite formation, in nature, occurs as a result of direct phase transformation (Yasuda *et al.*, 1983). Protoenstatite is a stable high temperature (> 1100 °C) phase that gradually converts to clinoenstatite at room temperature; there are several ways that complete conversion can be achieved - long standing at room temperature,

heating to 1400 °C and mechanical grinding. Proto to clino and clino to proto transitions are rapid martensitic transformations causing, in many cases, large cracks in the transformed clinoenstatite crystals as a result of shortening of the **c** axis (Dallwitz *et al.*, 1966). Clinoenstatite from meteorites is often found to have inverted from protoenstatite upon rapid cooling and is polysynthetically twinned in (100), meaning that multiple twins are aligned parallel to the (100) plane (Boyd *et al.*, 1965). Investigations have shown that cracks formed in clinoenstatite in this way can act as nucleation sites for talc and other fibrous crystals from the melt (Yasuda *et al.*, 1983). A martensitic phase transformation of this type leads to improved fracture toughness in the bulk material due to the deflection of micro-cracks along twin planes and retardation of crack propagation (El-Meliegy *et al.*, 2005). Referring to the diffraction pattern in figures 4.25 to 4.28 and the *Searchmatch* simulation in appendix 1.1, an apparently significant amount of metastable protoenstatite coexists with a smaller volume fraction of clinoenstatite at room temperature indicating that there is a substantial relaxation time for phase transition in this case.

The hexacesian-celsian ($\text{BaAl}_2\text{Si}_2\text{O}_8$) phase transformation has been well studied in the literature. At temperatures below 1590 °C and above 1200 °C celsian is the stable phase with the hexacelsian stability field extending from 1590 °C to 1760 °C, however, hexacelsian exists as a metastable phase below this. When celsian is synthesized by crystallisation of a glass preform, as in this case, hexacelsian always appears as a metastable phase first before the formation of celsian and phase transition is typically very slow (Lee *et al.*, 2000). There is also a second phase transformation between hexacelsian and orthocelsian polytypes at approximately 300 °C, which would compromise a BAS glass-ceramic; the diffraction patterns of both polytypes appear identical; however, it is sensible to assume that metastable hexacelsian is probably mostly orthocelsian at room temperature, in figure 4.26. Based on this discussion the main phases, in table 4.12, include celsian, orthocelsian, hexacelsian and protoenstatite with clinoenstatite as a minor phase.

A possible explanation for the different type of phase formation in thin disc samples compared with that in the bulk (section 4.2.2.3) is as follows. Surface layers on sample rods appear strongly dependant on the crystallisation hold temperature with the absence of any visible layer for temperatures below 1100 °C. Henry (2001) has suggested that fluorine is volatilised at the sample surface which suppresses the mica

formation found in the bulk and explains the apparent absence of fluorinated phases. Melting or re-crystallisation has been indirectly observed as the sample discs, in this case, appeared distorted with apparent warping of the surface when heat treated at 1150 °C; it is likely, therefore, that depleted F-kinoshitalite (section 4.2.1) may form as a pre-cursor phase in these materials. It can be theorised that the phase formation mechanism is as follows: - loss of fluorine from the sample exterior, surface nucleation of hexacelsian, dissolution of F-kinoshitalite as a result of contact between the phases, celsian ($\text{BaAl}_2\text{Si}_2\text{O}_8$) and kinoshitalite ($\text{BaMg}_3[\text{Al}_2\text{Si}_2]\text{O}_{10}\text{F}_2$) form a reaction interface when in contact (King *et al.*, 2000), conversion of the F-kinoshitalite to hexacelsian and protoenstatite, subsequent phase transition to monoclinic celsian and clinoenstatite and finally orthocelsian at room temperature. The reaction formula is written as (King *et al.*, 2000):



Protoenstatite formation is possibly augmented by MgO at high temperatures.

4.2.2.3 XRD Analysis of Bulk Sample Cerammed by Standard Heat Treatment

As already stated phase composition of the bulk glass ceramic is known to be markedly different from that of the surface and includes fluoro-kinoshitalite or at least a depleted variant. Powdered bulk samples for XRD analysis were prepared from 18 mm glass-ceramic rods, heat-treated at 1150 °C, by first stripping the surface layer, sectioning into thin discs (~ 1 mm) and hand-grinding with a pestle and mortar (chapter 3). The results of a multiple phase Le Bail fit in GSAS are shown in the figures 4.29 to 4.35. The quality of the fit, in this case, is given by a χ^2 parameter of 2.17, which appears to be the minimum attainable. Significant peak overlap is evident, however, a number of outstanding characteristic peaks allowed identification of several previously unknown phases. Data from the single crystal experiment (section 4.2.1) and several powdered samples enabled highly accurate determination of the lattice constants of the main mica phase. Excluded regions shown do not contain any peaks.

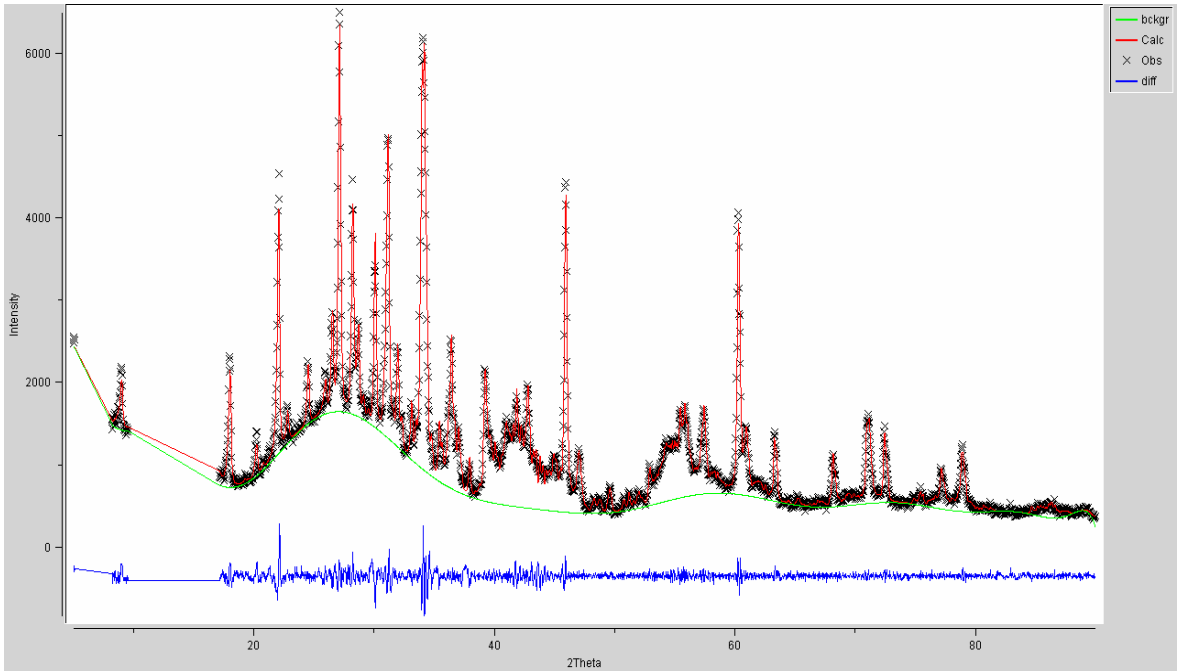


Figure 4.29. Le Bail fit of powder pattern of a sample of powdered LDIG 24 commercial glass-ceramic after standard heat treatment (@1150 °C for 3 hours).

The blue line represents the sigma squared value and the green line is a polynomial function background fit. Note the eccentric shape of the background in this case when compared with the previous surface nucleated example.

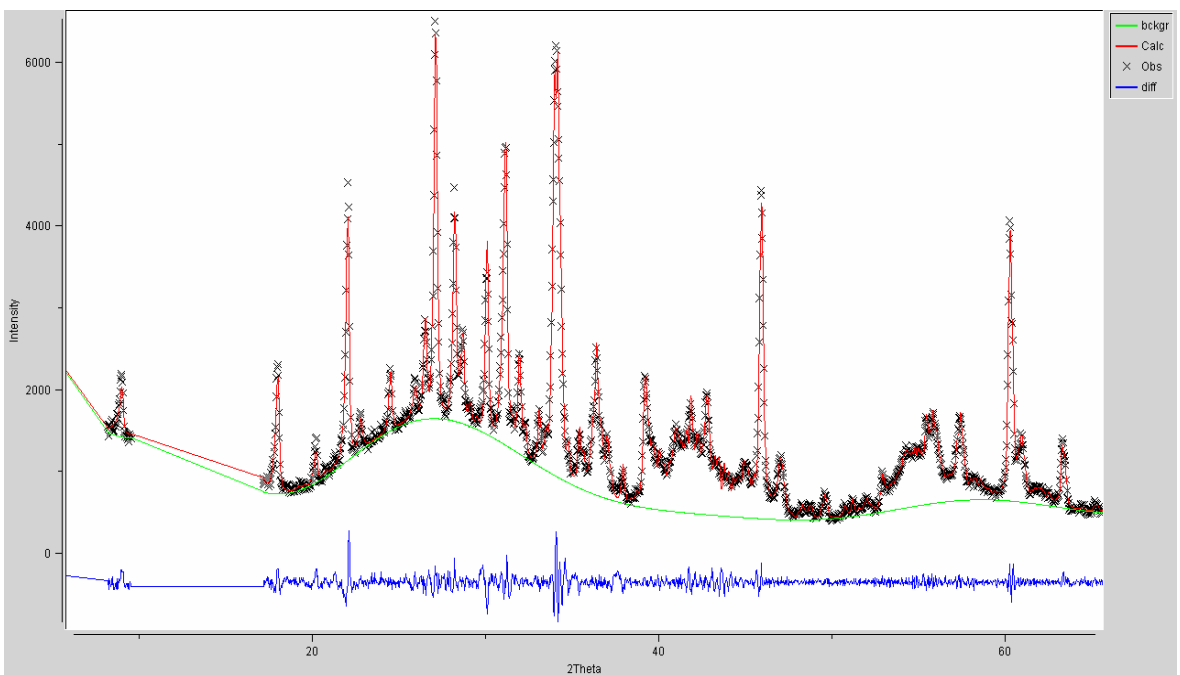


Figure 4.30. Le Bail fit with reduced 2 theta scale range.

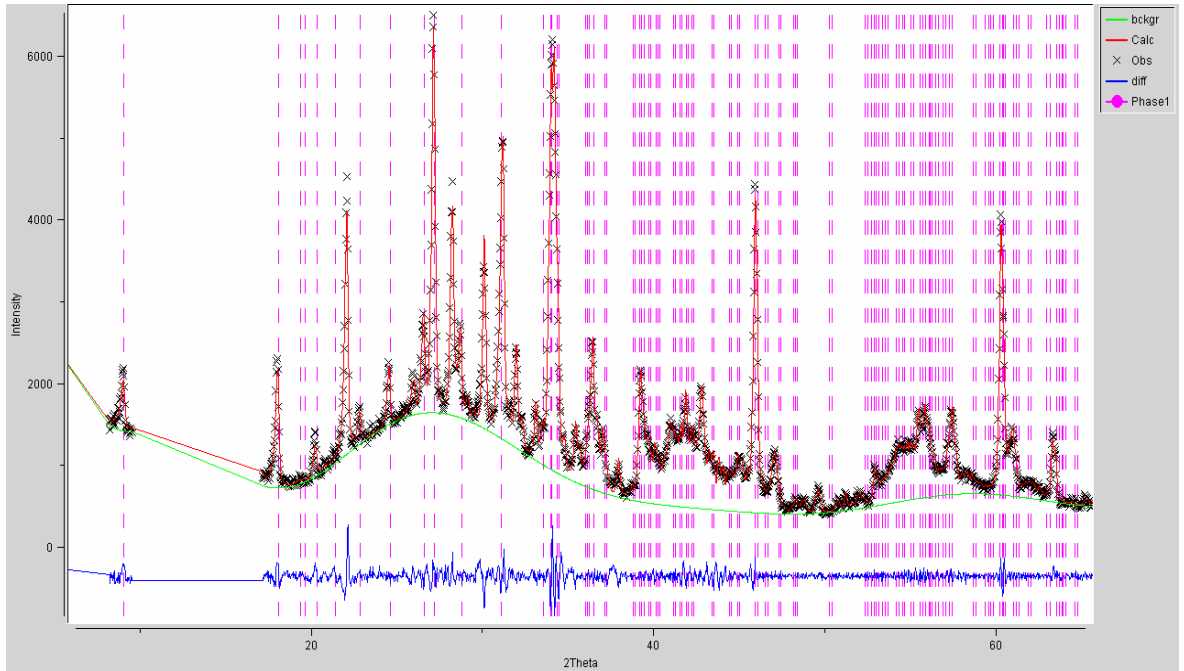


Figure 4.31. Le Bail fit with F-kinoshitalite phase marked in red.

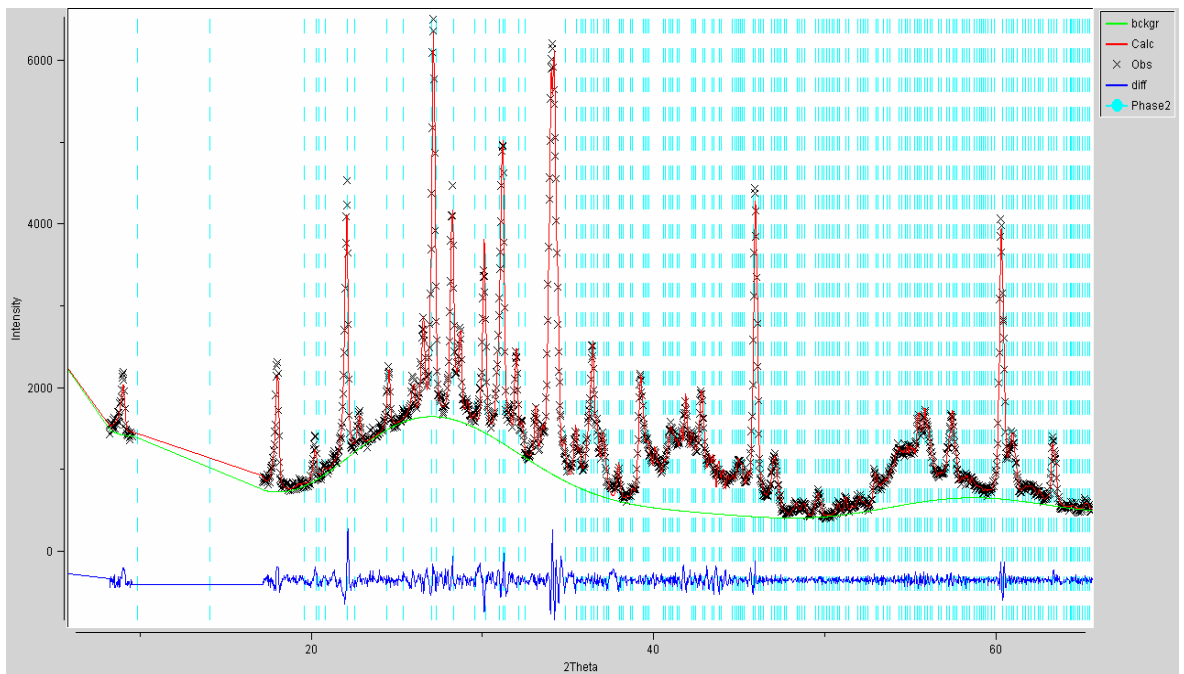


Figure 4.32. Le Bail fit with clinoenstatite phase marked in turquoise.

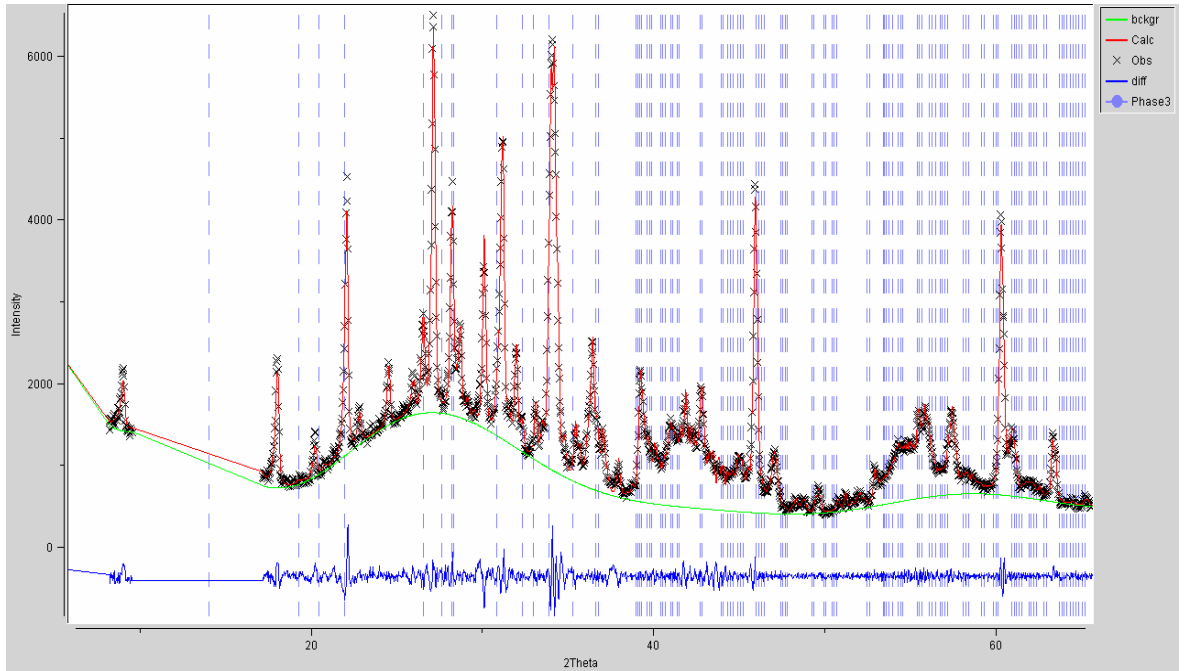


Figure 4.33. Le Bail fit with proto-enstatite phase marked in blue.

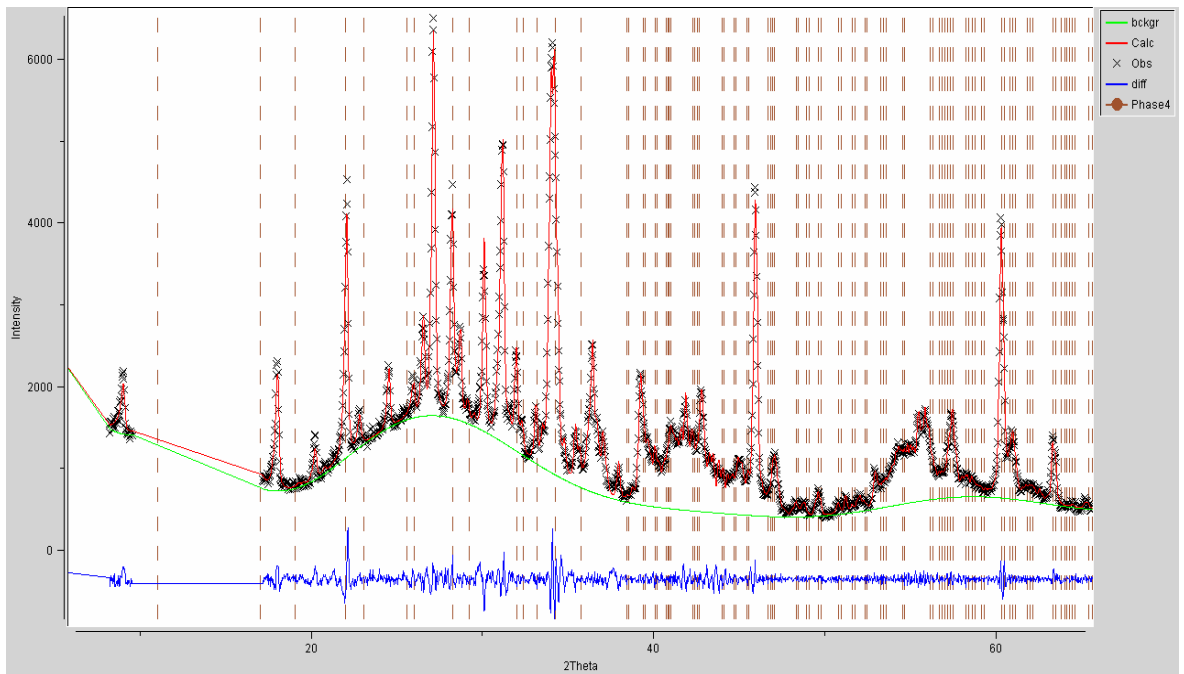


Figure 4.34. Le Bail fit with fluorapatite phase marked in brown.

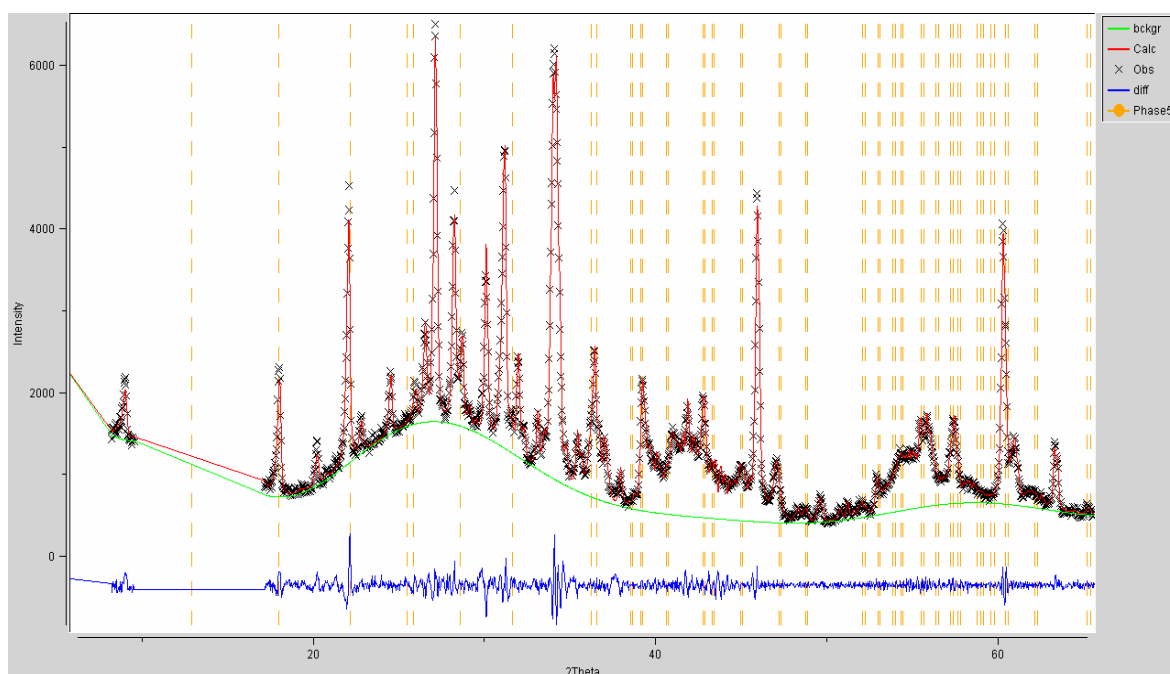


Figure 4.35. Le Bail fit with dummy phase (isostructural with cristobalite) in yellow.

	a(Å)	b(Å)	c(Å)	$\alpha(^{\circ})$	$\beta(^{\circ})$	$\gamma(^{\circ})$
Mica	5.314	9.219	10.042	90	100.20	90
	± 0.00020	± 0.00036	± 0.00035		± 0.0049	
Clinoenstatite	9.602	8.817	5.173	90	108.29	90
	± 0.00057	± 0.00049	± 0.00035		± 0.0056	
Protoenstatite	9.266	8.746	5.315	90	90	90
Fluorapatite	9.385	9.385	6.891	90	90	120
Dummy phase	4.973	4.973	6.924	90	90	90

Table 4.13. Phases and their respective lattice parameters used to fit the pattern; errors are shown where applicable.

4.2.2.3.1 Phase identification and discussion.

Profile coefficients (GU, GV, GW and GP) applied here are the same as those in section 4.2.2.2 for the surface nucleated case; the average crystallite sizes of both the mica and clinoenstatite phases were determined from the Lorentzian coefficients, as before, and were calculated, by application of the Scherrer equation, as 0.219 μm and 0.141 μm (3.s.f) respectively - with $K = 1.84$. A multi-phase simulation in *Searchmatch* of the pattern in figures 4.30 to 4.35 is shown in appendix 1.4. The absence of peaks at: - 11.35°, 13.56°, 15.1° and 19.23° two theta indicate that both celsian and hexacelsian do not form in the bulk; Ba-mica appears instead

(in appendix 1.12) with characteristic peaks at 8.9° (001) and 17.9° (002), in figure 4.31. Enstatite, (MgSiO_3) which could be expected from the surface nucleated case, is also evident from significant peaks at 30° (-221) and 28.12° (220) two theta, identifying clinoenstatite, and relatively minor peaks at 27.53° and 32.86° from protoenstatite. It is reasonable to assume that the formation mechanism, in this case, is the same, proto-clino or likely clino-proto martensitic phase transformation, albeit with mica not celsian. Fosterite (Mg_2SiO_4), found in K-mica glass-ceramics (Henry, 2001), is not evident with several primary peak absences at 22.89° (120), 32.35° (031) and 52.28° (222) two theta. The lattice parameters of the main mica phase also appear relatively constant irrespective of the sample, although, they differ significantly from those of the single crystal in section 4.2.1. This indicates that the composition of the bulk kinoshitalite mica phase is relatively constant, such that the composition of the single crystal cannot be representative of the average in the bulk.

The 'dummy' phase, table 4.13, is isostructural with cristobalite (SiO_2), in appendix 1.10, and was noted to improve the fitting of the large peak at 22° and match a smaller unidentified peak at 31.16° ; although rigorous identification on the basis of a couple of peaks in a multi-phase system is impossible without Rietveld refinement. Finally, the discovery of fluorapatite ($(\text{Ca}_5(\text{PO}_4)_3\text{F})$, $P6_3/m$ space group), in appendix 1.11, is unexpected for the current glass-system and indicates a poor understanding of crystallisation process in these materials. Fluorapatite (FAP) was identified by singular characteristic peaks at: - 31.92° , 33.10° , 29.10° and 25.87° two theta. The major phases in table 4.13, therefore, are: - mica, clinoenstatite and possibly cristobalite with minor phases protoenstatite and fluorapatite; preferred orientation in the sample (section 4.2.2.1) seems to prevent an accurate assessment of volume fractions, despite being powdered for phase analysis.

Studies by Bentley *et al.* (2007), of bioactive machinable fluormica-fluorapatite glass-ceramics have shown FAP to nucleate at around 1040°C which is much higher than the nucleation temperature of Ba-fluormica, $\sim 650^\circ\text{C}$ in this case. The majority of the fluorine content, therefore, is expected to have been consumed by the prior crystallisation of a large volume fraction of Ba-fluormica, which would suppress the fluorapatite phase. A reasonable explanation is that a lower mica volume fraction develops than that expected from stoichiometry alone, the parent glass composition assumes the formation of a 6 mol % calcium phosphate ($\text{Ca}_3(\text{PO}_4)_2$) phase, which is

a third deficient in $[\text{PO}_4]$. The maximum molar fraction of the FAP phase, therefore, should be 4 mol % - assuming sufficient calcium. It is likely that preferred orientation alters the perceived phase fraction based on the analysis of the pattern in figures 4.29 to 4.35; however, if one assumes that the crystalline weight fraction is substantially below 100 %, relatively large volume fractions of fluorapatite might be possible. As a general rule, the amount of fluorapatite precipitated depends on the stoichiometric weight fraction in the feedstock (Moorehead *et al.*, ILL report, 2007), however, this is known to be an over-simplification. The presence of fluorapatite in this material is supported by subsequent EDS work in appendix 2.2.

Work by Xiang *et al.* (2007) on $x:(100 - x)$ wt % Ca-phlogopite and fluorapatite glass-ceramics, cerammed at 925 °C for 12 hrs, has shown that a high content of CaO and P_2O_5 leads to intense phase separation in the glass. In crystal chemistry theory, the P^{5+} ion has a higher ionic field strength than the Si^{4+} ion (field strength is measured by the charge to atomic radius ratio), hence, P^{5+} ions can coordinate with O^{2-} ions from the silicate network, which is rather open to various interstitial or modifying cations and often contains large quantities of ‘non-bridging’ oxygens. Since P^{5+} is a pentavalent network-forming cation, neutrality is ensured only if one of the four oxygen ions around P^{5+} ion is doubly bonded to the central P^{5+} cation. The double bond in the $[\text{PO}_4]$ tetrahedral is shorter in length than other three single bonds (1.424 Å compared to 1.595 Å); resulting in asymmetry of the $[\text{PO}_4]$ tetrahedron and disruption of bonding in the glass network. Phase separation, therefore, is likely to occur, and the phosphate-rich and silicate-rich phases are separated from the parent glass. In their conclusion, fluorapatite ($\text{Ca}_5(\text{PO}_4)_3\text{F}$) was precipitated from the droplet phase with high concentrations of Ca and P; for lower concentrations (< 10% apatite) they found that nanocrystalline CaF_2 had nucleated instead, however, fluorapatite formation did occur after temperature holds of up to 12 hours; indicating a significant activation energy for fluorapatite nucleation in this case.

4.2.2.4 Rietveld/Le Bail fit of Powdered Single Crystal Bulk Sample (Untreated)

In order to help with the identification of secondary phases, a sample was taken from the crystallised material used to precipitate large mica crystals for the single crystal diffraction experiment (section 4.2.1); XRD was performed on this sample,

after grinding, to determine whether the phase composition was comparable to that found in the standard cerammed condition and how this could be exploited. Initial phase matching in *Searchmatch* (see appendix 1.3) led to the identification of another phosphate phase, apparently related to the fluorapatite phase (with the same $[\text{PO}_4]$ structural unit) but largely in place of it. The software assumed a match with barite (BaSO_4), in appendix 1.16, which seems odd as sulphur is not present in the sample. Examination of this problem reveals an explanation - both sulphur and phosphorus (~ 100 pm) have very similar atomic radii as do fluorine and oxygen (~ 60 pm) allowing isostructural solid solutions of both species to occur. The match was confirmed by the identification of several visible peaks, separate from significant peaks of any previously known or suspected phases, with positions: - 31.6° , 32.8° , 25.9° , 24.9° and 23.6° two theta. The pattern, in figures 4.36 to 4.38, attempts a combined Le Bail-Rietveld fit, despite the presence of some obvious preferred orientation, as before. The Le-Bail fit was for the phases identified in section 4.2.2.3, excluding F-apatite which appears to be very minor and cristobalite which does not appear at all - with no peak at 22° . The Rietveld fit attempted to prove the existence of this new phase based on a modified barite *.cif* file (which seemed reasonable); the formula BaPO_3F was devised for this new phase and a scale factor was determined from the height of the 25.9° peak. The quality of this fit was comparable with the previous (figures 4.36 to 4.38) with no significant misfit due to the simulated BFP (barium fluorophosphates phase); proving that the structure had been correctly derived in this case. Subsequent SEM/EDS work on the same specimen, in appendices 2.1 to 2.3, shows evidence of phase separation of the phosphate rich phases and high concentrations of Ba, Mg, P and F around single crystals of fluorapatite.

The first discovery of the existence of isostructural barite (BaSO_4) and BaPO_3F was by Rentsson (1941) (Walford). A study, by Prison *et al.* (2008), on barium-magnesium phosphate glasses with composition $x\text{MgO} \cdot (1-x)(60\text{P}_2\text{O}_5 \cdot 40\text{BaO})$ mol % has shown that increasing MgO content (x), up to $x = 30$ mol %, improves thermal stability against crystallisation such that T_c , the crystallisation temperature, increases. XRD analysis of a number of compositions, heat-treated at T_c for 10 hours, identified both Ba-phosphate ($\text{Ba}(\text{PO}_3)_2$) and Mg-phosphate ($\text{Mg}(\text{PO}_3)_2$) including a number of mixed phases in compositions with $x > 30$. It is conceivable,

therefore, that the high fluorine content of LDIG 24 glass-ceramics leads to fluorinated analogues of these phases - the barium fluorophosphates (BaPO_3F), identified here, and possibly wagnerite ($\text{Mg}_2\text{PO}_4\text{F}$), in appendix 1.15, although there is no evidence of the latter in the powder patterns. It is expected that in situations of high calcium content, fluorapatite is preferred due to the high tendency of CaO to react with P_2O_5 (Xiang *et al.*, 2007). The apparent formation of the BaPO_3F phase at the expense of fluorapatite (in contrast to section 4.2.2.3) may be a result of the higher temperature heat treatment employed in this case.

In summary, FAP/BFP phase formation occurs by the initial phase separation of a phosphate rich droplet phase and resultant nucleation and growth at > 1050 °C, evident in appendix 2.1. Apart from the discrepancy of FAP/BFP, all of the other phases previously identified in the standard bulk (section 4.2.2.3) were found and, therefore, phase separation/nucleation and crystal growth processes must be essentially the same.

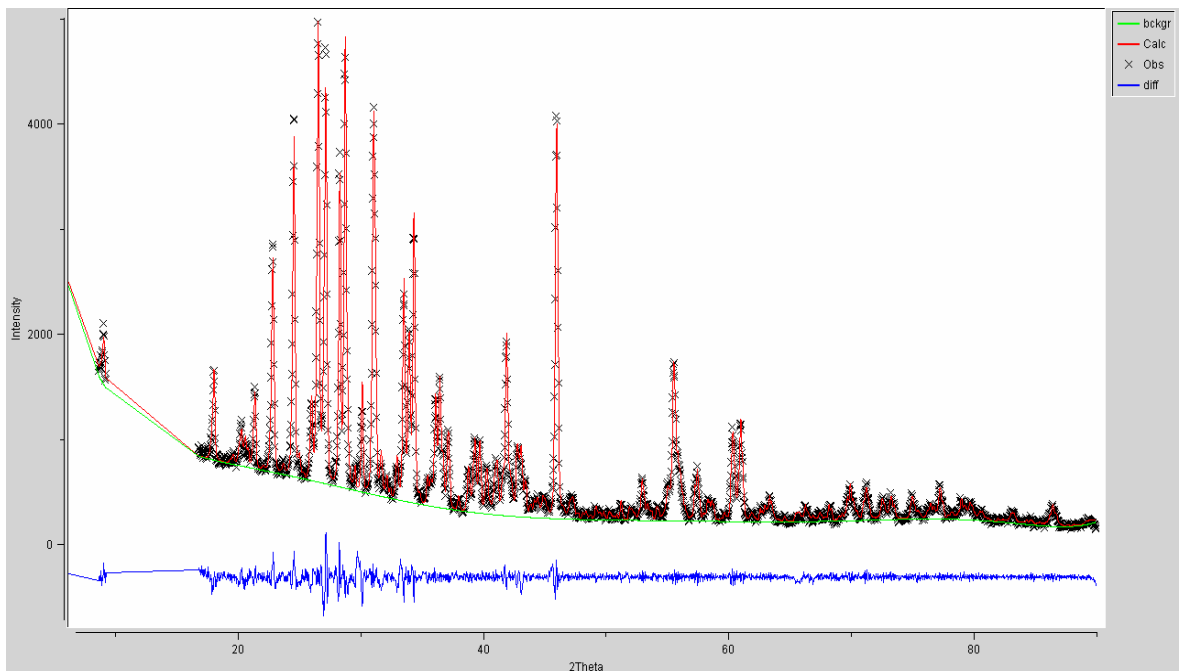


Figure 4.36. Combined Rietveld/Le Bail fit of the powdered bulk single crystal sample.

As before, the green line is the background, the blue is the fit quality and the red line is I_{calc} . Heat treatment is as described in section 3.15.

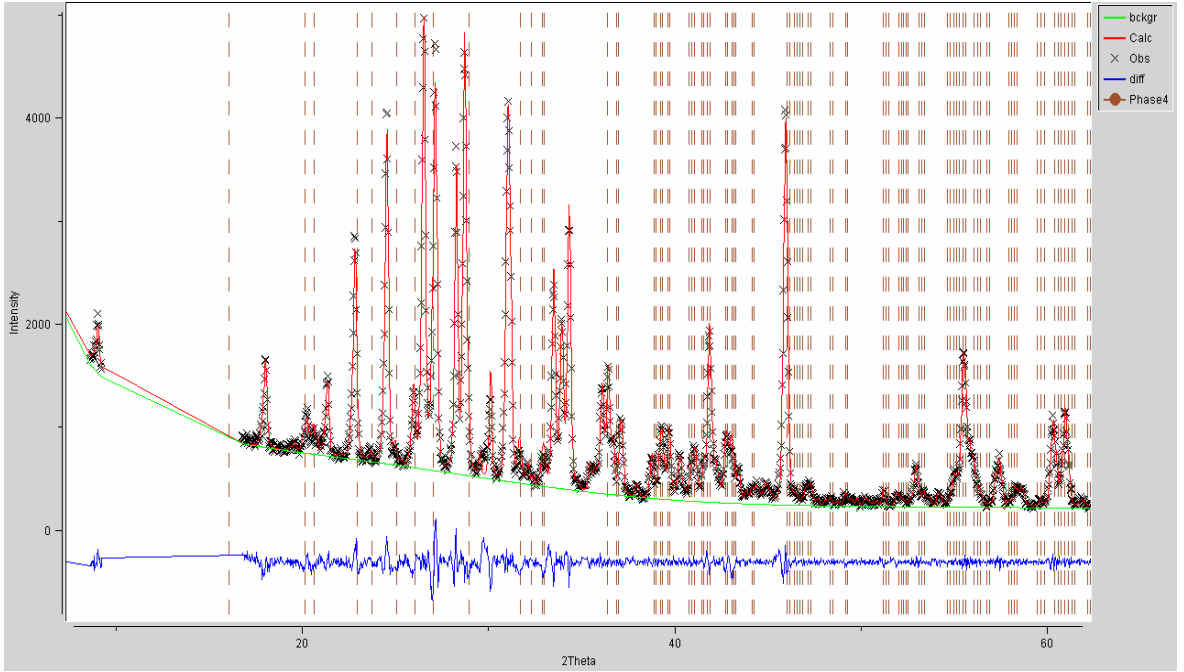


Figure 4.37. Fit with the barium fluorophosphates phase (BFP) marked in brown.

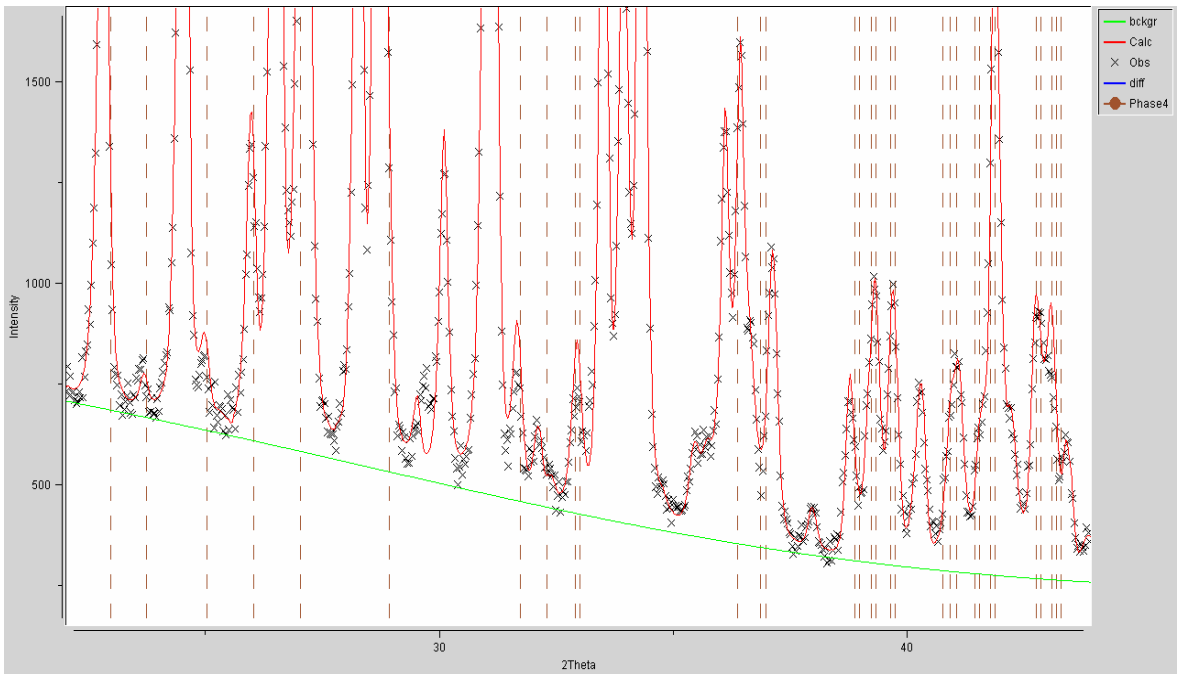


Figure 4.38. Close up of fit with BFP phase marked in brown.

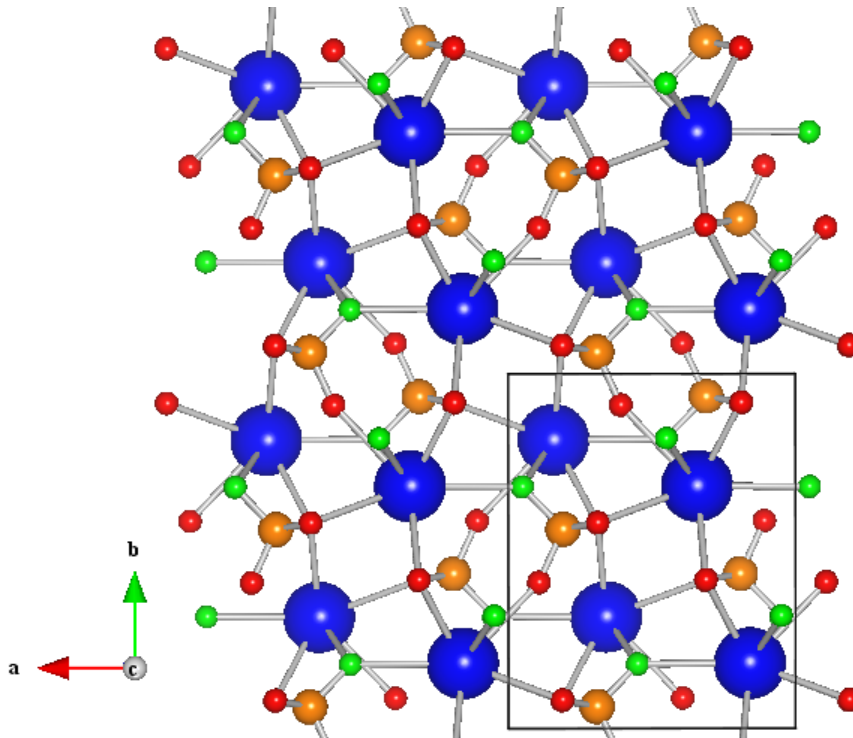


Figure 4.39. Visualisation of the BFP .cif (Crystallographic Information File) created to fit the pattern.

The lattice parameters of the orthorhombic unit cell, shown by the outline, are: - $a = 7.15 \text{ \AA}$, $b = 8.87 \text{ \AA}$, $c = 5.44 \text{ \AA}$ with a space group of Pbnm (appendix 5.1). Barium is blue, phosphorus is orange, oxygen is red and fluorine is green.

4.2.2.5 Full Rietveld Refinement of Powdered Single Crystal Bulk Sample

As previously mentioned, difficulties in subtracting the background from glass-ceramic samples have meant that full pattern Rietveld analysis has not been possible. Rietveld refinement is often the only way to properly characterise materials and quantify each phase. The success of the single crystal experiment allowed identification of several main phases; however, phase quantification was still not possible due to problems with preferred orientation. A number of techniques were devised (chapter 3) to help solve these problems and permit full pattern refinement of a glass-ceramic material. Investigations have noted that dissolution of powdered glass-ceramic in HCl leads to a significant mass loss ($\sim 50 \text{ wt \%}$) which was inferred to be a direct result of dissolution of the residual glass phase. Corrosion, in the case of acid (proton exchange) dissolution of amorphous silicates, arises from three main mechanisms: - hydration, hydrolysis of ionic-covalent network and exchange between alkali or alkali-earth ions and protons in solution. Leaching of soluble cations from the glass surface leads to the formation of a hydrated silica gel which

gradually thickens and may act to slow dissolution depending on the experimental conditions (Cailleteau *et al.*, 2008).

The first stage was to use 4M hydrochloric acid (HCl) to dissolve the amorphous background of a pre-powdered sample; it was known that only one of the minor phases, the phosphates, would dissolve as mica and clinoenstatite are insoluble (Speight, 2005). The second stage consisted of a spray drying technique that was employed to ensure that powdered samples were randomly orientated, this is a condition which appears difficult to obtain for these materials; however, Rietveld refinements will fail in cases where very strong crystallite orientation exists. As previously shown (4.2.2.4), phase formation in the single crystal sample is mostly identical to that found in bulk samples cerammed by standard heat treatment with the advantage that peak resolution appears higher than in the standard samples – possibly due to reduced disorder in the crystalline phase. The average hold temperature for the single crystal experiment was 1230 °C whereas the maximum crystallisation hold currently employed for this material is 1150 °C; it is expected, therefore, that quantitative phase analysis will be representative of a bulk sample heat treated in the standard way.

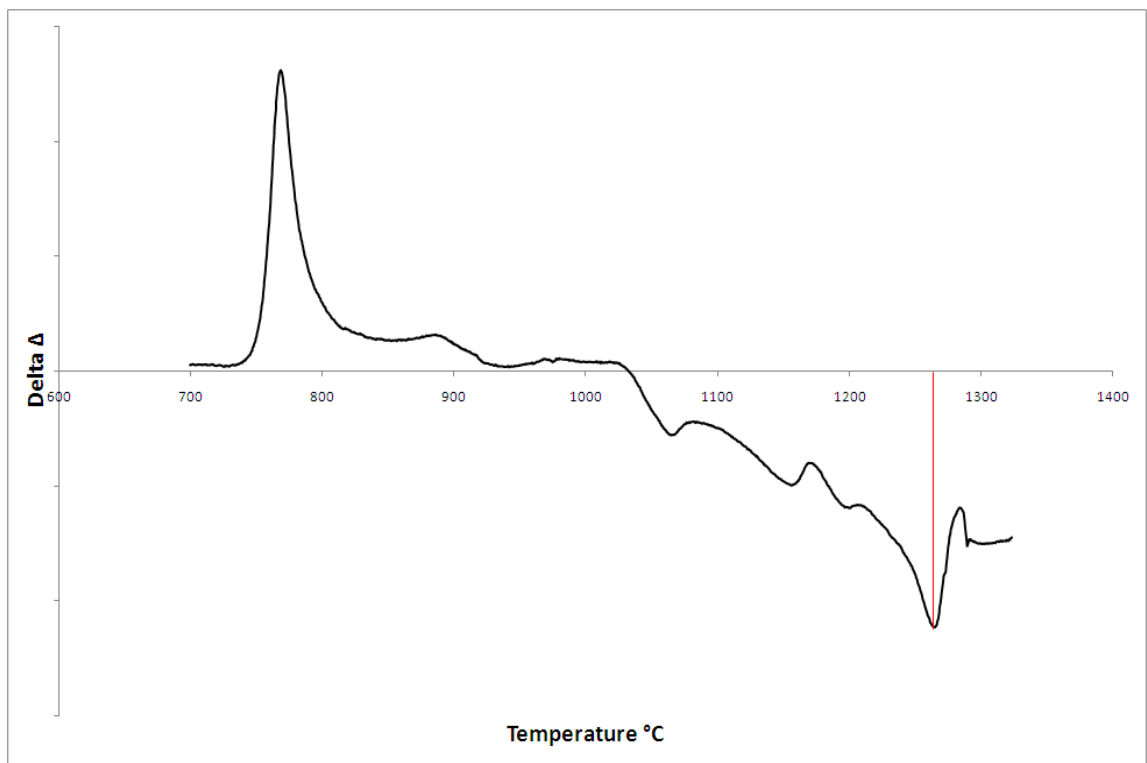


Figure 4.40. DTA trace of LDIG 24 commercial frit showing melting endotherm (red line).

The DTA trace in figure 4.40 shows a distinct melting endotherm for LDIG 24 commercial at 1260 °C which represents the point at which all crystalline phases redissolve into the residual glass; crystallites, therefore, can only precipitate at temperatures below 1260 °C. This has been confirmed experimentally by quenching nickel foil parcels containing glass frit from temperatures ranging between 1200 °C and 1280 °C. Note that the endotherm is relatively sharp in this case indicating that the dissolution of a crystal phase, with a well defined melting point, may be responsible.

Figures 4.42 to 4.47 are the result of a full Rietveld refinement of powdered glass-ceramic material from the single crystal growth experiment after acid treatment and spray drying. The mica phase has been refined with the aid of EDS, performed on two single crystals extracted from the bulk (figure 4.41). Several previously unseen peaks have appeared as a result of a significant reduction in preferred orientation allowing the identification of three further phases and quantification by weight and volume of each main phase with respect to the mica phase. The quality of the fit (blue line) is given by a χ^2 parameter of 5.43, which is acceptable in this case. The large gap in the patterns shown is a result of the exclusion of an amorphous hump, apparently from the sample holder, which was difficult to fit with the background function and did not contain any peaks.

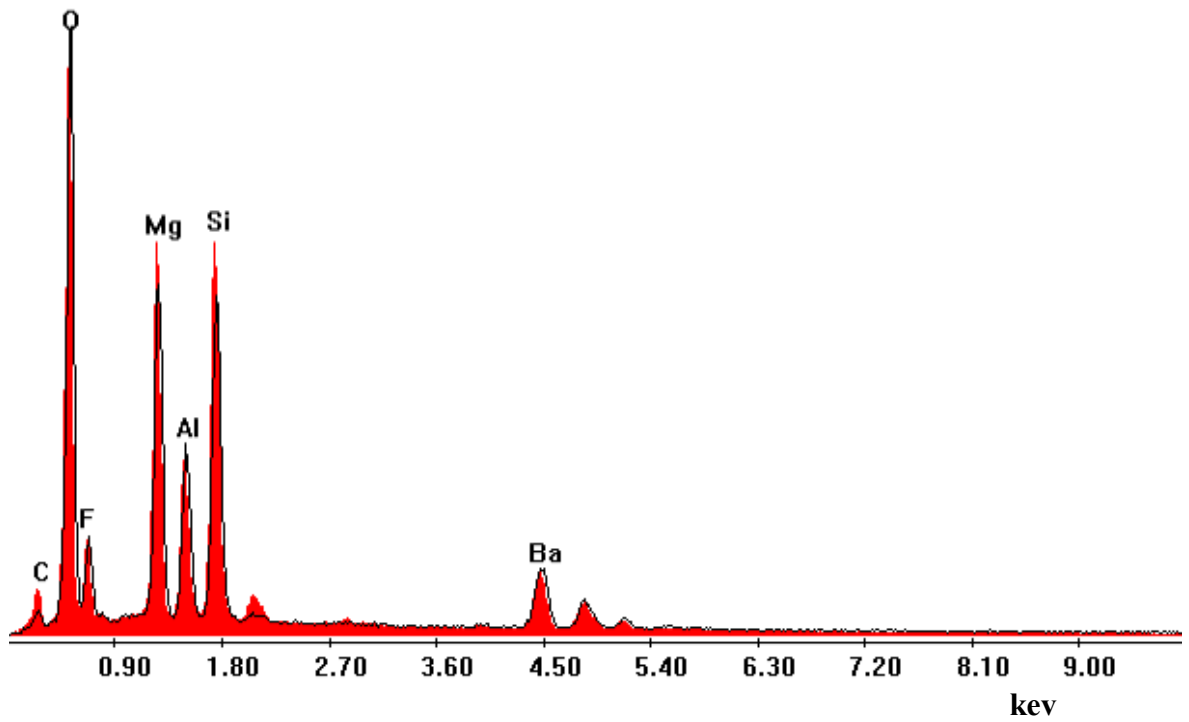


Figure 4.41. Overlapping EDS spectra of two single crystals (platelets) of mica taken from the bulk specimen of section 4.2.2.4 (the black line is from the other crystal)

Note the good agreement between the compositions of both samples. This is clearly not the composition of a tri-silicic mica with the Al:Si ratio closer to 1:2 rather than 1:3; which confirms that the mica phase is a depleted kinoshitalite with a Ba occupancy of $\sim 2/3$ in the bulk.

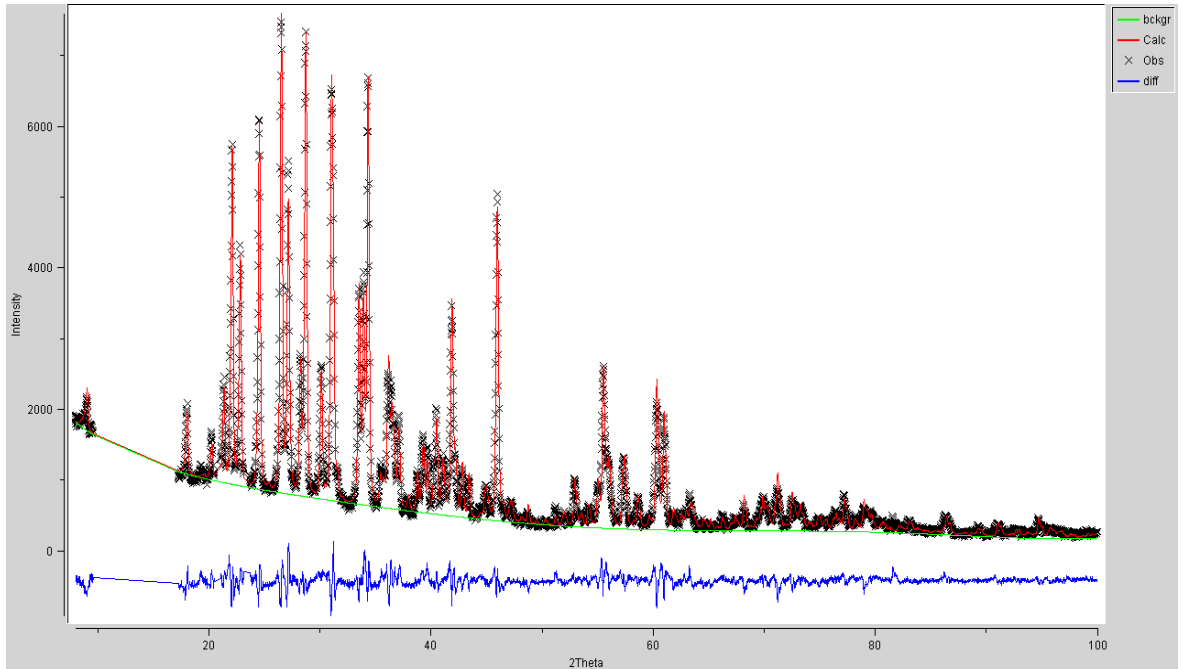


Figure 4.42. Full pattern Rietveld refinement of LDIG 24 commercial glass-ceramic taken from the single crystal growth experiment.

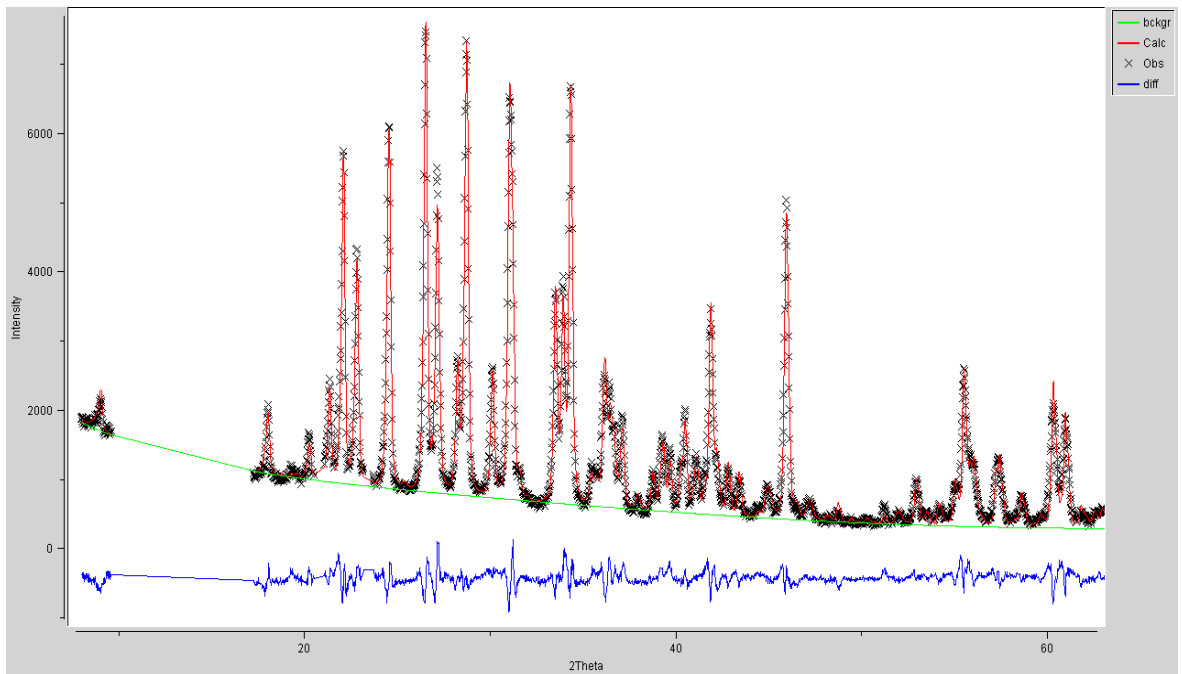


Figure 4.43. Rietveld refinement of the same pattern showing reduced 2 theta range.

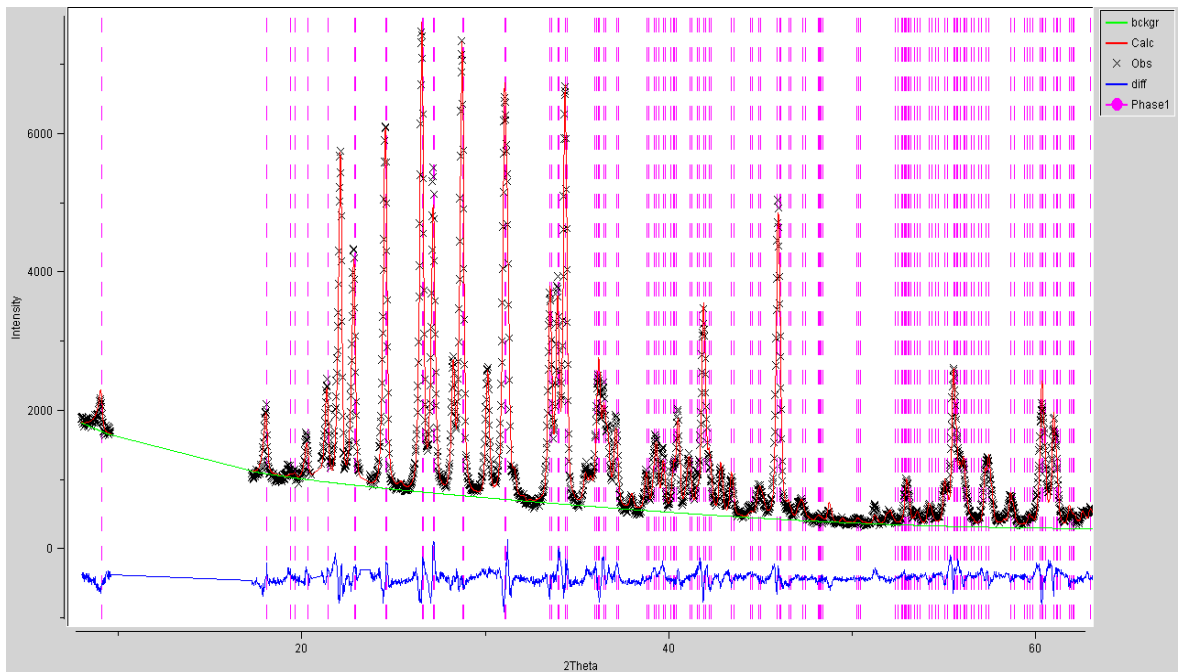


Figure 4.44. Rietveld refinement with refined depleted F-kinoshitalite phase marked in pink.

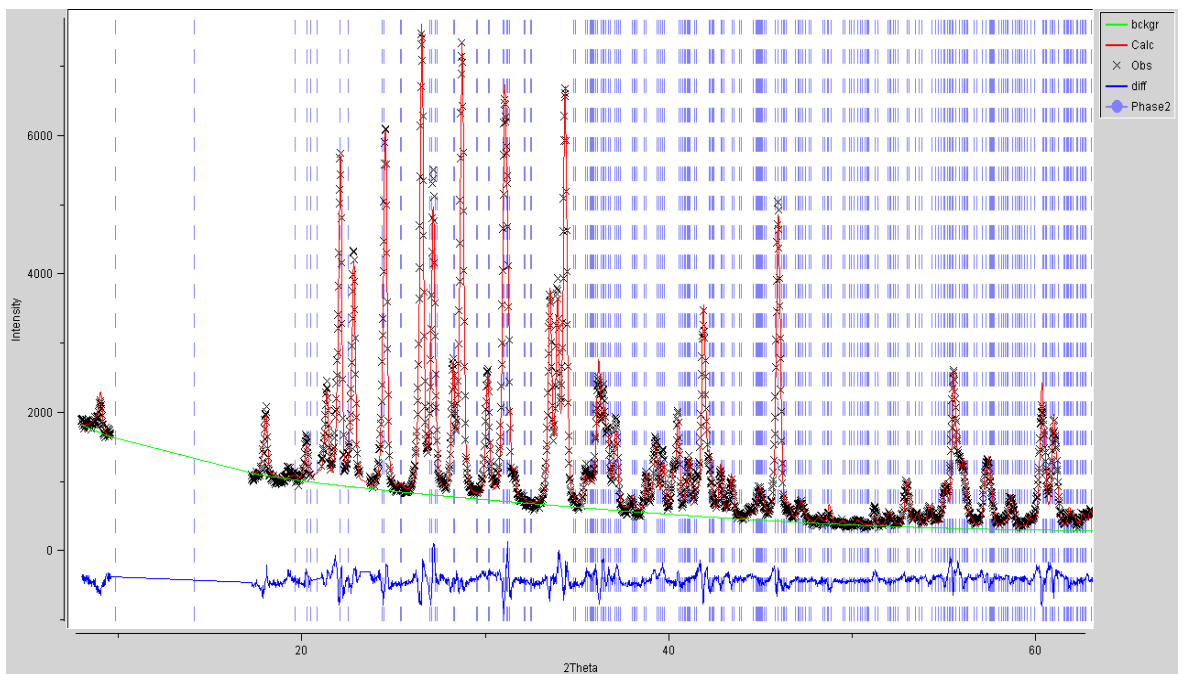


Figure 4.45. Rietveld refinement with clinostatite phase marked in blue.

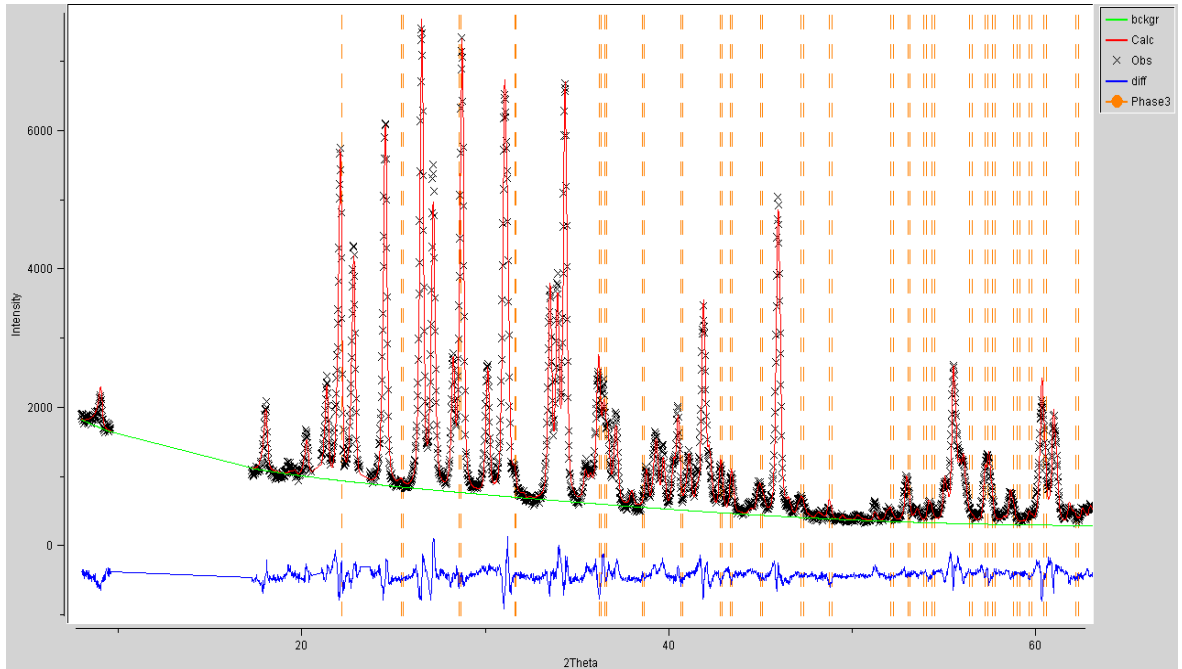


Figure 4.46. Rietveld refinement with cristobalite phase marked in yellow.

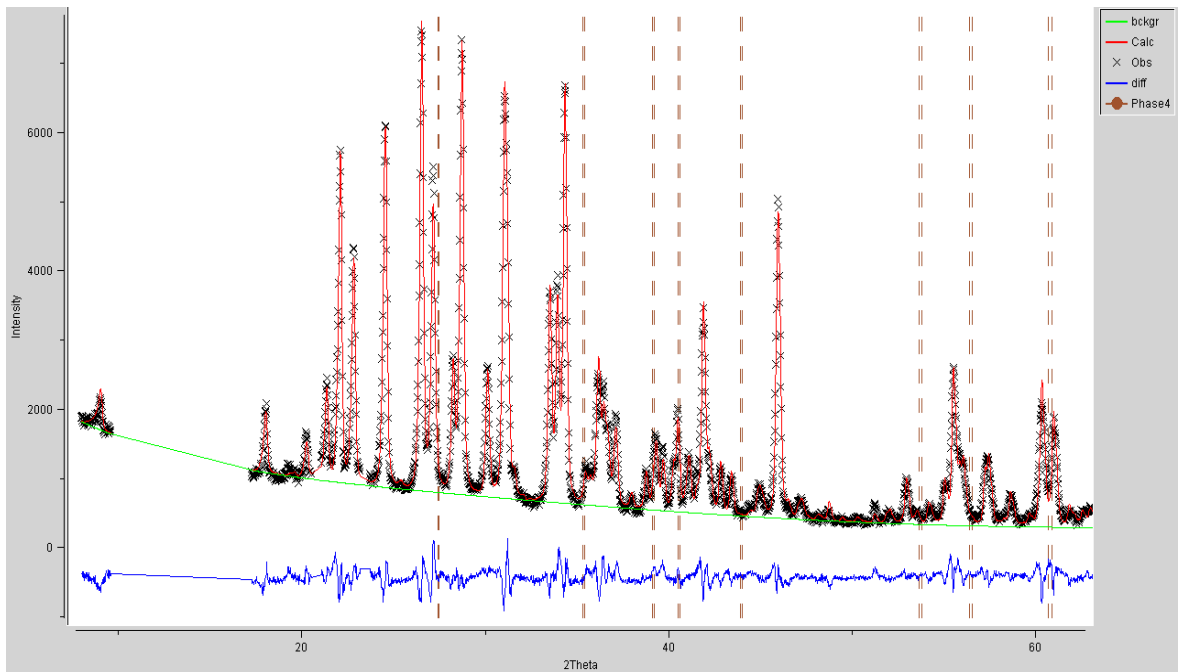


Figure 4.47. Rietveld refinement with sellaite phase marked in brown.

	a(Å)	b(Å)	c(Å)	α(°)	β(°)	γ(°)
Mica	5.316	9.217	10.044	90	100.22	90
	±0.000221	±0.000336	±0.000209		±0.0028	
Clinoenstatite	9.602	8.817	5.173	90	108.29	90
	±0.000793	±0.000718	±0.000435		±0.0084	
Cristobalite	4.977	4.974	6.92	90	90	90
	±0.000648	±0.000648	±0.001627			
Sellaite	4.621	4.621	3.055	90	90	90
	±0.003550	±0.003550	±0.002086			

Table 4.14. Lattice parameters used in the refinement with absolute errors listed underneath.

	Weight fraction (%)	Volume fraction (%)	Scale fraction
Mica	70.2	67.7	2.95
Clinoenstatite	21.3	21.0	1.07
Cristobalite	8.06	10.9	1.35
Sellaite	0.45	0.45	0.14

Table 4.15. Showing the calculated weight fraction and volume fraction for each phase in the sample, after acid treatment, with the associated scale fractions produced by *GSAS*.

The densities of each phase, required for the vol % calculation, were calculated by *GSAS*; the average density of LDIG 24 commercial glass-frit is 3g/cm³

4.2.2.5.1 Phase Identification and Discussion

A multi-phase simulation of the phases, in table 4.14, with the pattern, in figures 4.42 to 4.47, is shown in appendix 1.5. The composition of the bulk mica phase, in figure 4.21, clearly shows a slight discrepancy with that determined for the single crystal (table 4.07) with average Si:Al ratios of ~ 2, and ~ 1.6 for the bulk mica phase and single crystal respectively. This is consistent with the significant discrepancy between the lattice parameters in tables 4.10 and 4.14. Rietveld refinement of the bulk mica phase focussed on refinement of the occupancies and UISO parameters of the single crystal structure (table 4.09) in order to best fit the powder data; this produced a barium interlayer occupancy of 0.70 (2.s.f) which is lower than that of the single crystal (0.76). The refined bulk mica structure is

presented in appendix 5.2; the derived chemical formula is: $\text{Ba}_{0.70}\text{Mg}_3(\text{Al}_{1.4}\text{Si}_{2.6})\text{O}_{10}\text{F}_2$.

Referring to table 4.15 and figures 4.42 to 4.47, cristobalite (SiO_2) with characteristic peaks at 22.0° and 31.16° and sellaite (MgF_2), in appendix 1.14, with a primary peak at 40.5° have been identified and fitted; confirming the presence of cristobalite which is evidently difficult to detect in samples with strong preferred orientation (section 4.2.2.4). Protoenstatite has apparently disappeared with no visible (221) or (331) peaks at $\sim 32.83^\circ$ and $\sim 35.15^\circ$ two theta respectively; however, alterations to the sample preparation such as wet grinding in acetone and time taken to ensure the finest particle sizes are probably responsible for this change (Goeuriot *et al.*, 1998). The diffraction pattern also indicates the formation of small quantities of tridymite (SiO_2), with a peak at $\sim 23.33^\circ$, which is a lower temperature polymorph of cristobalite. Mica, clinoenstatite, cristobalite are insoluble in HCl under normal conditions, although sellaite is known to be slightly soluble (Speight, 2005). Lorentzian coefficients of 8.69, 9.20 and 5.00 were extracted for the main phases of Ba-mica, clinoenstatite and cristobalite respectively, corresponding to crystallite dimensions of $0.187 \mu\text{m}$, $0.177 \mu\text{m}$ and $0.168 \mu\text{m}$ after substitution into the Scherrer equation. Cristobalite is assumed to be spherulitic, with $K = 0.91$ (Roberts *et al.*, 1985), whereas both mica and clinoenstatite have been proven to be plate-like, in this case, with $K = 1.84$ (appendix 2.5).

The Rietveld fit was achieved by application of the *GSAS* spherical harmonic function for the Ba-mica phase and the March-Dollase function (defined in section 3.17.5) for the secondary phases. This is very tricky as one can easily bias the phase scale fractions; the spherical harmonic function produces a texture index parameter > 1 , where unity means perfect random orientation, which was minimised to 1.89 in order to ensure that the pattern was not over fitted. Subsequent refinement of the thermal parameters (UISO) gave reasonable results, indicating that the mica phase fit was good. Few parameters were needed to fit the secondary phases and were refined relatively quickly. The final values of the phase scale fractions, listed in table 4.15, are close to those initially estimated directly from the pattern - using peaks that appeared to have changed least when compared to the powder pattern of this material prior to acid treatment and spray drying, in figures 4.36 to 4.38. Weight fractions of each phase, based on the phase fractions, were determined by *GSAS* and

outputted in the relevant *.list* file. Attempts to eliminate preferred orientation by experimental means, therefore, have not been entirely successful, although significant improvement is noted. The acid treatment, however, has worked as expected with no visible trace of BaPO_3F , or any other phosphate phase, in the pattern and significant improvement of the peak height and signal to noise ratio. By reference to table 4.15 and the fact that 50 % of the original mass of the sample was dissolved in HCl, the weight fraction of the refined mica phase in the original sample is: $\sim 35.1\%$ (32.4% by volume) and the total crystalline volume fraction, prior to acid treatment, is: $> 50\%$. These volume fractions of the original sample are approximate as they omit the phosphate phases which account for a couple of percent, however, they are much lower than expected by stoichiometry and may result from competition between phases although fluorine loss during the glass making process is also probable.

One can prove that the phase analysis in table 4.15 is, at least reasonably, correct by using the density and weight fraction of each phase to calculate the total volume of crystalline phases in an arbitrary mass of the original sample. The total mass of the pre-treated sample is approximately twice that of the crystalline phases and, if one assumes that the volume of this sample is invariant before and after heat treatment, it is possible to determine that the average density of the crystalline phases is: $- 3.16 \text{ g/cm}^3$ and that the average density of the amorphous phase (plus phosphate phases) is: $- 2.85 \text{ g/cm}^3$ (3.s.f). Logically, one assumes that the density of the residual glass is at most no greater than that of the base glass (3 g/cm^3).

MAS-NMR studies on as cast LDIG 24 commercial base glass, by Hill *et al.* (2009), have shown that large quantities of F-Mg(n) bonding, at about 170 ppm - close to $n = 2$, and smaller quantities of F-Ca(n), at about 100 ppm, are present; which could support initial sellaite crystallisation at higher temperatures, although further work would be required to confirm this. As a glass-ceramic, heat treated @ 1150 °C for 3 hours, very small quantities of either Al-F-Ca(n) or Al-F-Mg(n) were detected alongside a much larger peak corresponding to F-Mg₃ which is characteristic of mica; however, sellaite (MgF_2) was not apparent. One does not expect to find this Ca or Mg aluminium fluoride phase in the pattern, in figures 4.42 to 4.47, as both aluminium and aluminium fluoride are soluble in HCl, although, the presence of both phases may also support a type of MgF_2 precursor phase formation which has

not been found for barium mica glass-ceramics (Henry *et al.*, 2003). The volume fraction of sellaite (table 4.15) is very small and yet this phase is known to form as a mica precursor in K-phlogopite and lithium mica glass-ceramics, Beall (1972), Denry *et al.* (2001). Sellaite formation involves separation from the droplet phase, whereas chondrodite ($\text{Mg}_4(\text{SiO}_4)\cdot\text{MgF}_2$), another mica pre-cursor, separates at the interface between the droplet phase and the matrix phase (Taruta *et al.*, 2001). The low weight/volume fraction of sellaite in table 4.14 would not be unexpected (Beall, 1972) as mica formation would consume as much as possible.

It is notable that the major melting endotherm on the DTA trace at 1260 °C, shown in figure 4.40, corresponds to the melting point of sellaite (1255 °C) which is the lowest of all phases currently identified, appendix 1.17; indicating that a small but significant volume fraction of sellaite exists in bulk samples, heat treated above T_c , which may trigger the dissolution of crystalline phases observed. Work by Saraswati *et al.* (1990), on mica formation in $\text{K}_2\text{O-SiO}_2\text{-MgO-MgF}_2$ glasses has identified endotherms in DTA traces at 1180 °C and 1250 °C corresponding to the melting of tetrasilicic mica and sellaite respectively. The epitaxial growth of mica crystals seen in this study is also likely when MgF_2 nuclei are present. These conclusions are supported by observations made during the single crystal growth experiment (section 4.2.1); logically, the phase separation of secondary phases must be inhibited just below the liquidus (< 1260 °C) in order to allow sufficient space for large single crystals of mica ($\sim 5 \text{ mm}^2$) to precipitate, in a region known as the metastable zone of supercooling. Crystals in this region can grow if the melt is seeded but generally no nuclei can be formed as the critical radius for a stable nucleus is very large (Shelby, 2005). Indeed, Wang *et al.* (2009) has shown that bulk crystallisation does not occur in a K-mica glass without nucleating agents when reheated at 1100 °C for 2 hours; however, MgF_2 has been used as an additive to nucleate glass-melts in a similar way to ZrO_2 (El-Shennawi *et al.*, 2006). Since MgF_2 is a major component of the LDIG 24 feedstock (13 mol %), it is reasonable to assume that sellaite crystallises just below the liquidus as a mica pre-cursor, in this case. It is theorised, therefore, that mica formation, may rely on the initial precipitation of sellaite irrespective of whether crystallisation occurs as a result of cooling from the melt or a standard two-step heat treatment.

The presence of cristobalite can be attributed to high silica content of the parent glass (Bush, 1976). The discovery of a small quantity of tridymite, in figures 4.43 to 4.48, indicates that a number of phase transitions are likely to occur. Quartz (SiO_2) is a common precursor of cristobalite with a melting point of 1710°C , when heated from room temperature alpha-quartz will transform to beta-quartz at 573°C accompanied by a volume change of 2 %; a second change subsequently occurs at 873°C when beta-quartz converts to tridymite with a final transformation between tridymite and cristobalite at 1470°C . There is clearly a significant discrepancy between the phase transformation to cristobalite and the maximum formation temperature possible in LDIG 24 commercial glass-ceramics.

A study by Arahori *et al.* (1987) has investigated the likely mechanism by which this occurs. It was theorised that the transformation was caused by impurities which lowered the tridymite-cristobalite transformation temperature. After investigating the effects of a number of impurity additions on silica refractories, it was found that only samples containing alumina (Al_2O_3) transformed to cristobalite at reduced temperatures. The SiO_2 - Al_2O_3 phase diagram, by Muan and Osborn, clearly shows a marked reduction in the transformation temperature for compositions with Al_2O_3 greater than 4 wt %; increasing alumina additions over this have little effect and the transformation remains constant at approximately 1200°C . The calculated activation energy for cristobalite formation below 1470°C was 176 kJmol^{-1} , which was significantly lower than that found for pure silica. The phase transformation mechanism, applicable in this case, for tridymite to cristobalite at low temperatures is by penetration of Al_2O_3 around the crystal which is likely to contain Ca^{+2} , due to instability of pure tridymite. A liquid phase is then produced which becomes an amorphous $\text{CaO-Al}_2\text{O}_3\text{-SiO}_2$ phase with a eutectic at approximately 1170°C and saturated SiO_2 precipitating as pure cristobalite. The weight fraction of alumina in the sample is approximately 10 % which supports the theory of how this unusual transformation has occurred. Cristobalite and its polymorphs are hard phases that reduce machinability in glass-ceramics and increase tool wear, therefore, a significant volume fraction of cristobalite is a problem in materials intended for CAD/CAM. It is also conceivable that cristobalite formation, at the expense of silica content in the residual glass, may reduce the acid resistance of glass-ceramics which would cause problems in oral applications.

A method of suppressing cristobalite formation in high silica lithium glass frits, by E.A.Bush (1976), may prove useful in this case. Cristobalite formation in a LAS (lithium aluminium silicate) system was effectively eliminated by the additions to either raw batch or frit of a cristobalite suppressant selected from NaO_2 , K_2O , Cs_2O , MgO , SrO , CaO , BaO , La_2O_3 , Nb_2O_5 , TiO_2 , Ta_2O_5 and PbO . Oxides with di-valent or tetra-valent cations were added at concentrations of up to 0.02 moles per 100 grams, whereas oxides with odd valence cations were permitted up to a maximum of 0.01 moles per 100 grams. These oxides were notable for being effective at suppressing cristobalite in refractory LAS glass-ceramics in relatively low concentrations. A relationship between the ionic radius of the suppressant oxide and the efficacy of cristobalite suppression was found, with larger cations proving most effective at lower temperatures ($< 1275\text{ }^\circ\text{C}$). Considering the above, it is clear that an effective suppressant for LDIG 24 commercial glass-ceramic is likely to be a large ionic radius oxide, effective at lower temperatures $< 1200\text{ }^\circ\text{C}$, which does not partake in any known phase formation. A suitable candidate would seem to be La_2O_3 ; lanthanum has a large ionic radius (195 pm) and is known to be a poor nucleator in glass-ceramics (Wang *et al.*, 2009) and, therefore, is likely to remain in the residual glass. Lanthanum also has the advantage of being large enough to disrupt and reduce the effect of Ostwald ripening such that La-doped glass-ceramics display much finer microstructures, which are important developing optical translucence for dental applications.

4.2.2.6 Spray Dried Sample of Bulk Cerammed by Standard Heat Treatment

Phase quantification by XRD remains a challenge throughout this work due to preferred orientation; however, the previous section has shown that spray drying and careful sample preparation can eliminate this to some extent. Spray drying of the untreated sample material in 4.2.2.3 has been carried out in order to accurately quantify previously identified phases in table 4.13; comparison of the total crystalline volume fraction is also made with a non-spray dried sample, heat treated at $925\text{ }^\circ\text{C}$ for 3 hours, in figure 4.49.

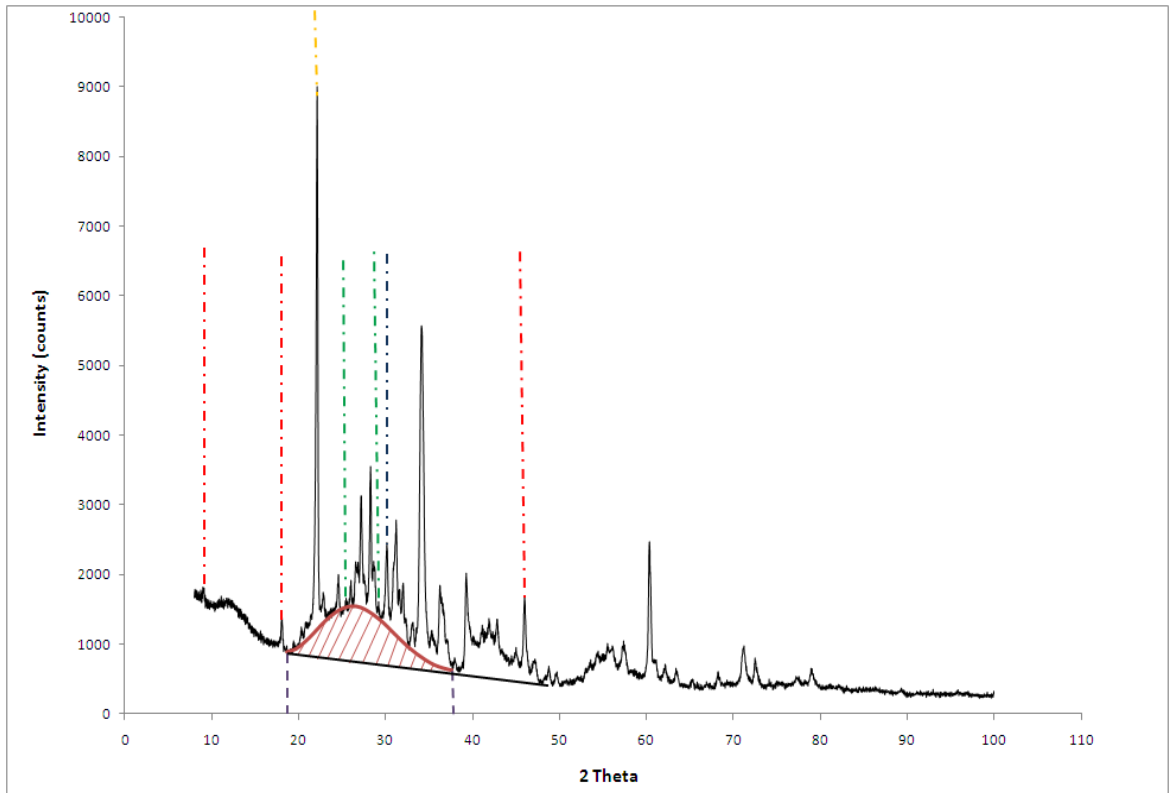


Figure 4.48. Spray dried sample heat treated @ 1150 °C for 3 hours.

The crystalline volume fraction of the sample has been calculated using the intensity ratio method. The dashed lines mark peaks used for phase quantitative analysis; red for Ba-mica, blue for clinoenstatite (MgSiO_3), orange for cristobalite (SiO_2) and green for fluorapatite ($\text{Ca}_5(\text{PO}_4)_3\text{F}$).

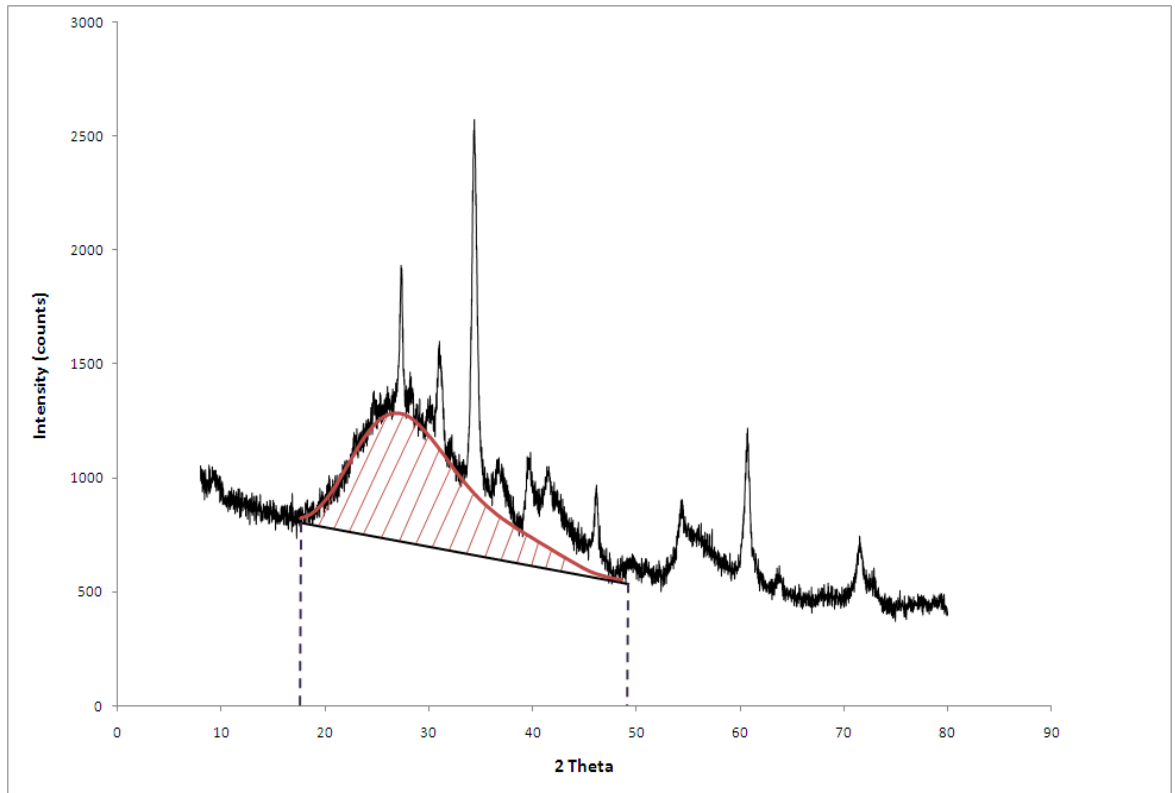


Figure 4.49. Sample heat treated @ 925 °C for 3 hours (not spray dried).

This pattern is from a non-powdered sample, thus, some stronger preferred orientation than in figure 4.48 may persist.

The crystalline volume fraction of both patterns in figures 4.48 and 4.49 has been estimated using a standardless technique outlined by Chung *et al.* (1999), an algorithm, written in *Pascal*, has been used for the calculations. An estimate of the instrument background has been constructed from a straight line under the only prominent amorphous band in the patterns. The volume fraction of residual glass phase was calculated by first integrating the pattern between the purple dashed lines and the fitted curve of the amorphous background using Simpson's rule (appendix 4.1); the area underneath the straight line background was then subtracted in each case. The ratio of the checked area in the figures to the total area under the pattern in the region of interest yielded the amorphous volume fraction of each sample; the crystalline volume fraction was calculated by simply subtracting this value from unity, which gave crystalline volume fractions of 62.7 % and 37.8 % (3.s.f) for figures 4.48 and 4.49 respectively. It is clear, therefore, that LDIG 24 commercial glass heat treated at 1150 °C precipitates a much larger volume fraction of crystalline phases compared with that heat treated at 925 °C.

Phase quantitative analysis of the pattern in figure 4.48 was performed in GSAS. The mica phase was assumed be identical to that refined in section 4.2.2.5. Preferred orientation still remains to some degree as before; however, this has been corrected for the mica phase by application of the March-Dollase function in fitting the 001, 002 and 005 peaks respectively, highlighted by the red dashed lines. Protoenstatite (MgSiO_3) has also been approximately quantified using peaks at 27.62° (222), 35.28° (311) and 32.98° (221) two theta. Full pattern Rietveld refinement, in this case, was not possible due to poorer resolution of the peaks than found in section 4.2.2.5 – which suggests some disorder in the structure of the crystalline phases as a consequence of precipitation in the solid state, well below the liquidus.

	Weight fraction (%)	Volume fraction (%)	Scale fraction
Mica	21.0	19.2	1.06
Clinoenstatite	16.8	15.7	1.00
Protoenstatite	~8.08	~7.83	~0.48
Cristobalite	13.0	16.7	2.58
Fluorapatite	4.37	3.2	0.16

Table 4.16. Showing the calculated weight fraction, volume fraction and scale fraction for each phase in the pattern of figure 4.48.

These values are based on the calculated crystalline volume fraction of 62.7% and an average LDIG 24 commercial glass density of 3g/cm³. Porosity in the unpowdered material has not been accounted for by these calculations which assume that: - crystalline volume + amorphous volume = total volume.

The mica volume fraction is clearly much lower than the value of 32 % determined in section 4.2.2.5 and the volume fraction of the cristobalite phase has approximately tripled. This suggests that cooling through the liquidus preferentially precipitates mica and further corroborates the theory that mica is nucleated by another phase as the phase separation of secondary phases appears relatively reduced in table 4.15 compared to table 4.16. It is also notable that the total crystalline volume fraction of the pattern, in figure 4.48, is similar to that of the bulk single crystal sample (> 50 vol %) which supports the applicability of the intensity ratio method for this work. The average density of the crystalline phases (2.98 g/cm³) in table 4.16 matches that determined for LDIG 24 commercial glass prior to heat treatment.

4.2.2.7 Summary

Surface nucleated material, in section 4.2.2.2, has been investigated for the first time and analysis has revealed that the phase composition is markedly different from the bulk with major phases of: - celsian (BaAl₂Si₂O₈), hexacelsian/orthocelsian and protoenstatite (MgSiO₃). This appears to result from the dissolution of the original mica phase at temperatures above 1100 °C after changes to the composition of the residual glass phase following the evolution of silicon tetra-fluoride (SiF₄) gas.

Lattice parameters of the depleted F-kinoshitalite mica phase for the bulk (sections 4.2.2.3 - 4.2.2.5) do not match those of the single crystal (section 4.2.1); a Rietveld

fit has allowed refinement of the atom occupancies of the original single crystal structure in order to best match the data in figures 4.42 to 4.47. This shows that the depleted interlayer site of the single crystal has a higher barium occupancy compared to that of the mica phase precipitated inside the sample. The chemical formula of the single crystal is: - $\text{Ba}_{0.76}\text{Mg}_3(\text{Al}_{1.53}\text{Si}_{2.47})\text{O}_{10}\text{F}_2$, whereas the formula derived from the powder data is: - $\text{Ba}_{0.7}\text{Mg}_3(\text{Al}_{1.4}\text{Si}_{2.6})\text{O}_{10}\text{F}_2$. A possible reason is that the single crystal was nucleated on the melt surface where there is likely to be a slightly different composition compared to that in the bulk; fully occupied kinoshitalite does not seem to appear due to the fact that compositional stoichiometry favours half occupancy of the barium cation. One would expect at least some compositional shift due to differing occupancies of barium, however, the lattice parameters, listed in table 4.14, show good accuracy and fitting of the profiles of individual peaks. It is theorised that an energetically favoured state, phyllosilicates in nature are rarely depleted, results in a Ba-occupancy close to 0.70 at the interlayer sites. The expanded unit cell of single crystal is probably the result of displacement away from this energetic minimum towards full occupancy. The refined Ba occupancy, in section 4.2.2.5, can be confirmed by reference to the **c**-axis lattice parameter which is significantly shorter than that found for the single crystal (table 4.10).

Full occupancy of the brucite layer, with **a** and **b** parameters remaining relatively close to those found in fully occupied kinoshitalite in table 4.14, means that only shortening along the [001] direction (**c**-axis) is found. One can use two different layer silicate structures from nature: - kinoshitalite ($\text{BaMg}_3[\text{Al}_2\text{Si}_2\text{O}_{10}](\text{OH})_2$) and triclinic talc ($\text{Mg}_3[\text{Si}_4\text{O}_{10}](\text{OH})_2$), to estimate the refined occupancy (Fleet, 2003), in this case. Both structures are fully occupied with the **c**-axis dimensions largely a result of the size or absence of the interlayer cation, the relative ratios of aluminium and silicon in the tetrahedral sites are unimportant as both possess the same atomic radius. The equation below was applied to this example.

$$Cp = ((1 - x).Ck) + (x.Cc)$$

Where:

- C_p = c-parameter of depleted kinoshitalite refined from powder data (10.04)
- C_k = c-parameter of normal kinoshitalite (10.25)
- C_c = c-parameter of normal talc (9.46)
- x = fractional occupancy of barium (solution)

Rearranging the above and solving for x gives a value of 0.73 (2.d.p) for the barium occupancy; this matches the value refined and, therefore, validates the assumptions made. As shown in tables 4.15 and 4.16, the single crystal bulk powder sample, in section 4.2.2.5, appears to have an overall higher weight fraction of mica, probably as a consequence of the higher temperatures of formation, yet the composition, based on the comparison of unit cell parameters, is the same. The apparent constancy of the Ba occupancy in the bulk, irrespective of whether the mica was precipitated by cooling from the melt (single crystal bulk sample) or whether the mica was nucleated at lower temperatures as part of the standard heat treatment (sections 4.2.2.3 and 4.2.2.6), seems to indicate that mica formation is reduced by the depletion of atomic species lost to secondary phases (table 4.16).

The pronounced amorphous background from LDIG 24 commercial glass-ceramic after a two step heat treatment, in contrast to samples cooled through the liquidus (section 4.2.2.5), is probably the result of a different residual glass phase composition as identified in section 4.2.2.6. A point of note is to compare the backgrounds of the surface and bulk nucleated samples in sections 4.2.2.2 and 4.2.2.3 respectively; the background in the surface case is relatively minor and exhibits no large amorphous ‘humps’ – which is also the case for the powder pattern of the single crystal sample prior to acid treatment, indicating that the absence of a large amorphous signal is the result of depletion of fluorine from the residual glass. This logic supports the conclusion that the mica volume fraction of the single crystal bulk sample, in table 4.15, is significantly higher than that of the standard sample in table 4.16. There is no significant difference between the crystallite sizes determined for the bulk single crystal sample, in section 4.2.2.5, and that of the standard sample, heat treated at 1150 °C, in section 4.2.2.6.

At least three stages of phase formation in the bulk have been identified by XRD alone; the first is the phase separation of nucleating precursor phases: - sellaite (MgF_2), identified from the pattern in figures 4.43 to 4.48 and, possibly, fluorite (CaF_2), although the latter has not been confirmed. The second step is the nucleation

of a depleted kinoshitalite mica, with Ba-occupancy close to 0.70, and the final stage is the formation of refractory phases cristobalite (SiO_2), tridymite, clinoenstatite (MgSiO_3), protoenstatite, fluorapatite ($\text{Ca}_5(\text{PO}_4)_3\text{F}$), and barium fluorophosphates (BaPO_3F); the latter has been found only in the single crystal bulk sample (section 4.2.2.4) and wagnerite ($\text{Mg}_2\text{PO}_4\text{F}$) is also a possibility although no direct evidence of this phase has been found. Given the complexity of this system, it is likely that other phases are present but in trace amounts, with little or no bearing on material properties. These main phases and relevant physical properties are listed in appendix 1.17. Clinoenstatite and related polytypes have been independently identified by SEM/EDS in appendices 2.5 – 2.6.

4.2.2.8 Relationships with Material Properties of LDIG 24 Commercial

One can begin to relate the mechanical properties and gloss measurements of LDIG 24 commercial glass-ceramics, in sections 4.1.6 and 4.1.7, to the phase compositions and volume fractions determined in section 4.2. It is notable that the hardness of these materials, table 4.08, reduces with increasing crystallisation hold temperatures despite the fact that a relatively significant volume fraction appears to be cristobalite (SiO_2), with a hardness of 6.5 Mohs compared with 5.5 and ~ 2.5 for enstatite and mica respectively (Deer *et al.*, 1992). This suggests a proportional relationship between the residual glass volume fraction and hardness of these materials with the low temperature sample, in figure 4.49, apparently ~ 1.6 times as hard with ~ 1.6 times the amorphous volume fraction of that heat-treated @ 1150 °C, in figure 4.48.

The hardness of a glass-ceramic composite can also be related to the shear moduli (GPa), resistance to shear strains, of the matrix (G_m) and crystalline phases (G_c), such that the hardness increases with increasing crystalline volume fraction when $G_c > G_m$, assuming an initially high amorphous volume fraction (Miyata *et al.*, 1982). Generally, the average shear modulus of the crystalline phases exceeds that of the depleted matrix making glass-ceramics harder (McMillan, 1979), which indicates that the glass structure is unusual in this case. SEM/optical micrographs, in section 4.1.7 and appendix 2.7, show voids in the residual glass apparently, as a direct result of crystalline phase formation. A study of the effect of microporosity on SiC ceramics by Slutsker *et al.* (2008), determined a near linear inverse relationship between hardness and increasing porosity; which explains the observed behaviour in

figure 4.08. One can, therefore, theorise that this void structure is responsible for the proportional relationship between the hardness and amorphous volume fraction of LDIG 24 commercial glass-ceramics. Increasing porosity in the residual glass appears to correlate with the loss of the amorphous volume fraction at temperatures over 950 °C. One could theorise that porosity in these glass-ceramics is caused by phase transformations such as proto to clino–enstatite which is a volume contraction (Goeuriot *et al.*, 1998); however this needs to be established by future work.

Gloss measurements, in section 4.1.8, also appear to be related to the amorphous volume fraction in the sample with gloss proportional to this and inversely proportional to the temperature hold – the fact, however, that amorphous volume fractions remain high, even with high crystallisation hold temperatures when opacity is greatly increased, indicates that porosity and crystallite coarsening also have a role.

The strength, as measured by biaxial-flexure, in section 4.1.6, and the machinability, which has not been directly measured in this study but is approximately inversely proportional to hardness (Boccaccini, 1997), of LDIG 24 commercial glass-ceramics appear to depend more on the microstructure and crystalline volume fraction than the hardness alone in agreement with previous studies (Hing *et al.*, 1973). The structure, therefore, of the residual glass phase, not just the crystalline phase composition, seems key to understanding many of the physical properties desired for CAD/CAM dental restorative materials.

4.3 Neutron Diffraction

This chapter presents analysis and data from two different neutron experiments on D20 at ILL, France, in 2002 and 2007 respectively. The former was performed by Dr. Phillip Bentley as part of his post-doctoral research on LDIG 24 glass-ceramics whereas the most recent experiment is my own work. The results concern kinetic diffraction studies of both commercial and original LDIG 24 glasses during the heat treatment process up to a crystallisation hold temperature of 1225 °C. The neutron wavelength in both experiments was 2.4189 Å.

4.3.1 Experimental Problems

There is a single issue with both experiments discussed that, although unknown at the time, may make a direct comparison between LDIG 24 glass-ceramics produced by the original practices, featured in the vacuum experiment, and those of the newer type less than ideal. The authors' samples were housed in a lightly shielded mirror furnace (section 3.20.1) with an alumina sample stick containing platinum-rhodium thermocouples placed directly in the beam. In the earlier experiment, sample rods, 14 mm in diameter, were contained in niobium foil cans and held inside an aluminium ILL vacuum pool furnace equipped with a cylindrical niobium heating element. Patterns, in figures 4.50 to 4.53, from both experiments seem to show unidentifiable peaks in their 'backgrounds'

A pattern from the vacuum experiment of a sample prior to heat treatment at room temperature, figure 4.52, identifies unmatched peaks at 60.55°, 65.6°, 76.9°, 110° and 125° two theta, where one would only expect to see niobium and aluminium, again indicating that there are possibly several unknown phases that are either part of the sample environment or inside the sample. Peaks at 65.6°, 76.9° and 125° two theta appear to correspond a cubic (Fm3m) lattice with an **a** parameter equal to ~ 3.87 Å, this is between platinum and rhodium, 3.90 and 3.80 Å respectively, and significantly lower than cubic aluminium (~ 4.05 Å). One possibility is that an alloy of aluminium rather than pure aluminium is responsible, at least in the vacuum case, another is that platinum-rhodium thermocouples are in the beam; the latter being more likely as ILL do not identify any alloys of aluminium as beam contaminants. Early in the vacuum experiment, before the heat treatment could be started, the pool

furnace, to which the pattern in figure 4.51 relates, failed and needed replacement. Runs were resumed as before but one could see that the background had changed; figure 4.52 shows a background plus amorphous pattern taken at 500 °C, after failure. One can clearly see that the peak at 60.55° is now missing, allowing one to conclude that its source was in the broken furnace and that most if not all of the unidentified peaks come from the sample environment. Further work, however, would be required to prove categorically that there is no contribution from the sample prior to heat treatment.

A neutron diffraction pattern of the empty sample holder of the mirror furnace in air, at room temperature, is shown in figure 4.50, a significant unidentified peak appears at $\sim 108^\circ$ two theta which indicates that there is a contaminant phase in the beam apart from alpha alumina (corundum – Al_2O_3), R-3c space group, platinum, rhodium and aluminium, although the latter was not detected. Sample preparation in the case of the mirror furnace experiment was meticulous, and only those rods which were both optically clear and free from inclusions, normally insoluble material from the crucible, were judged fit. Figure 4.53 shows the presence of both corundum (Al_2O_3) and platinum (Pt) from the thermocouple but the *Searchmatch* routine has failed to identify any phases with a principal peak at 108° . The presence of unknown peaks in both data sets frustrates analysis and makes precise fitting using the Le Bail method in *GSAS* very difficult, if not impossible, as straight forward background subtraction can only work if one has a background pattern at the same temperature as the sample, which is rarely possible in a kinetic experiment, where patterns are taken every 3 minutes over a pre-defined heat treatment schedule. Future neutron experiments should seek to eliminate all non-sample contamination in the beam prior to data collection, in order to give the experimenter the best chance of a comprehensive analysis.

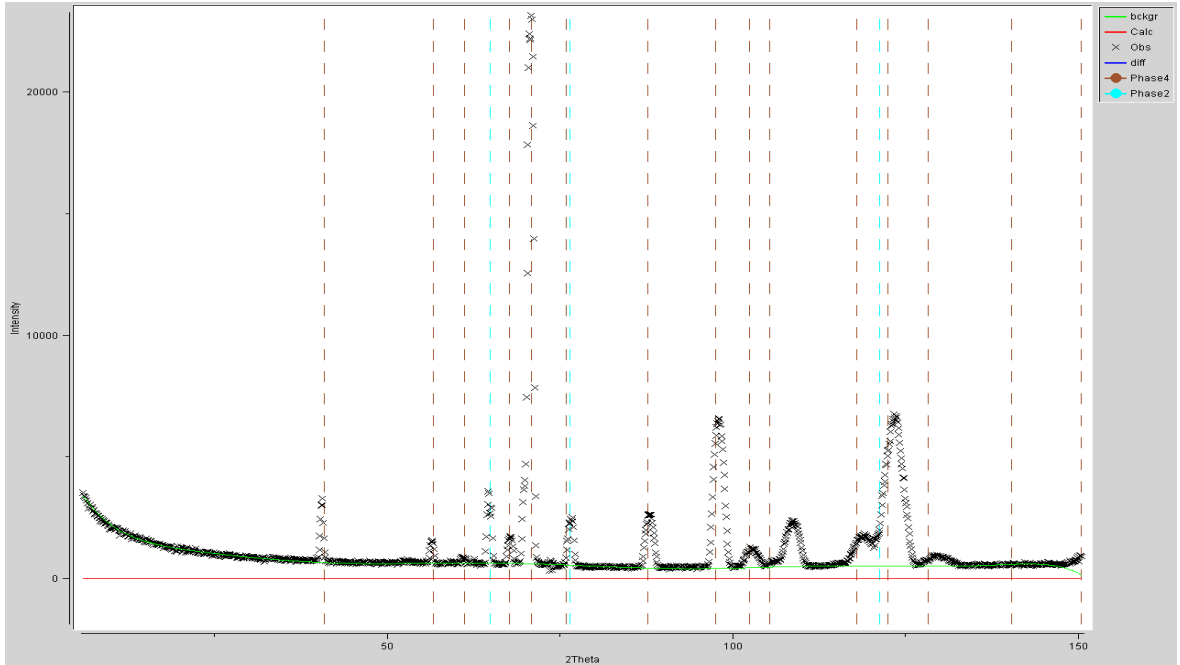


Figure 4.50. Neutron pattern of the sample holder in *GSAS*.

Mirror furnace sample holder in the beam with no sample at room temperature. Alpha-alumina (corundum) is the most dominant phase (marked in brown).

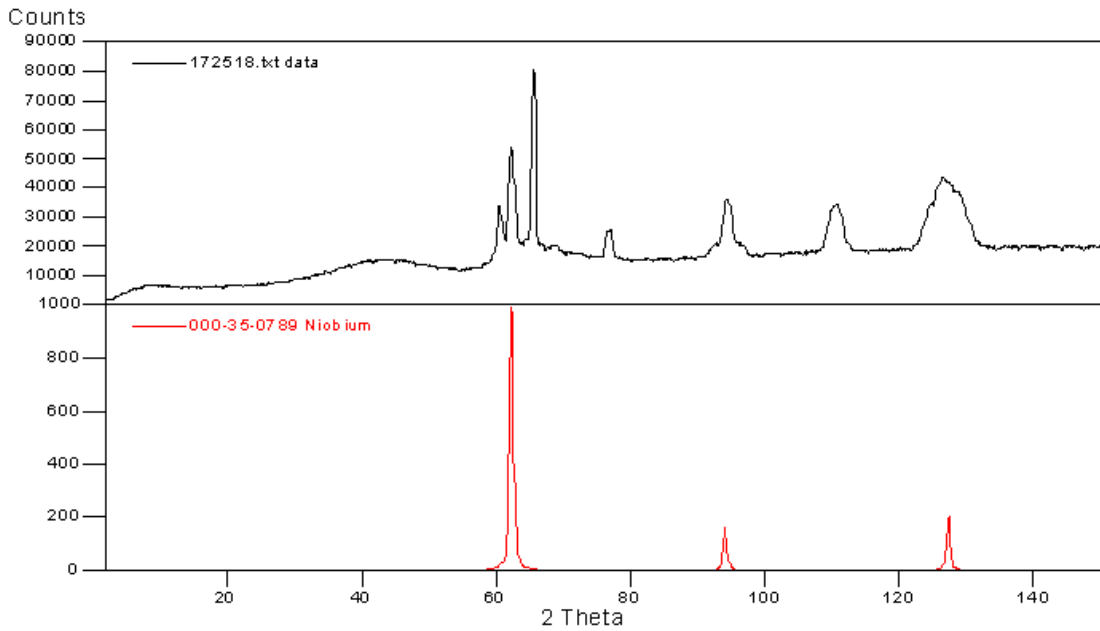


Figure 4.51. Attempted match in *Searchmatch* with niobium (vacuum experiment).

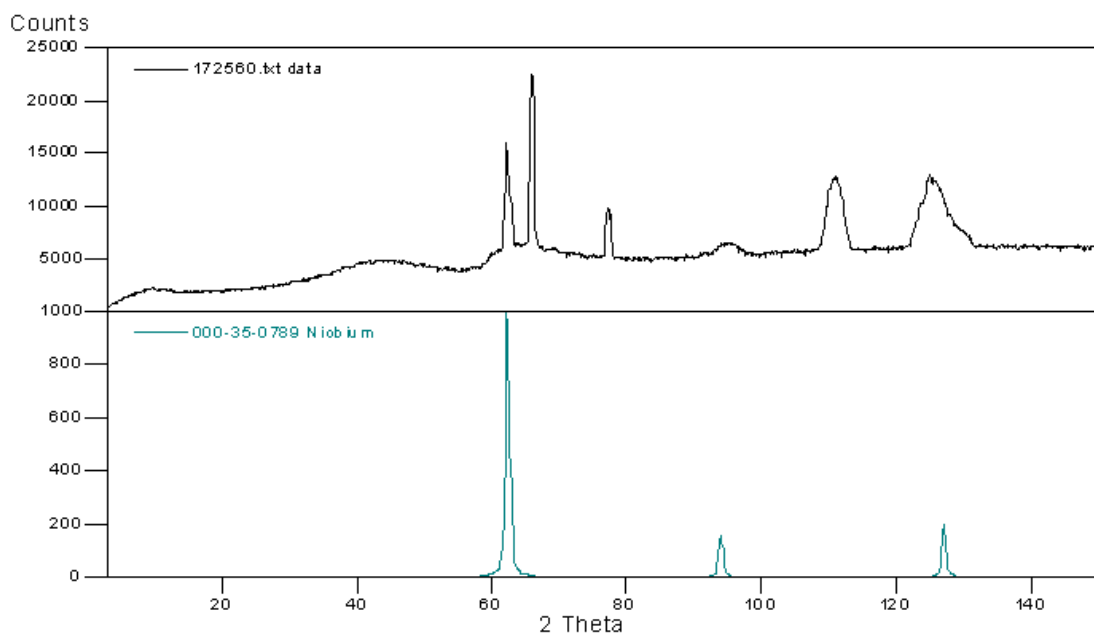


Figure 4.52. Background image after initial vacuum furnace replacement; note the missing peak at $\sim 60^\circ$.

Note the presence of a number of unidentifiable peaks.

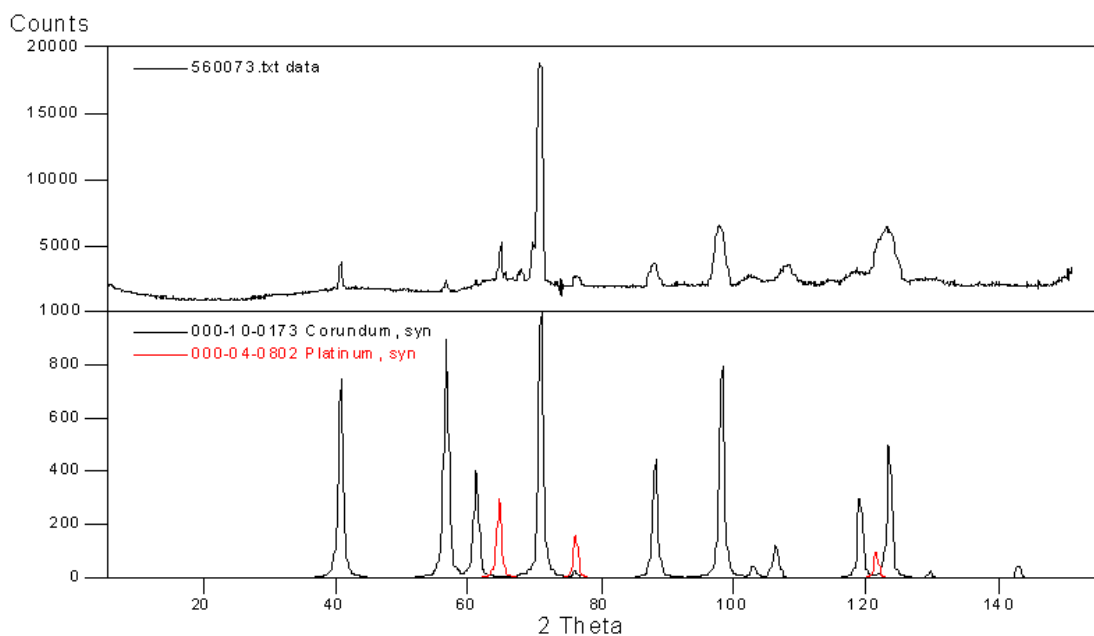


Figure 4.53. Pattern of background plus amorphous signal with corundum and platinum patterns shown in black and red respectively.

Mirror furnace sample at 570°C , before the onset of crystallisation.

4.3.2 Vacuum Neutron Diffraction on LDIG 24 Glass-Ceramics (28/6/2002)

The original neutron experiment on the original LDIG 24 glass-ceramics raised some interesting questions – one was whether the action of the vacuum changed the crystallisation products or altered the thermal properties of the material due to silicon tetrafluoride (SiF_4) volatilisation. One particular ramp, where overshoot of the furnace temperature controller occurs, is examined - as it reveals features of phase formation that were unobserved at the time. A thermogram of this ramp is shown in figures 4.54 to 4.55 along with several plots, in figures 4.56 to 4.61, that may provide direct evidence of the sellaite (MgF_2) precursor phase, postulated from evidence in the XRD chapter, which either nucleates or indirectly initiates other types of phase formation in the parent LDIG 24 glass. Assuming that figures 4.56 to 4.61 have been correctly interpreted, this would be the first time that precursor nucleation has been experimentally observed in these materials.

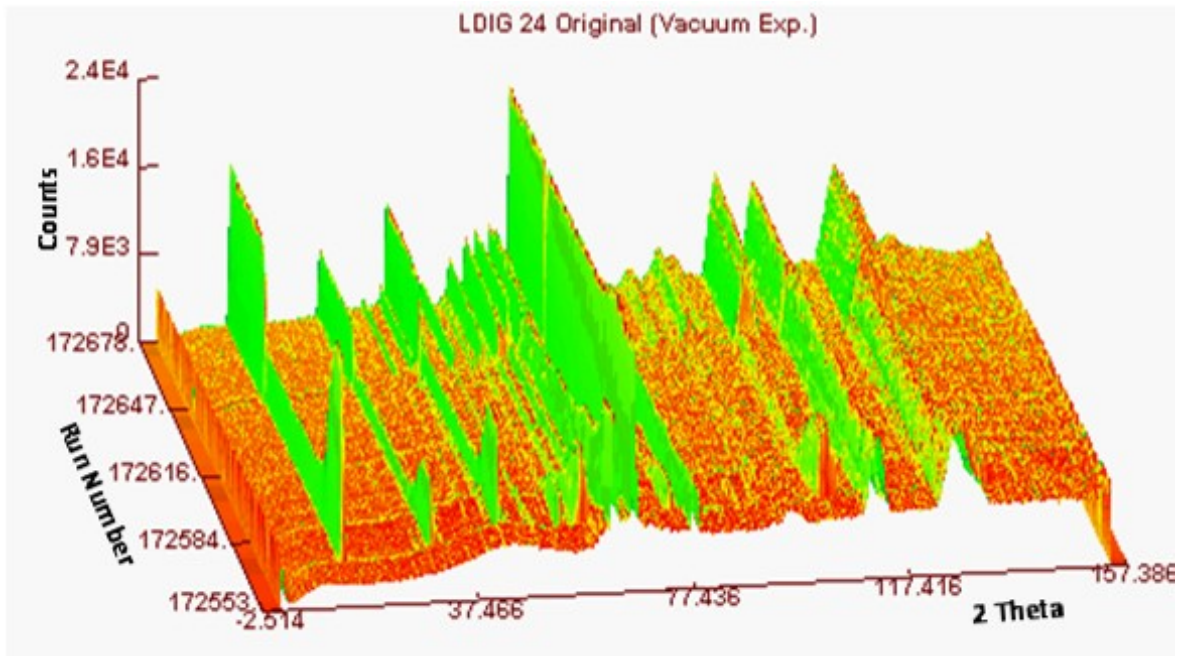


Figure 4.54. Thermogram of full pattern over heat treatment cycle.

Note the sudden drop in intensity produced when the furnace overshoots at 1200 °C, the recovery is associated with cooling.

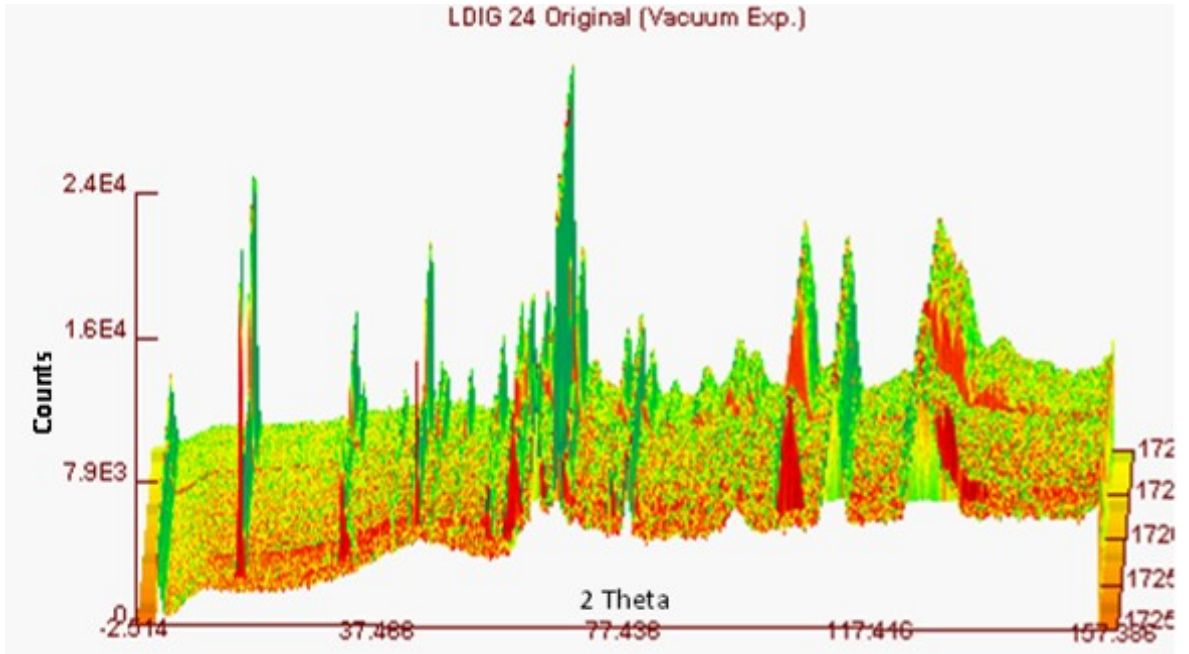


Figure 4.55. Thermogram of the same ramp viewing, front, the onset of crystallisation and growth.

Heat treatment includes a ramp @ 10 °C/min to 1225 °C, a hold @ 1225 °C for 3 h and cooling at 10 °C/min to room temperature.

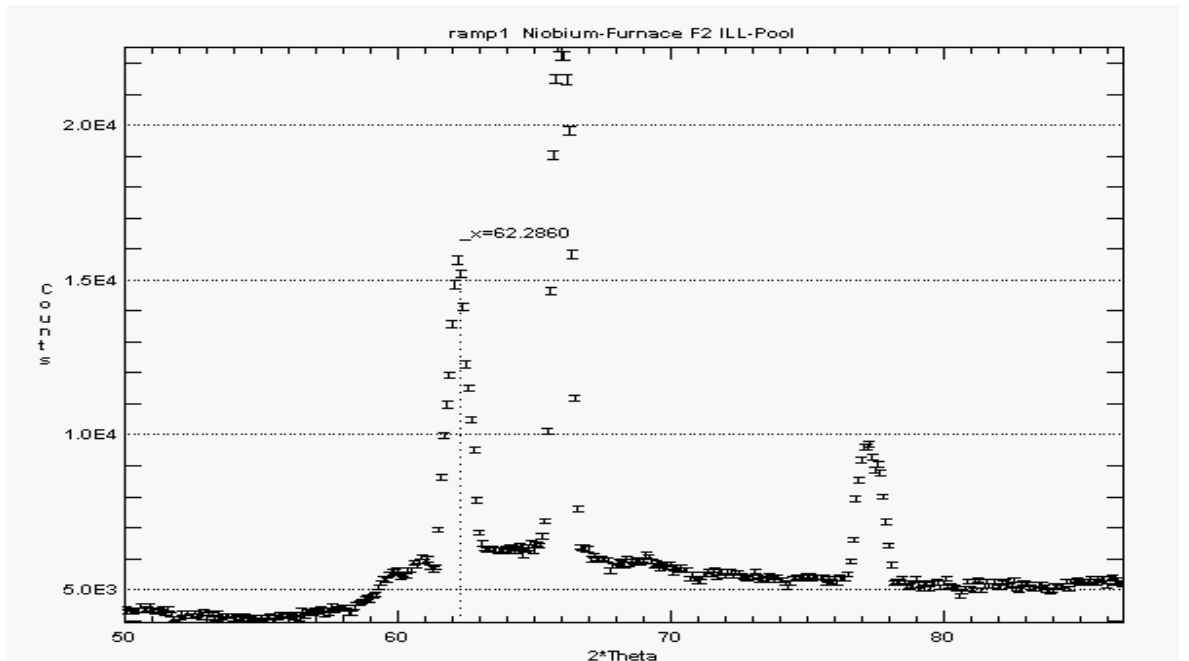


Figure 4.56. Peak at 62.20° marked out previously, at a temperature of 805 °C just before the onset of crystallisation.

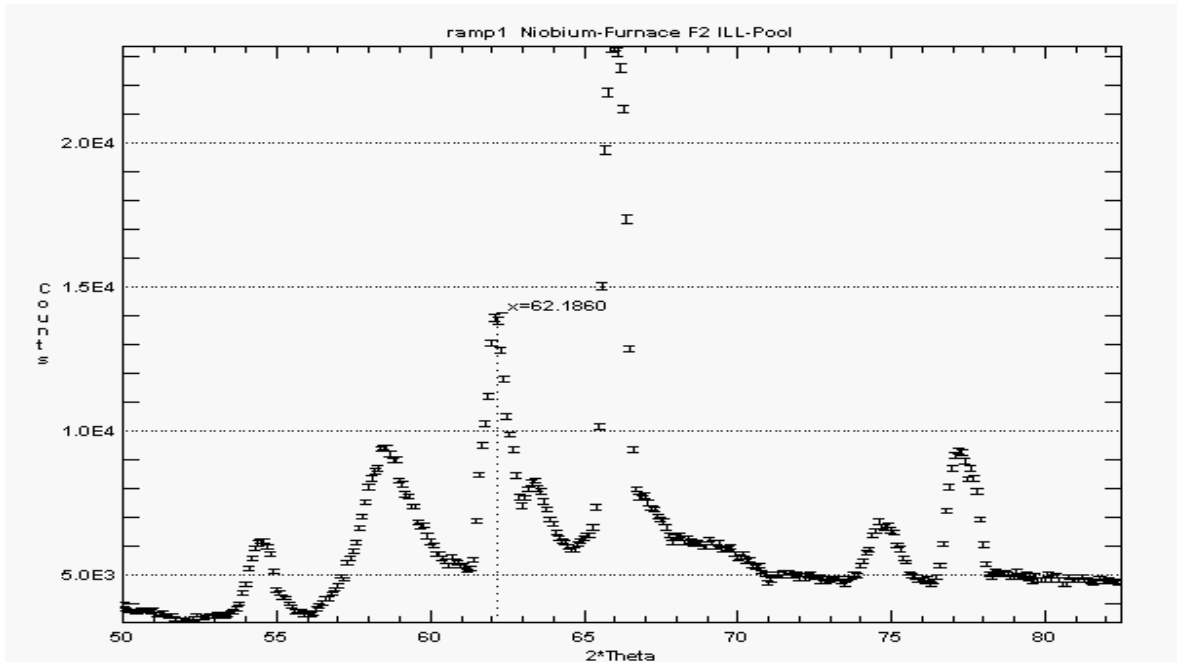


Figure 4.57. Onset of crystallisation at 845 °C.

Note the marked peak is dropping in intensity despite the rising background below it.

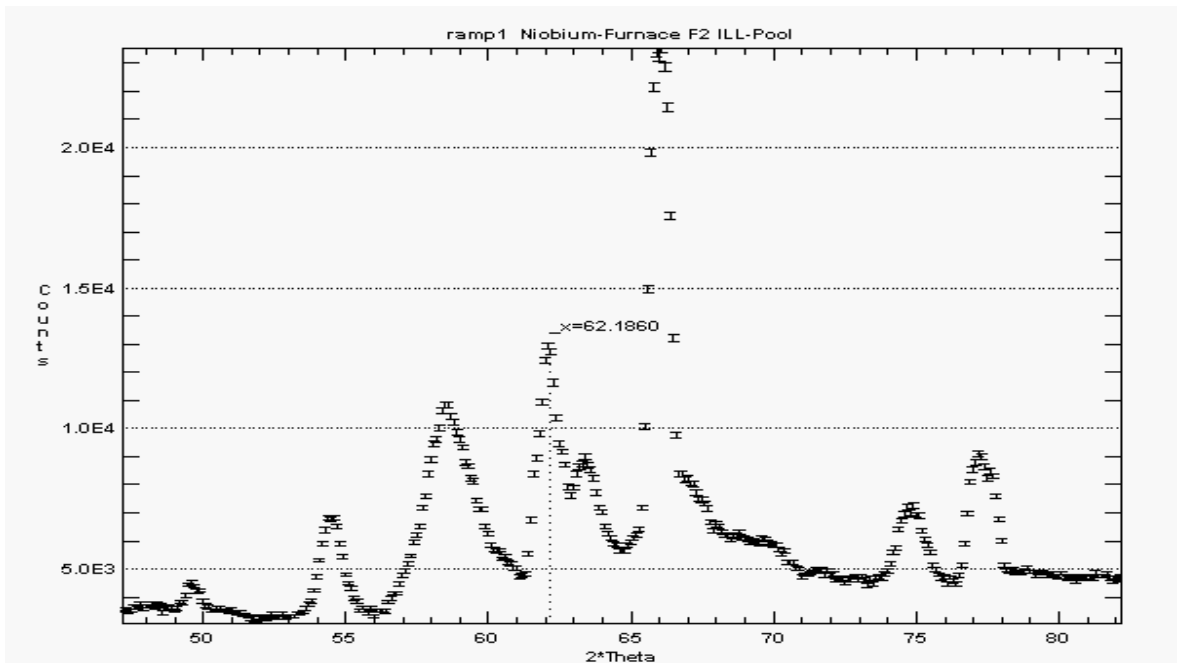


Figure 4.58. @ 945 °C.

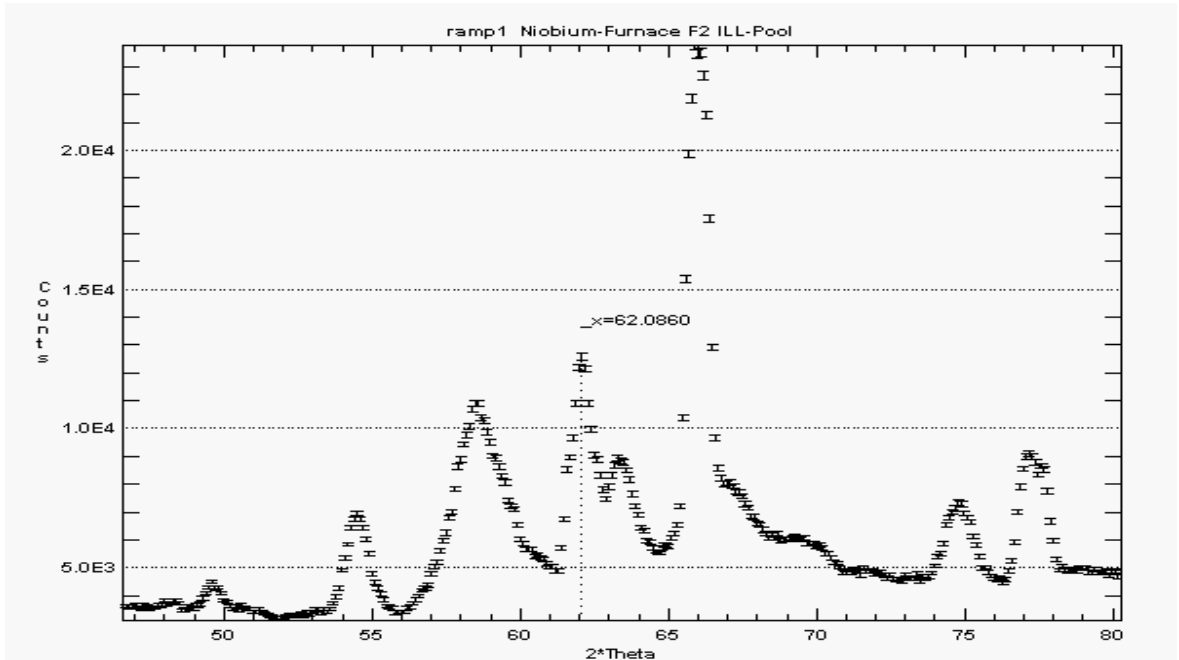


Figure 4.59. @ 906 °C.

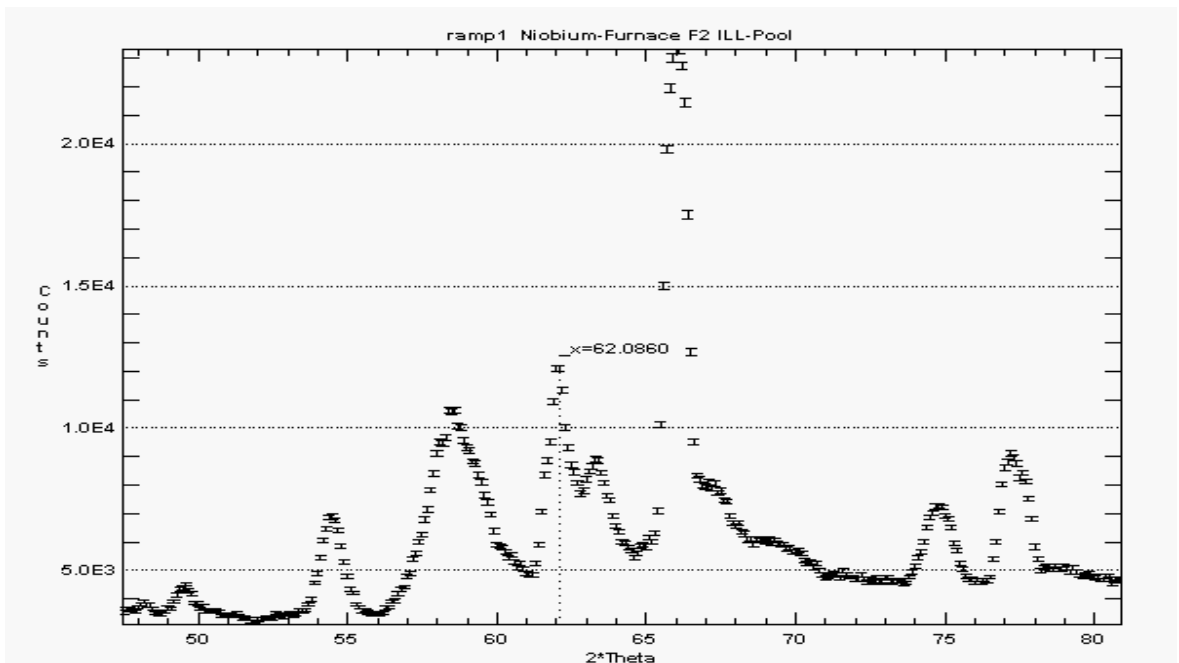


Figure 4.60. @ 1002 °C.

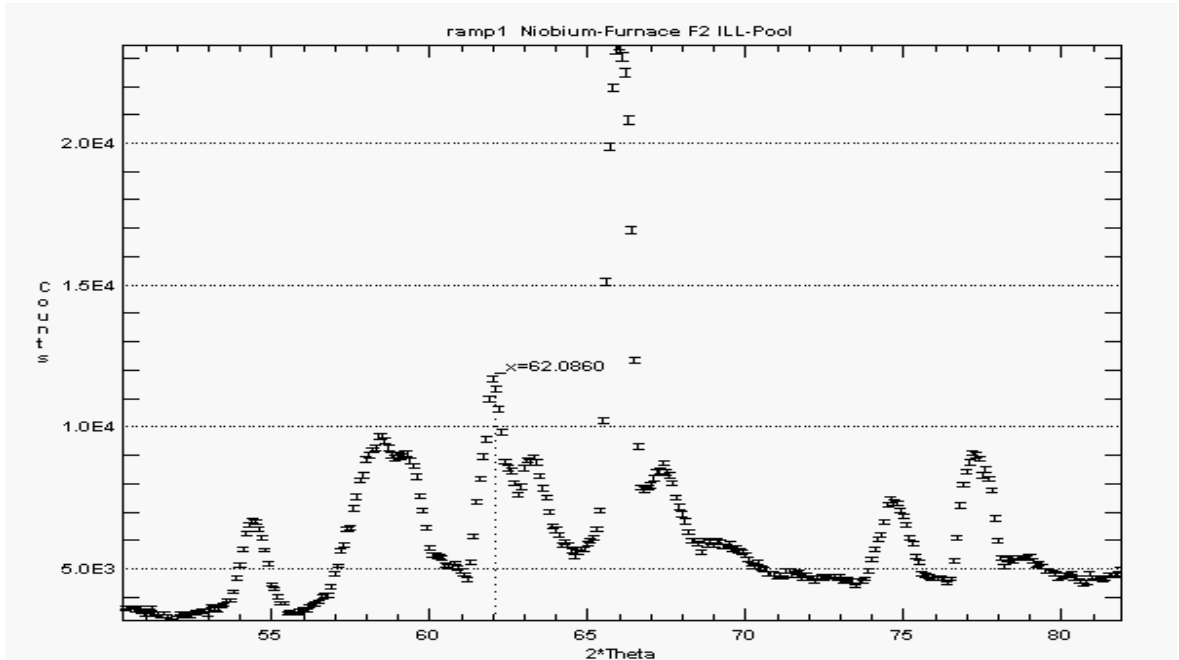


Figure 4.61. @ 1066 °C.

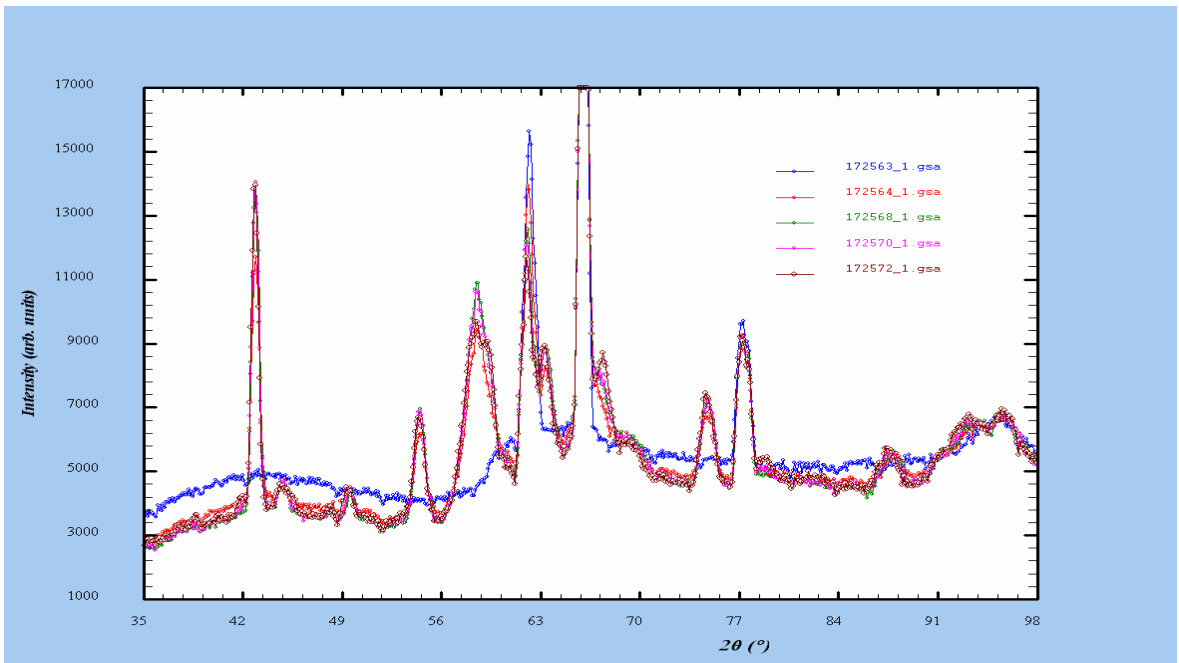


Figure 4.62. Overlain patterns from above one can clearly see a fall in the 62 ° peak as the others rise.

The blue line is the original amorphous background.

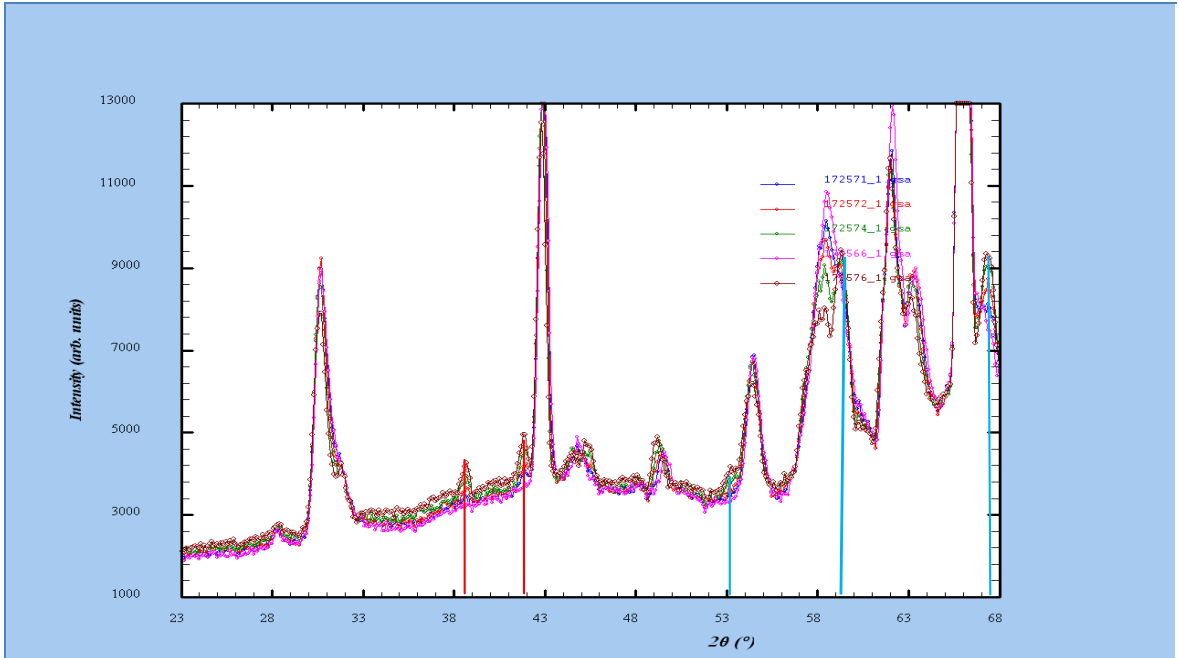


Figure 4.63. Fluorapatite peaks.

Highlighted in red, are overlain by a number of patterns at different temperatures; the presence of fluorapatite in LDIG 24 has been proven by both neutron and X-ray experiments and SEM/EDS in appendices 2.1 to 2.2.

The peak position in figure 4.56, is 62.2° at 805°C , whereas the (020) peak of sellaite (MgF_2) at room temperature, corresponding to a neutron wavelength of 2.4189 \AA , is 63.14° ; the slight discrepancy appears to be on account of thermal expansion. It is notable that a principal (110) peak of niobium at $\sim 62.3^\circ$ two theta would possibly overlap with sellaite in this case; however, niobium is unlikely to be the cause of the apparent drop in intensity observed through figures 4.56 to 4.61 - although some further investigation is justified. As previously discussed, this peak appears in the amorphous pattern at full height indicating, if one assumes sellaite, that it has precipitated during the annealing stage of the glass rod @ ($T_g - 50$) or $\sim 590^\circ\text{C}$ as a nanocrystalline phase. This is a very low temperature and would prove that sellaite nucleates in the parent glass before fluormica or any other phase. Most of the crystallisation in the sample occurs over a period of 3 frames, equivalent to 9 minutes in real time, with the suspected sellaite peak steadily reducing by 15 % during this time and eventually by 25 % after 26 minutes to 1055°C . The fact that a significant amount of sellaite apparently remains suggests that the mica volume fraction in the cerammed sample is low and that higher temperatures do not increase the nucleation density of mica, one may also surmise that sellaite is not involved in the nucleation of any other secondary phases.

As the furnace approaches the crystallisation hold temperature @ 1225 °C, in figure 4.63, an interesting phenomenon occurs, the mica peaks most clearly identified with the (001) and (003) peaks, 14.15° and 42.84° respectively, start to reduce and the formation of a secondary phase is indicated at approximately 1060 °C. This indicates some sort of dissolution of the mica phase which is unusual as kinoshitalite mica is highly refractory, King *et al.* (2000), and would normally be expected to survive until the glass-ceramic had revitrified. The peaks that rise from the general background, in figure 4.63, seem to coincide with those of fluorapatite ($\text{Ca}_5(\text{PO}_4)_3\text{F}$) with peaks at 38.51° and 41.08° two theta; identified as (021) and (002), respectively. This apparent phase dissolution has not been observed elsewhere and certainly not in air, the formation of F-apatite is probably just a coincidence as the nucleation temperature seems to approximate that found with mica-fluorapatite compositions of ~1050 °C (Bentley *et al.*, 2007).

One possibility is that the vacuum effectively increases the vapour pressure of silicon tetrafluoride gas (SiF_4) allowing much larger quantities to escape than would be the case in air, this would alter the composition of the residual glass and perhaps lead to types of phase formation that are incompatible with mica in a similar way to the mechanism described for surface nucleation, in section 4.2.2.2. Referring to the melting section of the thermograms, in figures 4.54 to 4.55, one can now understand why the peak intensities fail to return once the hold temperature has returned to normal; at the crystallisation hold temperature the mica phase is well within the 'metastable zone of supercooling', close to the melting point of the glass - at these temperatures bulk nucleation is not possible and, therefore, the volume fraction of the main phase, in this case, cannot recover. This explains why an almost complete recovery is observed on cooling as nucleation rates are favoured by lower temperatures; fine crystallisation when cooling from a melt does not occur as sufficient nucleation density is prohibited by the high temperatures. Observation of the run numbers suggests that the maximum effective nucleation temperature for mica is 976 °C, which is significantly higher than any optimum value calculated by DTA analysis.

The peaks in blue, in figure 4.63, are a secondary phase apparently formed during and unaffected by the dissolution of the mica main phase and maintain or increase their amplitude in spite of it, they closely match high temperature hexagonal celsian,

which makes sense considering the discussion previously on XRD. Peaks in the pattern were found at: - 59.3° , 67.4° , 78.5° and 52.9° two theta which corresponds with hexacelsian peaks at room temperature of 63.47° , 66.87° , 76.61° and 54.19° , respectively. Once the furnace overshoots, at over 1225°C in figures 4.54 to 4.55, all of the peaks decrease in amplitude through a combination of a reduction in background and dissolution of phases. The Le-Bail fits, in figures 4.64 to 4.69, are the first to be attempted by the author and were relatively difficult due to the lack of well defined peaks in the diffraction trace. The lattice parameters used were a refinement of those values already known from XRD analysis. Due to the relatively small difference in sample temperatures, it was possible to apply the same parameters in each case; for mica: - $\mathbf{a} = 5.39$, $\mathbf{b} = 9.28$, $\mathbf{c} = 10.125 \text{ \AA}$ and for clinoenstatite: - $\mathbf{a} = 9.54$, $\mathbf{b} = 8.93$, $\mathbf{c} = 5.16 \text{ \AA}$. The main (001) peak of the mica phase was fitted to determine the mica crystallite size; a value of $\sim 0.16 \mu\text{m}$ was calculated from the Lorentzian parameter, as in section 4.2, which supports the conclusion that crystal size is generally unaffected by grinding.

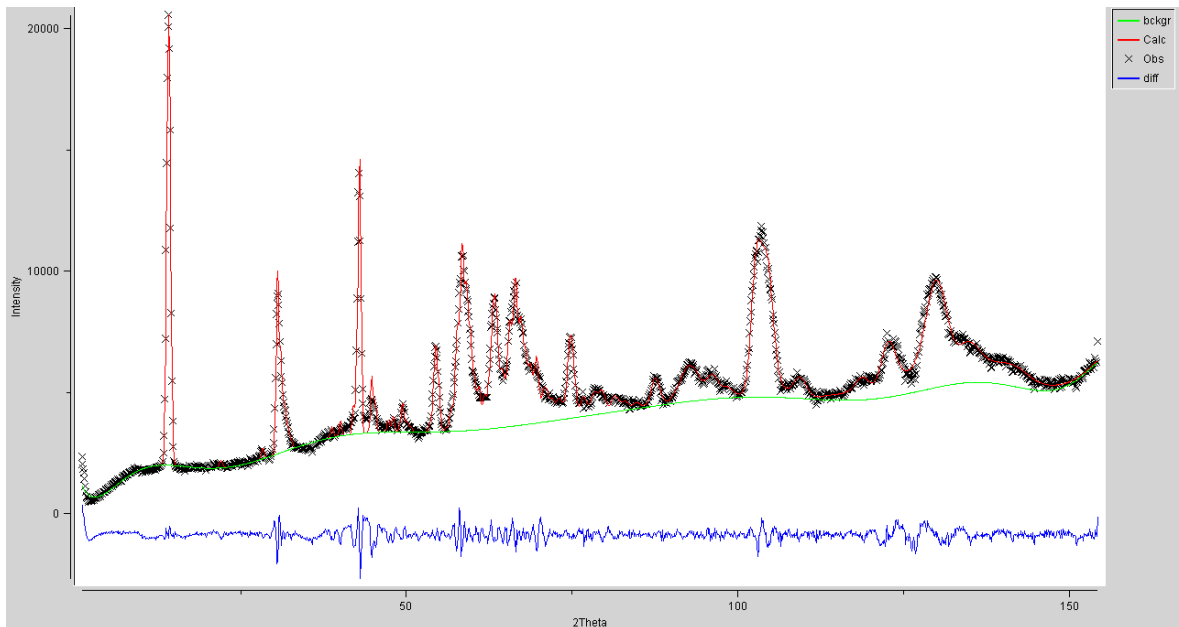


Figure 4.64. Le Bail fit of pattern after subtraction of background by computer program, the temperature of the sample is 1201°C .

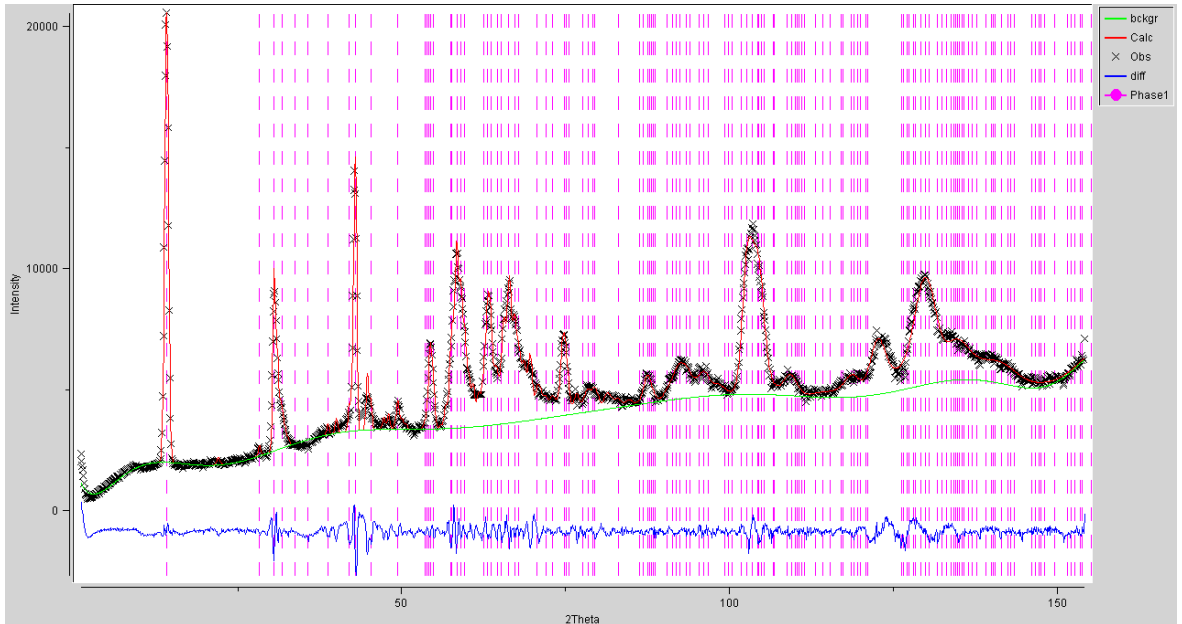


Figure 4.65. Le Bail fit of 1201 °C pattern with F-kinoshitalite phase marked in red.

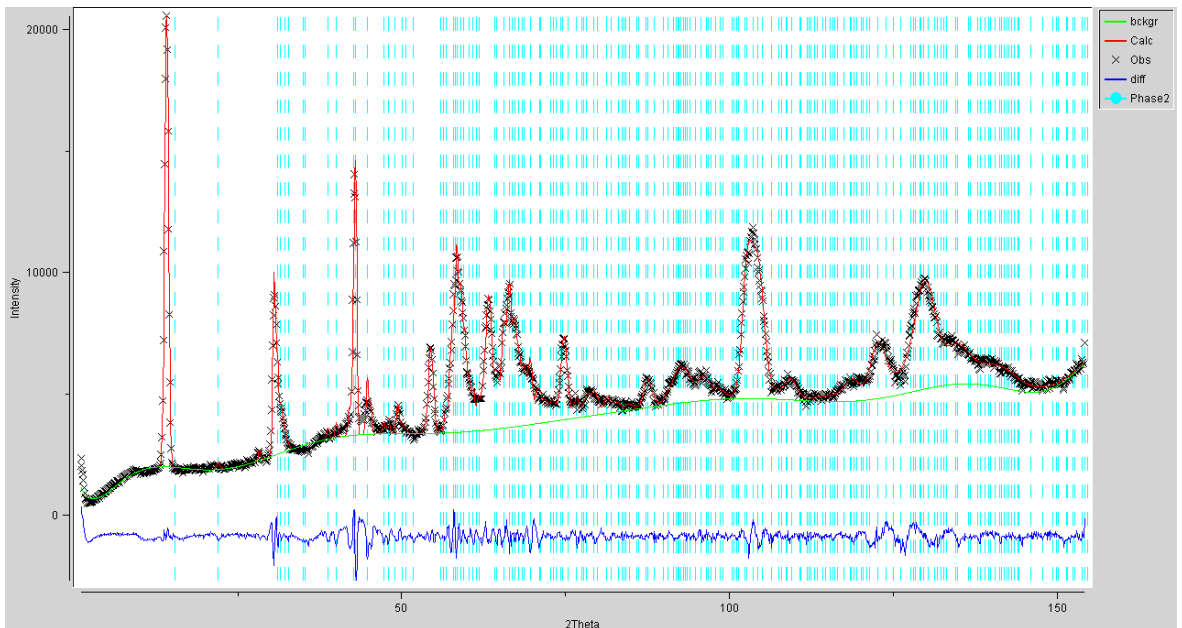


Figure 4.66. Le Bail fit of 1201 °C with clinoenstatite phase marked in blue.

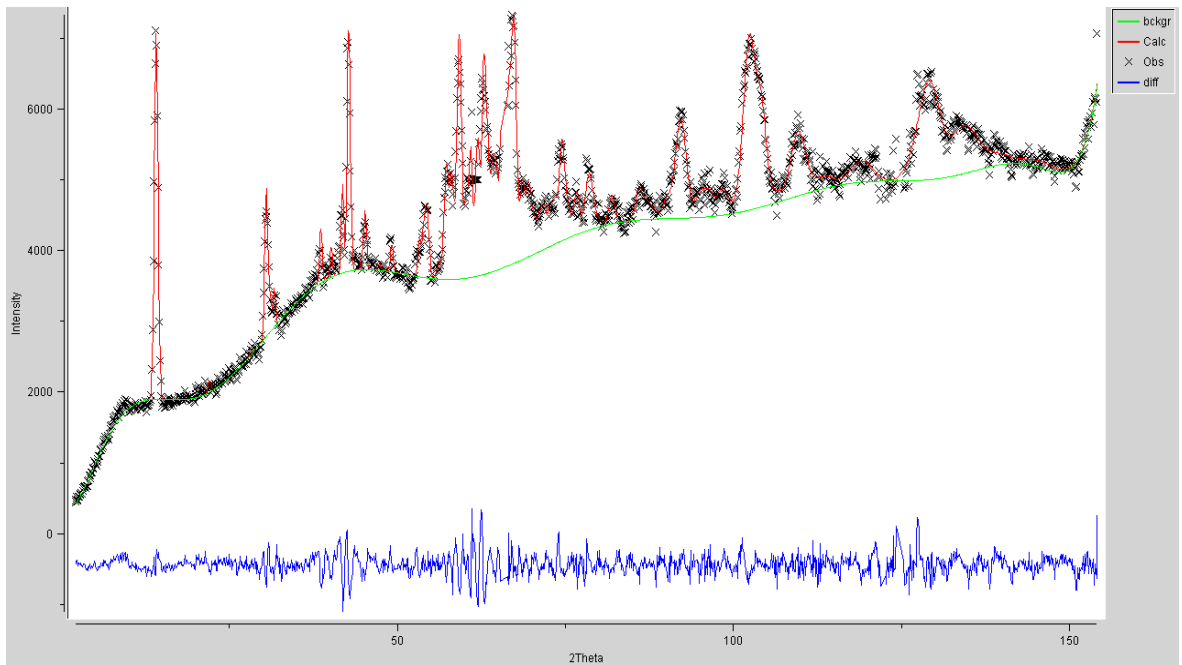


Figure 4.67. Le Bail fit of pattern at 1225 °C.

The relatively poor signal-noise ratio made background subtraction very difficult.

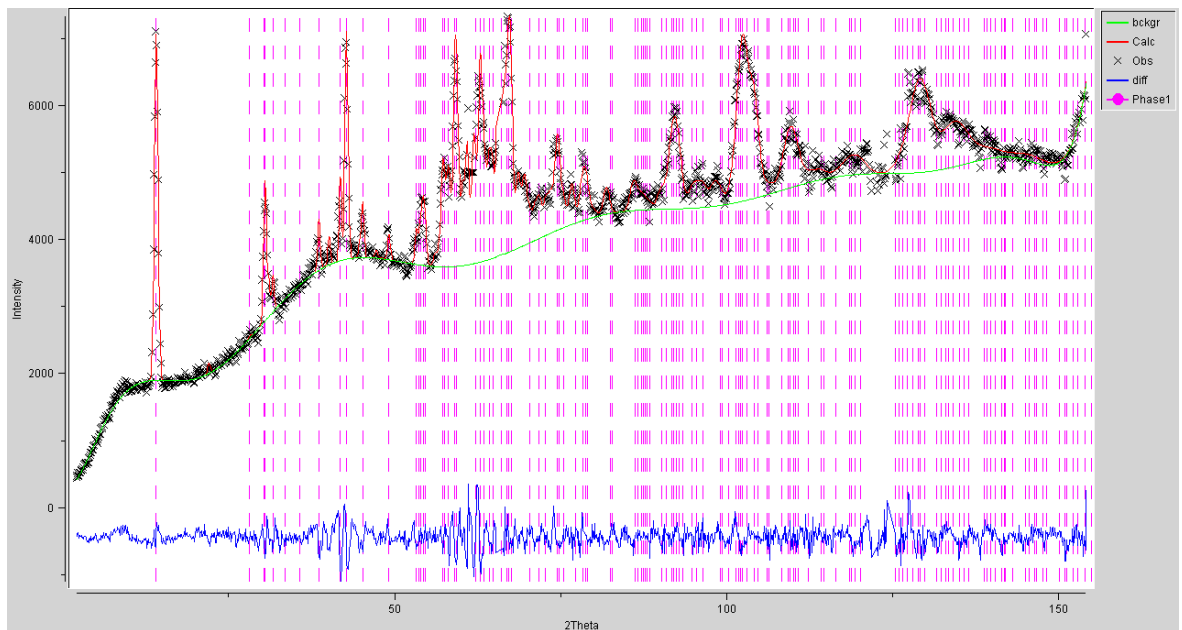


Figure 4.68. Le-Bail fit of 1225 °C pattern showing match with F-kinoshitalite.

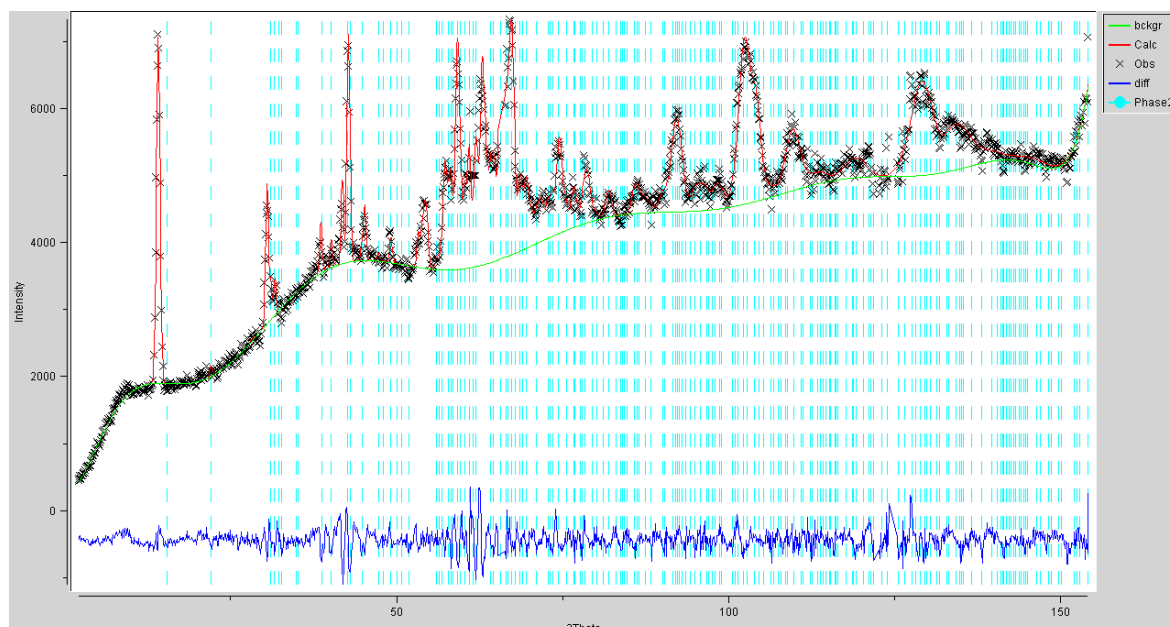


Figure 4.69. Le-Bail fit of 1225 °C pattern showing match with clinoenstatite.

4.3.3 Neutron diffraction in Air Experiment with Mirror Furnace (2/5/2007)

Neutron experiments performed with similar but smaller samples in the mirror furnace (with rods 8 mm in diameter and 10 mm high) attempted to mimic the conditions of commercial manufacture where the cost of a complex vacuum furnace would be prohibitive. Fortunately, many of the results of the previous experiment (section 4.3.2) were replicated with this one. The major difficulty is in interpreting the small amplitudes of the sample which are, in places, overwhelmed by a strong background. A run has been chosen with the commercial sample composition, in figures 4.70 to 4.71, to give a useful comparison between the two. Apart from the melting mishap of the previous sample both appear to exhibit identical structure. By reference to the figures below, crystal growth rates appear similar in both commercial and original LDIG 24 samples; suggesting that commercial manufacturing would be suitable for a future development of this material. Hexacelsian was not detected in the air samples indicating that its formation in the vacuum experiment was a direct result of volatilisation of SiF_4 at high temperatures, which conceivably reduced the fluorine content of the residual glass to the point where nucleation and growth of another phase became possible.

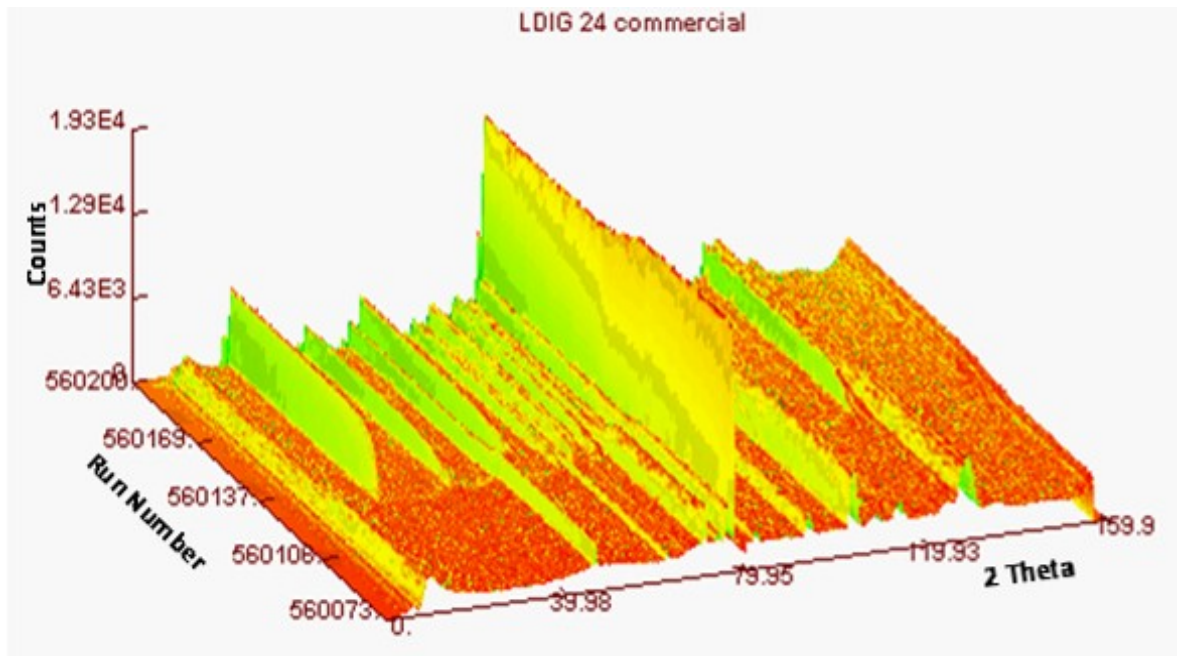


Figure 4.70. Thermogram of entire run.

The heat treatment in this case consisted of a ramp @ 10 °C/min to 644 °C, a hold at 644 °C for 2 hours, then a ramp @ 10 °C/min to 1225 °C and an isothermal hold for 3 hours followed by rapid cooling (air quenching) to room temperature.

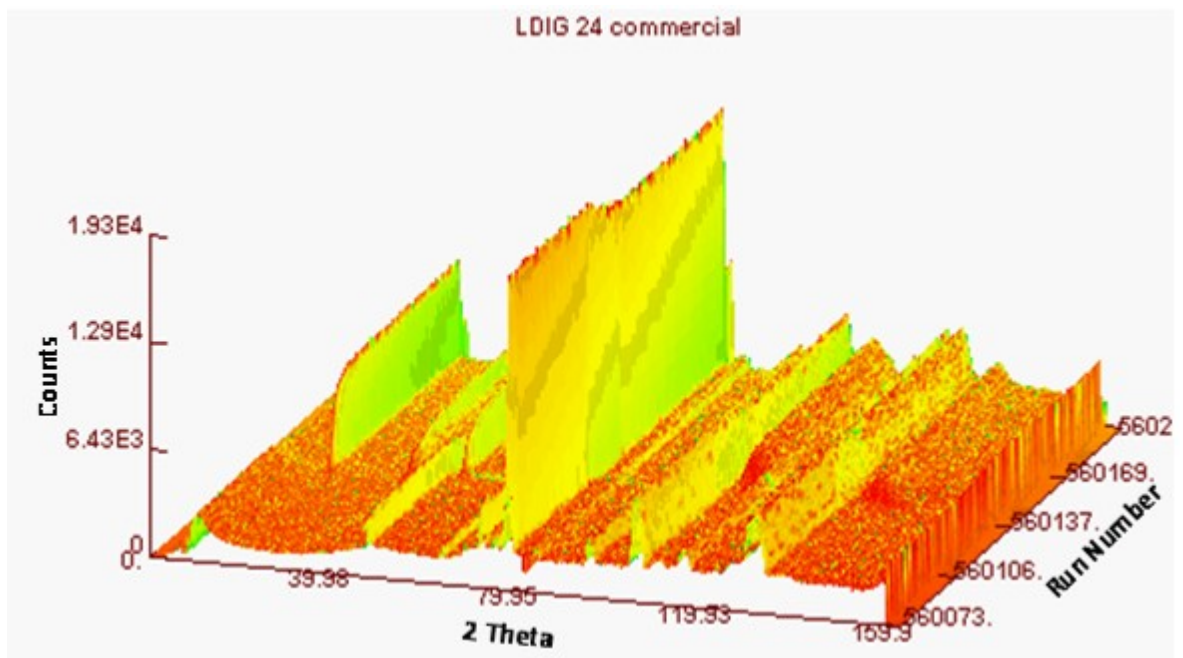


Figure 4.71. Same thermogram with a different view.

Note the dominance of the sample background.

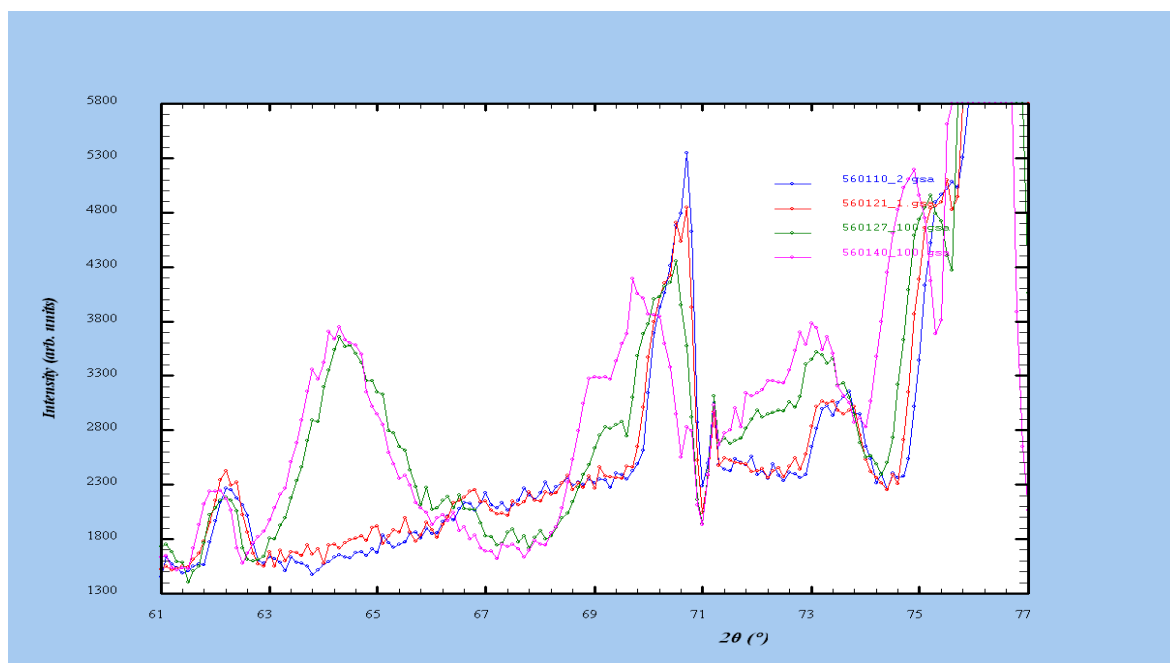


Figure 4.72. Possible sellaite and main phase interactions.

One can clearly see a possible sellaite (MgF_2) peak, at $\sim 64^\circ$ when adjusted for offset, fall away once the main phase begins to form although this is less clear due to much lower sample intensity. One would expect, however, that this type of nucleation is a characteristic of both samples not just their respective sample environments.

Understanding how the nucleation of mica occurs by the precipitation of a precursor phase will help improve crystallinity and particularly the mica volume fraction of these materials, which is relatively low compared to commercial materials such as Dicor® (Beall, 1972) as evidenced in section 4.2.2.6. Introducing an alternative nucleator to sellaite may be an effective way of improving the mica volume fraction in this case. A suitable nucleator would be zirconia (ZrO_2) as both structures are tetragonal and have similar lattice parameters; zirconia is also recognised as having one of the highest cationic field strengths, facilitating accumulation of species from the glass matrix, of any material and, therefore, makes an excellent choice (Wang *et al.*, 2009).

5 Conclusions

- Two types of LDIG 24 glass-ceramic, denoted commercial and original and each of similar nominal composition as proven by EDS, have been compared to assess the commercial viability of this material in the field of CAD/CAM restorative dentistry. It was assumed that any physical discrepancies between variants, under identical conditions, would be a direct result of differences in impurity levels of the respective feedstock compositions as the processing routes are identical. Optimum nucleation temperatures and activation energies have been determined by DTA and appear to show little distinction between either variant although bulk nucleation with 3D crystal growth is indicated; peak crystallisation (T_{p1}) and glass transition temperatures (T_g) also coincide. Major discrepancies do occur in relative solubilities and apparent melt viscosity which manifests as a greater resistance to slumping at high temperatures, in the original case. It has been theorised that additional alumina in the original composition is responsible and that this increases both melt viscosity and acid resistance. The source appears to be the original mullite crucibles previously used in glass-making that were replaced at the beginning of this work due to apparent contamination of the melt glass.
- Mechanical testing, consisting of BFS (Biaxial Flexure Strength) and micro-hardness (VHN), demonstrates a strong relationship between mechanical properties and applied crystallisation hold temperatures; with noticeable deterioration occurring over 1100 °C. Lower temperatures produce excessive hardness for dental applications and, therefore, there is no clear way of reducing hardness while maintaining strength by appropriate changes to the heat-treatment schedule alone. It is theorised that the hardness of LDIG 24 commercial glass-ceramics is largely dependent on the amorphous volume fraction rather than the type of crystalline phases present – a large volume fraction of cristobalite (SiO_2) was found in samples heat treated @1150 °C and yet these were found to be only half as hard as samples heat treated @ 925 °C.

- Gloss measurements show that LDIG 24 commercial generally becomes more opaque with increasing hold temperatures in proportion with the amorphous volume fraction. This may also indicate that crystallites increase in size, by Ostwald ripening, and that the volume fraction of particles with dimensions approaching the wavelengths of visible light ($\ll 1\mu\text{m}$) is significantly reduced. Theorised changes to the microstructure based on surface gloss appear to support the observed transition in mechanical properties from high to low strength at higher temperatures.
- SEM and optical micrographs of commercial LDIG 24 samples, heat treated at a range of temperatures, show evidence of phase separation, voids and phase formations of varying hardness making preparation of a smooth flat surface by polishing difficult. This supports evidence of poor measurement repeatability with the microhardness indenter for the majority of samples.
- Dopants, added to commercial LDIG 24, have been found that impart colour to both parent glass and glass-ceramic forms. Additions containing Ni(II)O_2 appear to show the most promise as these colour the bulk glass-ceramic yellow; this has been confirmed by colour space measurements on a range of samples including those containing Ni(II) and those without. Surface nucleation of frit samples appears to alter the colour compared with that in the bulk and surface samples generally appear darker.
- Rietveld refinement has shown that Ba-mica precipitated in the bulk is depleted with the chemical formula: - $\text{Ba}_{0.7}\text{Mg}_3(\text{Al}_{1.4}\text{Si}_{2.6})\text{O}_{10}\text{F}_2$; this is different to that assumed by the ternary composition phase diagram for this system – $\text{Ba}_{0.5}\text{Mg}_3(\text{Si}_3\text{AlO}_{10})\text{F}_2$. The latter is a Ba-fluorophlogopite mica, whereas, the former resembles kinoshitalite. Initial assumptions, therefore, about phase formation in this system are wrong. The structure of the single crystal was determined by refinement of the single crystal diffraction data and EMPA analysis; the chemical formula of this sample ($\text{Ba}_{0.76}\text{Mg}_3(\text{Al}_{1.53}\text{Si}_{2.47})\text{O}_{10}\text{F}_2$) differs from that of the mica phase in the bulk.

- Powder XRD measurements and a variety of novel techniques have shown that the mica phase is not as dominant as assumed either. There is evidence of multi-phase precipitation in both surface and bulk nucleated samples with significant volume fractions of phase transformed enstatite (MgSiO_3) and cristobalite (SiO_2). The presence of sellaite (MgF_2) was also supported by Rietveld refinement of XRD data. It can be theorised, by reference to the literature, that sellaite nucleates the mica in this case. The observed phase dissolution of LDIG 24 glass-ceramics (shown by DTA), at a lower temperature than would be expected, corresponds with the melting point of sellaite ($\sim 1260\text{ }^\circ\text{C}$) and indicates that MgF_2 may have a fundamental role in phase precipitation.
- Powder XRD has also shown that surface nucleated samples lack fluorinated phases such as fluorapatite, found in the bulk; this suggests that fluorine is lost prior to phase formation as SiF_4 and that the depletion of fluorine from the sample triggers an alternative type of phase precipitation.
- XRD patterns have shown the presence of a significant amorphous background in bulk samples heat treated by two step heat treatment up to $1150\text{ }^\circ\text{C}$, whereas, when the glass melt is cooled slowly through the liquidus (single crystal experiment) or the glass-ceramic surface nucleated, as in section 4.2.2.2, no such background forms. It is theorised that this is due to different phase compositions on account of different heat treatments with a lower volume fraction of Ba-mica found in LDIG 24 commercial samples heat treated below the liquidus, resulting in a higher fluorine content in the residual glass.
- Data sets from neutron diffraction experiments at ILL seem to confirm findings based on XRD and appear to show that a nanocrystalline sellaite phase nucleates depleted kinoshitalite mica in a Ba-phlogopite stoichiometry glass-ceramic, which is a first. Neutron data also confirm the formation of fluorapatite in the bulk glass-ceramic.

- This study has shown that commercial LDIG 24 glass-ceramics for CAD/CAM dental applications are feasible. Significant development is still required; however, advances in the understanding of phase formation and relationships with general mechanical properties, as a result of this work, should guide the future development of these materials.

5.1 Future Work

A number of difficult problems will need to be solved for LDIG 24 glass-ceramics to be competitive in the commercial market. Solving problems with solubility, however, may be relatively straight forward. It is well known that high silica glass, e.g. Pyrex, demonstrates high acid resistance; so increasing the silica content of any glass-ceramic should do the same. Cristobalite and possible tridymite formation after the standard heat treatment will deplete the residual glass phase and almost certainly impair chemical resistance. Suppression of cristobalite/tridymite precipitation, as discussed, with additions such as lanthanum (La) oxide may be highly effective in this case. The addition of up to 3 - 5 mol % of B₂O₃ (boric oxide) should also significantly increase acid resistance of commercial LDIG 24 glass-ceramics produced by lower temperature heat treatments (Scholze, 1991). Improvements to the surface finish, at higher temperatures, may require a reduction or elimination of porosity in the bulk and requires further study.

If lower temperature heat treatments are preferred then attempts should be made to reduce hardness while maintaining as much strength and toughness as possible. One possibility may be the introduction of an effective nucleating agent such as zirconia (ZrO₂) to compliment the sellaite phase; this would increase the volume fraction of mica at the expense of the residual glass leading to an overall reduction in material hardness and related improvements in machinability; a nanocrystalline zirconia phase would no doubt produce the best results. The lower temperature of the crystallisation hold, in this case, should ensure that a fine microstructure is precipitated, as with the undoped samples, developing improvements in strength and optical translucence – essential for teeth. Once mechanical and optical problems have been overcome, colour development can begin by starting with one of the Ni(II)O₂ compositions developed in this work. The author is confident that many remaining problems are tractable, at least to some degree, and that future developments in commercial LDIG 24 commercial glass-ceramics are possible.

References

- Abdel-Hameed.A.M. *et al.*, 'Effect of alumina on ceramic properties of cordierite glass-ceramic for basalt rock', JECS, volume 27, Issues 2-3, 2007, pages 1893-1897, 2006.
- Al-Shammary.H., 'Novel machinable mica based glass-ceramics and their clinical applications using Cerec CAD/CAM system', PhD thesis, Leeds University, 2003.
- Arahoru.T *et al.*, 'Transformation of tridymite to cristobalite below 1470 °C in silica refractories', Journal of Materials Science 22, pages 2248-2252, 1987.
- Bapna.M.S. *et al.*, 'Study of devitrification of Dicor glass', Biomaterials 17, pages 2045-2052, 1996.
- Beall.G.H., 'Mica-Glass Ceramics', U.S. patent number 3,689,293, 1972.
- Beall.G.H. *et al.*, 'Nanophase Glass-Ceramics', J. Am. Ceram. Soc., 82[1], pages 5 – 16, 1999.
- Beurskens.P.T., 'Dirdif 2008', Dirdif Manual, Crystallography Laboratory, Radboud University Nijmegen, The Netherlands.
- Bentley.P.M *et al.*, 'Kinetic neutron diffraction and SANS studies of phase formation in bioactive machinable glass-ceramics', Biomed. Mater. 2, pages 151-157, 2007.
- Boyd.F.R. *et al.*, 'The rhombic enstatite-clinoenstatite inversion' Carnegie Inst. Washington Ann Rept. Dir. Geophys Lab 1964-1965: pages 117-120.
- Boccaccini.A.R. 'Machinability and brittleness of glass-ceramics', Journal of Materials Processing Technology 65, pages 302-304. 1997.
- Borland, 'Turbo Pascal® Language Guide', Borland International Inc, 1992.
- Brown *et al.*, 'The crystal structure of solids', Edward Arnold Ltd, 1973.
- Breusov.O.N. 'Polymorphism of Magnesium Fluoride', Zhurnal Strukturnoi Khimii, Vol. 2, N° 2, pages 173 – 177, 1960.
- Bush.E.A, 'Cristobalite Suppression in High-Silica Li₂O-Al₂O-SiO₂ Devitrified Glass Frits', U.S. Patent number 3,951,670, (1976).

Cailleteau.C. *et al.*, 'Insight into silicate-glass corrosion mechanisms', *Nature Materials*. Pages 7,978 – 983, 2008.

Carter.C. 'Spinodal Decomposition' lecture notes; Department of Materials and Engineering, MIT, 2002, <http://pruffle.mit.edu> (visited 6/2009).

Chaysuwan.D. 'Novel high-strength machinable glass-ceramics.', PhD thesis, Leeds University.

Chemistry Department, UCL, 2005, <http://pd.chem.ucl.ac.uk> (visited 1/2007).

Chen.X. *et al.*, 'Investigation on Phase Separation, Nucleation and Crystallization in Bioactive Glass-Ceramics Containing Fluorophlogopite and Fluorapatite.', *Ceramics International* 24, pages 401-410, 1998.

Chung.F.H. *et al.*, 'Industrial applications of X-Ray diffraction', CRC Press, 1999.

Dasgupta.S. *et al.*, 'Compositional characteristics of kinoshitalite from the Sausar Group', India, *American Mineralogist*, 74, pages 200-202, 1989.

'Dental Ceramics', EN ISO 6872:1998.

Denry.L. *et al.*, 'Effect of Additives on the microstructure and thermal properties of a mica based glass-ceramic', *J.Biomed Mater. Res (Appl. Biomater)* 63, Pages 146-151, 2001.

Deer.W.A. *et al.*, 'An introduction to rock forming minerals', 2nd edition, Pearson Education Ltd, 1992.

Dollase.W.A. 'Reinvestigation of the structure of low cristobalite', *Zeitschrift Für Kristallograpie*, Bd. 121, pages 369 – 377, 1965.

Drummond.G. *et al.*, 'Kinetic study on the hexacelsian-celsian phase transformation', *Journal of Materials Science Letters* 13, pages 423-424, 1994.

Elliott.S.R. 'Physics of Amorphous Materials', Longman, 1983.

El-Meliegy.E.A.M *et al.*, 'Enstatite-celsian glass-ceramics', *Materials Characterization* 55, pages 28-34, 2005.

El-Shennawi.A.W.A *et al.*, 'Effect of fluoride nucleating catalyst on crystallisation of cordierite from modified basalt-based glasses', *Journal of the European Ceramic Society* 27, pages 1829-1833, 2007.

Fleet.M.E. 'Micas, Second Edition', Volume 3A, The Geological Society, 2002.

Finsy.R. 'On the critical radius in Ostwald ripening', *Langmuir* 20, pages 2975 – 2976, 2004.

Giacovazzo.C. *et al.*, 'Fundamentals of Crystallography', Second Edition, Oxford Science Publications, 2002.

Gnos.E. *et al.*, 'Kinoshitalite, Ba(Mg)₃(Al₂Si₂)O₁₀(OH,F)₂, a brittle mica from a manganese deposit in Oman:Paragenesis and crystal chemistry', *American Mineralogist*, Volume 85, pages 242-250, 2000.

Goldschmidt.V.M, *Geochemische Verteilungsgesetze der Element viii*, Vid, Akad, 1926.

Goodman.C.H.L, *Phys. chem. Glasses*, 26, 1985.

Goeuriot.D., 'Enstatite Based Ceramics for Machinable Prosthesis Applications', *Journal of the European Ceramic Society* 18, pages 2045 – 2056, 1998.

Grossmann.D.G., 'Tetrasilicic Mica Glass-Ceramic article' U.S. patent number 3,839,055, 1974.

Hammond.C, 'The Basics of Crystallography and Diffraction', 2nd edition, Oxford Science, 2001.

Henry.J.P., 'An Investigation into the Composition-Structure-Property Relationships of Novel Machinable Fluormica Based Glass-Ceramics.' Ph.D. Thesis, 2001.

Henry.J.P. *et al.*, 'The influence of Lithia content on the properties of fluorphlogopite glass-ceramics. I. Nucleation and crystallisation behaviour', *Journal of Non-Crystalline solids* 319 1-12, 2003.

Hill.R.G. *et al.*, 'Apatite-mullite glass-ceramics', *Journal of non-crystalline solids* 196 (1996), pages 346-351.

Hill.R.G. *et al.*, 'Influence of alumina content on the nucleation crystallisation and microstructure of barium fluorphlogopite glass-ceramics based on 8SiO₂.YAl₂O₃4MgO2MgF₂BaO', *Journal of Materials Science* 39, pages 2499 – 2507, 2004.

- Hill.R.G. *et al.*, 'Characterisation of fluorine containing glasses and glass-ceramics by ^{19}F magic angle spinning nuclear magnetic resonance spectroscopy' *Journal of the European Ceramic Society* 29, pages 2185-2191, 2009.
- Hillier S. 'Use of an air-brush to spray dry samples for X-ray powder diffraction', *Clay Minerals*, 34, pages 127-135, 1999.
- Hing.P. 'The strength and fraction properties of glass-ceramics', *Journal of Materials Science* 8, pages 1041 – 1048, 1973.
- Hoda.S.N. and Beall.G.H., 'Alkaline Earth Mica Glass-Ceramics', *Journal of the American Ceramic Society*,4, pages 287-300, 1982 .
- Institut Laue-Langevin website, <http://www.ill.eu/> (visited 1/2007).
- Jambi.S.M., 'Novel Zirconia Toughened Micaceous Glass-Ceramics for Dental Applications using CAD/CAM systems.', Ph.D. Thesis, 2007.
- King.T.T. *et al.*, 'Thermochemical reactions and equilibria between fluoromicas and silicate matrices: A petromimetic perspective on the structural ceramic composites', *J. Am. Ceram. Soc.*, 83[9], pages 2287-96, 2006.
- Kittel.C., 'Introduction to Solid State Physics' Wiley, 1996.
- Klaus.M. *et al.*, U.S. patent number 5098942, 'Binder for Metal or Ceramic Powder', March 24th 1992.
- Kuehni.R.G. 'Color Space and its Divisions', Wiley & Sons publishing, 2003.
- Larson.A.C. *et al.*, 'GSAS Manual', University of California, 1985-2004.
- Lee.K.T. *et al.*, 'Synthesis of Hexacelsian Barium Aluminosilicate by a Solid-State Process' *J.Am.Ceram.Soc*, 83 [12], pages 2907-12 (2000).
- Lee.W.E. *et al.*, 'The importance of crystallisation hierarchies in microstructural evolution of silicate glass-ceramics', *J. Am. Ceram. Soc.*, 90 [3], pages 1551-2916, 2007.
- Li.H. *et al.*, 'Study on machinable glass-ceramic containing fluorophlogopite for dental CAD/CAM system', *J Mater Sci: Mater Med* 17: pages 1133-1137, 2006.
- Marotta.A, 'Heterogeneous bulk nucleation and differential thermal analysis' *Journal of Thermal Analysis*, vol. 21, pages 227-233, 1981.

Matusita.K. and Saka.S. 'Kinetic study on crystallization of glass by differential thermal analysis – criterion on application of Kissinger plot.' *Journal of Non-Crystalline Solids*, 38&39, pages 741-746, 1980.

Marotta.A., Buri.A. and Branda.F. 'Nucleation in Glass and Differential Thermal Analysis.' *Journal of Materials Science*, 16, pages 341-344, 1981.

Ma.D.S. *et al.*, *Journal of Radioanalytical and Nuclear Chemistry*, vol. 217. N° 2, pages 225-227, 1997.

McCusker.L.B. *et al.*, 'Rietveld refinement guidelines.' *J. Appl. Cryst.* (1999). 32, pages 36-50, 1998.

McMillan, P.W., 'Glass ceramics', 2nd Edition. London and New York: Academic Press, 1979.

Miyata.N. 'Discussion of the indentation hardness of a glass-ceramic with particulate microstructure', *Journal of Materials Sciences* 17, pages 2693 – 2699, 1982.

Moorehead.R. *et al.*, 'Crystallisation of fluorapatite-fluormica based bioceramics', ILL Experimental Report, 15/10/2007.

Momma.K. *et al.* 'Vesta: a three dimensional visualisation system for electronic and structural analysis', *J. Appl. Crystallography* 41, pages 653-658, 2008.

Ochi.Y, 'Orientated crystallization of fresnoite glass-ceramics by using a thermal gradient.', *Journal of the European Ceramic Society* 26 (2006) 627-630.

Ostrogorsky.A.G., 'Single-crystal growth by submerged heater method', *Meas. Sci. Technol.* 1 (1990) 463-464.

Prison.J.M. *et al.*, 'Crystallization of barium magnesium phosphate glasses determined by differential thermal analysis and X-ray diffraction', *Journal of Non-Crystalline Solids* 354, pages 4723-4726, 2008.

Qin-bo.W. *et al.* 'On the critical radius in generalized Ostwald ripening', *Journal of Zhejiang University Science*, volume 6B (8), pages 705-707, 2005.

Randall.D, 'Instruments for the measurement of color', Datacolor International, Charlotte, NC.

Ray.N.H, 'Inorganic Polymers', London, New York and San Francisco: Academic Press.

Reise.M. *et al.*, 'High-Strength, Translucent Mica Glass-Ceramics', patent n° 6,080,692, Jun. 27th 2000.

Rietveld.H.M. 'A profile refinement method for nuclear and magnetic structures', Journal of applied crystallography 2, pages 65-71, 1969.

Sadale.S.B. *et al.*, 'Synthesis of type-II textured tungsten disulfide films with bismuth interfacial layer as a texture promoter.', Thin Solid Films 515, pages 2935-2942, 2007.

Sarswati.V. *et al.*, 'Crystallisation of Mica in the K₂O-SiO₂-MgO-MgF₂ glass system', Bull. Material Science, vol. 13, N° 4, pages 283-291, September 1990.

Scholze.H. 'Glass: Nature, Structure, and Properties', Springer-Verlag Berlin and Heidelberg GmbH, 1991.

Sheldrick.G.M. 'A short history of Shelx', Acta. Cryst. A64, pages 112-122, 2008.

Shelby.J.E. 'Introduction to Glass Science and Technology', RSC series, 2005.

Silva.G.W.C. *et al.*, 'Micro-structural characterization of precipitation – synthesized fluorapatite nano-material by transmission electron microscopy using different sample preparation techniques', Micron, Volume 39, Issue 3, pages 269 – 274, 2008.

Slutsker.A.I *et al.*, 'Hardness of microporous SiC ceramics', Technical Physics, Vol 53, N° 12. Pages 1591 – 1596, 2008.

Smith.D. *et al.*, 'High temperature X-ray studies on the polymorphism of MgSiO₃', Z Kristallogr. 118, pages 186-212, 1963.

Speight.J. 'Lange's Handbook of Chemistry', 16th Edition, McGraw-Hill, 2005.

Speck.A.L. 'Platon, a multipurpose crystallographic tool', Utrecht University, Utrecht, The Netherlands, 2001.

Squires.G.L, 'Introduction to the Theory of Thermal Neutron Scattering', Dover, 1996.

Tammann.G. 'Aggregatzustände', second edition Voss, 1923.

- Taruta.S. *et al.*, 'Crystallisation process and some properties of calcium mica-apatite glass-ceramics.', *Journal of Non-crystalline Solids* 296 (2001), pages 201-211.
- Thompson.J.Y. *et al.*, 'Mechanical properties of a new mica based glass-ceramic for CAD/CAM restorations', *J. Prosth. Dent.* 76, pages 619-623, 1996.
- Uno.T. *et al.*, 'High-Strength Mica-Containing Glass-Ceramic', *J.Am. Ceram. Soc.*, 74 [12], pages 3139-41, 1991.
- Uno.T. *et al.*, 'Microstructure of Mica-Based Nanocomposite Glass-Ceramics', *J. Am. Ceram. Soc.* 76[2], pages 539-541, 1993.
- Vogel.W., 'Structure and Crystallisation of Glass', Oxford, Pergammon Press, 1971.
- Wang.Z. *et al.*, 'Coloration of mica glass-ceramic for use in CAD/CAM system', *Material Letters* 57, pages 425-428, 2002.
- Wang.P. *et al.*, 'Influence of nucleation agents on crystallisation and machinability of mica glass ceramics' *Ceramics International*, Volume 35, Issue 7, Pages 2633-2638, Sept. 2009.
- Walford.L.K., 'Single crystal and powder data for lead fluorophosphates', *Acta Cryst.* (1967), 22, page 324, 1966.
- Wolf.G. *et al.*, *J.Dent Res* 1973; 52; page 467. 1973
- Wood.D. *et al.*, 'Glass Ceramics', patent WO/2004071979, (26/8/2004).
- Xiang *et al.*, 'Nucleation and growth of needle like fluorapatite crystals in bioactive glass-ceramics' *Journal of non-crystalline solids*, Volume 354, Issues 10-11, Pages 938 – 944, February 2008.
- Yasuda.M. *et al.*, 'Electron Microscopy of Clinoenstatite from a Boninite and a Chondrite', *Phys Chem Minerals*, pages 192-196, 1983.
- Yasukama.K. *et al.*, 'Crystallinity analysis of glass-ceramics by Rietveld method.' *J. Am. Ceram. Soc.*, 81[11], pages 2978-82, 1998.
- Yoshii.M. *et al.*, 'On the intensity changes of basal reflections with relation to barium content in maganoan phlogopites and kinoshitalite', *Bulletin of the Geological Survey of Japan*, 24, pages 1-8, 1973.
- Zarchariasen.W.H, 'The atomic arrangement in glass', *J.Am. Ceram. Soc.*, 54, 1932.

Zarzycki.J. 'Glasses and the vitreous state', Cambridge Solid Sciences Series, Cambridge University Press 1991.

Zheng.H.Y. *et al.*, 'Hall-Petch relationship in nanocrystalline selenium prepared by crystallisation from the amorphous state', J. Appl. Phys, Vol 77, N^o 6, pages 2811 – 2813, 1994.

APPENDICES

A1.1-1.5: *Searchmatch* simulations

A1.6-A1.16: PDF cards

A1.17: Phases and properties in bulk LDIG 24 commercial

A2.1-A2.7: Additional SEM/EDS work

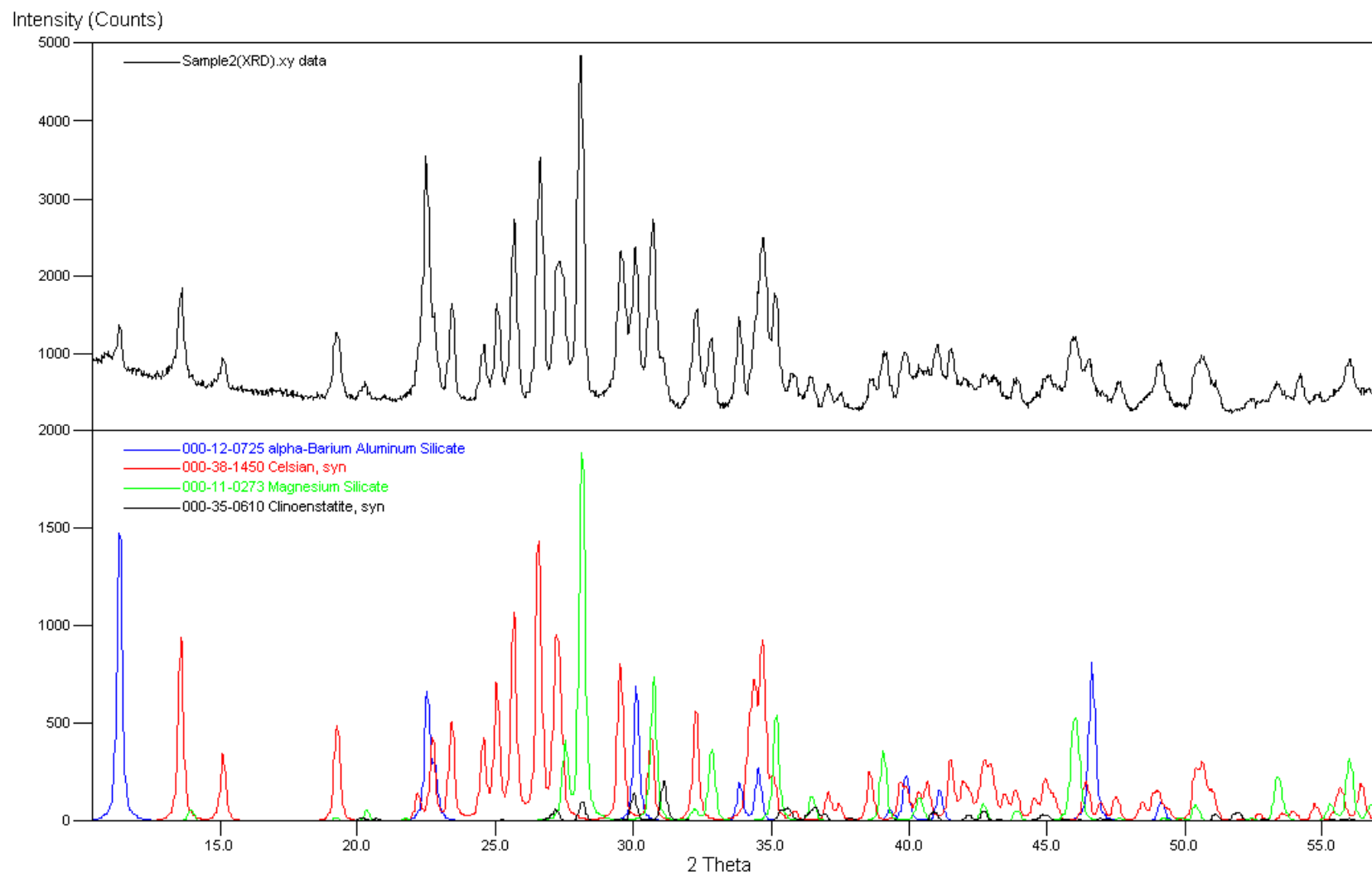
A3.1: Thermal modelling of single crystal growth experiment

A4.1: Simpson's rule

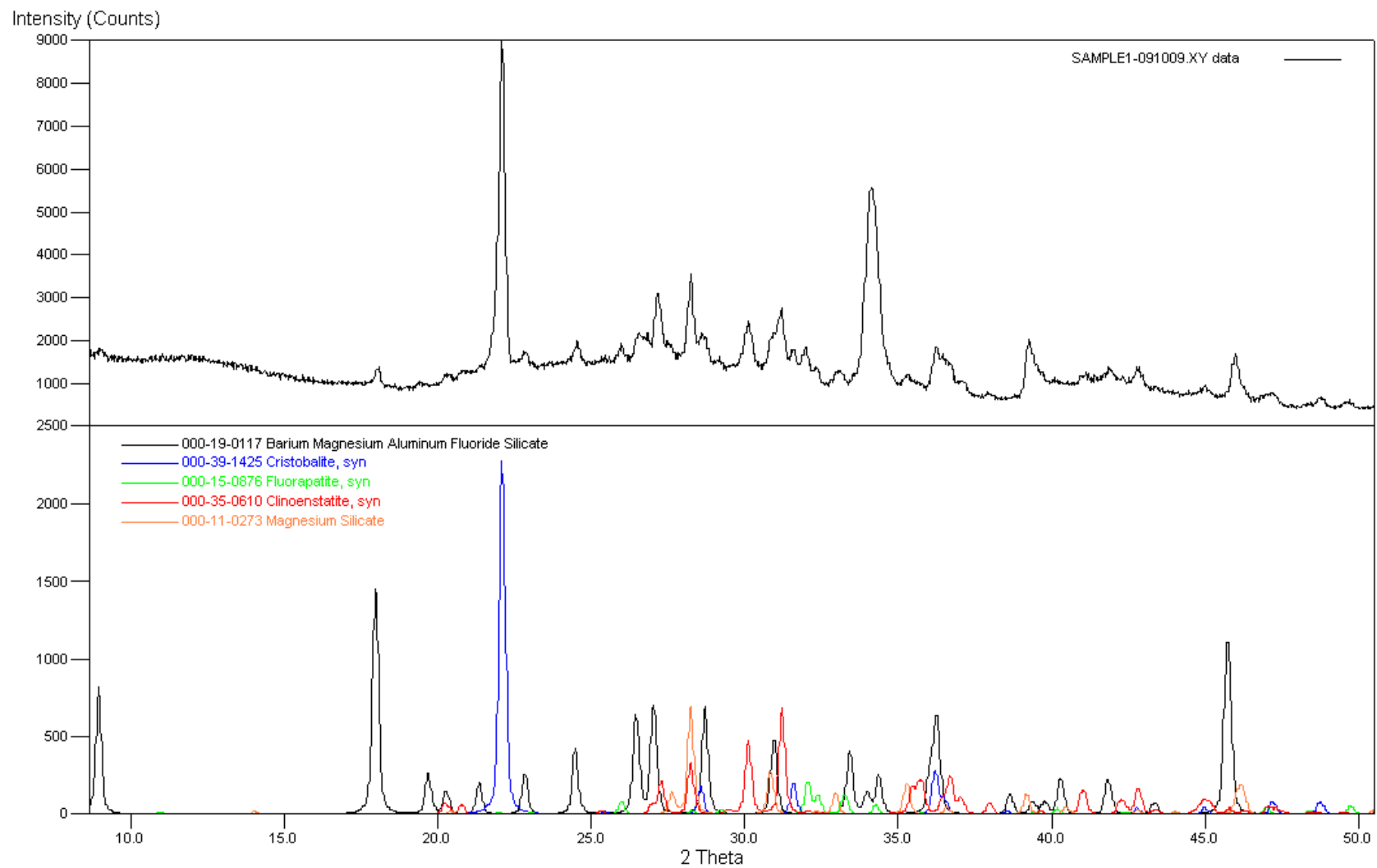
A5.1-A5.2: Structure of bulk Mica and BFP phases

A6.1: Presentations

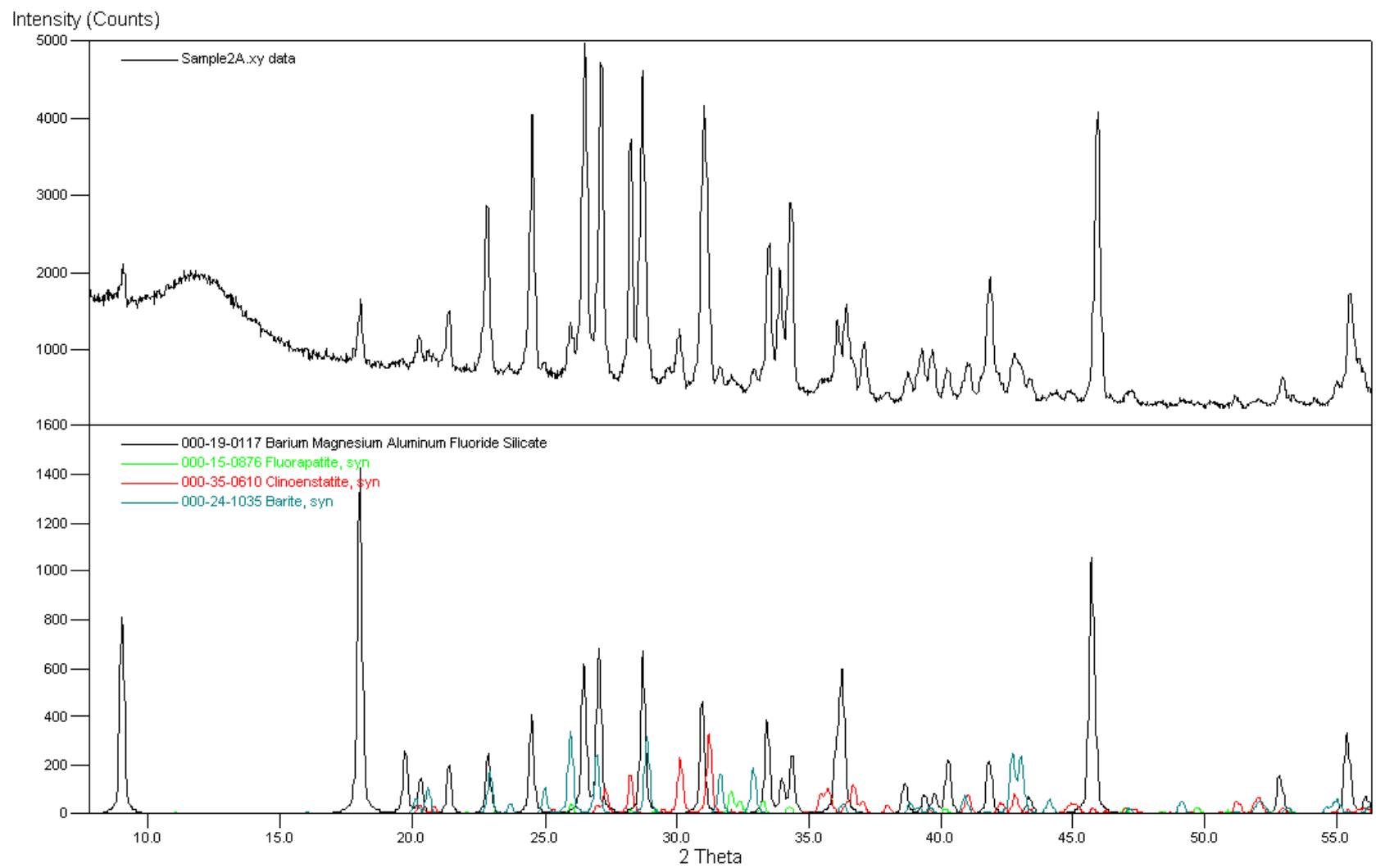
A7.1: *Shelx 97 .FCF* output file from single crystal refinement



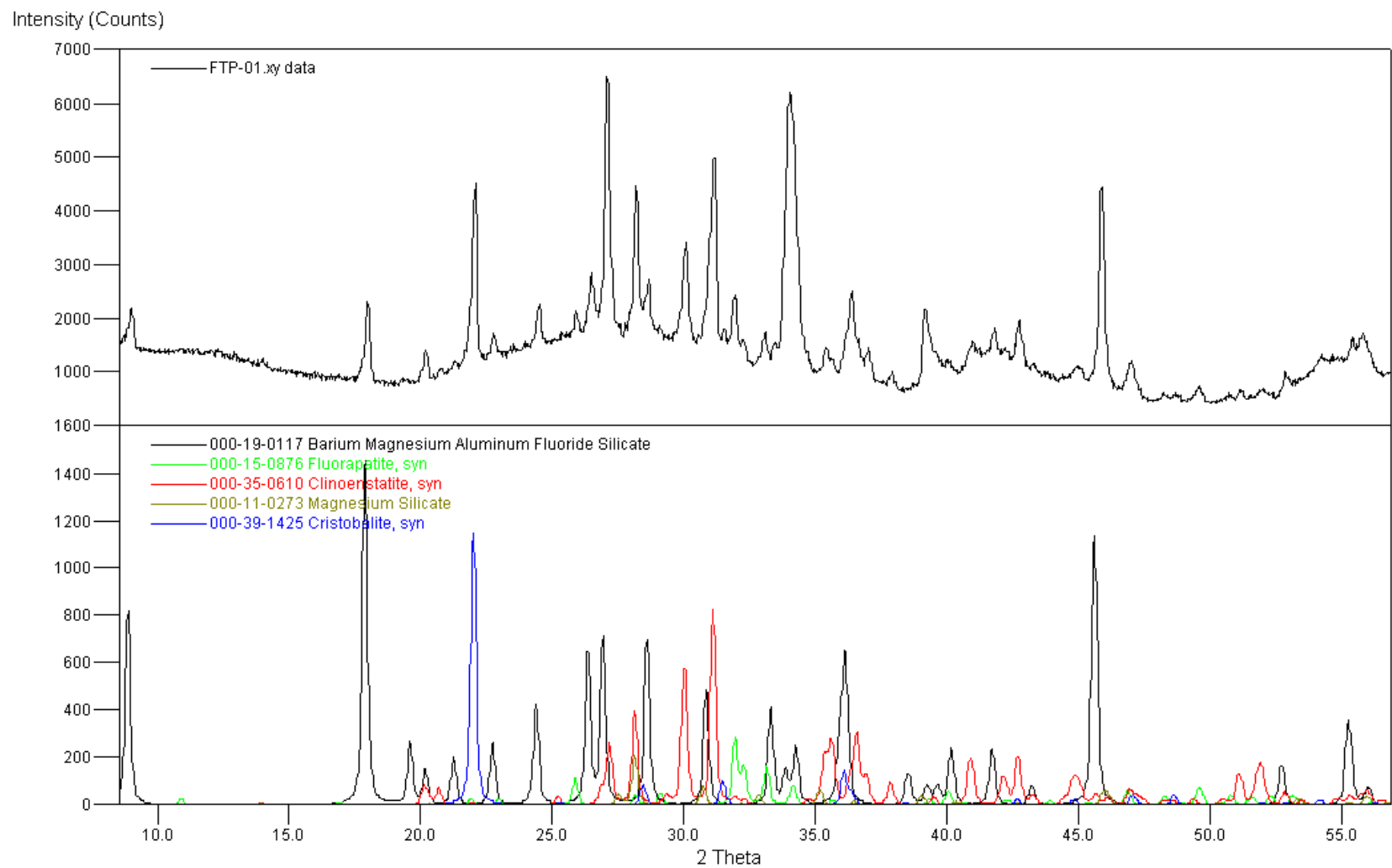
AI.2 Multi-Phase Simulation of Figure 4.48



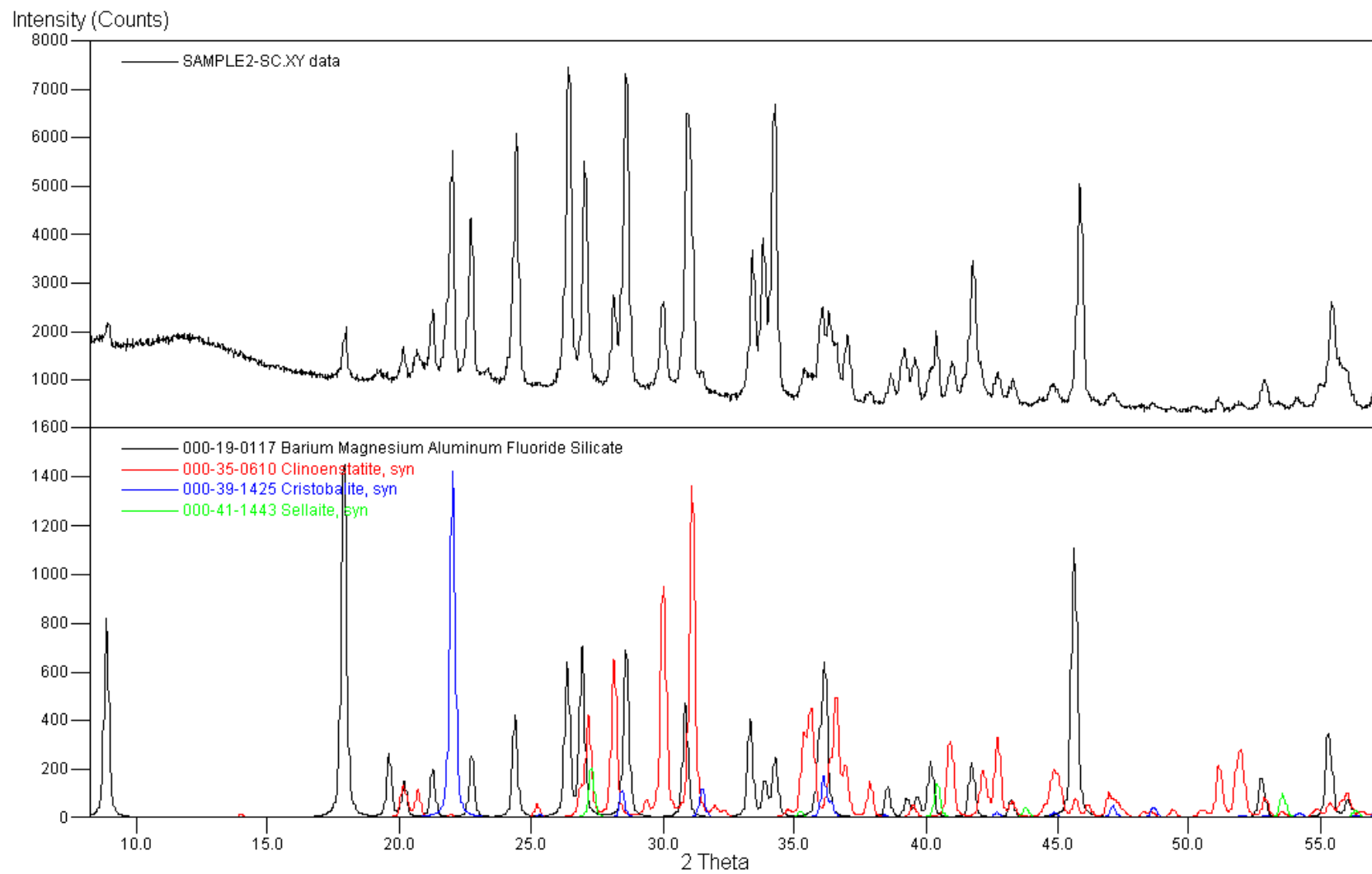
A1.3 Multi-Phase Simulation of Figures 4.36 – 4.38



A1.4 Multi-Phase Simulation of Figures 4.29 – 4.35



A1.5 Multi-Phase Simulation of Figures 4.42 - 4.47



A1.6 Barium Aluminum Silicate (Celsian, Synthetic)

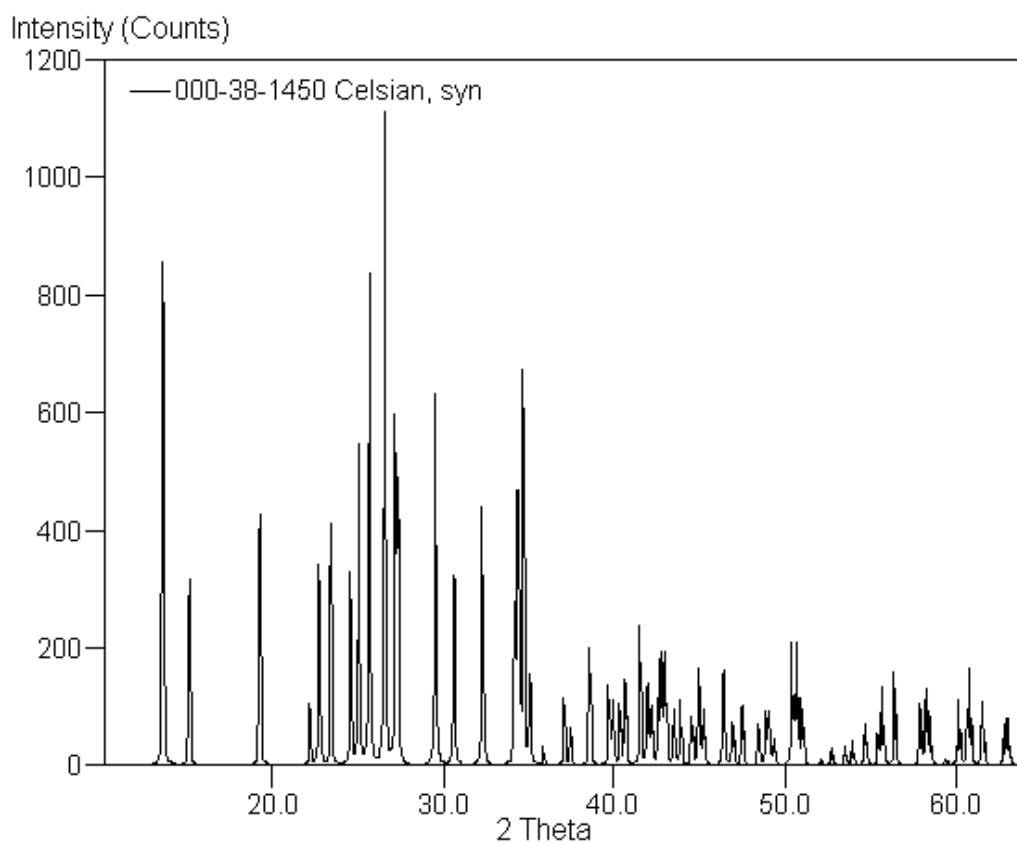
Formula: Ba Al₂ Si₂ O₈
PDF Number: 000-38-1450
Quality: star

Cell and Symmetry Information

System: monoclinic
a: 8.6411 Å **b:** 13.047 Å
β: 115.075°
Density: 3.380 **Z:** 4

Space Group: C2/m
c: 7.2031 Å

Wavelength: - 1.5406 Å



A1.7 Alpha-Barium Aluminum Silicate

Formula: Ba Al₂ Si₂ O₈

PDF Number: 000-12-0725

Quality: indexed

Cell and Symmetry Information

System: orthorhombic

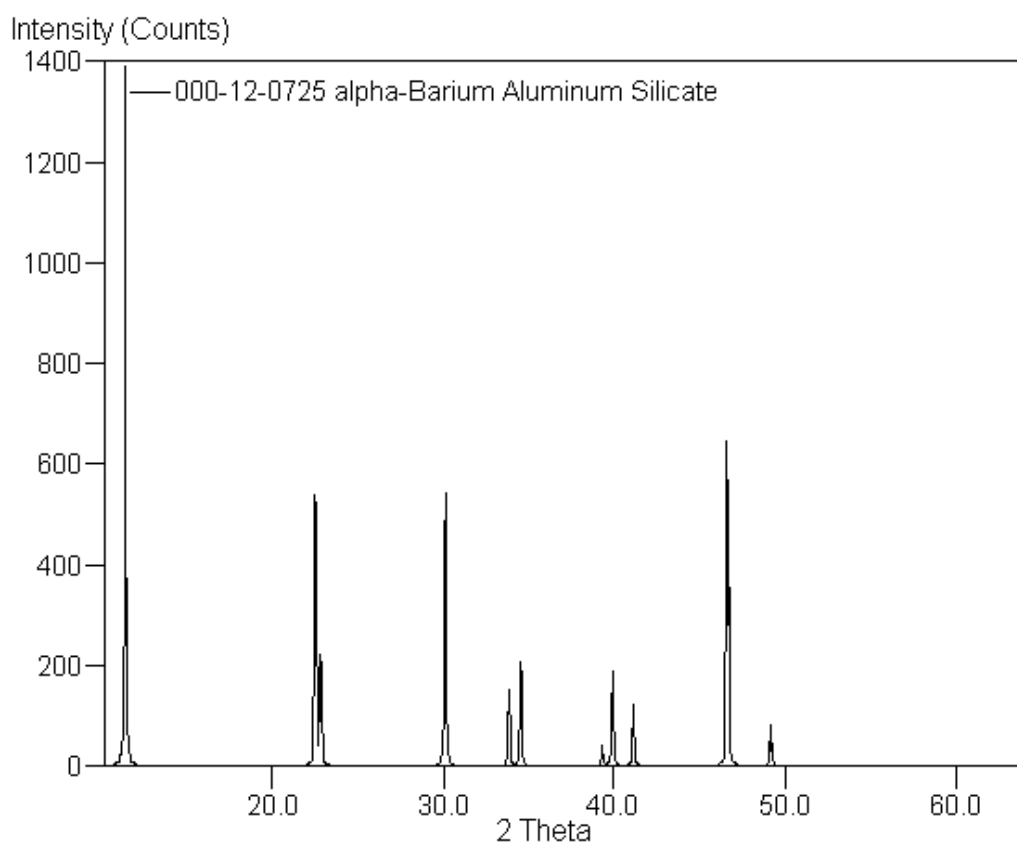
a: 5.293 Å **b:** 9.168 Å

Density: 3.290 **Z:** 2

Space Group: P6₃/mcm

c: 7.790 Å

Wavelength: - 1.5406 Å



A1.8 Magnesium Silicate (Proto-enstatite)

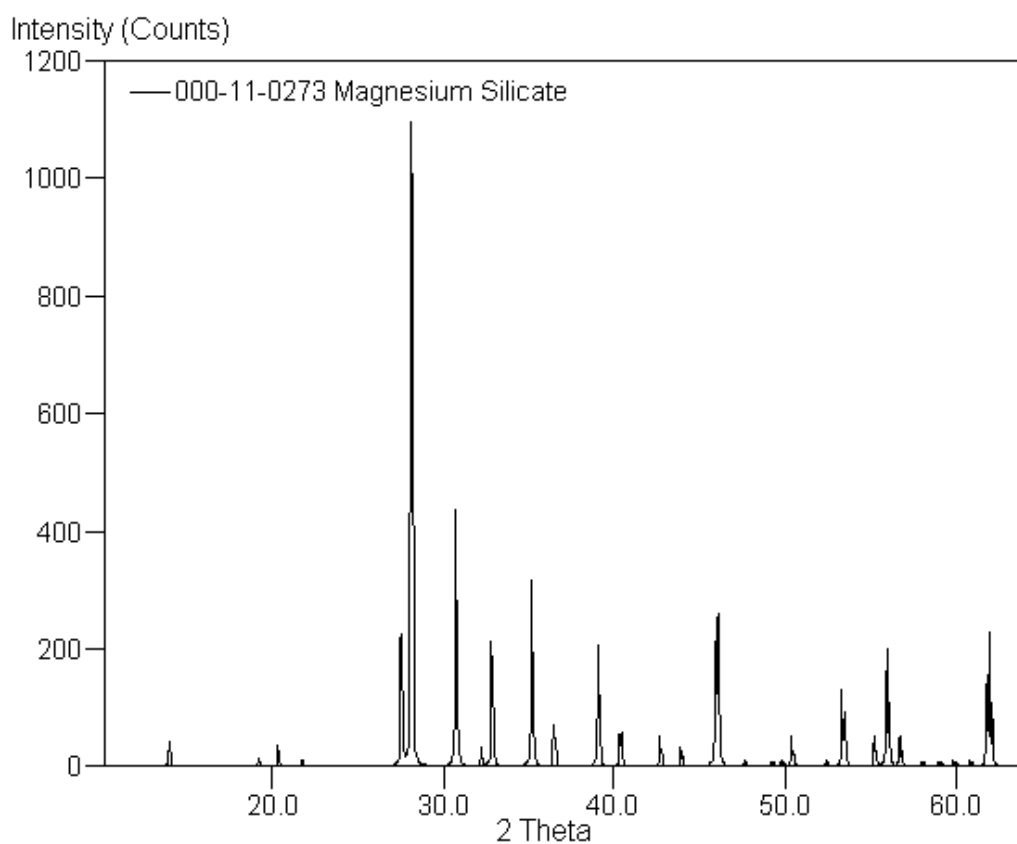
Formula: Mg Si O₃
PDF Number: 000-11-0273
Quality: indexed

Cell and Symmetry Information

System: orthorhombic
a: 9.25 Å **b:** 8.74 Å
Density: 3.101 **Z:** 8

Space Group: Pbcn
c: 5.32 Å

Wavelength: - 1.5406 Å



A1.9 Magnesium Silicate (Clinoenstatite, Synthetic)

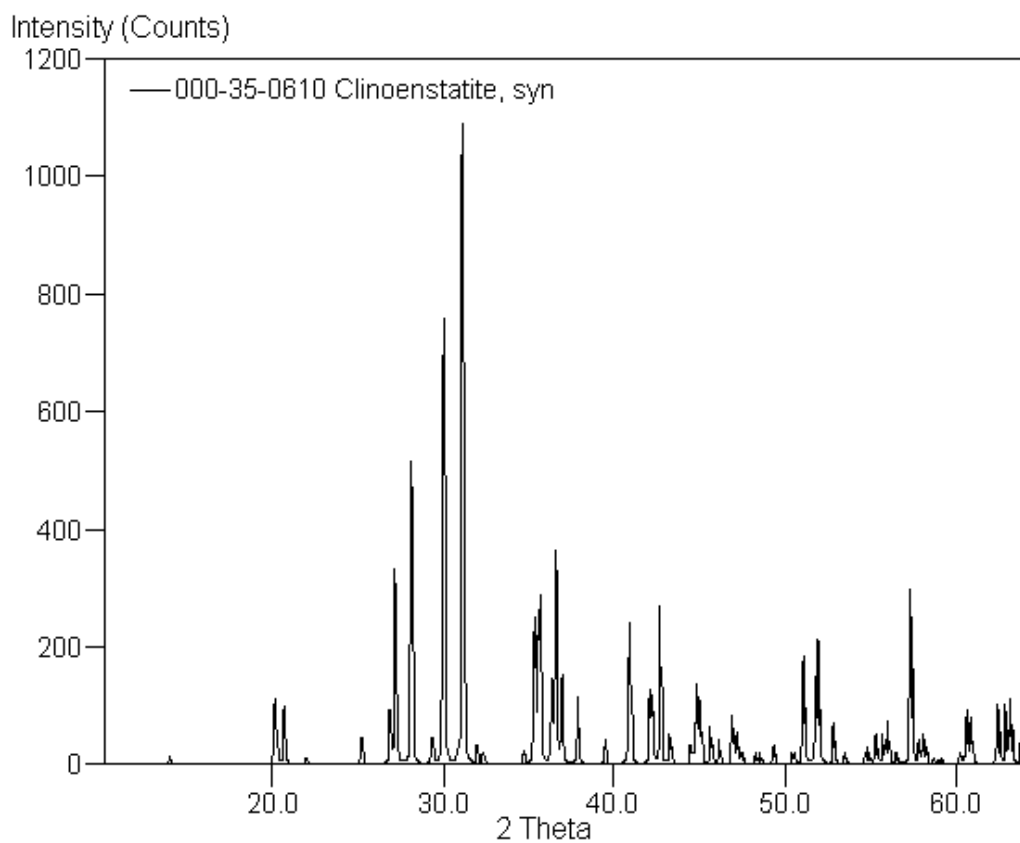
Formula: Mg Si O₃
PDF Number: 000-35-0610
Quality: star

Cell and Symmetry Information

System: monoclinic
a: 9.6061 Å **b:** 8.8185 Å
β: 108.289°
Density: 3.206 **Z:** 8

Space Group: P2₁/c
c: 5.1710 Å

Wavelength: - 1.5406 Å



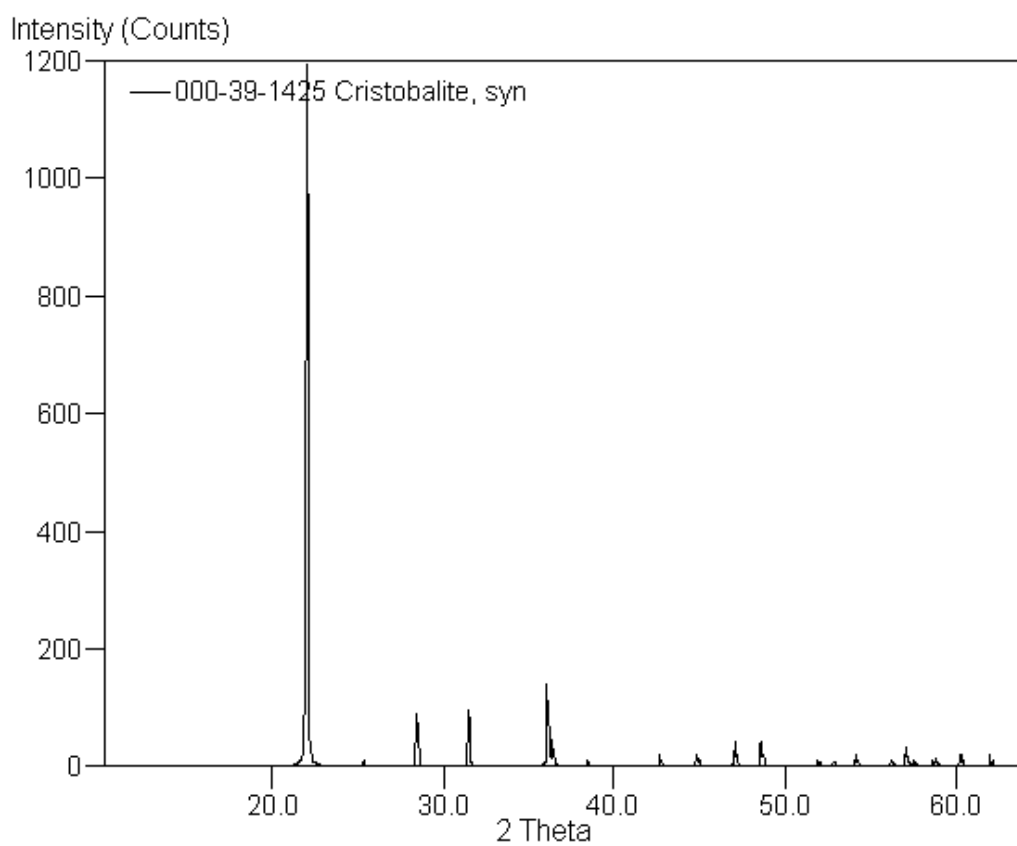
A1.10 Silicon Oxide (Cristobalite, Synthetic)

Formula: Si O₂
PDF Number: 000-39-1425
Quality: star

Cell and Symmetry Information

System: tetragonal **Space Group:** P41212
a: 4.9732 Å **c:** 6.9236 Å
Z: 4

Wavelength: - 1.5406 Å



A1.11 Calcium Fluoride Phosphate (Fluorapatite, Synthetic)

Formula: $\text{Ca}_5 (\text{P O}_4)_3 \text{F}$

PDF Number: 000-15-0876

Quality: star

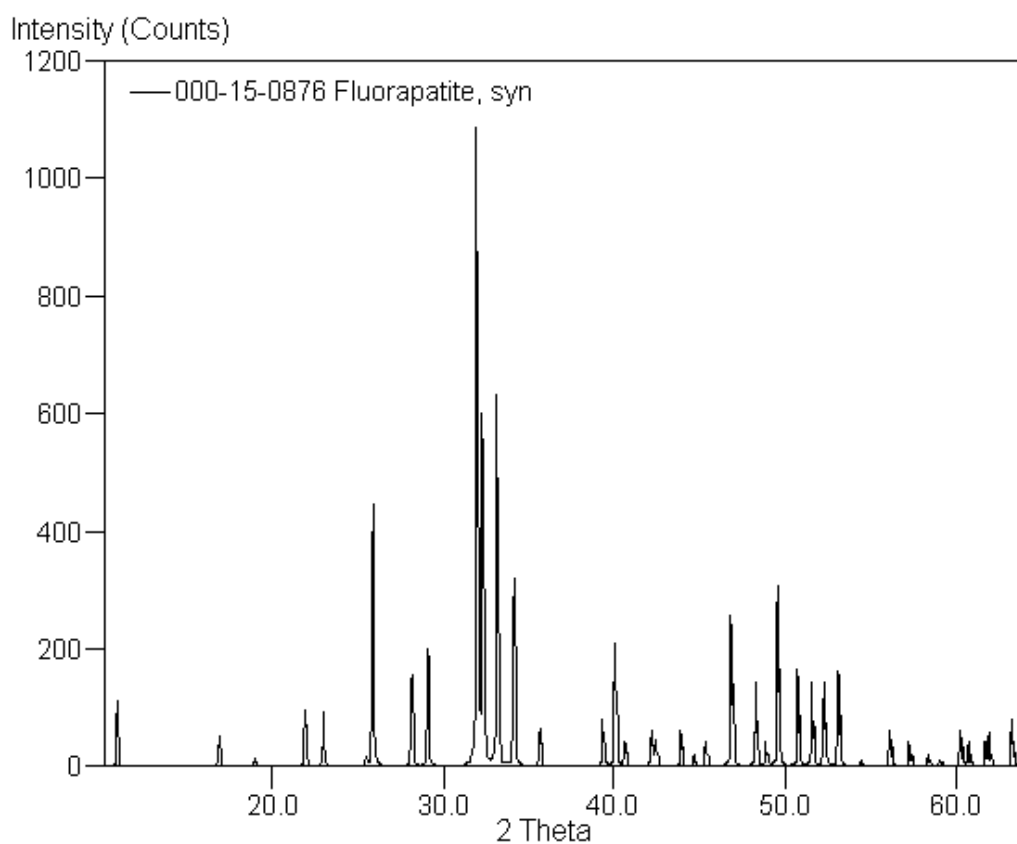
Cell and Symmetry Information

System: hexagonal **Space Group:** P63/m

a: 9.3684 Å **c:** 6.8841 Å

Density: 3.15 **Z:** 2

Wavelength: - 1.5406 Å



A1.12 Barium Magnesium Aluminum Fluoride Silicate (Ba-Mica)

Formula: Ba Mg₃ Al₂ Si₂ O₁₀ F₂

PDF Number: 000-19-0117

Quality: unknown

Cell and Symmetry Information

System: monoclinic

a: 5.312 Å **b:** 9.226 Å

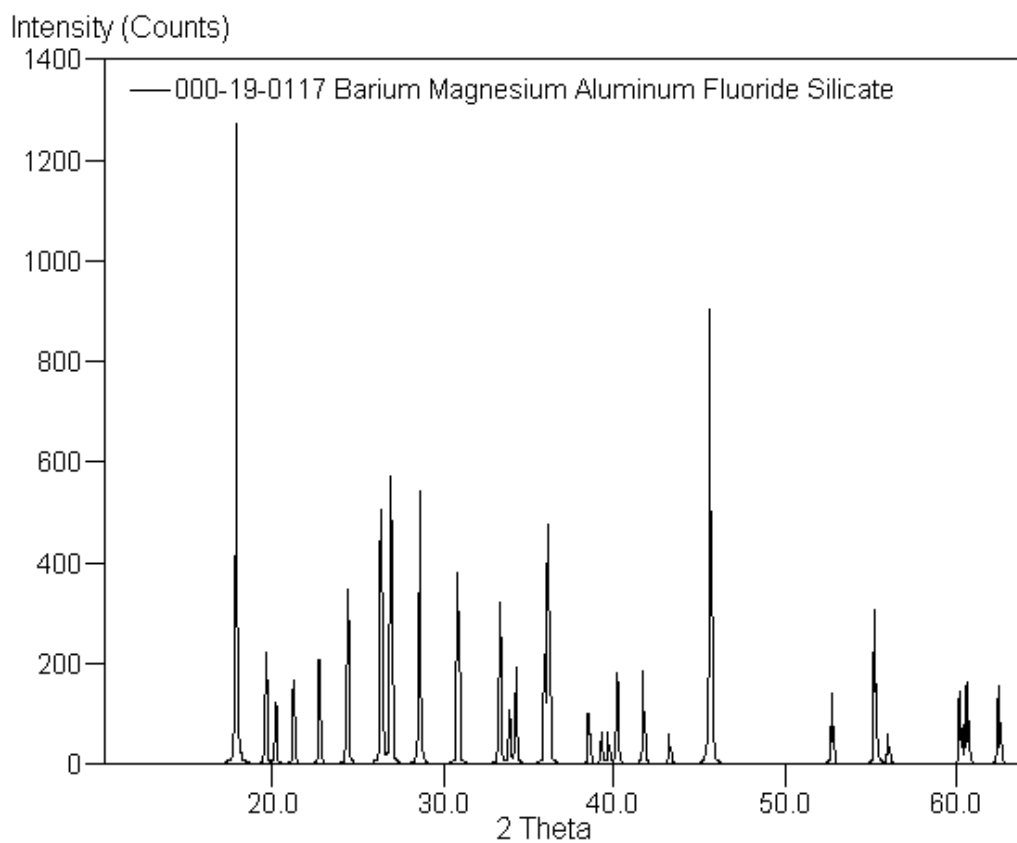
β: 100.2°

Density: 3.566 **Z:** 2

Space Group: C2/m

c: 10.100 Å

Wavelength: - 1.5406 Å



A1.13 Barium Aluminum Silicate (Hexa-celsian)

Formula: Ba Al₂ Si₂ O₈

PDF Number: 000-26-0137

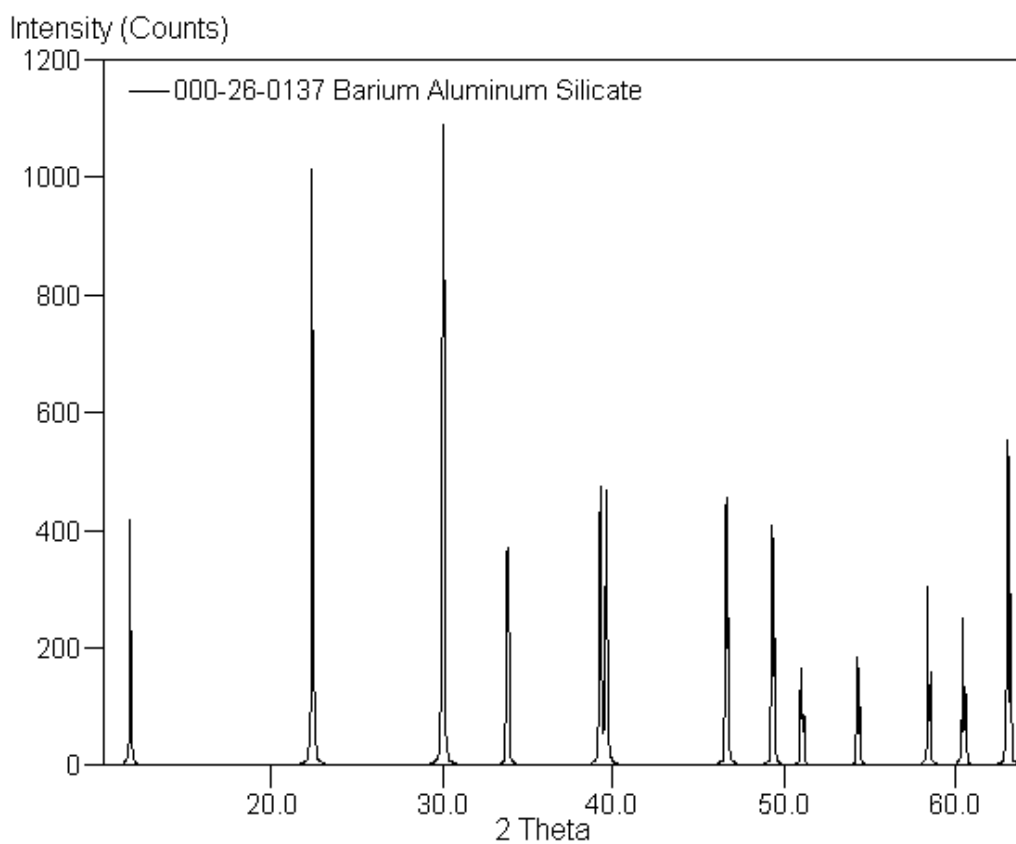
Quality: unknown

Cell and Symmetry Information

System: hexagonal **Space Group:** P6/mmm

a: 5.304 Å **c:** 7.789 Å

Wavelength: - 1.5406 Å



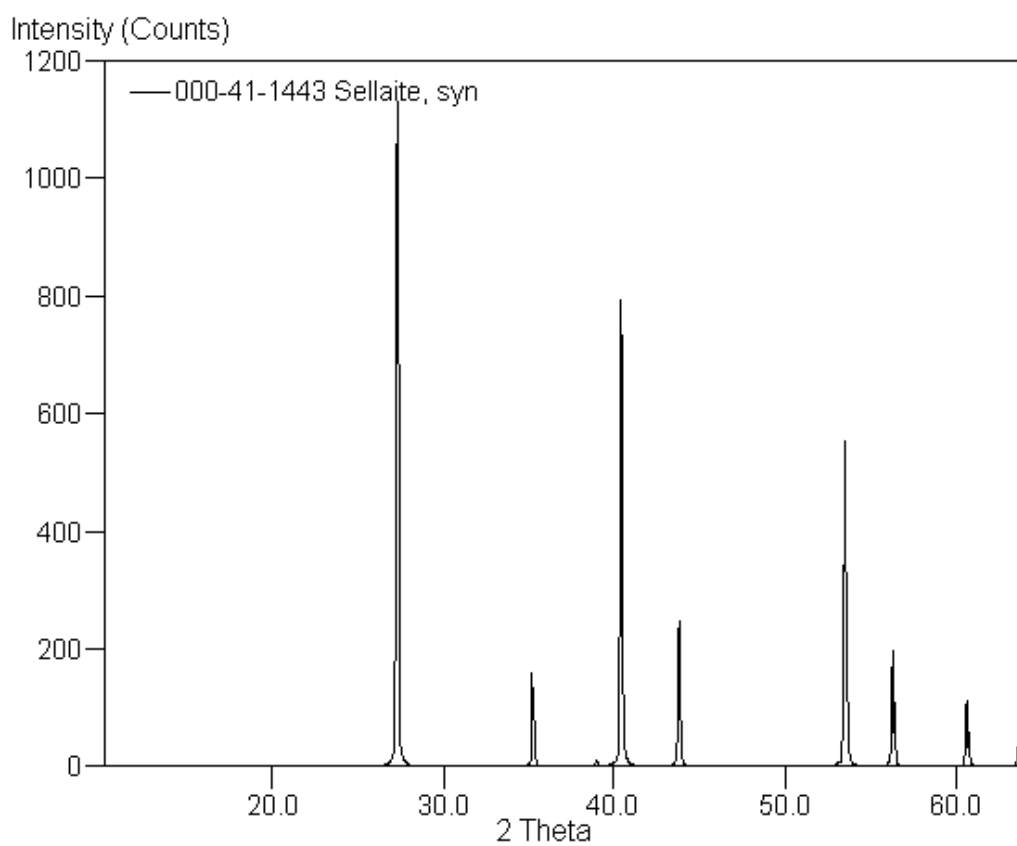
A1.14 Magnesium Fluoride (Sellaite, Synthetic)

Formula: Mg F₂
PDF Number: 000-41-1443
Quality: star

Cell and Symmetry Information

System: tetragonal **Space Group:** P42/mnm
a: 4.6200 Å **c:** 3.0509 Å
Density: 3.150 **Z:** 2

Wavelength: - 1.5406 Å



A1.15 Magnesium Fluoride Phosphate (Wagnerite)

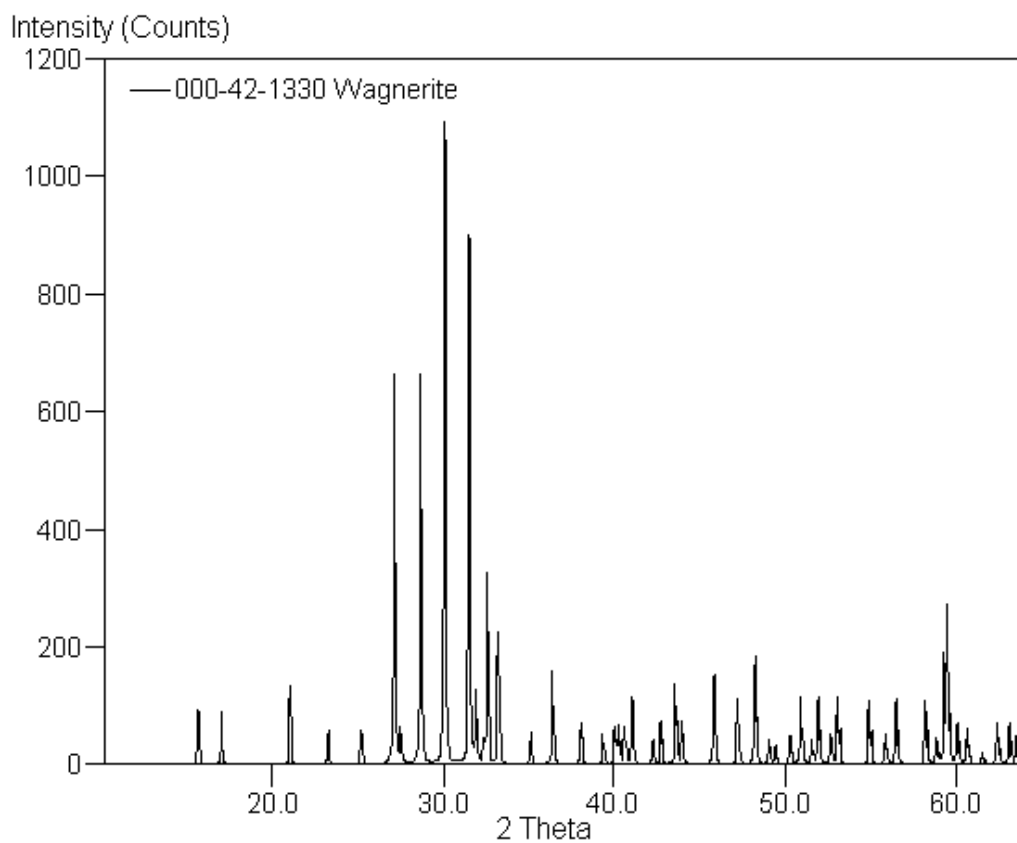
Formula: Mg₂ P O₄ F
PDF Number: 000-42-1330
Quality: indexed

Cell and Symmetry Information

System: monoclinic
a: 11.9263 Å **b:** 12.6707 Å
β: 108.283°
Density: 3.130 **Z:** 16

Space Group: P21/a
c: 9.6411 Å

Wavelength: - 1.5406 Å



A1.16 Barium Sulphate (Barite, Synthetic)

Isostructural with proposed barium fluorophosphates phase (BaPO₃F).

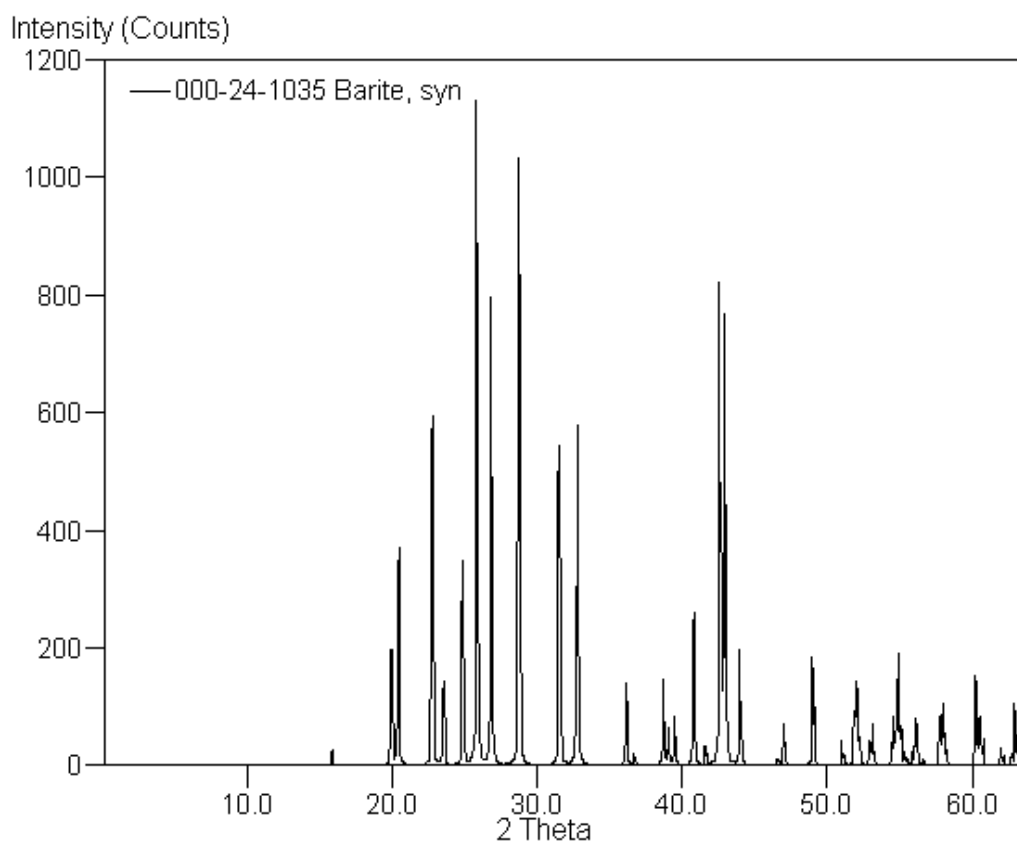
Formula: Ba S O₄
PDF Number: 000-24-1035
Quality: star

Cell and Symmetry Information

System: orthorhombic
a: 7.1565 Å **b:** 8.8811 Å
Density: 4.500 **Z:** 4

Space Group: Pbnm
c: 5.4541 Å

Wavelength: - 1.5406 Å

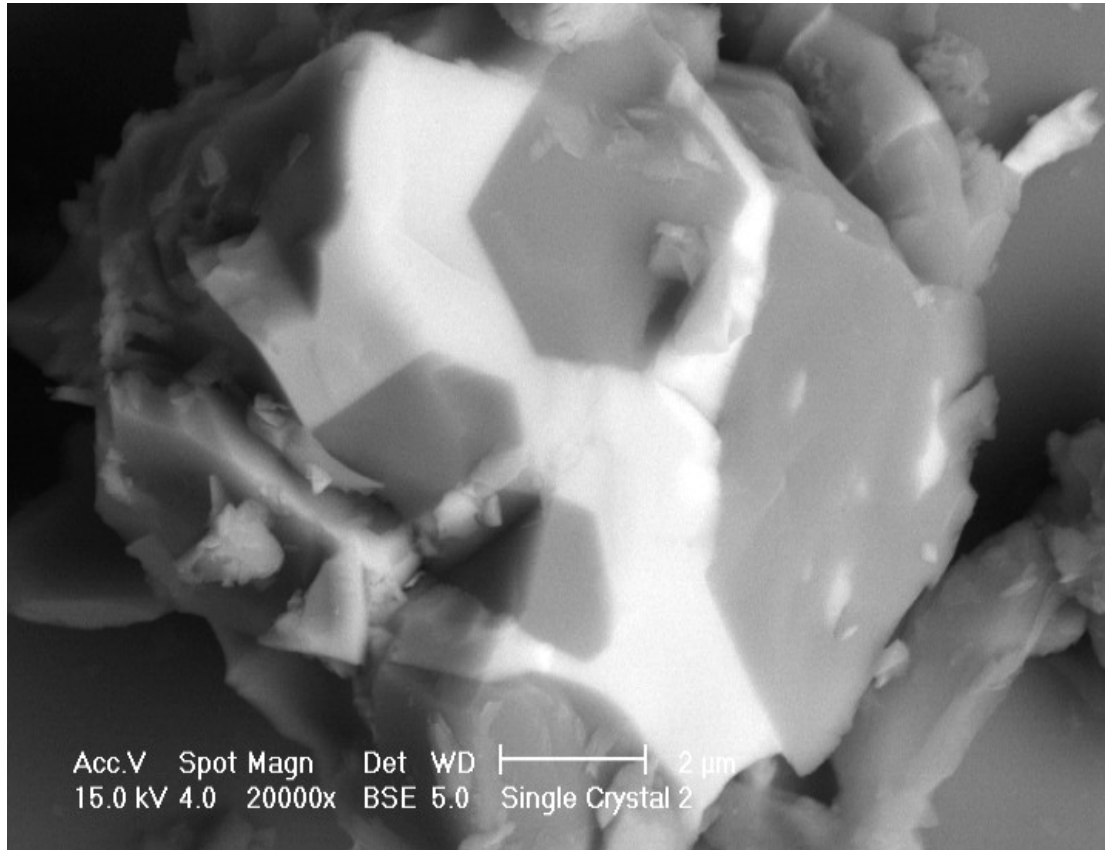


A1.17 Phases and Properties in Bulk LDIG 24 Commercial

Crystal Phase	Lattice/Space Group	a(Å)	b(Å)	c(Å)	β (°)	Hardness (Mohs)	Density (g/cm ³)	Solubility in Concentrated. HCl at 25°C	Melting Point (°C)
Kinoshitalite (Ba Depleted) (Ba _{0.7} Mg ₃ (Al _{1.4} Si _{2.6})O ₁₀ F ₂)	Monoclinic (C2/m)	5.32	9.22	10.04	100.22	2.5	3.28	No	1460 (Gnos <i>et al.</i> , 2000)
Clinoenstatite (MgSiO ₃)	Monoclinic (P2 ₁ /m)	9.60	8.82	5.17	108.29	5.5	3.21	No	1557 (Yasuda <i>et al.</i> , 1983)
Protoenstatite (MgSiO ₃)	Orthorhombic (Pbcn)	9.27	8.74	5.32	90	5.5	3.09	No	1557 (Yasuda <i>et al.</i> , 1983)
Cristobalite (SiO ₂)	Tetragonal (P41212)	4.97	4.97	6.92	90	6.5	2.33	No	1728 (Dollase <i>et al.</i> , 1965)
Fluorapatite (Ca ₅ (PO ₄) ₃ F)	Hexagonal (P6 ₃ /m)	9.39	9.39	6.89	90	5	3.18	Dissolves	1650 (Silva <i>et al.</i> , 2008)
Sellaite (MgF ₂)	Tetragonal P4 ₂ /mmm	4.62	4.62	3.06	90	5.5 (Deer <i>et al.</i> , 1992)	3.15	Slight (Speight, 2005)	1255 (Breusov, 1960)

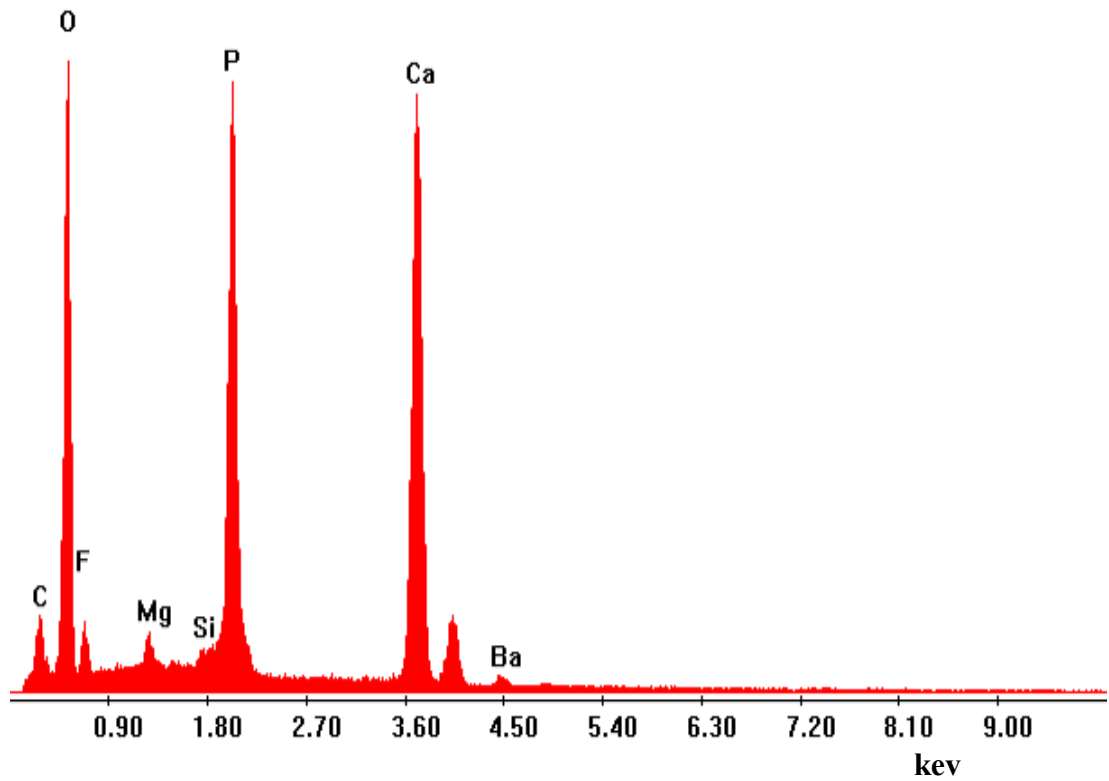
The hardness values in the table are in Mohs. The Mohs scale of hardness is ordinal and ranks the ability of one mineral to scratch another. Diamond has a Mohs hardness of 10 and is 8 times harder, in real terms, than a mineral with a Mohs hardness of 8.

A2.1 BS Micrograph of a Polycrystalline Grain from the Single Crystal Bulk Material.



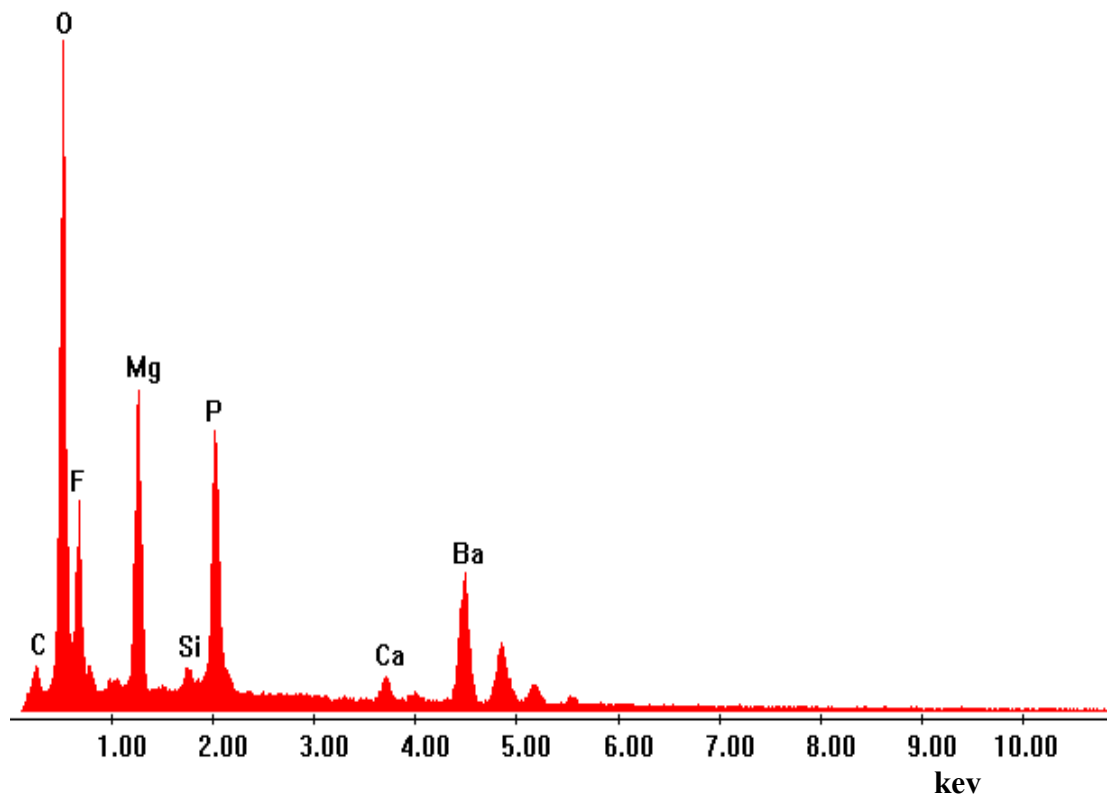
The back-scattered image above shows the higher density areas as light and the lowest as dark. Hexagonal lower density single crystals are clearly visible in contrast to the apparently barium-rich surroundings.

A2.2 EDS Spectrum of A2.1 (Hexagonal Phase)



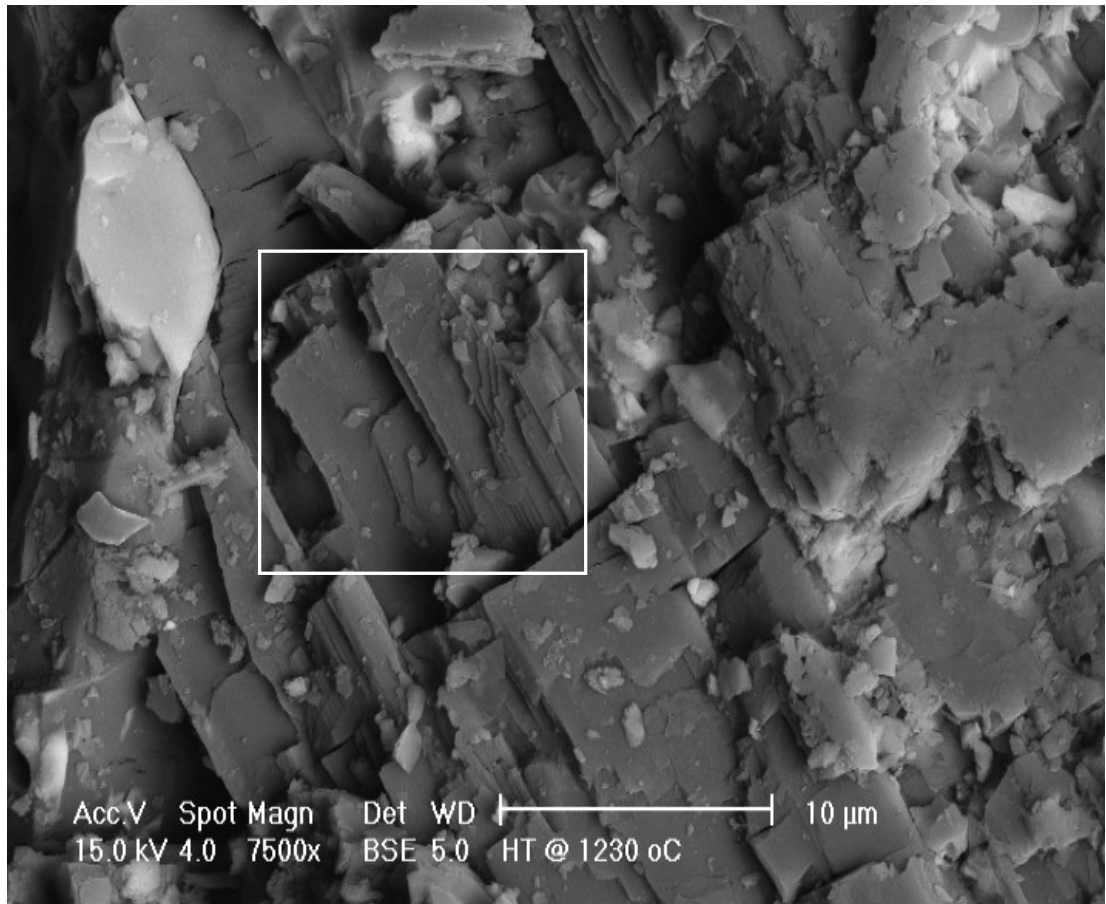
EDS on the dark areas indicates the presence of a pure calcium apatite phase with formula - $\text{Ca}_5(\text{PO}_4)_3\text{F}$; the amounts of Mg, Si and Ba are relatively negligible and are probably contamination.

A2.3 EDS Spectrum of A2.1 (Light Phase)



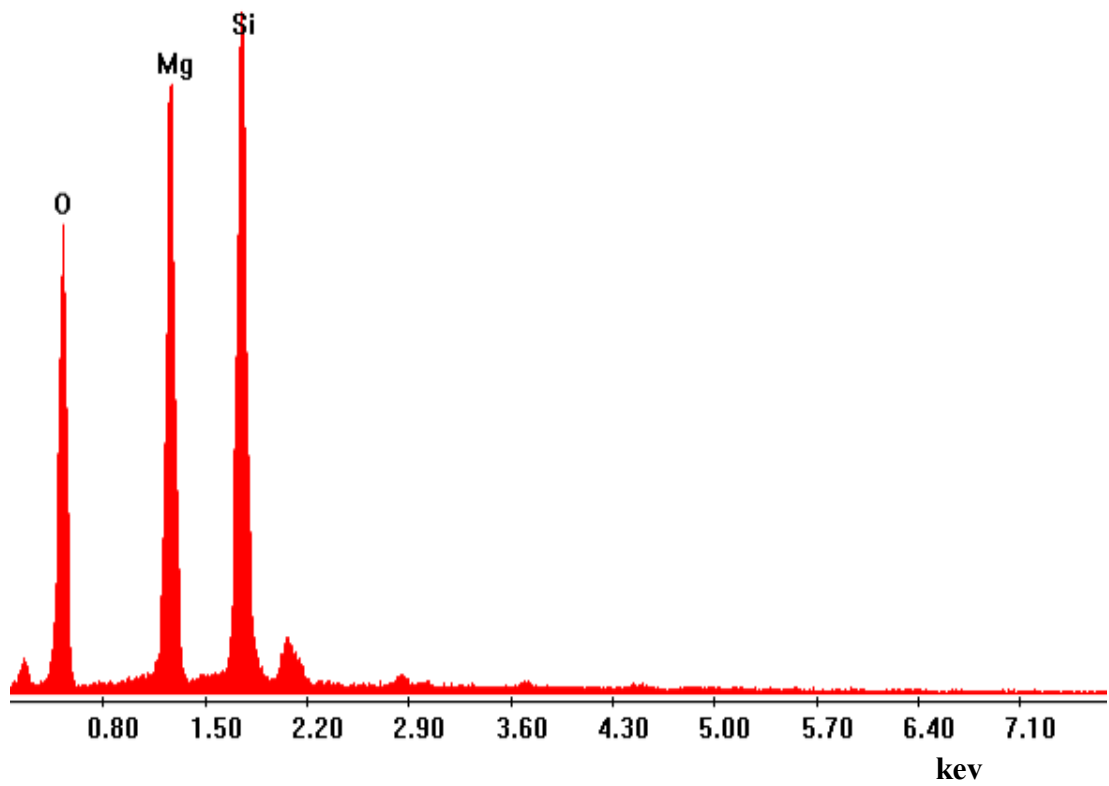
Lighter regions show a significant concentration of barium, as expected, in place of calcium, however, larger quantities of magnesium and fluorine also appear – the ratio of Ba:Mg:P:F in atomic % is 17:32:21:29. This supports the formation of Ba-apatite (BaPO_3F) and perhaps wagnerite ($\text{Mg}_2\text{PO}_4\text{F}$).

A2.5 BS Micrograph of a Crystal Lath from the Single Crystal Bulk Material.



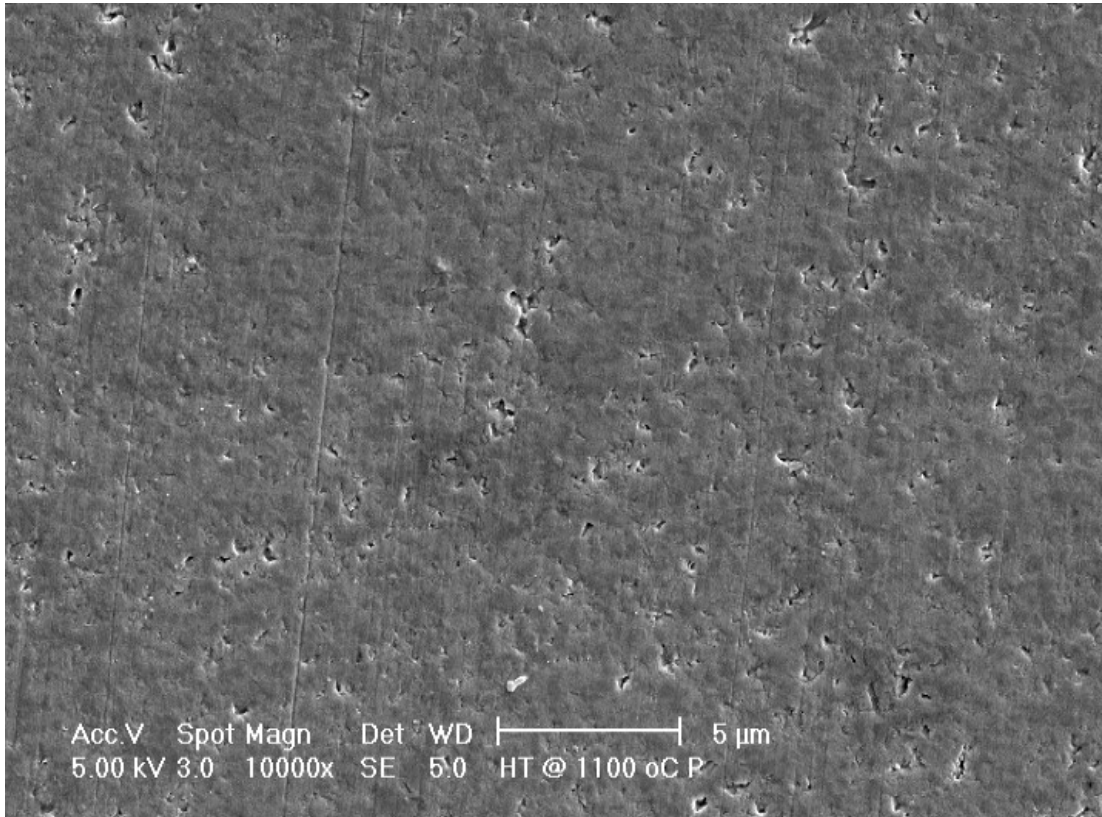
Fine wafer-like single crystals are evident in this BS image (highlighted by the box). This dark image indicates low overall barium content.

A2.6 EDS Spectrum of Crystal Phase in A2.5



The single crystal identified in A2.5 is a magnesium silicate with an approximately equal ratio of Mg and Si atoms. This corresponds to the clinoenstatite phase (and other polytypes) identified in this work with chemical formula: - MgSiO_3 .

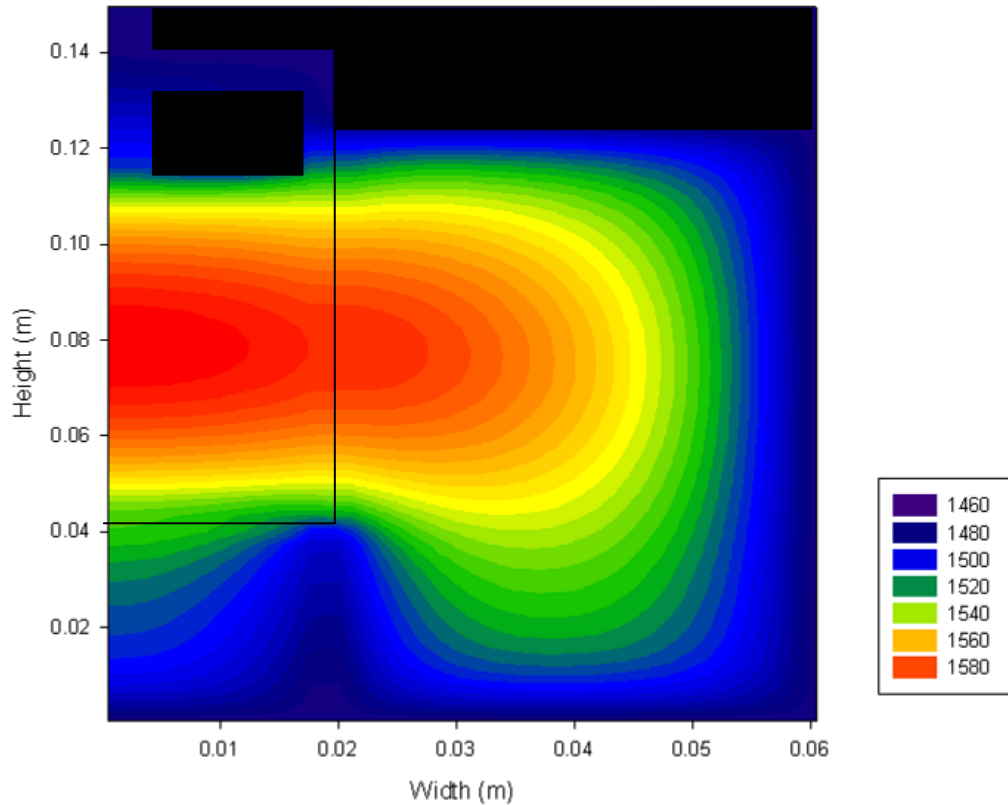
**A2.7 SEM Micrograph of the Surface of a Polished Disc Section
from a Bulk Rod Heat Treated @ 1050 °C.**



This image clearly shows the presence of porosity throughout the bulk of the sample, which is also shown in figure 4.11.

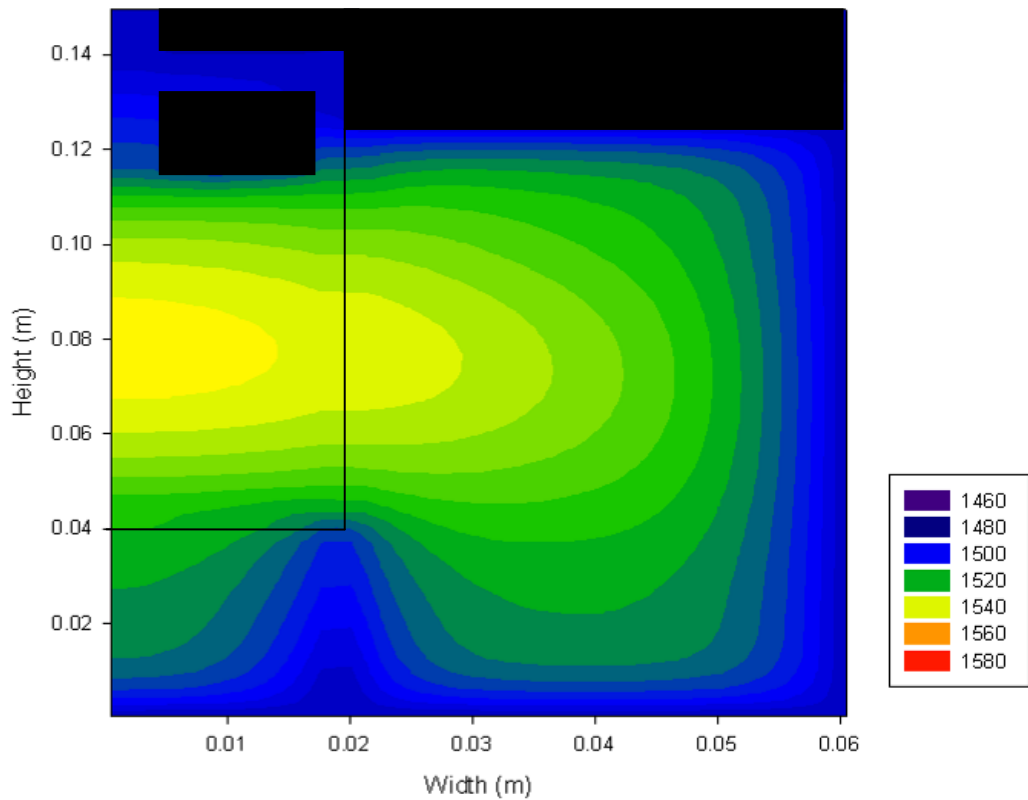
A3.1 Thermographs from single crystal growth experiment.

Thermograph of single crystal apparatus after 15 minutes from lid replacement



The above image has been produced by a computer program, written in *Pascal* language by the author, designed to simulate the effects of thermal conduction through the apparatus and variations of temperature gradients with time. Individual elements such as the inner and outer alumina crucibles, glass melt and alumina powder compact were modelled as separate materials with bulk values for thermal conductivity (W/mK), density (kg/m^3) and thermal capacity (kJ/kgK) used in the calculations; the key at the right is in Kelvin (K).

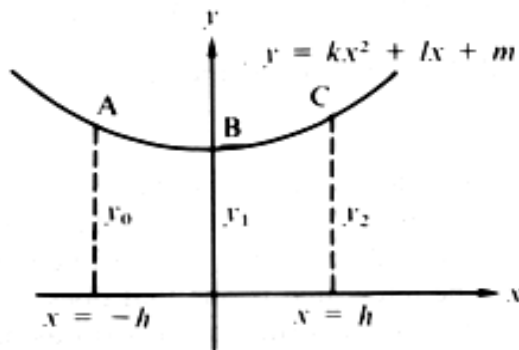
Thermograph of single crystal apparatus after 30 minutes from lid replacement



This simulation shows that after 30 minutes of temperature cycling, between 1200 °C and 1260 °C, the core temperature has reduced, however, significant melt stratification still remains particularly at the melt surface near the top of the crucible, which is crucial for crystal growth.

A4.1 Simpson's Rule – A Numerical Method of Integration

An accurate approximation of the integral of any curve can be obtained by Simpson's rule. This technique treats the area underneath a curve as a series of strips with the top of each strip approximating to a quadratic curve shown in the diagram below.



Suppose that a curve of the form $y = kx^2 + lx + m$ passes through the points: - **A**(-h, y_0), **B**(0, y_1) and **C**(h, y_2). The area under the curve between the coordinates $x = -h$ and $x = h$ is given by:-

$$\int_{x=-h}^{x=h} (kx^2 + lx + m)dx = \left[\frac{kx^3}{3} + \frac{lx^2}{2} + mx \right]_{-h}^h$$
$$= \frac{2}{3} h(kh^2 + 3m) \quad (1)$$

Since A, B and C lie on the curve,

$$y_0 = kh^2 - lh + m \quad (2)$$

$$y_1 = m \quad (3)$$

$$y_2 = kh^2 + lh + m \quad (4)$$

Adding equations (2) and (4) and substituting for m from equation (3) gives:-

$$\frac{1}{2}(y_0 + y_2) - y_2 = kh^2$$

Finally, substituting these values of m and kh^2 into equation (1) gives:-

$$\begin{aligned} \int_{x=-h}^{x=h} (kx^2 + lx + m)dx &= \frac{2}{3}h \left[\frac{1}{2}(y_0 + y_2) - y_1 + 3y_1 \right] \\ &= \frac{1}{3}h(y_0 + 4y_1 + y_2) \quad (5) \end{aligned}$$

The above expression (5) can be summed over all pairs of strips with a numerical algorithm; accuracy with this technique requires that the number of segments subtended by a curve is high.

Reference:-

‘Understanding Pure Mathematics’, A.J.Sadler, Oxford University Press (1999).

A5.1 Structure of Barium Fluoro-Phosphates Phase (BaPO₃F)

	x	y	z	Occupancy	UIISO
Ba	0.158	0.185	0.25	1	0.025
P	0.191	0.437	0.75	1	0.025
O	0.107	0.587	0.75	1	0.025
F	0.050	0.318	0.75	1	0.025
O	0.312	0.419	0.97	1	0.025

A5.2 Structure of the Bulk Ba-Mica Phase.

	x	y	z	Occupancy	UIISO
Ba	0.5	0.5	0.5	0.70	0.038
Si	0.075	0.333	-0.278	0.65	0.031
Al	0.075	0.333	-0.278	0.35	0.031
Mg	0.0	0.5	0.0	1	0.016
Mg	0.0	0.169	0.0	1	0.016
O	0.011	0.5	0.341	1	0.012
O	0.175	0.229	0.340	1	0.012
O	0.131	0.334	-0.110	1	0.012
F	0.131	0.0	-0.110	1	0.029

Both the barium occupancy and the UIISO parameters, above, have been refined in GSAS as part of the Rietveld refinement in section 4.2.2.5.

A6.1 Poster/Talk Presentations

LDI Research Day Poster (11/2007)

'A Study of Novel Aesthetic Dental Materials'

19th European Dental Materials Conference Poster (8/2007)

'Effect of Feedstock on the Crystallisation of Mica Glass-Ceramic'

Nottingham University Neutron and Muon User Meeting (3/2008)

'Novel Aesthetic Dental Restorative Materials'

LDI Research Day Talk (11/2008)

'Structure of Novel Aesthetic Dental Materials'

iPRD Pre-symposium on Crystallisation Science and Engineering Talk. (3/2009)

'Structural Solution of Novel Aesthetic Dental Materials'

IADR Miami Conference Poster (4/2009)

'Structural Solution of Novel Aesthetic Dental Materials'

A7.1 *Shelx 97*® Output *.FCF* file from Single Crystal Refinement.

An *.FCF* file produced by *Shelx*® '97 refinement of single crystal data. $F^2(\text{Calc})$ and $F^2(\text{Obs})$ are the calculated and observed structure factors squared respectively. $F^2(\text{Sigma})$ is the predicted error.

h	k	l	$F^2(\text{Calc})$	$F^2(\text{Obs})$	$F^2(\text{Sigma})$
-3	-5	1	950.26	1007.49	25.36
-2	-5	1	760.54	825.44	25.97
-3	-4	1	705.19	738.44	17.67
1	-4	1	1212.47	1431.3	36.54
-4	-3	1	1951.31	1900.21	28.3
-2	-3	1	1878.4	1863.57	24.94
-1	-3	1	1126.56	1230.44	17.45
3	-3	1	2282.08	2399.92	56.91
-3	-2	1	1408.39	1400.67	19.24
-2	-2	1	1536.76	1476.83	18.22
2	-2	1	2647.47	2686.82	33.27
-4	-1	1	1958.23	1838.37	30.91
-3	-1	1	1393.89	1412.16	22.05
-1	-1	1	1484.59	1479.29	16.06
1	-1	1	5847.2	5544.97	52.96
4	-1	1	902.93	818.21	20.27
-3	1	1	698.9	729.08	14.33
-2	1	1	1874.45	1786.88	22.55
2	1	1	2544.85	2392.21	34.01
5	1	1	1205.14	1387.2	77.99
-3	2	1	956.04	898.06	19.28
-1	2	1	1125.24	1159.53	18.36
1	2	1	5864.9	5841.79	56.73
2	2	1	1784.41	1777.13	19.42
4	2	1	2636.64	2467.55	36.17
-2	3	1	762.16	785.12	23.75
3	3	1	8798.1	8702.06	95.86
2	4	1	2671.49	2789.76	39.55
5	4	1	1211.6	1253.76	26.56
1	5	1	1230.01	1695.64	36.48
4	5	1	896.85	832.33	27.4
3	6	1	2287.41	2720.66	58.82
5	7	1	669.36	745.34	81.11
-3	-4	2	927.63	914.26	17.82
-1	-4	2	937.96	1036.65	21.32
-2	-3	2	2230.28	2155.12	28.47

h	k	l	F ² (Calc)	F ² (Obs)	F ² (Sigma)
-1	-3	2	2692.65	2869.97	36.39
1	-3	2	1439.92	1501.78	23.68
-3	-2	2	1272.98	1198.91	17.72
1	-2	2	940.52	1010.94	14.08
-3	-1	2	1264.46	1213.48	18.16
-2	-1	2	4751.99	4506.89	49.57
-1	-1	2	4244.48	4071.03	40.05
4	-1	2	1228.37	1280.42	25.68
-3	1	2	924.92	897.64	13.41
-2	1	2	2211.46	2116.84	25.91
1	1	2	2718.81	2664.81	26.95
5	1	2	886.03	843.01	54.25
-1	2	2	2713.42	2679.52	32.33
2	2	2	1541.5	1530.62	18.27
4	2	2	4009.28	3907.11	58.79
-1	3	2	930.7	986.47	17.65
1	3	2	941.14	1039.82	14.63
6	3	2	2294.38	2383.75	52.87
1	4	2	1448.95	1562.66	25.71
5	4	2	888.01	878.48	23
4	5	2	1236.73	1314.35	40.51
6	6	2	1779.07	2095.53	79.77
-3	-6	3	1041.17	1062.96	39.41
-5	-4	3	2716.36	2797.31	66.59
-1	-4	3	710.6	700.2	17.68
-3	-3	3	1932.66	1876.81	26.77
1	-3	3	1665.25	1663.06	25.24
2	-3	3	747.71	761.1	26.55
-1	-2	3	2519.59	2564.28	27.97
1	-2	3	1559.29	1600.65	21.6
-5	-1	3	2723.41	2631.34	67.58
-1	-1	3	1611.17	1597.96	18.11
1	-1	3	4696.72	4740.1	49.43
2	-1	3	1655.19	1641.17	19.8
3	-1	3	1858.58	1734.27	26.48
-1	1	3	2526	2531.22	30.01
1	1	3	3779.17	3654.85	38.26
3	1	3	2579.78	2439.95	34.05
1	2	3	4715.85	4840.47	46.93
2	2	3	1031.43	959.02	13.37
3	2	3	2575.8	2488.97	32.02
-3	3	3	1034.27	1086.1	35.5
-1	3	3	706.13	706.44	15.07

h	k	l	F ² (Calc)	F ² (Obs)	F ² (Sigma)
1	3	3	1555.52	1631.89	21.84
2	3	3	1667.29	1682.95	22.31
1	4	3	1672.81	1747.85	29.24
3	4	3	1862.91	1790.46	29.04
2	5	3	751.85	830.92	23.78
3	5	3	705.06	744.75	21.65
-4	-5	4	1177.5	1273.78	38.05
-2	-4	4	3929.94	3998.84	62.17
-3	-3	4	1494.22	1433.82	22.62
-4	-2	4	3244.14	3138.77	54.36
-1	-2	4	1523.22	1512.75	18.74
-2	-1	4	6663.37	6215.75	70.7
2	-1	4	874.5	846.58	13.56
3	-1	4	1037.49	1006.76	16.66
-4	1	4	1182.19	1213.44	34.75
-1	1	4	1528.67	1514.58	20.82
1	1	4	864.56	861.54	11.6
2	1	4	2453.77	2330.31	27.63
3	1	4	1346.63	1252.37	15.97
4	1	4	992.59	982.17	17.19
-2	2	4	3910.89	3811.01	55.2
3	2	4	1355.12	1280.98	18.16
5	2	4	906.89	835.81	19.71
-3	3	4	738.2	738.92	40.08
2	3	4	873.58	871.07	14.85
4	3	4	993.82	1015.61	17.62
5	3	4	921.23	874.55	22.35
3	4	4	1037.92	1035.3	19.7
-1	-5	5	1194.24	1310.59	37.36
-4	-4	5	722.19	741.84	26.21
1	-4	5	2754.49	2773.13	80.64
-2	-2	5	1195.1	1206.23	20.15
-1	-2	5	5609.9	5296.37	56.6
1	-1	5	6770.99	6380.17	69.34
-1	1	5	5642.07	5147.1	63.11
2	1	5	1500.22	1439.81	22.49
1	2	5	6751.25	6581.82	72.71
3	3	5	1928.22	1891.65	29.21
-1	4	5	1193.95	1291.07	47.31
1	5	5	2749.49	3035.91	78.23
-2	-3	6	923.47	942.45	20.61
-2	-2	6	2088.48	2034.19	36.87
-1	-2	6	1883.61	1782	26.31

h	k	l	F ² (Calc)	F ² (Obs)	F ² (Sigma)
2	-2	6	3254.86	3252.35	50.95
-1	-1	6	807.62	746.36	13.73
4	-1	6	2738.46	2780.28	57.92
-2	1	6	938.32	931.63	18.13
-1	1	6	1877.48	1670.64	34.62
2	1	6	5595.61	5039.52	71.42
2	2	6	715.39	729.06	12.98
4	2	6	3927.51	3737.82	58.96
3	3	6	1499.1	1436.51	26.1
6	3	6	1021.41	1037.58	27.86
2	4	6	3274.19	3325.55	63.11
4	5	6	2740.64	2807.96	72.33
-3	-3	7	1412.93	1249.26	37.06
-1	-3	7	786.73	822.13	21.59
1	-3	7	683.76	700.75	22.6
-1	-1	7	950.88	908.01	16.93
1	1	7	1118.56	1079.4	20.51
2	1	7	1843.84	1627.7	26.92
5	1	7	1186.09	1187.22	39.51
-1	2	7	794.56	824.36	21.08
2	2	7	2019.4	1942.83	29.2
6	3	7	743.39	719.02	28.13
5	4	7	1193.31	1255.13	42.05
-4	-2	8	697.36	720.12	36.34
-2	-1	8	1979.66	1967.39	42.25
3	-1	8	763.08	710.59	27.52
3	1	8	976.49	956.76	30.04
-2	2	8	702.18	743.61	31.6
2	2	8	1251.54	1173.32	25.4
3	2	8	982.54	964.36	20.75
3	4	8	757.24	767.74	30.67
4	4	8	886.95	850.94	32.79
-3	-3	9	1091.1	951.85	52.22
-1	-2	9	1934.92	1765.94	39.08
1	-1	9	1946.42	1805.47	63.49
-1	1	9	1926.29	1876.95	53.45
1	2	9	1961.88	1809.58	39.73
3	3	9	1379.87	1297.18	35.72
2	1	10	1936.5	2006.46	42.58
3	3	11	1108.93	1240.13	74.04
-2	-1	12	813.06	814.9	63.38
1	2	13	796.68	769.73	50.52